DI-MUONS NEAR THE Υ RESONANCES IN ATLAS

Yi Yang

Submitted to the faculty of the University Graduate School
in partial fullfilment of the requirements
for the degree
Doctor of Philosophy
in the Department of Physics,
Indiana University
June 2012

Accepted by the Graduate Faculty, Indiana University, in partial fulfillment of the requirements for the degree of Doctor of Philosophy.

Doctoral Committee

Harold G. Evans, Ph.D.

Micheal S. Berger, Ph.D.

Sabine Lammers, Ph.D.

Harold O. Ogren, Ph.D.

Richard J. Van Kooten, Ph.D.

April 23, 2012

To my parents

Acknowledgments

First of all, I would like to thank my thesis advisor Professor Hal Evans. From him I learned so much. He teaches me not only on how to solve problems in analyses, but also on how to be a good physicist. He always has infinite patience to help me with the research. Without his guidance, my Ph.D. research wouldn't be able to go so smoothly. However, physics was not the only thing I learned from him, he also introduced us lots of delicious foods (one of the most important ingredients to do good physics).

I also would like to thank Professor Harold Ogren. When I applied for admission to graduate school, he was the first one who contacted me, and coming to Bloomington is no doubt one of the best things and decisions I had ever made. He showed us the correct attitude to be a good scientist: always being enthusiastic about all kind of physics. I was so touched that he attended my thesis defense via Skype after a serious car accident right before my defense.

And then, many thanks to Dr. Darren Price, I had a great time to work with him, and we do have lots of great results. I learned lots of quarkonium physics from him, and he gave me a lot of help with the analyses.

I would like to thank Dr. Fred Luehring, and his wife Donna Lafferty for providing

me a place to stay and letting me to feel like home when I moved back to the States to write my thesis. And special thanks to their lovely cats, Sukey, Cleo, Billie, Meatloaf and Maxie. They are my great helper when I was writing my thesis, and I had lots of fun with them every night.

We have a great high energy physics group in Indiana University. I have to thank to everybody in the group for giving my great five years. Especially I would like to thank Thom Sulanke for maintaining our computer cluster and helping me with many computing problems. Dr. Daria Zieminska also taught me a lot when we did "boosted top quark" analysis in my first year at IU. In addition, I really have to thank Dr. Peter Cwetanski for helping me with my French issues to make my life much easier at CERN.

Many thanks to the rest of thesis committee members, Professor Micheal Berger, Professor Sabine Lammers, and Professor Rick Van Kooten for many valuable suggestions and comments to make this thesis better.

Besides, I would like to thank the ATLAS Collaboration, especially to B-physics and Higgs groups, without the smooth running experiment, is was impossible for my analyses to be finished. Many thanks also to Dr. James Catmore who prepared the analysis framework for B-physics group and helped me a lot with many software issues.

My dear friends also did a good job to make my PhD life to be more enjoyable, especially would like to thank Fang-Chin Yeh, Denver Whittington, Peng Guo, Liming Zhou, Leo Mesquita, and John Penwell from IU, and Jianrong Deng, Xianguo Lu from CERN, and CC Chiang, KZ Chen, JJ Bao and Pei-Chun Liu from Taiwan. And thanks to my friends whom I don't mention here – you know I remember you!

Finally, my deepest thank goes to my parents, my brother and his wife – without their supports and encouragements, I wasn't able to finish my PhD study.

Yi Yang at Indiana University, Bloomington. May 05, 2012

Yi Yang

Di-Muons near the Υ resonances in ATLAS

We present measurements of the production cross-section of Upsilon mesons with di-muon final state in pp collision at a 7 TeV center-of-mass energy. The data were collected with the ATLAS detector at CERN with a corresponding integrated luminosity of 1.85 fb^{-1}. We also report a search for a very light CP-odd Higgs boson, a_1, decaying to di-muon pairs. Such a light Higgs boson is predicted in Next-to-Minimal extensions of the Supersymmetric Standard Model (NMSSM). We set limits on the production cross-section times branching ratio for a_1 masses of 6 – 9 GeV and 11 – 12 GeV, avoiding the region dominated by the Upsilon resonances.

Contents

List of Figures

List of Tables

Chapter 1

Introduction

"There are two possible outcomes: if the result confirms the hypothesis, then you've made a measurement. If the result is contrary to the hypothesis, then you've made a discovery."

– **E. Fermi**

"Why is high energy particle physics important?", "Why do we have to spend so much money on building a high energy collider? Is this really necessary?" I always get these kinds of questions from my friends, and honestly these questions can not be answered easily. Generally speaking, our lives won't feel any different if Higgs bosons exist or not, if neutrinos travel faster than light or not, etc. However, understanding the fundamental physical laws of the world in which we live is always fascinating, isn't it? High energy physicists try to determine these fundamental physical laws.

Since the last century, our knowledge of the elementary particles has expanded rapidly. For instance, we now realize there are four types of interactions, there are three generations of elementary particles, etc. We also have already had remarkable success in comparisons between theoretical predictions and experimental measurements. Still, people might ask again: "Do we really need a new collider?" I respond to this question by quoting from my favorite movie – Apollo 13: "Imagine if Christopher Columbus came back from the New World, and no one returned in his footsteps" said Jim Lovell when asked about why we want to keep sending people to the moon after the Apollo 11 project. In high energy particle physics, we are just opening a door to let us see the world more clearly, and there are still many unsolved problems. Why should we stop? The Large Hadron Collider started operation in 2009, and this provides us a great opportunity to keep expanding our knowledge of fundamental physics.

This thesis covers three interesting topics in modern high energy particle physics: Quantum Chromodynamics, physics beyond the Standard Model (Supersymmetry), and the search for Higgs bosons (in a Supersymmetric model).

In Chapter 2, I first present an overview of the Standard Model of particle physics, with an emphasis on quarkonium physics. I then discuss physics beyond the Standard Model, in particular Supersymmetric Models. After the theoretical introduction, Chapter 3 presents an overview of the Large Hadron Collider and the ATLAS detector.

Chapter 4 summarizes the dataset and Monte Carlo simulations used in the thesis. The two analyses in this thesis, the Υ cross-section measurements and the search for the light CP-odd Higgs boson, are both performed using di-muon final states. Chapter 5 therefore discusses the di-muon selections and efficiency determinations for both muon reconstruction and the di-muon trigger. The following Chapter 6 presents the Υ production cross-section measurements in detail. Chapter 7 reports on the search for the light CP-odd Higgs in the Next-to-Minimal Supersymmetric Standard Model (NMSSM). Finally in Chapter 8, a summary of the thesis is presented. Appendices contain several plots that are relevant to the analyses.

Chapter 2

Theoretical Overview

"If you can't explain it simply, you don't understand it well enough."

– **A. Einstein**

2.1 The Standard Model of Particle Physics

When Dirac married Quantum Mechanics and Relativity together successfully, he opened a door for Quantum Field Theory in the late 1920s [1]. Fermi proposed the first theory of the weak interaction in 1933 to explain beta decay [2], called "Fermi theory". Quantum Electrodynamics (QED) was developed by Tomonaga [3], Schwinger [4, 5], Feynman [6, 7, 8], Dyson [9, 10], etc., in the 50s. After that, Quantum Chromodynamics (QCD) was built, and then Gross, Politzer and Wilczek discovered asymptotic freedom in QCD theory [11]. Incorporating all these elements into a single framework, the properties of elementary particles and fundamental interactions can be described by the Standard Model of particle physics (SM) [14, 15, 16].

In this modern view, particles interact by exchanging particles (or force carriers, gauge bosons) that are described in gauge theories. There are four fundamental interactions in Nature: electromagnetic (EM), weak, strong and gravity, and the corresponding gauge bosons are the photon, the $W^{\pm}$ and Z^0, the gluons and the graviton[1], respectively (see Table 2.1). In the SM, twelve fermions (spin 1/2), leptons and quarks, are the elementary matter particles and are viewed as point particles (i.e., with no structure). They can be categorized into three generations. Between generations, particles have different quantum numbers (flavor) and masses, but have identical interactions. Quarks carry not only electric charge, but also "*color*" charge. Their properties are summarized in Table 2.2.

One of the most remarkable predictions of Dirac's relativistic quantum mechanics is that each particle has an associated anti-particle. Aside from the opposite electric charge, all other quantum numbers, like the spin or the mass, of the anti-particle are identical to those of the particle. For example, the positron (e^+) is the anti-particle

[1]The photon, the $W^{\pm}$ and Z^0 and the gluons are spin-1 gauge bosons; the graviton is a hypothetical particle with spin 2.

Interaction	EM	Weak		Strong
Gauge Boson	Photon (γ)	W boson ($W^{\pm}$)	Z boson (Z)	Gluon (g)
mass (GeV)	0	80.4	91.2	0
charge	0	± 1	0	0

Table 2.1: The gauge bosons in the SM and their properties.

Generation	1^{st}		2^{nd}		3^{rd}	
Leptons	e	ν_e	μ	ν_μ	τ	ν_τ
	Electron	Electron-neutrino	Muon	Muon-neutrino	Tau	Tau-neutrino
mass (MeV)	0.511	< 2.3 eV	106	< 0.19	1.78×10^{3}	< 18.2
charge	-1	0	-1	0	-1	0
Quarks	u	d	c	s	t	b
	Up	Down	Charm	Strange	Top	Bottom
mass (GeV)	1.5 – 3×10^{-3}	3 – 7×10^{-3}	1.25	9.5×10^{-5}	174.2	4.2
charge	$+2/3$	$-1/3$	$+2/3$	$-1/3$	$+2/3$	$-1/3$

Table 2.2: The elementary fermions in the SM.

of the electron and was discovered in 1932 by Anderson [12] in cosmic-ray data.

The composite particles that are made of quarks are called *hadrons*, and the bonding interaction between quarks in hadrons is the strong force. There are two categories of hadrons: *mesons* and *baryons*. Mesons are made of two quarks: one quark and one anti-quark; baryons are made of three quarks. For example, the pion (π) is composed of an up quark (u) and an anti-down ($\bar{d}$) quark, while the proton is composed of two up quarks and one down quark.

From the point of view of gauge field theory[2], there are three local symmetries in the SM combining to $SU(3)_{\text{color}} \otimes SU(2)_{\text{left}} \otimes U(1)_{\text{Y}}$. Interactions in the SM are constructed from three types of bosonic gauge fields that correspond to the three local symmetries. The strong interaction is described by Quantum Chromodynamics (QCD) and the corresponding gluon fields are invariant under the $SU(3)_{\text{color}}$ gauge transformation. The electroweak interaction (W and B fields) has $SU(2)_{\text{left}} \otimes U(1)_{\text{Y}}$ symmetry. The field components are:

$$\begin{aligned} \text{Gluon fields}: &\quad G^a_\mu \quad [\text{with } a = 1, 2, ..., 8], \qquad SU(3)_{\text{color}} \\ \text{Weak fields}: &\quad W^i_\mu \quad [\text{with } i = 1, 2, 3], \qquad SU(2)_{\text{left}} \\ \text{B fields}: &\quad B_\mu, \qquad U(1)_{\text{Y}} \end{aligned} \tag{2.1}$$

The three generations of fermionic matter fields in the SM (leptons and quarks) interact differently under the electroweak force depending on their helicity. Left-handed fermions form weak isospin doublets, and right-handed fermions are isospin singlets, as shown below:

$$\begin{aligned} \text{Quarks}: \quad Q^i_L &= \left(\begin{pmatrix} u^i \\ d^i \end{pmatrix}_{\text{L}}, \begin{pmatrix} c^i \\ s^i \end{pmatrix}_{\text{L}}, \begin{pmatrix} t^i \\ b^i \end{pmatrix}_{\text{L}} \right) \\ U^i_R &= (u^i_R,\ c^i_R,\ t^i_R) \end{aligned}$$

[2] "Gauge" refers to redundant degrees of freedom in the Lagrangian. The gauge field theory means the Lagrangian is invariant under a gauge transformation.

$$D_R^i = (d_R^i,\ s_R^i,\ b_R^i) \tag{2.2}$$

$$\begin{aligned} \text{Leptons}: \quad L &= \left(\begin{pmatrix} \nu_e \\ e \end{pmatrix}_{\mathrm{L}}, \begin{pmatrix} \nu_\mu \\ \mu \end{pmatrix}_{\mathrm{L}}, \begin{pmatrix} \nu_\tau \\ \tau \end{pmatrix}_{\mathrm{L}} \right) \\ R &= (e_R,\ \mu_R,\ \tau_R) \end{aligned}$$

where i is the color charge. Neutrinos are assumed to be massless and only left-handed components exist.

In the minimal version of the SM, a single doublet of complex scalar fields is introduced in order to break electroweak symmetry as described in next section. The field components of the scalar fields are:

$$\text{Higgs}: H = \begin{pmatrix} H^+ \\ H^0 \end{pmatrix}, \tag{2.3}$$

After putting all components (gauge, matter and Higgs sectors) together, the final Lagrangian of the SM can be written as:

$$\begin{aligned} \mathcal{L}_{\mathrm{SM}} = & \underbrace{-\frac{1}{4} W_{\mu\nu}^i \cdot W_i^{\mu\nu} - \frac{1}{4} B_{\mu\nu} B^{\mu\nu} - \frac{1}{4} G_{\mu\nu}^a \cdot G_a^{\mu\nu}}_{\mathrm{W^{\pm}},\ \mathrm{Z},\ \gamma \text{ and gluon kinetic energies and self-interactions}} \\ & + \underbrace{i\bar{L}_\alpha \gamma^\mu D_\mu L_\alpha + i\bar{R}_\alpha \gamma^\mu D_\mu R_\alpha}_{\text{Lepton's kinetic energies and their interactions with } \mathrm{W^{\pm}},\ \mathrm{Z} \text{ and } \gamma} \\ & + \underbrace{i\bar{Q}_\alpha \gamma^\mu D_\mu Q_\alpha + i\bar{U}_\alpha \gamma^\mu D_\mu U_\alpha + i\bar{D}_\alpha \gamma^\mu D_\mu D_\alpha}_{\text{Quark's kinetic energies and their interactions with } \mathrm{W^{\pm}},\ \mathrm{Z},\ \gamma \text{ and gluons}} \\ & + \underbrace{(D_\mu H)^\dagger (D_\mu H)}_{\mathrm{W^{\pm}},\ \mathrm{Z},\ \gamma\text{-Higgs couplings}} + \underbrace{\mu^2 H^\dagger H - \frac{\lambda}{2}(H^\dagger H)^2}_{\text{Higgs potential, mass terms and quartic coupling}} \\ & + \underbrace{y_{\alpha\beta}^L \bar{L}_\alpha R_\beta H + y_{\alpha\beta}^D \bar{Q}_\alpha D_\beta H + y_{\alpha\beta}^U \bar{Q}_\alpha U_\beta \tilde{H} + h.c.}_{\text{Leptons, Quarks-Higgs Yukawa coupling}} \end{aligned} \tag{2.4}$$

where,

$$W_{\mu\nu}^i = \partial_\mu W_\nu^i - \partial_\nu W_\mu^i + g\epsilon^{ijk} W_\mu^j W_\nu^k;$$

$$
\begin{aligned}
B_{\mu\nu} &= \partial_\mu B_\nu - \partial_\nu B_\mu; \\
G^a_{\mu\nu} &= \partial_\mu G^a_\nu - \partial_\nu G^a_\mu + g f^{abc} G^b_\mu G^b_\nu, \\
D_\mu L_\alpha &= \left(\partial_\mu - i\frac{g}{2}\tau^i W^i_\mu + i\frac{g'}{2}B_\mu\right) L_\alpha; \\
D_\mu R_\alpha &= \left(\partial_\mu + ig' B_\mu\right) R_\alpha; \\
D_\mu Q_\alpha &= \left(\partial_\mu - i\frac{g}{2}\tau^i W^i_\mu - i\frac{g'}{6}B_\mu - i\frac{g_s}{2}\lambda^a G^a_\mu\right) Q_\alpha; \\
D_\mu U_\alpha &= \left(\partial_\mu - i\frac{2}{3}g' B_\mu - i\frac{g_s}{2}\lambda^a G^a_\mu\right) U_\alpha; \\
D_\mu D_\alpha &= \left(\partial_\mu + i\frac{1}{3}g' B_\mu - i\frac{g_s}{2}\lambda^a G^a_\mu\right) D_\alpha; \\
D_\mu H &= \left(\partial_\mu + i\frac{g}{2}\tau^i W^i_\mu + i\frac{g'}{2}B_\mu\right) H; \\
\tilde{H} &= i\tau_2 H^\dagger
\end{aligned}
\tag{2.5}
$$

α, β = 1, 2...n (number of generations), τ_i are the Pauli matrices, and $\lambda^{\mathbf{a}}$ are the Gell-Mann matrics. The Lagrangian of the SM contains the following set of free parameters: 3 gauge coupling constants (g_s, g and g'), 3 Yukawa matrices ($y^L_{\alpha\beta}$, $y^D_{\alpha\beta}$ and $y^U_{\alpha\beta}$), the Higgs coupling constant (λ), the Higgs mass parameter (μ) and the number of generations (n).

2.1.1 Spontaneous Symmetry Breaking: Higgs Mechanism

Unlike the EM force that is a long distance force, the weak force is a short distance one that implies that the weak force carriers must be massive. An interesting question is then raised: how do the weak gauge bosons get their masses? In the SM without the Higgs sector, the fermions and gauge bosons are massless. If we put in by hand the mass term, such as $m^2 W^\mu W_\mu$, into the Lagrangian, the invariance of $SU(2)_{\text{left}} \otimes U(1)_{\text{Y}}$ would be broken, but the theory would not be renormalizable. This method of breaking the symmetry is called "hard symmetry breaking".

During the 1960's, the idea of "Spontaneous Symmetry Breaking (SSB)" [17] was

recognized to be an important concept to solve the mass term problem[3]. Higgs was the first to suggest adding a scalar complex field, known as the Higgs field, into the Lagrangian, and to couple this scalar field gauge invariantly with the rest of the system [18, 19]. A potential generated by this scalar complex field (the Higgs potential), with minima that are not symmetric under the gauge transformation, is also introduced into the Lagrangian. Furthermore, he assumed that the ground state corresponds to one of these non-gauge symmetric minima. With Higgs' idea, we have a Lagrangian that remains invariant under gauge transformations, but the symmetry is broken by the choice of the ground state. This soft symmetry breaking process is known as Spontaneous Symmetry Breaking. In 1967, Weinberg [20] and Salam [21] unified the electromagnetic and the weak interactions by using the $SU(2)_{\text{left}} \otimes U(1)_{\text{Y}}$ gauge group as the underlying gauge symmetry and give the gauge particles masses through the *Higgs Mechanism*. This is the famous *Weinberg-Salam Model*. In 1971, this electroweak theory was proved to be a renormalizable theory by 't Hooft, Veltmann [22] and B. Lee [23, 24]. After all this hard work and the remarkable predictions of the existence and masses of the $W^{\pm}$ and Z^0 bosons that were discovered at CERN in the early 80s [25], this electroweak theory became one of the most beautiful theories in modern physics. A good historical review of the Higgs boson can be found in [26].

The main purpose of the Higgs Mechanism is to softly break the $SU(2)_{\text{left}} \otimes U(1)_{\text{Y}}$ symmetry down to the $U(1)_{\text{EM}}$ symmetry. The unbroken $U_{\text{EM}}(1)$ symmetry guarantees that the photon remains massless. The Higgs potential, $V_{\text{Higgs}} = -\mu^2 H^\dagger H + \frac{\lambda}{2}(H^\dagger H)^2$, in Eq. 2.5 plays a key role in electroweak symmetry breaking. The simplest choice of field is shown in Eq. 2.3, and the non-zero vacuum expectation value (v.e.v.) that is taken as the minimum of the ground state solution of the Lagrangian with

[3]This idea was brought to the condensed matter community by Nambu and Goldstone, and then to the particle physics community by Nambu later on.

$\mu^2 < 0$ and $\lambda > 0$ of the Higgs field is:

$$\langle H \rangle_0 = \begin{pmatrix} 0 \\ v \end{pmatrix}, \qquad v = \frac{\mu}{\sqrt{\lambda}}, \tag{2.6}$$

The Higgs field can be re-written in the form [15, 27]:

$$H(x) = \begin{pmatrix} 0 \\ v + h(x) \end{pmatrix}, \tag{2.7}$$

where $h(x)$ is an excitation around the symmetry broken ground state solution v. The contributions to the weak gauge fields can be extracted by putting Eq. 2.7 into the $W^{\pm}/Z$, γ coupling term, $(D_\mu H)^\dagger (D_\mu H)$, in Eq. 2.5. The physical electroweak gauge fields are the linear combinations of the original fields that can be written as:

$$W_\mu^{\pm} = \frac{W_\mu^1 \mp i W_\mu^2}{\sqrt{2}}, \quad Z_\mu = -\sin\theta_W B_\mu + \cos\theta_W W_\mu^3, \quad A_\mu = \cos\theta_W B_\mu + \sin\theta_W W_\mu^3, \tag{2.8}$$

where θ_W is called *Weinberg angle*, that is defined as:

$$\cos\theta_W = \frac{g}{(g^2 + g'^2)^{\frac{1}{2}}}, \quad \tan\theta_W = \frac{g'}{g}, \tag{2.9}$$

where g and g' are the $SU(2)_{\text{left}}$ and the $U(1)_{\text{Y}}$ coupling constants, respectively.

With this shifting, mass terms appear automatically in the Lagrangian. For example, there are terms $m_W^2 W_\mu^+ W^{-\mu}$ and $m_Z^2 Z_\mu Z^\mu$ with $m_W = \frac{1}{\sqrt{2}} g v$ and $m_Z = m_W / \cos\theta_W$, respectively. A_μ is massless as expected. The Higgs mass can be determined in the Higgs potential term in Eq. 2.5 giving $m_H = \sqrt{2\lambda} v$. The v.e.v. (v) of the Higgs field can be calculated by using the relation between v and G_F[4], namely $v = (\sqrt{2} G_F)^{-\frac{1}{2}} \simeq 246$ GeV. From this, the W and Z masses are ∼80 GeV and ∼90 GeV that agree amazingly well with experimental measurements.

The Higgs boson is the only remaining particle that has not been observed in the Standard Model. The latest experimental exclusion limits on the SM Higgs boson

[4]Fermi constant: $\frac{G_F}{(\hbar c)^3} = \frac{\sqrt{2}}{8} \frac{g^2}{m_W^2} = 1.16637(1) \times 10^{-5}$ GeV^{-2}.

mass from the LHC (CERN) [28, 29] and the Tevatron (Fermilab) [30] are summarized in the Fig.2.1. The combined limits constrain the mass of SM Higgs boson to be around $115 - 130$ GeV, and both ATLAS and CMS experiments observe a hint at a mass of 125 GeV with $\sim 3\sigma$ significance.

2.2 Hadron Collider Physics

The mathematical description of hadron-hadron collisions basically follows the same treatment as electron-positron[5] collisions with the exception that the real colliding constituents in a hadron-hadron interaction are quarks or gluons, also known as *partons*, instead of the entire hadrons. In 1969, Feynman proposed a way to analyze high-energy hadron collisions – the so called "parton model [31]." An illustration of a proton-proton interaction is shown in Fig. 2.2.

Cross-sections for a variety of SM processes as a function of center-of-mass energy in $pp(\bar{p})$ collisions are shown in Fig. 2.3. In a 7 TeV pp collision, the bottom quark production rate is $\sim 1\%$ of the total production, and the SM Higgs boson (with $m_H = 150$ GeV) cross-section is $O(10^{-8})$ smaller than b-quark production. Calculation of each of the cross-sections displayed in Fig. 2.3 requires an understanding of all aspects of the formation of final state particles in proton-proton collisions. The main steps in this chain are described briefly in the following.

2.2.1 Initial and Final State Radiation

As shown in Fig. 2.2, the parton has some probability to lose energy by radiating a photon or a gluon before the collision. This process is referred to as initial-state radiation (ISR). Similar to ISR, the final state particle is also able to radiate a photon

[5] Good examples can be found in Ref. [15].

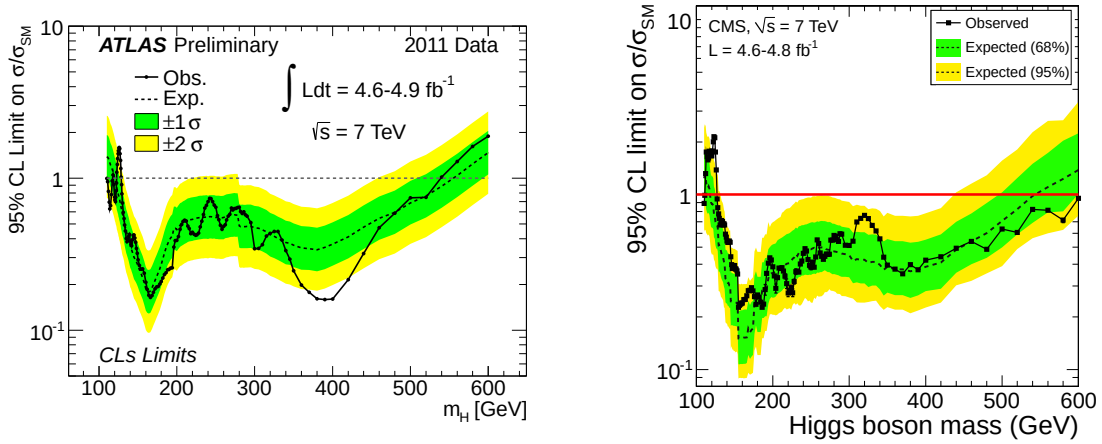

(a) (b)

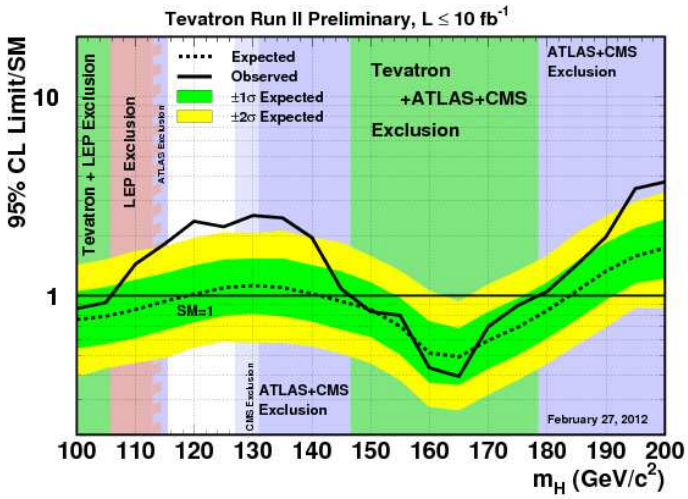

(c)

Figure 2.1: The latest exclusion limits on the mass of the Standard Model Higgs boson from (a) ATLAS, (b) CMS, and (c) the Tevatron. The combined limits constraint the mass of SM Higgs boson to be around $115-130$ GeV, and both ATLAS and CMS experiments observe a $\sim 3\sigma$ hint at 125 GeV.

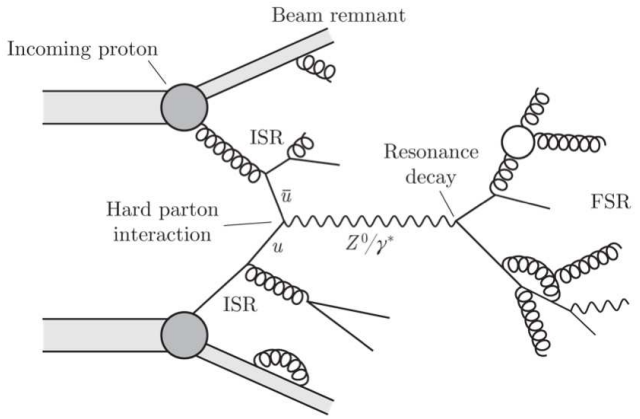

Figure 2.2: Feynman diagram for pp collision (taken from Ref. [32]). ISR stands for initial-state radiation, and FSR stands for final-state radiation.

or a gluon, known as final-state radiation (FSR). In principle, these higher-order corrections should be small, but in some cases they can be significant. For example, higher-order calculations in quarkonium production have been shown to be important as will be discussed later.

2.2.2 Parton Density Functions

During proton-proton collisions, only a fraction of the total proton energy transfers to the parton, and this is parameterized by Parton Density Functions (PDF's), the probability for finding a particle with a certain longitudinal momentum fraction x ($x = p_{\text{parton}}/E_{\text{beam}}$) at momentum transfer Q^2, which is usually denoted as $f_{i/A}(x_i, Q^2)$ where i is the parton in the initial hadron A. This is also written as $f_{i/A}(x_i, \mu_F)$ with μ_F as the factorization scale that separates hard and soft physics. Figure 2.4 shows examples of PDFs at $Q = 2$ and 100 GeV provided by the CTEQ6M PDF set [33].

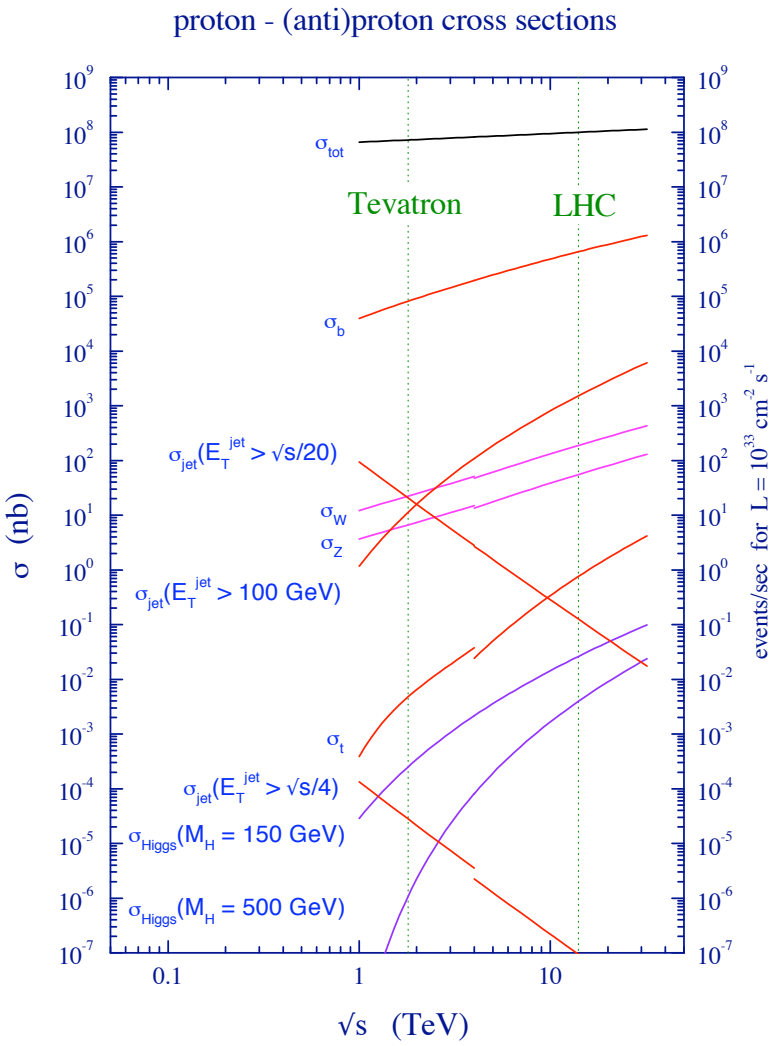

Figure 2.3: Cross-sections for a variety of SM reaction, as a function of center-of-mass energy in pp (LHC) and $p\bar{p}$ (Tevatron) collisions.

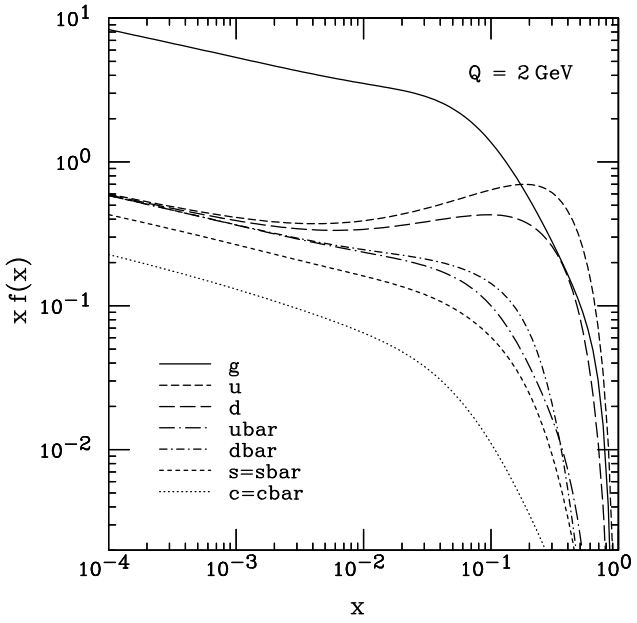

(a)

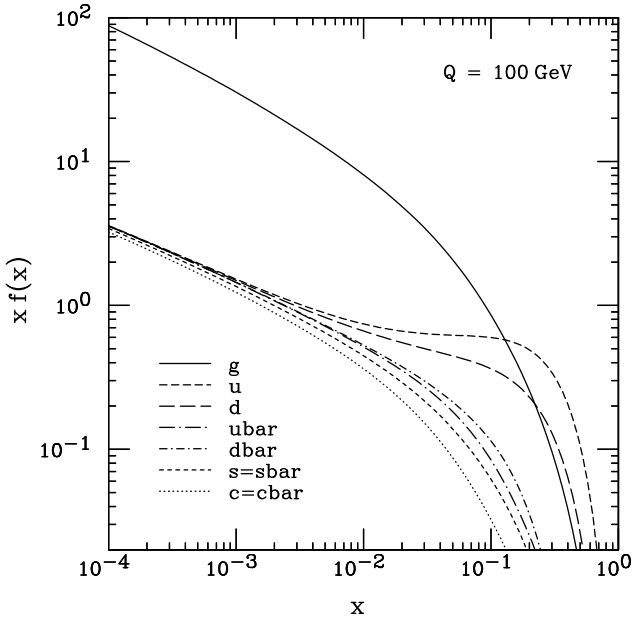

(b)

Figure 2.4: Summary of the CTEQ6M parton distribution functions at Q = 2 and 100 GeV that gives the probability $xf(x)$ of a gluon or (anti)quark at a certain longitudinal momentum fraction x.

2.2.3 Hadronization

Hadronization is the formation of a hadronic final state (meson or baryon) from the free quarks or gluons created from the collision. Several popular hadronization models are implemented into the Monte Carlo generator including the string fragmentation model [34] in PYTHIA, and the cluster hadronization model [35] in HERWIG. Figure 2.5 illustrates the basic difference between the string fragmentation and the cluster hadronization models. A thorough review can be found in Ref. [36].

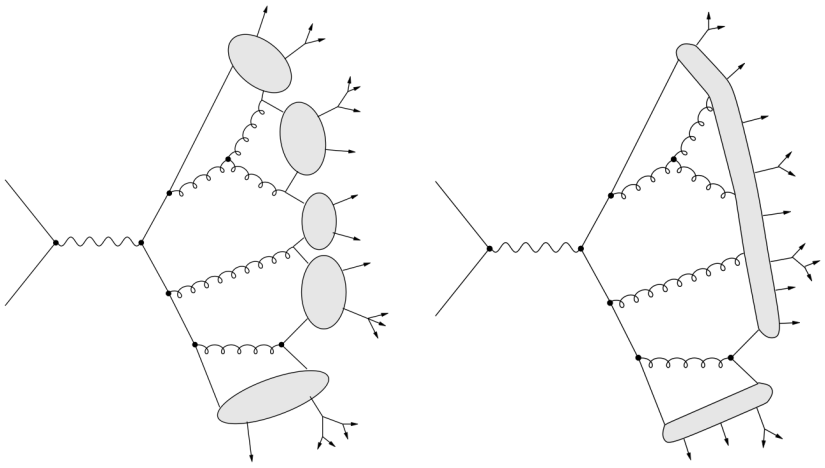

(a) (b)

Figure 2.5: (a) cluster hadronization, and (b) string fragmentation as alternative models to describe hadronization.

2.3 Quarkonium

Mesons that are composed of a quark and anti-quark of the same flavor are called "quarkonia". The lowest mass $c\bar{c}$ meson, J/ψ, was discovered in 1974 at Brookhaven

National Laboratory [37] and Standford Linear Accelerator Center simultaneously [38]. After the discovery of the J/ψ, a series of excited $c\bar{c}$ states, $\psi(2S)$, χ_c, etc., have been discovered. The first $b\bar{b}$ quarkonium state, $\Upsilon(1S)$, was first observed at Fermilab in 1977 [39].[6] Figures 2.6 and 2.7 show a summary of the charmonium and the bottomonium families, respectively.

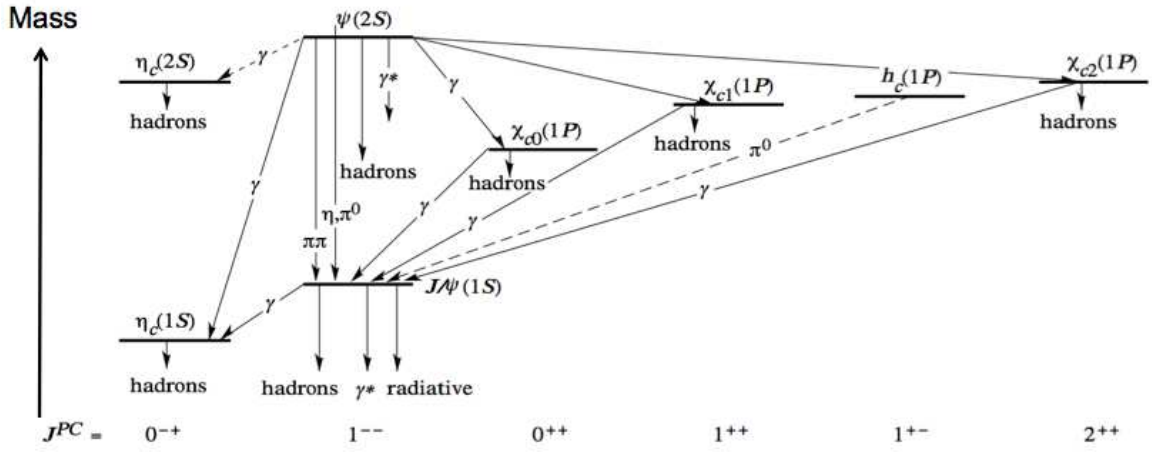

Figure 2.6: Mass levels of the charmonium $c\bar{c}$ system.

[6]Due to the fact that the light quarks (up, down, and strange) are much less massive than the heavier ones (charm, bottom), the physical states actually seen in experiments are quantum mechanical mixtures of the light quark states. Also since the mass differences between the charm and bottom quarks are much larger than the mass differences between lighter quarks, the physical states are well defined in terms of a quark-antiquark pair of a given flavor. Quarkonium therefore usually only refers to charmonium and bottomonium.

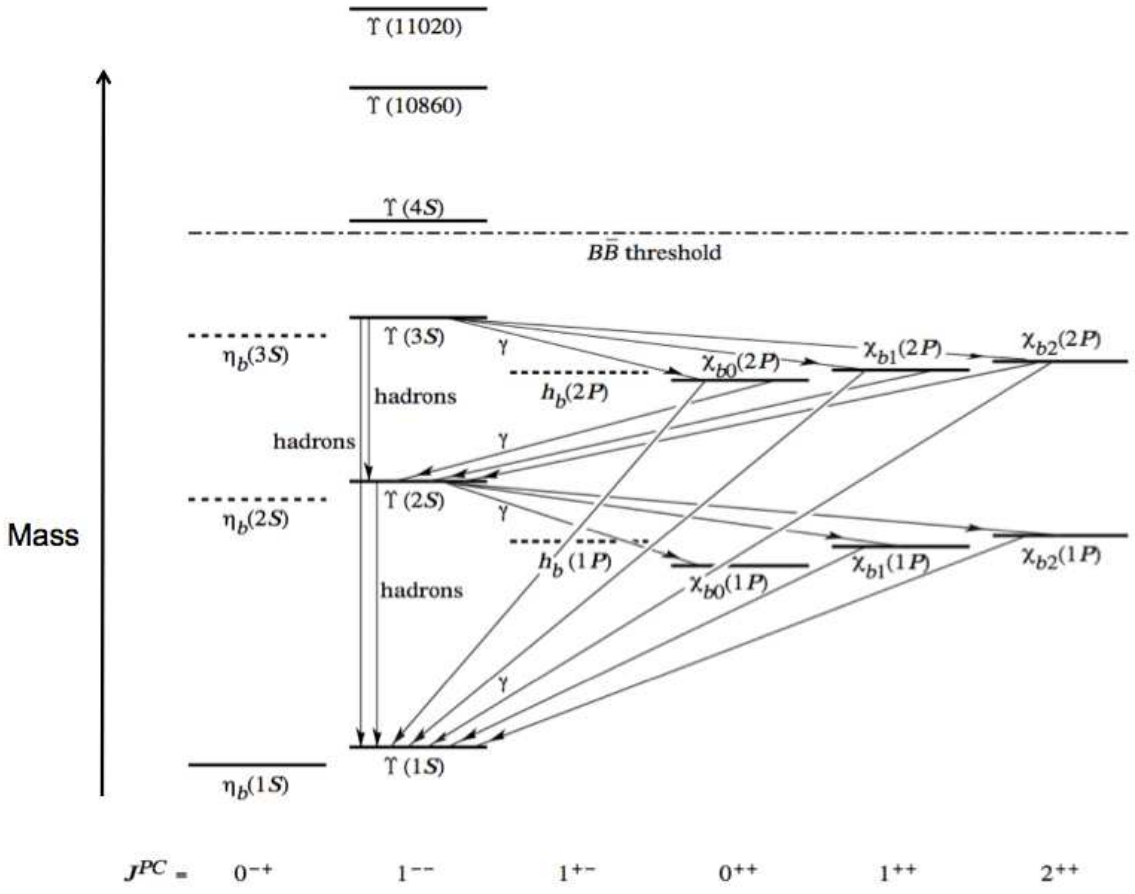

Figure 2.7: Mass levels of the bottomonium $b\bar{b}$ system.

2.3.1 Quarkonium Production

After the discovery of the J/ψ, the properties of quarkonia have been studied extensively. Among the most important of these properties are the mass, polarization, and production mechanism of the various states. The general form of the quarkonium (H state) production cross-section in pp collisions is written:

$$d\sigma(pp \to H + X) = \sum_{i,j} \int dx_1 dx_2 f_{i/A}(x_1, \mu_F) f_{i/B}(x_2, \mu_F) d\hat{\sigma}(ij \to H + X), \quad (2.10)$$

where, $f_{i/A}(x_i, \mu_F)$ are Parton Density Functions, $x = p_{\text{parton}}/E_{\text{beam}}$, and $d\hat{\sigma}(ij \to H + X)$ describes the production of the final quarkonium state from initial partons (i and j).

Three of the most popular models of quarkonium production are summarized briefly in this section. More details are available in References [40, 41, 42].

- **Color Singlet Model (CSM) [43]:** Assuming that the quantum numbers, such as the spin and the color, of the final quarkonium states and the initial quark and anti-quark states are the same, and since quarkonia are physical objects that must be in color singlet state, the initial quark pair must also be in a color singlet state. Figure 2.8 shows the Feynman diagrams for quarkonium production of in leading-order in α_s (LO) of $^3S_1$ and $^3P_1$ states.

  This model showed problems in its predictions of J/ψ results at UA1 [44], and then even larger discrepancies between experimental results and CSM predictions were observed in J/ψ production at DØ [45] and $\psi(2S)$ production at CDF [46], as shown in Fig. 2.9 and Fig. 2.10, respectively.

  Calculations at higher order of α_s (NNLO*)[7] in the CSM have recently been made [48], and the better agreement with experimental data are now observed at

[7] NNLO* is not a full next-to-next-to-leading order calculation, currently only real contributions up to α_s^5 has been calculated.

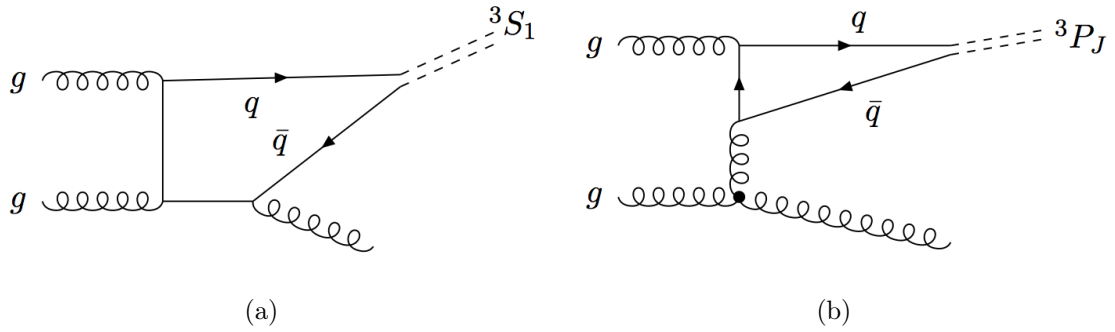

Figure 2.8: Example of leading-order (LO) Feynman diagrams for Color Singlet (a) $^3S_1$ and (b) $^3P_1$ quarkonium production.

the Tevatron [49] and in the latest measurements of J/ψ differential production cross-section in ATLAS [50], which are shown in Fig. 2.11.

- **Color Evaporation Model (CEM) [51]:** Unlike the CSM, the CEM is a pure phenomenological model. In the CEM, the initial quark pair is not restricted to be in a color singlet state, and it is allowed to be produced in a color octet state. The assumption here is that the color and the spin can be modified via numerous soft interactions with the color field. The CEM only predicts the total cross-section of heavy $Q\bar{Q}$ pairs (i.e., $c\bar{c}$ or $b\bar{b}$). The cross-section for a particular state can only be calculated by using a density coefficient that must be determined from fits to data. Comparisons between recent ATLAS measurements and CEM predictions of J/ψ production are also shown in Fig. 2.11. The CEM predicts good agreement in the high-p_T region, but underestimates the cross-section in the low-p_T region.

- **Color Octet Mechanism (COM) [52]:** Similar to the CEM, the quantum numbers of the initial quark pair in this model can be different than those of the

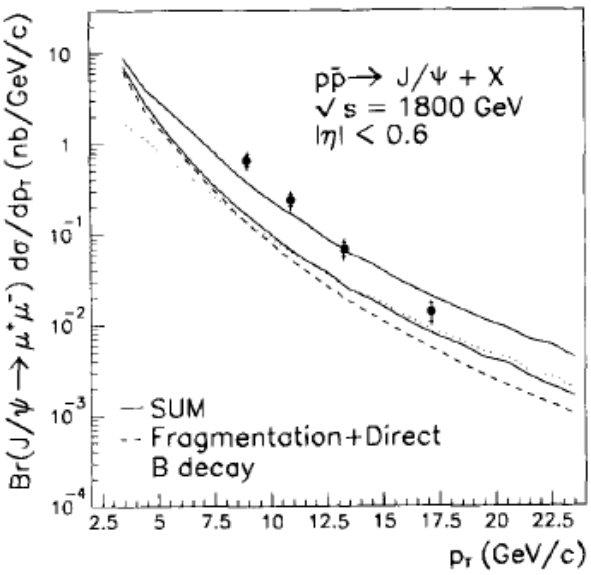

Figure 2.9: Differential cross-section for J/ψ production in $p\bar{p}$ collision at the Tevatron: the dotted line corresponds to predicted J/ψ production via B-meson decays. The dashed line corresponds to predicted prompt J/ψ production. Two solid lines represent the sum of theoretical prediction with uncertainties.

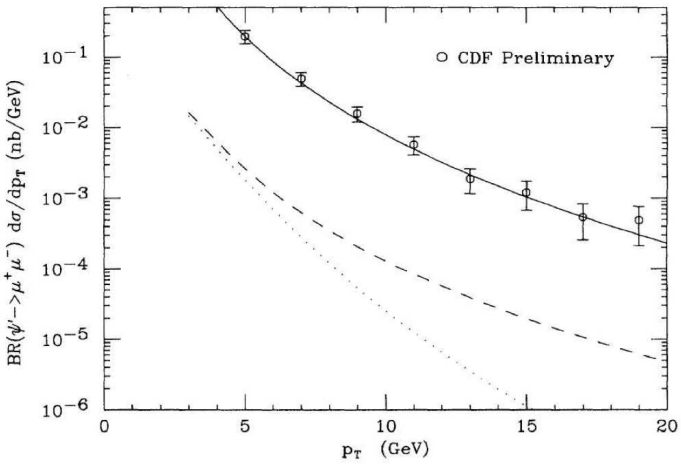

Figure 2.10: Differential cross-section for $\psi(2S)$ production in $p\bar{p}$ collision at the Tevatron: the dotted line is the prediction from the CSM; the dashed line includes contributions from singlet fragmentation processes [47]; the solid line is adding the color octet fragmentation contributions. (Taken from Ref. [47].)

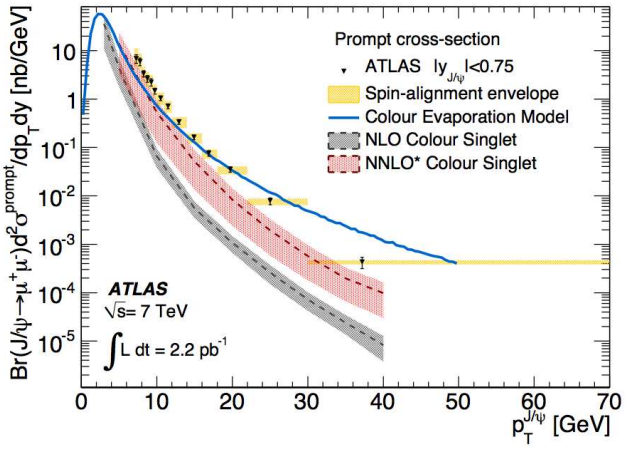

(a)

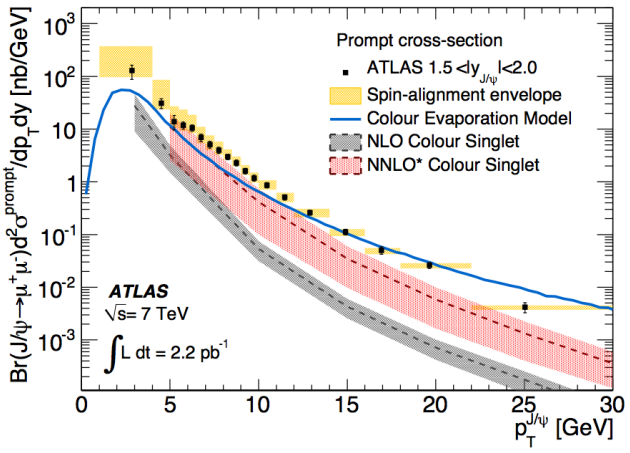

(b)

Figure 2.11: Measured differential J/ψ production cross-section as a function of $p_T(J/\psi)$ for rapidity, y, in the ranges: (a) $0.75 < |y| < 1.5$ and (b) $1.5 < |y| < 2.0$ compared to theoretical predictions.

final quarkonium state. They are allowed to evolve into a particular quarkonium state through radiation of soft gluons in the production process. The COM takes advantage of using the framework of an effective field theory known as Non-Relativistic Quantum Chromodynamics (NRQCD). The COM had great success in describing the Tevatron J/ψ and $\Upsilon(1S)$ results [53] as shown in Fig.2.12. The discrepancy between $\Upsilon(1S)$ measurements and predictions in the low-p_T region is understood as arising from missing higher-order contributions and multiple gluon radiation in the COM.

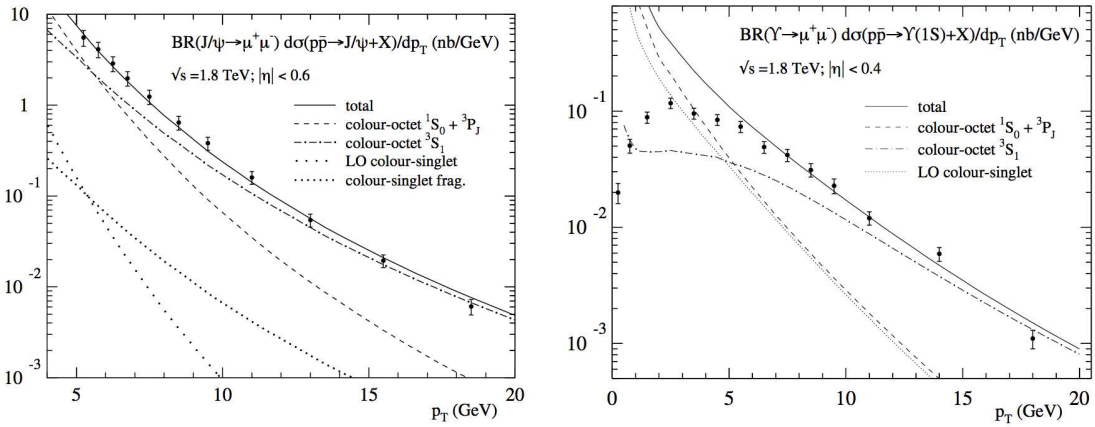

(a) (b)

Figure 2.12: The production cross-section of (a) J/ψ and (b) $\Upsilon(1S)$ as measured by CDF [53] compared to theoretical models.

2.3.2 Quarkonium Polarization

The good agreement between the experimental measurements and theoretical predictions for quarkonium production cross-section seemed to be a happy ending to the

quarkonium story. However, a new puzzle appeared when the polarizations of quarkonia states were measured and new discrepancies once again appeared. By using the di-lepton final states ($q\bar{q} \rightarrow \ell^+\ell^-$), the simplest quantity to determine the polarization is the angle of the ℓ^+ in the rest frame of the vector quarkonium meson with respect to the vector-meson boost direction in the laboratory system referred to as $\theta^\star$. The angular distribution is written as

$$\frac{dN}{d\cos\theta^\star} \propto 1 + \alpha\cos^2\theta^\star, \tag{2.11}$$

where α can be in the range from -1 (fully longitudinal) to $+1$ (fully transverse). The mixture of transverse and longitudinal polarization is determined by measuring the values of α.

Two interesting dilemmas arose from recent J/ψ, $\psi(2S)$ and $\Upsilon(1S)$ polarization results produced by the CDF and DØ experiments in $p\bar{p}$ collisions:

1. **Disagreement between experiment and theory:** The polarizations for J/ψ and $\psi(2S)$ from CDF cannot be described by the theoretical calculations as shown in Fig. 2.13 [54].

2. **Disagreement between two experiments:** The $\Upsilon(1S)$ polarizations measured by the CDF and DØ Collaborations behave completely differently, as shown in Fig. 2.14 [55, 56].

Theorists have recently pointed out [57] that values of α extracted from fits to $\theta^\star$ distributions alone can be biased by effects related to another angle sensitive to the polarization, $\phi^\star$. Figure. 2.16 shows the non-trivial relationship between $\theta^\star$, $\phi^\star$ and the ATLAS detector acceptance in J/ψ production. Therefore, polarization measurements should be performed by measuring two angles, $\theta^\star$ and $\phi^\star$. The full observable angular distribution can be written as:

$$\frac{d^2N}{d\cos\theta^\star d\phi^\star} \propto 1 + \lambda_\theta\cos^2\theta^\star + \lambda_\phi\sin^2\theta^\star\cos 2\phi^\star + \lambda_{\theta\phi}\sin 2\theta^\star\cos\phi^\star, \tag{2.12}$$

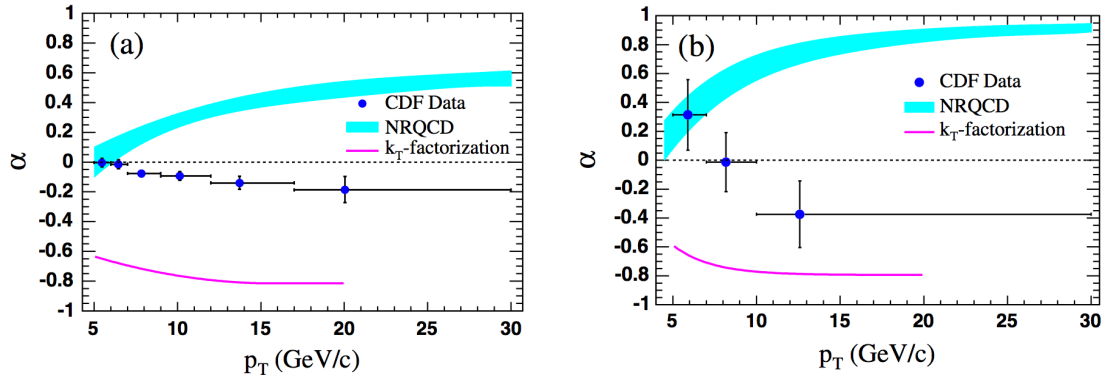

(a) (b)

Figure 2.13: Polarization measurements of (a) J/ψ (b) $\psi(2S)$ as a function of p_T as measured by CDF [54].

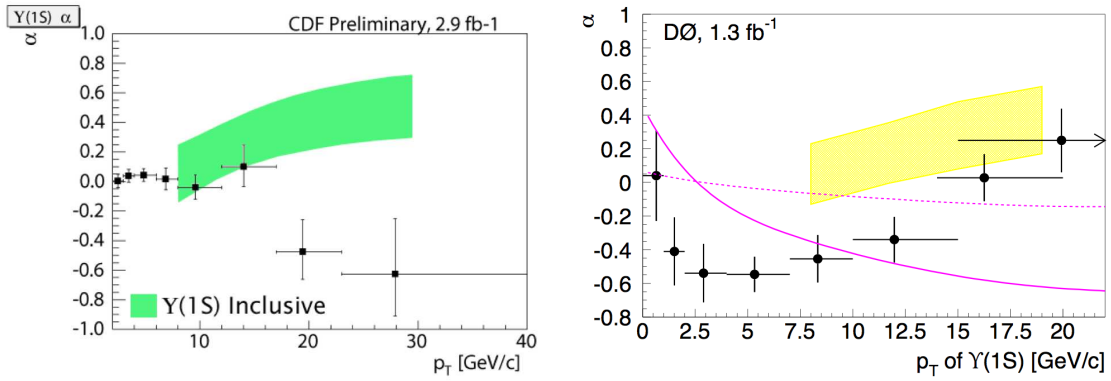

(a) (b)

Figure 2.14: Polarization measurements of $\Upsilon(1S)$ by (a) CDF [55] and (b) DØ [56].

where $\theta^\star$ is the same as before, while $\phi^\star$ is defined as the angle between the quarkonium production and decay planes in the lab frame (see Figure 2.15, Ref. [57] and references therein).

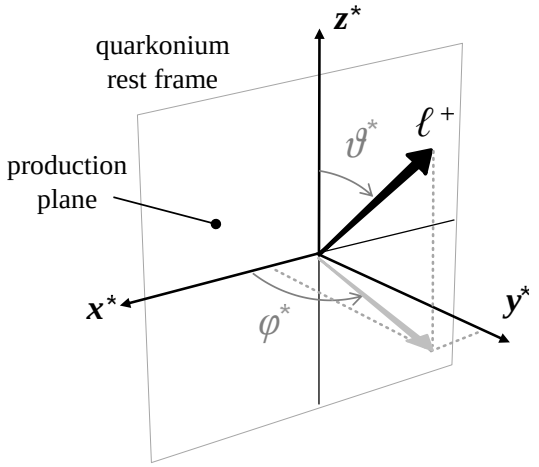

Figure 2.15: The coordinate system for the definition of quarkonium polarization (taken from Ref. [57]).

The latest (2011) $\Upsilon(nS)$ polarization [58] measurements from CDF using a dual angular distribution analysis is shown in Fig. 2.17. The results indicate that the $\Upsilon(1S)$ polarization is close to the unpolarized scenario.

The purpose of this thesis is to not only measure the production cross-section of Υ mesons, but also to build a foundation for future polarization measurements of the Υ system in ATLAS.

2.4 Beyond the Standard Model

Although the SM has had tremendous success in many ways, there are still many unsolved problems such as the mechanism of electroweak symmetry breaking (the Higgs boson is still hidden somewhere, and the Higgs Mechanism is not the only

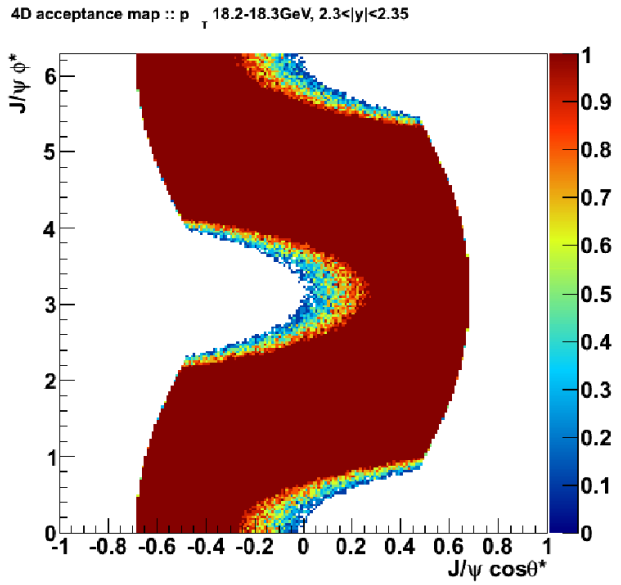

Figure 2.16: Two dimensional J/ψ acceptance in bins of $\phi^\star$ and $\cos\theta^\star$ in a particular slice of p_T and rapidity, $|y|$, showing the non-trivial dependence on $\phi^\star$.

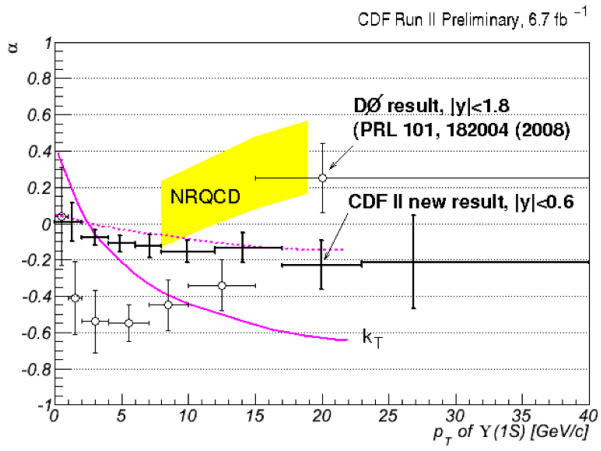

Figure 2.17: The latest polarization measurements of $\Upsilon(1S)$ from CDF [58].

way to deal with the electroweak symmetry breaking), the unification of the strong and the electroweak interactions, dark matter and dark energy from cosmological observations, and many more. Many theories provide possible solutions to these problems, and Supersymmetry (SUSY) is one of the most popular extensions of the Standard Model.

2.4.1 Supersymmetry and the Minimal Supersymmetric Standard Model

The basic idea of SUSY is that it is a symmetry between fermions and bosons [59, 60]. Under this symmetry transformation, each fermion has a corresponding boson that is referred to as *superpartner*, and vice versa. The SM particle and superpartner have exactly the same quantum numbers except the spin that differs by 1/2 unit. With these additional superparticles, SUSY may provide possible solutions to the

unification of gauge couplings, the hierarchy problem, providing the dark matter particle candidate, or even unification with gravity [59].

Quantum corrections to the Higgs boson mass from heavy fermion (top quark) loops are enormous, much larger than the electroweak symmetry breaking energy scale. This problem is to referred to as the hierarchy problem in particle physics. As a consequence of the existence of superparticles, the hierarchy problem is solved by the simple cancellation between the quadratic contribution from particle and superparticle to the Higgs mass as shown in Fig.2.18.

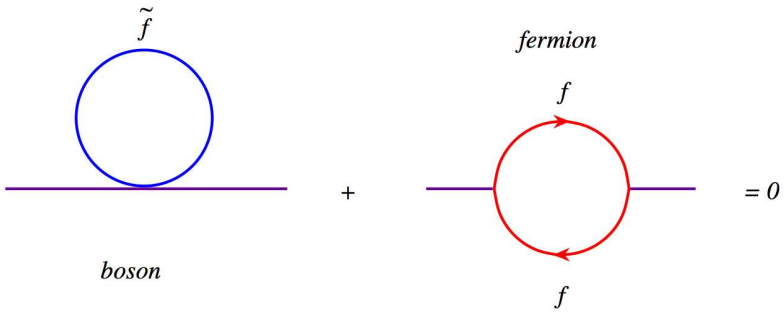

Figure 2.18: Cancellation of quadratic terms in SUSY.

Since we haven't yet observed any of the superparticles, the superparticles must be heavy; therefore, SUSY must be a broken symmetry. There are many mechanisms for SUSY breaking, such as gravity mediation (SUGRA), gauge mediation, anomaly mediation, and gaugino mediation. SUSY breaking yields several sets of parameters, such as gaugino Majorana masses, scalar squared-mass parameters for the SUSY particles, and trilinear interaction terms of Higgs-squark-squark, and Higgs-slepton-slepton [14]. An overview of these models can be found in Ref. [59].

Supersymmetrizing the Standard Model by expanding the particle content in a minimal way is referred to as the Minimal Supersymmetric Standard Model (MSSM).

Although this is the minimal extension of SM, it still contains 124 independent parameters, where 18 correspond to the SM, 1 is used for the Higgs sector, and 105 are totally new. The superpartners for leptons, quarks, the SM gauge bosons and Higgs boson are called sLeptons ($\tilde{\ell}$), sQuarks ($\tilde{q}$), Binos ($\tilde{B}$), Zinos ($\tilde{Z}$), Winos ($\tilde{W}$) and Higgsinos ($\tilde{H}$), respectively. In this minimal extension, two Higgs doublets, coupling separately to up- and down-type particles, are required in the Higgs sector. In the MSSM, or in any two Higgs doublets models [61], there are two neutral CP-even ($h,\ H$), one neutral CP-odd (A) and two charged ($H^{\pm}$) Higgs bosons. Four electrically neutral mass eigenstates, neutralinos ($\tilde{\chi}_1^0,\ \tilde{\chi}_2^0,\ \tilde{\chi}_3^0,\ \tilde{\chi}_4^0$), can be formed from the mixtures of Bino, Zino and neutral Higgsinos gauge eigenstates. Similarly, four charginos ($\tilde{\chi}_1^{\pm}, \tilde{\chi}_2^{\pm}$) are the mass eigenstates of the mixtures of Wino and charged Higgsinos. Neutralinos and charginos can couple to SM and SUSY particles. The field content of MSSM is summarized in Table 2.3.

A new quantity in the MSSM, R-parity $R = (-1)^{2j+3B+L}$, is introduced, where j is the spin, and B and L are the baryon and lepton numbers of the particle. The conservation of R-parity forces superparticles to be produced or annihilated in pairs. It preserves the proton life time result, and requires that the Lightest Supersymmetic Particle (LSP) be stable. If the LSP is electrically neutral and stable, i.e., the lightest neutralino, $\tilde{\chi}_i$, then it is an excellent candidate for dark matter.

In the MSSM superpotential, there is one term (μ-term), $\mu\hat{H}_u \cdot \hat{H}_d$, which is quadratic in the fields. This μ parameter is put into the model by hand without any obvious scale, and the natural choices are $\mu = 0$ or the Planck scale. Unfortunately both cases are disfavored by phenomenology. One possible phenomenologically acceptable choice is $\mu \sim$ electroweak symmetry breaking scale. However, as SUSY is not broken by the μ-term, this is not a natural choice. So the explanation of the μ-term is still a unsolved issue in the MSSM, and is referred to as the "μ-term problem" [62, 63].

	Boson Fields	Fermionic Partners	SU(3), SU(2), U(1) Quantum numbers
Matter	$(\tilde{\nu},\ \tilde{e}^-)_L$	$(\nu,\ e^-)_L$	1, 2, -1
	$\tilde{e}^-_R$	e^-_R	1, 1, -2
	$(\tilde{u},\ \tilde{d})_L$	$(u,\ d)_L$	3, 2, $1/3$
	$\tilde{u}_R$	u_R	3, 1, $4/3$
	$\tilde{d}_R$	d_R	3, 1, $-2/3$
Gauge	g	$\tilde{g}$	8, 1, 0
	$W^\pm$, W^0	$\tilde{W}^\pm$, $\tilde{W}^0$	1, 3, 0
	B	$\tilde{B}$	1, 1, 0
Higgs	$(H^0_d,\ H^-_d)$	$(\tilde{H}^0_d,\ \tilde{H}^-_d)$	1, 2, -1
	$(H^+_u,\ H^0_u)$	$(\tilde{H}^+_u,\ \tilde{H}^0_u)$	1, 2, 1

Table 2.3: The field content in the MSSM and their SU(3) $\times$ SU(2) $\times$ U(1) quantum numbers.

2.4.2 Next-to-Minimal Supersymmetric Standard Model

As mentioned in the previous section, the "μ-term problem" is a serious defect in the MSSM. The Next-to-Minimal Supersymmetric Standard Model (NMSSM) is one of the simplest ways to solve this problem by adding a singlet chiral superfield, $\hat{S}$ [64, 65]. The extension modifies the term $\mu\hat{H}_d\hat{H}_u$ in the superpotential to $\lambda\hat{H}_d\hat{H}_u\hat{S} + \frac{\kappa}{3}\hat{S}^3$ that is scale invariant. An effective μ term can be considered as $\mu_{eff} = \lambda s$, where s is the v.e.v. of $\hat{S}$. Since s comes from SUSY breaking, it is natural for μ_{eff} to reach the M_{SUSY} scale. More theoretical details are summarized in Ref.[14] in [64].

The additional singlet superfield changes the particle content in the NMSSM: one CP-even and one CP-odd Higgs state in the Higgs sector and one neutralino are added to the usual MSSM particle content. The additional neutralino provides an extra degree of freedom for satisfying dark matter limits [66].

2.4.3 Light CP-odd Higgs Boson a_1 in NMSSM

There are seven physical Higgs bosons in the NMSSM: three neutral CP-even (h_1, h_2, h_3), two neutral CP-odd (a_1, a_2), and two charged (H^+, H^-) Higgs bosons. The lightest CP-odd Higgs, a_1, which is considered in this thesis can be defined as:

$$a_1 = \cos\theta_A a_{MSSM} + \sin\theta_A a_S, \tag{2.13}$$

where θ_A is the mixing angle between the MSSM CP-odd scalar, a_{MSSM}, and the NMSSM CP-odd singlet, a_S.

The Higgs phenomenology in the SM or the MSSM can be changed dramatically by the existence of the light CP-odd Higgs boson a_1 that may open up new decay channels. If the a_1 boson is light enough, then $h_1 \to 2a_1$ could be the dominant decay channel, and the Higgs boson might be missed in the standard SM and MSSM search decay channels: $b\bar{b}$, $WW^\star$, $ZZ^\star$, $\tau^+\tau^-$, and $\gamma\gamma$. Also, $H^+ \to a_1 W^+$ could dominate

the standard charged Higgs boson search modes: $H^+ \to \tau^+\nu,\ c\bar{s},\ t\bar{b}$ [67, 68]. One of the most attractive features of the NMSSM is that if m_{a_1} is below the open-B threshold ($m_{a_1} < 2m_B$), the $h_1 \to 2a_1$ decay allows the h_1 to escape the LEP lower limit of $m_H \approx 114.4$ GeV by suppressing the $b\bar{b}$ channel. In this mode, which is referred to the *Ideal Higgs* scenario of the NMSSM, one can also explain the observed LEP excess in the $\ell^+\ell^- b\bar{b}$ channel near $m_{b\bar{b}} \approx 100$ GeV as shown in Fig. 2.19 [69, 70]. The preferred a_1 decay channels in this scenario are $a_1 \to \tau^+\tau^-,\ c\bar{c},\ gg$, and also $a_1 \to \mu^+\mu^-, s\bar{s}$ at suppressed levels [67].

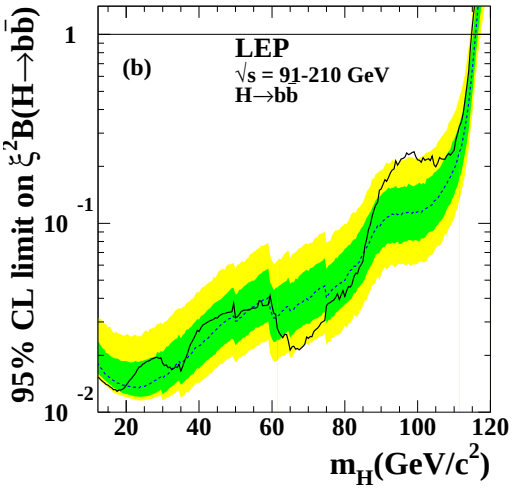

Figure 2.19: Limit on Higgs to $b\bar{b}$ in LEP [70].

Various searches for the *Ideal Higgs* scenario have been done in different experiments in the past few years. In 2009, results from BaBar using the radiative transition $\Upsilon \to \gamma a_1$ channel [71] and from DØ in the $h_1 \to 2a_1 \to 2\mu 2\tau, 4\mu$ channels [72] showed no evidence of the existence of the a_1 Higgs boson. The limits from these results ruled out most scenarios with $m_{a_1} < 2m_\tau$ [73], but this conclusion is disputed in

Ref. [74]. In 2010, the ALEPH collaboration revisited LEP data on the Zh production channel as shown in Fig.2.20(a) including the possibility of $h \to a_1 a_1 \to 4\tau$ [75]. The results constrained the phase-space in the range $2m_\tau < m_{a_1} < 2m_B$, and also disfavored NMSSM Ideal Higgs scenarios with m_{a_1} not close to $2m_B$ for $\tan\beta \geq 3$[8]. Results for the charged Higgs channel, $H^+ \to a_1 W^+$, via top quark decay, as shown in Fig. 2.20(b), were reported by CDF [76] in 2011.

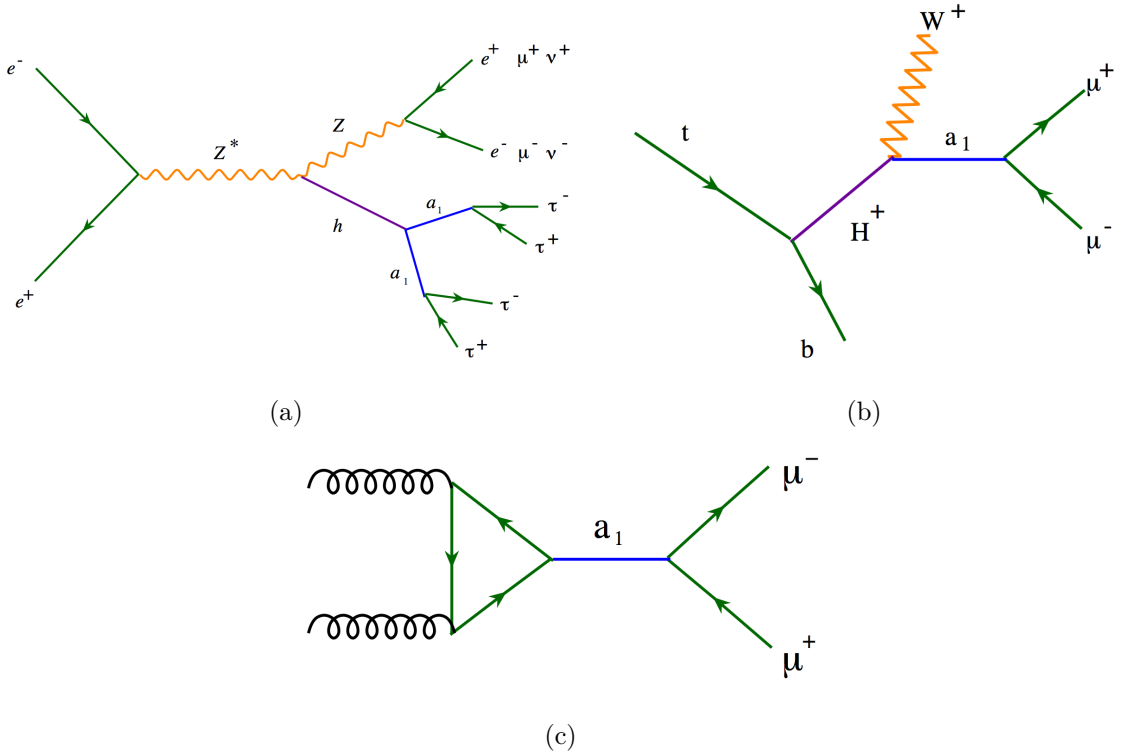

Figure 2.20: Feynman diagrams for (a) Zh production with $h \to 2a_1$, (b) $t \to bH^+ \to bW^+a_1$, and (c) $gg \to a_1 \to \mu^+\mu^-$.

In this thesis, the direct production of a_1 via gluon fusion with a_1 decay to muons,

[8] $\tan\beta$ is the ratio of the vacuum expectation values for the doublets giving mass to up-type quarks versus down-type quarks.

$gg \to a_1 \to \mu^+\mu^-$, is considered as shown in Fig. 2.20(c). The predictions [77] for the production cross-section, $gg \to a_1$, at $\sqrt{s} = 7$ TeV with different $\tan\beta = 1,\ 2,\ 3,\ 10$ and $\cos\theta_A = 1$ (where $\tan\beta$ is the ratio of v.e.v. for Higgs doublets giving up-type and down-type fermions mass) versus m_{a_1} are shown in Fig. 2.21(a), and for the branching ratio of $a_1 \to \mu^+\mu^-$ with various $\tan\beta$ values as shown in Fig. 2.21(b). We take advantage of high production cross-section and clear final states from di-muon pairs, but compromise on the small branching ratio of $a_1 \to \mu^+\mu^-$.

This analysis can suffer from $a_1 - \eta_b$ mixing [78, 79, 80]. This mixing can affect the total width of the a_1, and reduce the significance of the result. However, we ignore this possibility in the results presented here.

Aside from the rich new Higgs phenomenology, there are plenty of interesting features associated with the a_1 in the NMSSM. For example, there is a non-negligible contribution to the anomalous muon magnetic moment from a light a_1, if the a_1 has a mass between 9.2 to 12 GeV [81]. Also, a light a_1 may explain the discrepancy in the ratio of Υ widths $\Gamma(\Upsilon \to \tau^+\tau^-)/\Gamma(\Upsilon \to \mu^+\mu^-)$ between the BaBar measurement and the SM prediction [82, 83, 84], though agreement on the validity of the SM calculation is not universal [85].

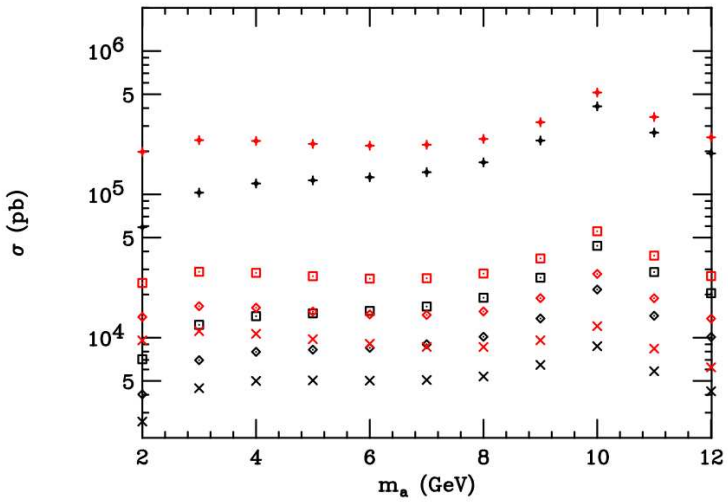

(a)

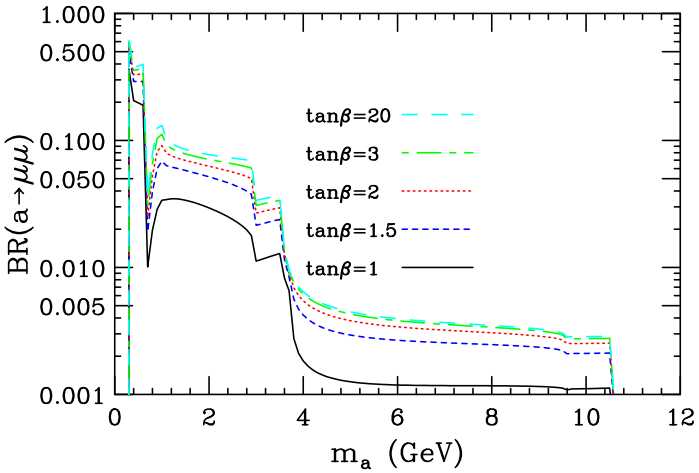

(b)

Figure 2.21: (a) Production cross sections for the $gg \to a_1$ process versus a_1 mass at $\sqrt{s} = 7$ TeV for $\tan\beta = 1,\ 2,\ 3,\ 10$ and $\cos\theta_A = 1$ (from lowest to highest point sets). Black (red) points correspond to cross sections calculated without (with) resolvable parton final state contributions ($gg \to a_1 g$). (b) Branching ratios for $a_1 \to \mu^+\mu^-$ versus a_1 mass in the Ideal Higgs scenario of NMSSM (taken from Ref. [77]).

Chapter 3

Experimental Apparatus

"I have done a terrible thing, I have postulated a particle that cannot be detected."
– **W. Pauli**

3.1 Large Hadron Collider

The Large Hadron Collider (LHC) at CERN is the highest energy particle accelerator and collider in the world after the honorable retirement of the Tevatron at Fermilab[1]. Unlike the Tevatron that is a proton-antiproton collider, the LHC is a proton-proton accelerator and collider and its designed collision energy is 14 TeV with an instantaneous luminosity of $\mathcal{L} = 10^{34}$ cm^{-2}s^{-1}. The LHC is installed in the old LEP ring tunnel of 26.7 km circumference, and it is 100 m underground, situated under France and Switzerland. More details are available in Ref. [86].

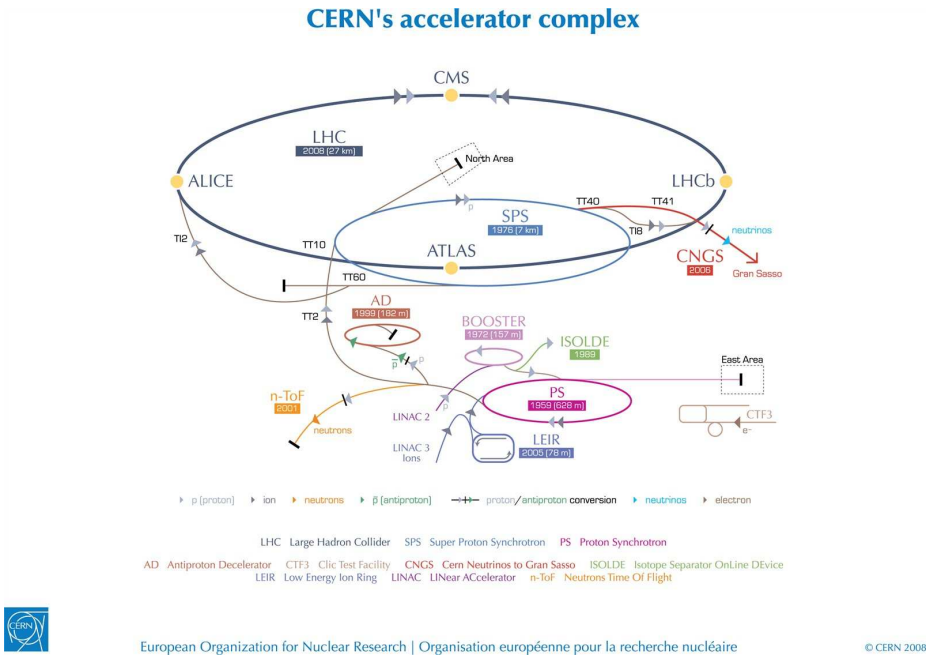

Figure 3.1: The LHC accelerator complex [87].

The complete proton accelerating chain in the LHC is shown in Fig. 3.1. The

[1]The center-of-energy of the Tevatron was 1.96 TeV, and it was officially retired at the end of September 2011.

protons undergo first-stage acceleration in a linear accelerator (LINACS) to an energy of $E = 50$ MeV, and then accelerated by the booster synchrotron (BOOSTER) to 1.4 GeV. The Proton Synchrotron (PS) and the Super Proton Synchrotron (SPS) accelerate protons from 1.4 GeV to 25 GeV, then to 450 GeV. After protons reach 450 GeV, they are injected to the LHC ring, then accelerated to the full collision energy. There are four major experiments at the LHC: ALICE, ATLAS, CMS and LHCb, and a few smaller experiments such as LHCf and TOTEM.

The LHC started proton-proton collisions with $\sqrt{s} = 7$ TeV (3.5 TeV for each beam) on March 30, 2010. The first heavy-ion (lead ion) collision with $\sqrt{s} = 2.76$ TeV followed eight months later. In 2011, the LHC ran at energies of 3.5 TeV per proton beam, and delivered about 5 fb^{-1} of integrated luminosity.

With this great success and experience, LHC has decided to increase the center-of-mass energy from 7 TeV to 8 TeV in the 2012 run. This will enhance by about 30% the sensitivity to Standard Model Higgs bosons [88], and also will open more phase-space for new physics. There will be a major technical shutdown of the LHC for about one and half years following the 2012 run, and several major upgrades will be installed during that period. The LHC will be re-started in 2014 with the full design collision energy of $\sqrt{s} = 14$ TeV and instantaneous luminosity, and will allow us to explore the new energy regime.

3.2 The ATLAS Detector

ATLAS is an abbreviation of **A** **T***oroidal* **L***HC* **A***pparatu***S** and is shown schematically in Fig. 3.2. The ATLAS detector is a general purpose particle detector, and also is one of the most complex particle detectors in the world. It is composed of the Magnet System, the Inner Detector (ID), the Calorimeters (Calo), the Muon Spectrometer (MS) and the Trigger System (TS). The ATLAS detector is 44 m long and

25 m in diameter, and weights about 7,000 tons.

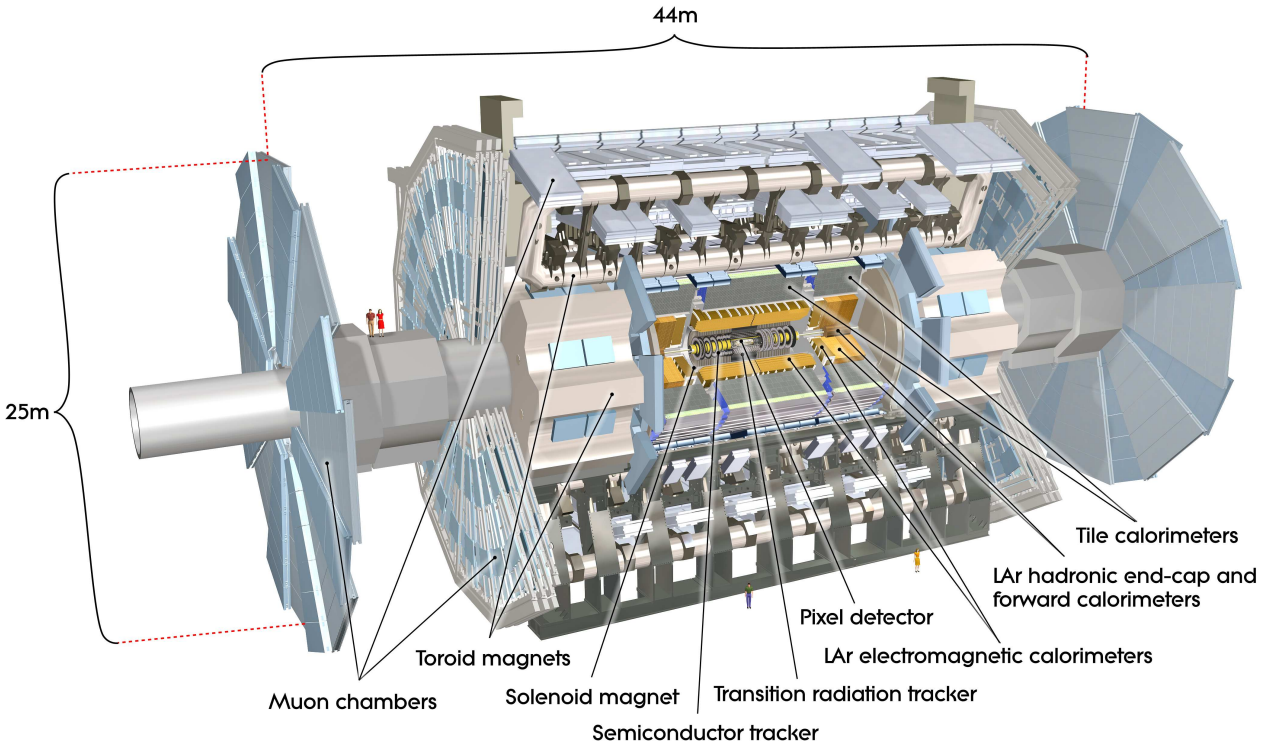

Figure 3.2: Schematic of the ATLAS detector.

The coordinate system of the ATLAS detector is defined with the following Cartesian coordinates: the z-axis is the beam direction, and the positive z direction is pointing to the detector side A, the negative direction points to side C. The positive x direction is pointing to the center of the LHC ring from the interaction point, and the positive y direction is pointing up to the surface. The azimuthal angle ϕ measures the angle around the beam axis. Pseudo-rapidity is defined as $\eta = -\ln(\tan\frac{\theta}{2})$ with θ as the angle between the particle's momentum and the z axis.

A review of the ATLAS detector in detail can be found in Ref. [89].

3.2.1 The Magnet System

The main purpose for the Magnet System is to bend the paths of charged particles so that we can measure their momenta. The Magnet System in ATLAS is built using superconducting magnets. Inside the ID, the magnet field is provided by the central solenoid with 2 T. In the MS, the strength of magnet field is 0.5 T from the toroids (one in barrel and two in end-cap). The Magnet System is cooled by liquid helium at 4.8 K (−268 °C).

3.2.2 The Inner Detector

The Inner Detector (ID) is the innermost detector in ATLAS (see Fig. 3.3), and is responsible for particle identification as well as measuring the positions and the transverse momenta (p_T) of charged particles. Charged particles leave a series of localized energy deposits (hits) when they travel through the ID that are used to reconstruct *tracks*. Precise measurements of tracks is not only crucial to the p_T determination, but also to the trajectory (i.e., angles) of the charged particle. These trajectories can be used to determine the primary interaction vertex (PV), representing the point(s) of pp collisions in the event. They are also used to reconstruct any secondary vertices (SV) in the event that could arise from the decay of long-lived particles such as b hadrons.

There are three subdetectors in the ID system, which are the high resolution silicon pixel detector (Pixel), the semiconductor tracker (SCT), and the transition radiation tracker (TRT). The ID covers the full azimuthal angle (ϕ) and the $|\eta| < 2.5$ region, and is surrounded by the superconducting solenoid magnet that provides strong bending power for charged particles due to its 2 T magnetic field strength.

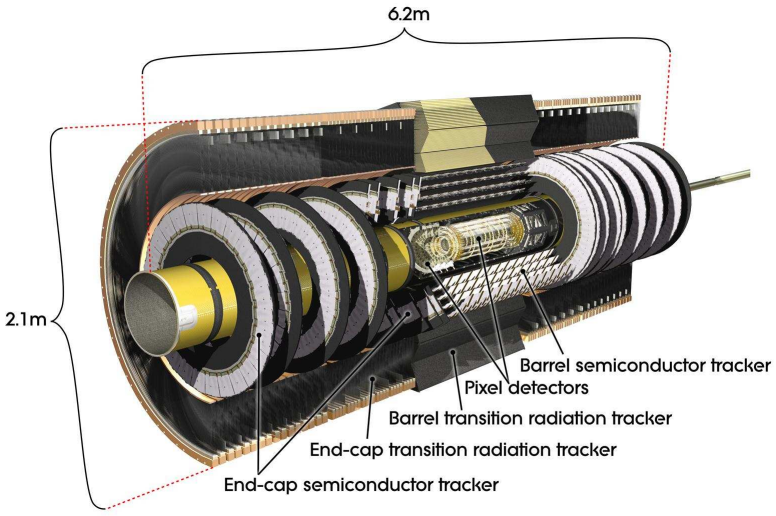

(a)

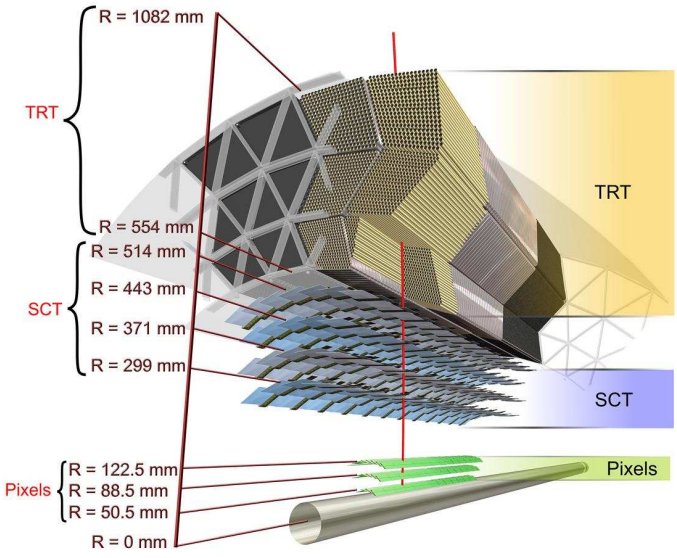

(b)

Figure 3.3: Schematic of the ATLAS Inner Detector, and its major components.

A schematic showing the ID with some technical details is shown in Fig. 3.4. The overall transverse momentum resolution for the ID is:

$$\sigma(1/p_T) = (0.34 - 0.41 \text{ TeV}^{-1}) \left(1 \oplus \frac{44 - 80 \text{ GeV}}{p_T}\right), \tag{3.1}$$

where the values vary as η varies in its range.

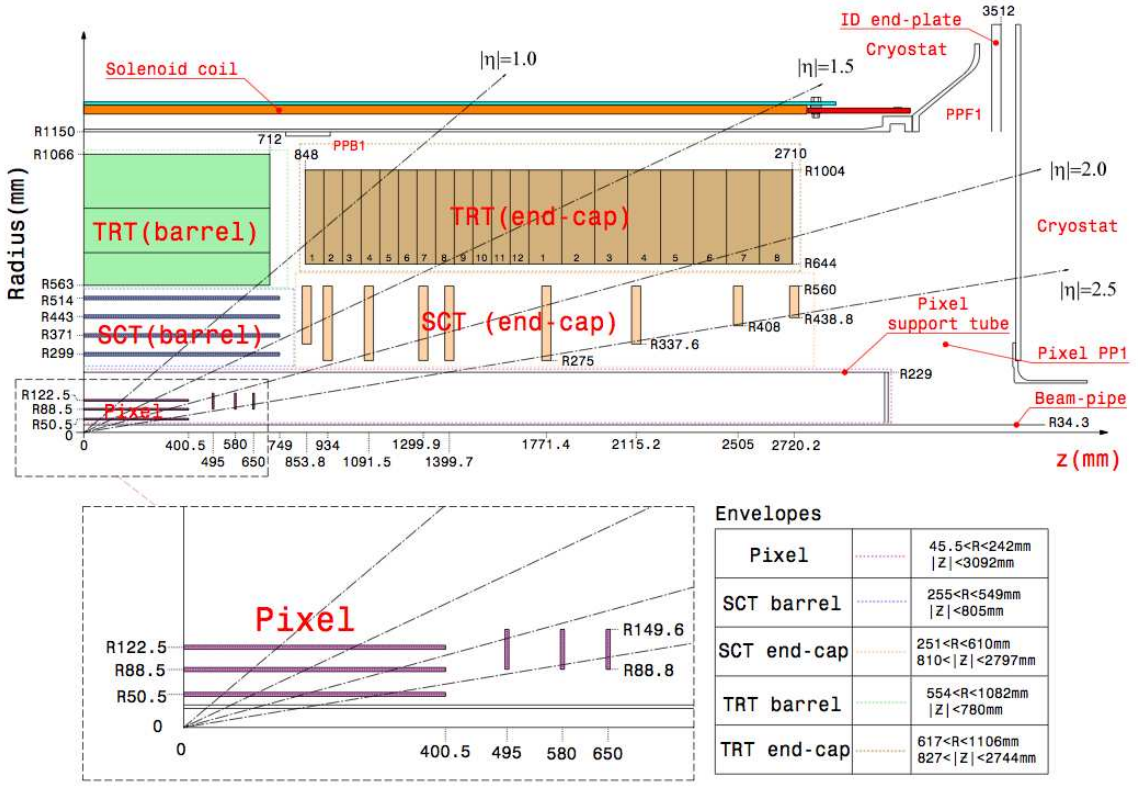

Figure 3.4: Schematic of the ATLAS Inner Detector in the r-z plane (all dimensions are in mm) [89].

- **The Pixel Detector**

  The pixel detector is the closest component to the beam pipe, only a few centimeters away in radius, so it is extremely important for vertex determination.

This subdetector uses solid state technology, and consists of 1744 identical modules. The accuracies in r-ϕ (the pixel size) and z measurements are 10 μm and 115 μm, respectively.

There are three layers in the barrel and three disk layers in the each end-cap. The innermost layer in the barrel, referred to as the B-layer, is only 50.5 mm away from the design interaction point to allow for good secondary vertex reconstruction. This is particularly important for the B physics and b-jet identification (b tagging), since b hadrons have typical lifetimes of $\sim$1.5 ps corresponding to decay length of $O(mm)$ in ATLAS. These particles thus produce SV's that can be reconstructed using the precise tracking of the ID. As a consequence of the proximity of the B-layer and the interaction point, the radiation damage is significantly larger here than for any other subdetectors, so the B-layer is designed so that it can be replaced every few years.

- **The SemiConducting Tracker (SCT)**

The SCT is the second component, from inside out, in the ID. It is based on similar technology as the Pixel detector; the major difference is that the sensitive element of the SCT are strips, instead of pixels. The track density is lower in the SCT, and this allows the requirement of the readout channels to be fewer. There are four barrel layers (double-sided) and two end-cap sections (nine disks each) in the SCT system. Each barrel module is made of a pair of strip detectors with 80 μm pitch, and are placed back-to-back with another pair with a stereo angle of 40 mrad. The precisions of each module are 17 μm in r-ϕ and 580 μm in the z direction. The end-cap modules provide wider coverage in η, and when combining the Pixel and SCT together, they give total coverage for $|\eta| < 2.5$.

- **The Transition Radiation Tracker (TRT)**

  The outermost component of the ID is the TRT subdetector that measures tracks by detecting ionization of a gas by the passage of a charged particle. The TRT provides only two-dimensional information in r-ϕ plane with a resolution of 130 μm. Although the overall tracking resolution of the TRT is not as good as the silicon detectors, the TRT still significantly improves the momentum measurement due to the larger tracking lever arm.

  The basic detecting elements of the TRT are polyimide drift (straw) tubes of 4 mm diameter. Charged particles passing through the radiator material placed between the straws produce transition radiation photons. Each straw is filled with a gas mixture, of 70% Xe, 27% CO_2, and 3% O_2, and the gas is ionized when a charged particle passes through accompanied by transition radiation photons. Like other inner subdetectors, the TRT is a combination of a barrel region with straws that are 144 cm long and parallel to z-direction with a coverage in $|\eta| < 0.7$, and two end-caps, covering $0.7 < |\eta| < 2.5$, with 37 cm long straws that are aligned radially to the r-direction.

3.2.3 The Calorimeters

Outside the ID are the calorimeters that are used to measure energy of the particles. There are two different types of calorimeters for measuring energies from electromagnetic and hadronic interactions. Neutrinos or other particles that have no interactions with the detector material can be determined from balancing the total energy in the transverse plane (E_T), which is usually referred as the missing transverse energy $\not{E}_T$. A schematic view of the ATLAS Calorimetry system is depicted in Fig. 3.5.

- **Electromagnetic Calorimeter (ECAL)**

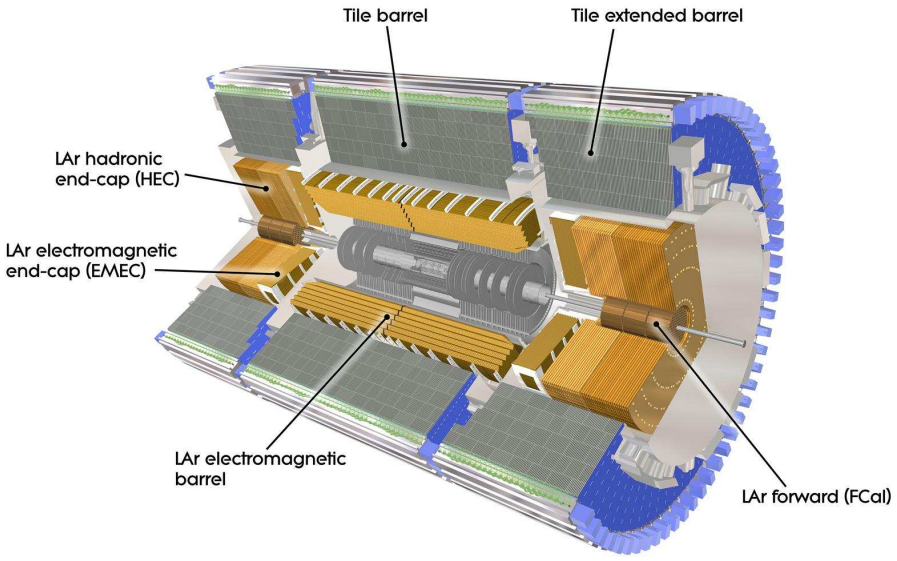

Figure 3.5: Schematic of the Electromagnetic and Hadronic Calorimeters in the ATLAS detector.

There is one barrel ($|\eta| < 1.475$) and two end-cap ($1.375 < |\eta| < 3.2$) components in the ECAL system. The barrel ECAL is divided into two pieces at $\eta = 0$ with a 6 mm gap. The main purpose for the ECAL is to measure the energies deposited from electrons and photons (the particles with EM interactions). The ECAL uses lead as an absorber and Liquid Argon (LAr) as the active medium, and the signal is recorded by accordion-shaped Kapton electrodes. The granularity of ECAL detector cells varies across η and at each layer with the range $\Delta\eta = 0.003 - 0.1$ and $\Delta\phi = 0.025 - 0.1$. To correct for the energy loss of particles before they enter the calorimeter, an additional ECAL layer, the presampler, is installed between the solenoid and the main calorimeter. The overall energy resolution of the ECAL is:

$$\frac{\Delta E}{E} = \frac{11.5\%}{\sqrt{E}} \oplus 0.5\%, \tag{3.2}$$

where the unit of the energy (E) is GeV.

- **Hadronic Calorimeter (HCAL)**

  The task for the HCAL is to measure the energy of particles that interact hadronically. The HCAL is composed of three components: the barrel ($|\eta| < 1.7$), the end-caps ($1.5 < |\eta| < 3.2$) and the forward region ($3.1 < |\eta| < 4.9$). The barrel HCAL uses steel as absorber and scintillator tiles as active material. For both the end-caps and the forward HCAL's, LAr was chosen as the active medium. This is done so as to endure the high level of radiation in the forward region. The end-cap HCAL uses copper as absorber, while the forward HCAL uses copper and tungsten as absorbers. The detector cell granularity of the HCAL varies with different η regions: for $|\eta| < 2.5$, it is $\Delta\eta \times \Delta\phi = 0.1 \times 0.1$; for $|\eta| > 2.5$, it is $\Delta\eta \times \Delta\phi = 0.2 \times 0.2$.

The thickness of the HCAL, about 11 interaction lengths[2] is large enough to make the probability of punch-through of hadronic showers to the muon system negligible. This reduces backgrounds from jets leaking into the muon system to a very small level, improving muon identification. The expected energy resolution for the hadronic calorimeter for the barrel region is:

$$\frac{\Delta E}{E} = \frac{50\%}{\sqrt{E}} \oplus 3\%, \tag{3.3}$$

and for the end-cap region:

$$\frac{\Delta E}{E} = \frac{100\%}{\sqrt{E}} \oplus 10\%, \tag{3.4}$$

where the unit of the energy (E) is again GeV.

3.2.4 The Muon Spectrometer

The outermost component of the ATLAS detector is the Muon Spectrometer (MS) system. Since almost all objects other than muons and neutrinos are absorbed in the ID or Calorimeters, the MS plays an important role in muon identification and momentum measurement. The MS is built around an air-core toroidal magnet system that provides an average field strength of 0.5 T. A schematic view of the ATLAS MS system is shown in Fig. 3.6.

The MS has two major purposes: the first one is to trigger on muons, and the second is to precisely measure their momenta and positions.

- **The Trigger Chambers**

  The trigger component is built of Resistive Plate Chambers (RPCs) in the barrel region ($|\eta| < 1.05$) and Thin Gap Chambers (TGCs) in the end-cap region (1.05

[2]Hadronic interaction length is the mean free path of a high-energy hadron before undergoing an interaction.

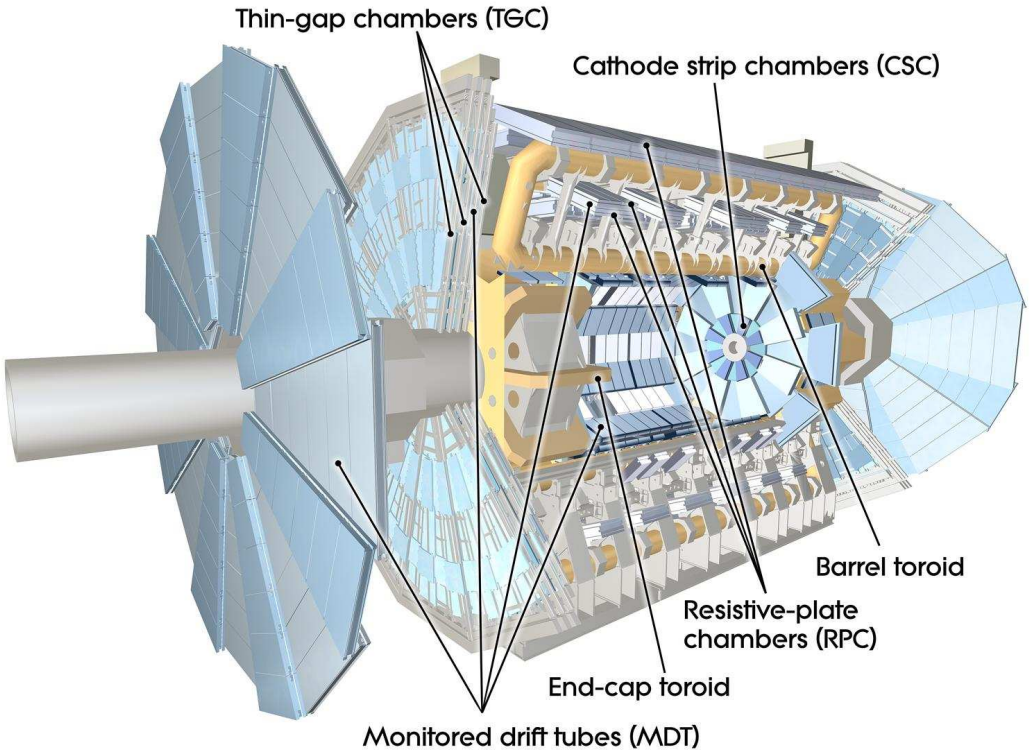

Figure 3.6: Schematic of the Muon Spectrometer in the ATLAS detector.

$< |\eta| < 2.4$). A precise measurement is not the first priority here, but rather the trigger chambers are required to have a fast response time (faster than the LHC bunch crossing of 25 ns). The RPCs are composed of a pair of parallel plates with a narrow gas gap in between, and with an applied high electric field. The TGCs are basically multi-wire proportional chambers, except that the anode wire pitch is larger. The granularity of the trigger chambers cells is about $\Delta\eta \times \Delta\phi = 0.1 \times 0.1$.

- **The Precision Measurement Chambers**

  The two types of chambers used for precision measurements are the Monitored Drift Tubes (MDTs) and the Cathode Strip Chambers (CSCs).

  The MDTs provide precision measurement of muon tracks in both the barrel and the end-cap regions over the pseudorapidity ranges of $|\eta| < 1.05$ and $1.05 < |\eta| < 2.7$, respectively. The MDTs are aluminum tubes of 30 mm diameter and 400 μm thickness with central W-Re wires and a mixture of gases (93% Ar, 7% CO_2). The track position resolution in the MDTs is about 80 μm.

  At very high pseudorapidity region ($2.0 < |\eta| < 2.6$), the CSCs will provide additional track information with a resolution of about 60 μm by using proportional chamber technology with a 30% Ar, 50% CO2, 20% CF4 gas mixture.

The Muon Spectrometer in ATLAS gives good momentum resolution of about 2% for a 20 GeV muon, or 10% precision for a very high p_T, 1 TeV, muon.

3.2.5 The Trigger and Data Acquisition System

During LHC operations, most events come from QCD production of light quarks and gluons that have little interest to the physicists. Due to the high bunch crossing rate of 40 MHz and the large amount of data produced by the detector for each event

(∼1.5 MB/event), it is impossible to record every single collision. The trigger system is designed to filter these background events in real time in order to reduce the event rate to a manageable level. There are three levels in the ATLAS trigger system: Level-1 (L1), Level-2 (L2) and the Event Filter (EF) which are shown in Fig 3.7.

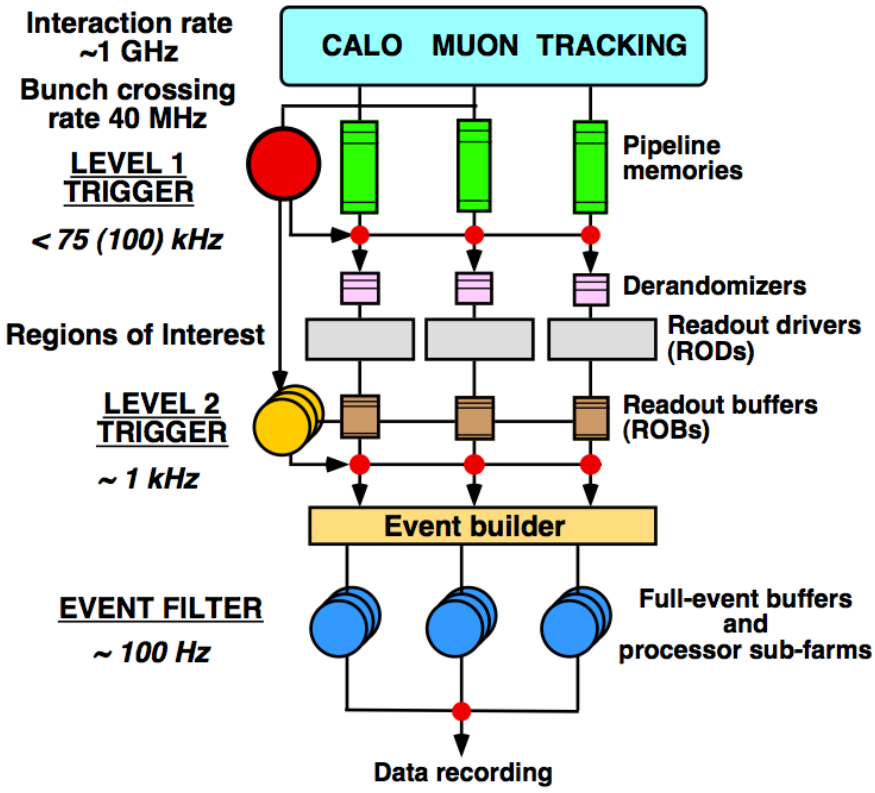

Figure 3.7: Schematic diagram of the ATLAS trigger system.

Level-1 is a hardware-based trigger system, accepting information from the muon trigger chambers (RPC, TGC) and reduced-granularity ($\Delta\eta \times \Delta\phi = 0.1 \times 0.1$) calorimeter information. L1 defines Regions-of-Interest (RoI) with size of $\Delta\eta \times \Delta\phi = 0.1 \times 0.1$ in the barrel and $\Delta\eta \times \Delta\phi = 0.25 \times 0.25$ in the end-cap, and has 2.5 μs to

make a decision on whether to let an event to pass to the next stage, L2. L1 accepts events at a rate of up to 75 kHz. Trigger items include leptons, jets, photons and missing energy. For example, the L1 muon trigger looks for hit coincidences within the muon trigger chambers that define the muon p_T, and then selects muons with p_T above six programmable thresholds and gives a rough estimate of their positions to construct the muon RoIs.

Level-2 is a software-based trigger that uses RoI information from L1. The L2 trigger has full detector information around the RoI. For example, hit information from the ID, and it is able to reduce to event rate to around 1 kHz, using about 40 ms for making the decision.

The final stage, the Event Filter, is also a software-based trigger, which uses information from the full detector, not just an RoI, and implements algorithms that are identical (or at least similar) to those used in offline reconstruction. The EF constructs complex objects, such as vertices, tracks, invariant masses, etc., so as to make the final decision on whether or not to store the event for offline analysis. The L2 and EF trigger are also referred to as the "High Level Trigger", or HLT.

3.2.6 Data Storage

ATLAS is expected to collect ∼4 petabytes of data per year, therefore the data storage is impossible to be done by a single institution or facility. A distributed computing infrastructure, GRID, is developed for solving this situation. In this model, the raw data from ATLAS is first processed and stored at the Tier-0 facility (CERN). The replica of the raw data is distributed to the approximately ten Tier-1 centers around the world. The Tier-1 centers are also in charge of reprocessing data and running the Monte Carlo simulations. Each Tier-1 center has several Tier-2 centers that are hosted by universities or laboratories, Tier-2's provide the Monte Carlo

simulation capacity for the experiment. Many smaller computing resources serve as Tier-3 facilities for physics analysis. Indiana University co-hosts the Midwest Tier-2 center with University of Chicago and University of Illinois at Urbana-Champaign, and also provides Tier-3 computing resources.

Chapter 4

Data and Monte Carlo Simulations

"Not only is the Universe stranger than we think, it is stranger than we can think."
– **W. Heisenberg**

4.1 Data

In this thesis the data used were collected by the ATLAS detector during the LHC proton-proton data-taking period between B2 and K4 in 2011. Figure 4.1 shows a summary of the luminosity delivered to ATLAS in 2011. Events in the data samples were selected using a trigger that contains two muons each having $p_T > 4$ GeV, $|\eta| < 2.4$ with opposite charges, an acceptable common vertex, and a $2-14$ GeV cut on the di-muon invariant mass (EF_2mu4_DiMu trigger). Only those events acquired during stable LHC beam conditions and while the Inner Detector and the Muon Spectrometer were fully operational are used in the analyses reported here.

Since the EF_2mu4_DiMu selection criteria for muons changed after period K4 data to require coincident hits in all three muon trigger layer, the muon reconstruction and trigger efficiencies need to be calculated separately before and after period K4 data. To simplify the analysis, this thesis only uses 2011 data before period K4 data (March through August). The total corresponding integrated luminosity of this dataset is 1.85 ± 0.07 fb^{-1} [102]. Table 4.1 shows a breakdown of 2011 data taking periods.

The data were processed using release 17 ATHENA[1] software [90], and the offline analysis is also be performed using the same ATHENA release.

4.2 ATLAS Data Model

The raw data collected from ATLAS has a size about 1.5 MB per event in order to allow physicists to implement analyses with an acceptable data size. ATLAS provides several different stages of datasets:

[1] ATHENA is the software framework in ATLAS.

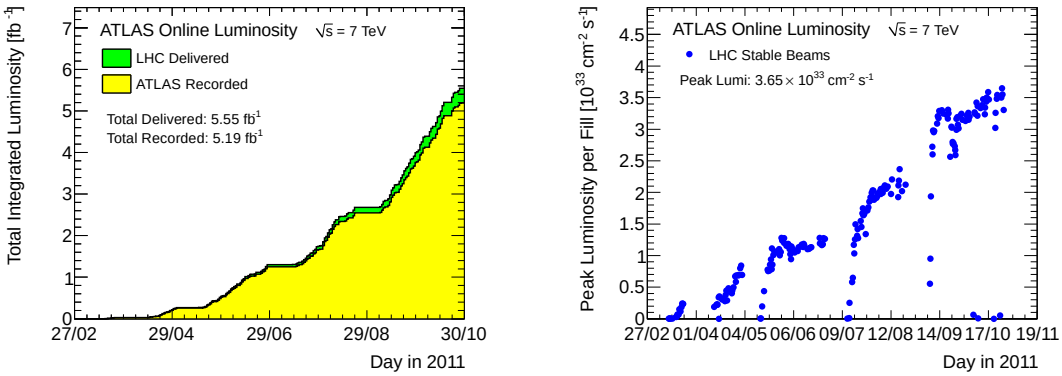

(a) (b)

Figure 4.1: The ATLAS data-taking performance in 2011: (a) integrated luminosity, and (b) instantaneous luminosity versus time.

Period	Run Nos.	Trigger	Prescale	Eff. Lumi. (pb^{-1})
B2	178044 - 178109	EF_2mu4_DiMu	1.0	12.7
D	179710 - 180481	EF_2mu4_DiMu	1.0	171.0
E	180614 - 180776	EF_2mu4_DiMu	1.0	49.8
F2, F3	182161 - 182519	EF_2mu4_DiMu	1.0	149.2
G	182726 - 183462	EF_2mu4_DiMu	1.0	550.9
H	183544 - 184169	EF_2mu4_DiMu	1.0	270.3
I	185353 - 186493	EF_2mu4_DiMu	1.0	391.8
J	186516 - 186755	EF_2mu4_DiMu	1.0	230.6
K1 - K4	186873 - 187763	EF_2mu4_DiMu	26.0	21.9
Total				1848.2

Table 4.1: Data information by run and period used in this thesis.

- **Event Summary Data (ESD)** is produced directly from the raw data, and it contains sufficient information to allow particle identification, track refitting, jet calibration, etc. The size for the ESD is ∼500 kB per event.

- **Analysis Object Data (AOD)** stores reconstruction objects in the event that are more direct to physics analyses. It is produced from the ESD that means that it loses some information from the raw data. The size for the AOD is ∼100 kB per event.

- **Developed Analysis Object Data (DAOD)** has exactly the same data structure as AOD with exception that only useful reconstruction objects for particular physics analyses are stored in the event which is decided by different physics groups. For example, the jet information is not stored in the B-physics DAOD.

- **Ntuples (B-ntuple, D3PD...):** To have a more comfortable size to do the analysis, physics groups also provide the datasets at the ntuple level which contain more physical variables such as vertex fitting, lifetime information, etc.

4.3 Monte Carlo Simulations

Monte Carlo (MC) simulation provides the information on how well we understand the detector performance and also on how different types of events are reconstructed in the detector. There are four steps in generating MC samples, namely, generation, simulation, digitization and reconstruction. Figure 4.2 illustrates the full chain of MC generation in ATLAS. Brief descriptions of each step are summarized in the following.

- **Generation:** In this stage, the parton-level events and hadronization are generated from the matrix elements of the physical processes. Several different

generator packages are used in ATLAS, such as PYTHIA [91], MC@NLO [92] and others. More details of PYTHIA and MC@NLO will be discussed later. Other parameters, for example, the collision center-of-mass energy, or the Parton Density Functions (PDFs), are also set here. The generator provides the four-momenta of the physical particles which will be used in the next stage.

- **Simulation:** This step simulates the response of the ATLAS detector to the particles produced in the "Generation" step. GEANT4 [94] is used to model the signals produced in each ATLAS detector element, yielding G4Hits, which are passed to the next stage.

- **Digitization:** The actual electronics response to the signals produced by particles traversing the detector (G4Hits) are simulated at this stage, the output of which approximates real raw data from the physical detector.

- **Reconstruction:** This process reconstructs the raw data (time, voltages, etc.) into physical objects, such as tracks and energy deposits.

Since the Υ cross-section measurements in this thesis are totally independent of the MC, MC samples are only used minimally. Only closure tests of di-muon trigger efficiencies and cross-checks of the bin migration effects use MC, as will be discussed later.

4.3.1 PYTHIA

PYTHIA is a complete MC generator package that can generate and simulate the events from initial hard process to particle decays included hadronization. In ATLAS, the heavy quarkonium states, such as J/ψ and Υ, are simulated by PYTHIA with the MRST LO* [95] parton density functions.

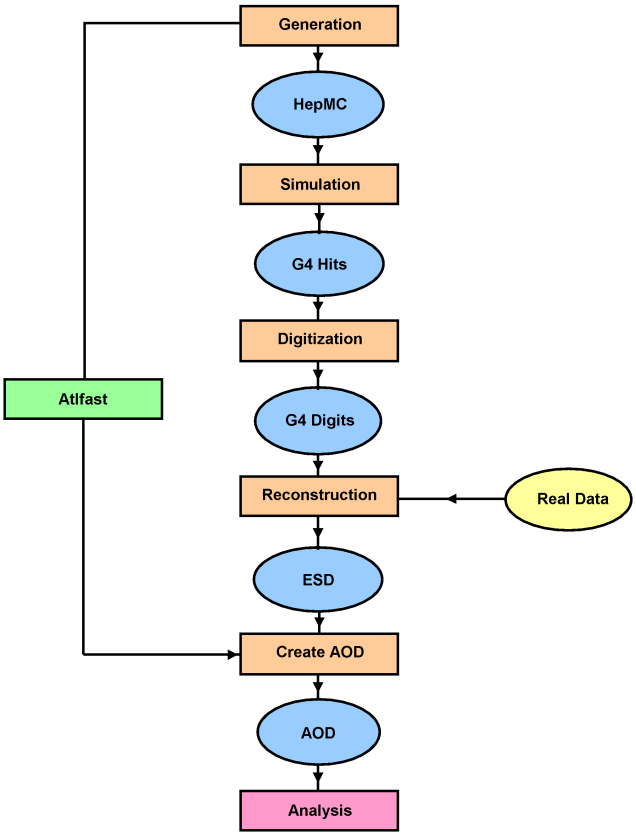

Figure 4.2: The full chain of the Monte Carlo generation in ATLAS.

To save processing time and to avoid the generation of too many unused events, a filter cut is employed. Each lepton produced in an quarkonium decay from the quarkonia candidates must have $p_T^\ell > 2.5$ GeV and $|\eta^\ell| < 2.5$.

4.3.2 MC@NLO

The MC@NLO generator incorporates Next-to-Leading-Order (NLO) contributions from QCD processes, it uses full NLO matrix elements to simulate the events and combines with the HERWIG package [93] to simulate the hadronization processes and the underlying events. Possible light CP-odd Higgs (a_1) signals at different masses are generated using this generator with CTEQ6.6 [96] Parton Density Functions. The signals were generated by using the same setting as those used for the standard MSSM CP-odd Higgs (A^0) in ATLAS, with the following modifications: (i) scaling down the signal mass, (ii) setting the neutral decay width to be 0.9 MeV [2], and (iii) forcing the a_1 to decay to two muons.

The signal a_1 simulations also employ similar filter cut to those used for the heavy quarkonium MCs, with exception that we now require $|\eta^\mu| < 3.0$. The efficiency of this filter cut varies from about 20% to 60% for $m_{a_1} = 6$ to 11.5 GeV, as the leptons' kinematics are highly dependent on the mass of the a_1 candidate. Figure 4.3 and 4.4 show the kinematic distributions at generator level for the a_1 and muons respectively with different m_{a_1}.

[2] This is a very narrow resonance.

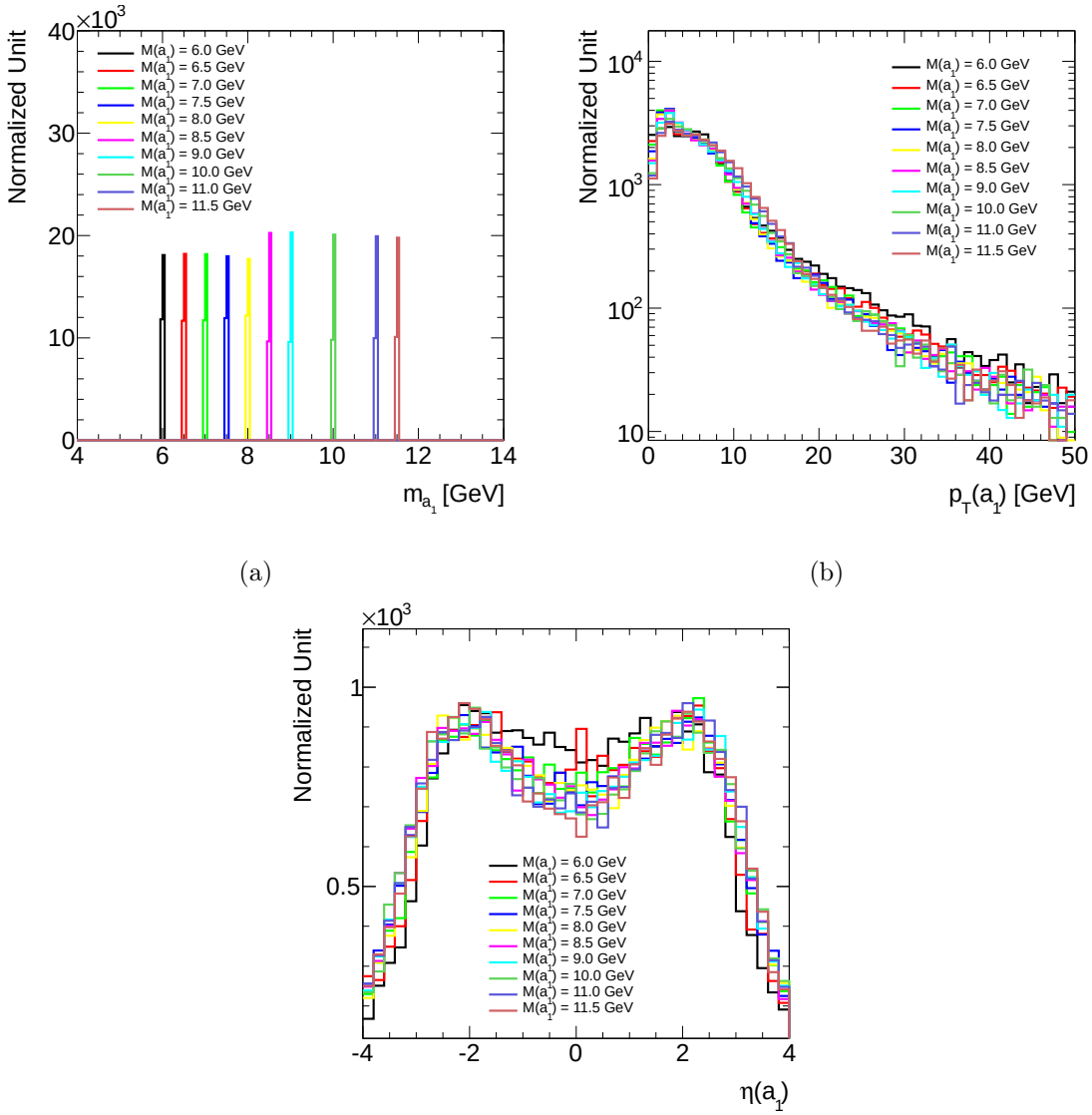

(a) (b)

(c)

Figure 4.3: Kinematic distributions of the a_1 Higgs boson: (a) m_{a_1}, (b) $p_T(a_1)$, and (c) $\eta(a_1)$.

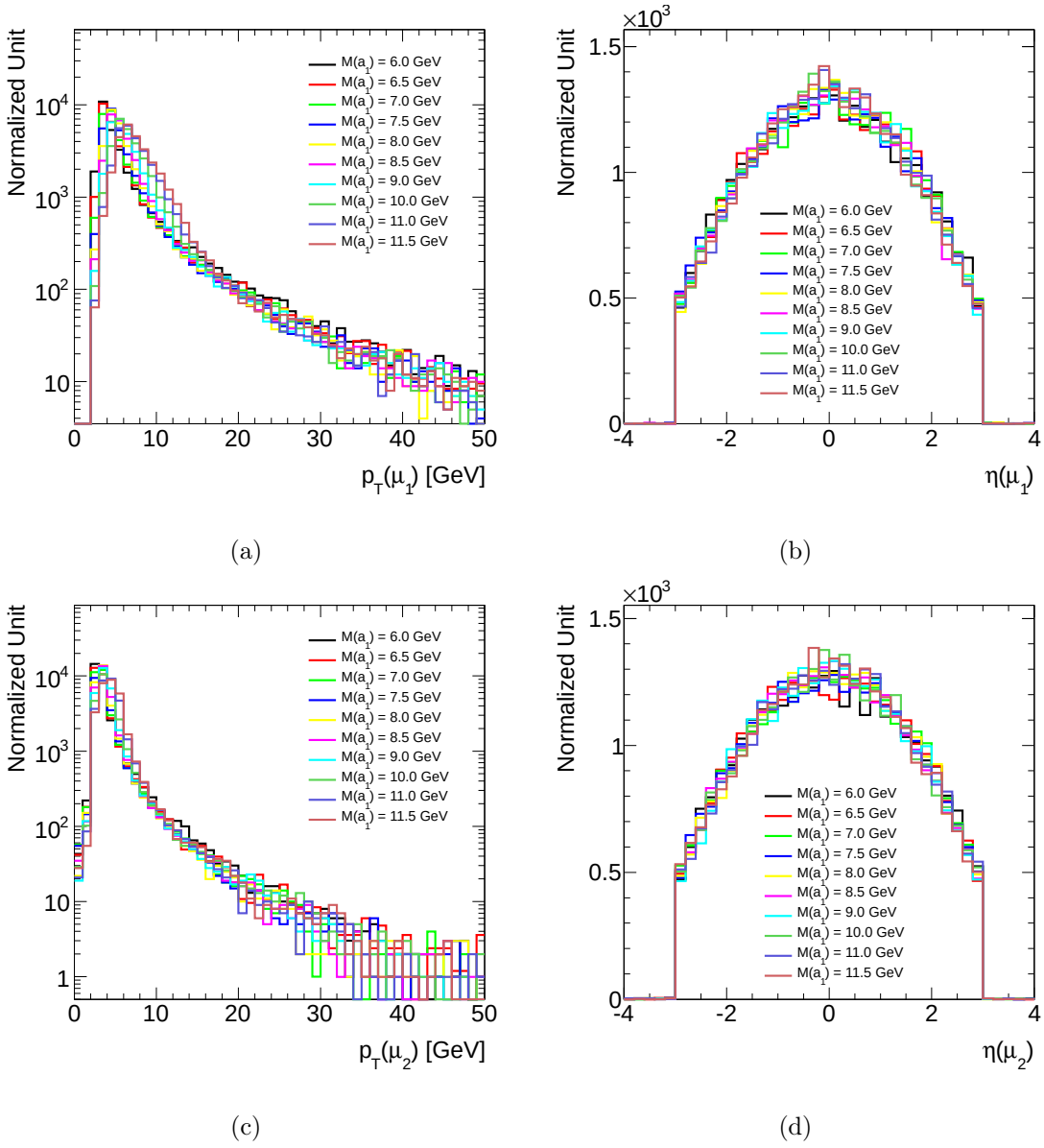

Figure 4.4: Muon kinematic distributions: (a) leading muon p_T, (b) leading muon η, (c) subleading muon p_T, and (d) subleading muon η.

Chapter 5

Di-Muon Selection

"An expert is a man who has made all the mistakes which can be made, in a narrow field."

– **N. Bohr**

In this chapter, muon and di-muon candidate selections are described. Section 5.1 summarizes the muon identification and reconstruction, and also describes the efficiency measurements. Trigger efficiency measurements are discussed in Section 5.2. The technique employed to estimate di-muon trigger efficiencies was developed for this analysis. Finally the di-muon mass spectra with different triggers are shown in Section 5.3.

5.1 Muon Identification and Reconstruction

The ATLAS detector has an impressive muon system as we have described in Section 3.2.4. Muon identification and reconstruction are extended to $|\eta| < 2.7$ with accurate p_T measurements ranging from 1 GeV to more than 1 TeV. Three categories of reconstructed muons are defined in ATLAS:

- **Standalone Muons** are constructed entirely based on signals collected by the Muon Spectrometer (MS). Track parameters are obtained from MS tracks and are extrapolated to the interaction point. This extrapolation takes into account multiple scattering and energy losses in the traversed material. Since precise tracking information from the Inner Detector (ID) is not used, these standalone muons have larger backgrounds, poorer momentum and spatial resolutions than those muons in the other categories.

- **Segment Tagged Muons (Tagged Muons)** are formed by segments that are not associated with an MS track, but that are matched to ID tracks extrapolated to the MS. Such a reconstructed muon adopts the measured parameters of the associated ID track.

- **Muons from combined reconstruction (Combined Muons)** require a combined fit of a standalone MS track and an ID track. Due to the ID coverage,

the combined reconstruction covers $|\eta| < 2.5$. The combined muons used all tracking information available in the ATLAS detector, so these have the best purity and resolutions among all three types of muons. Because of the large amount of material in the calorimeters and MS system, improvements in track parameter resolution due to the addition of MS tracks to those formed only from the ID tracks is expected to be small. Thus track parameter for combined muons are often taken from ID-only fits with MS tracks being used primarily to decrease backgrounds.

In this thesis only *Combined* muons with ID track parameters are used. We thus have the most pure and high quality di-muon samples in our analysis.

5.1.1 Muon Reconstruction Efficiency

I The Tag-and-Probe Method

The reconstruction efficiency for combined muons is calculated for those muons falling into the acceptance: $p_T^{\mu} > 4$ GeV and $|\eta^{\mu}| < 2.4$. It is determined by using the standard tag-and-probe method [98]. The basic idea of this method is to use muon and track combination with J/ψ mass, and then to check if the track identified as muon. Events containing at least one combined muon and one ID-track are used. The events also are required to fire at least one of the following single muon triggers: EF_mu4, EF_mu13, EF_mu15, EF_mu18, EF_mu20 or EF_mu40[1], so as to avoid bias from the di-muon triggers. This method uses two ID-tracks that have a common vertex and form a di-muon candidate with invariant mass close to the J/ψ mass. The *tagged* and *probed* muons both require the following selection cuts on the ID-tracks:

- ≥ 1 Pixel hits;

[1]These triggers have p_T thresholds of 4, 13, 15, 18, 20 and 40 GeV, respectively, and require at least one muon RoI.

- ≥ 6 SCT hits;
- $p_T > 4$ GeV;
- $|\eta| < 2.5$;

Additional cuts from the ATLAS Muon Combined Performance Group recommendation are applied to *tagged muons* candidates by following:

- No expected B-Layer hit or number of B-Layer hits > 0;
- Number of Pixel hits + number of crossed dead Pixel sensors > 1;
- Number of SCT hits + number of crossed dead SCT sensors ≥ 6;
- Number of Pixel holes + number of SCT holes < 2;
- Let nTRThits denote the number of TRT hits on the muon track, nTRToutliers the number of TRT outliers on the muon track
  n = nTRThits + nTRToutliers
  Case 1: $\eta < 1.9$. Require $n > 5$ and nTRToutliers $< 0.9\ n$
  Case 2: $\eta \geq 1.9$. If $n > 5$, then require nTRToutliers $< 0.9\ n$;

Tagged muons are also required to be matched to a muon trigger object. *Probed muon* candidates are required to be separated from the tagged muon by $\Delta\eta > 0.4$ and $\Delta\phi > 0.2$.

The muon reconstruction efficiency is calculated by comparing the J/ψ yield from *tagged muon*-ID track pair and the yield from *tagged muon*-ID track pair where the ID track is also required to be associated with a combined muon candidate.

II J/ψ Mass Fits

Di-muon mass distributions are divided into fine p_T and $q\times\eta$ bins (13×27). The J/ψ signal is extracted using fits to a single Gaussian signal and second-order polynomial background. Alternate fits using a double Gaussian and a third-order polynomial are used to estimate systematic uncertainties.

To exclude contributions from the $\psi(2S)$, the mass region $3.5 - 3.8$ GeV is not used in the J/ψ mass fit. Figure 5.1(a) shows an example of a di-muon mass fit for *probed* muons that have low-p_T and fall in the barrel region, Figure 5.1(b) presents an example for high-p_T and end-cap muons.

III Final Muon Reconstruction Maps

The final two-dimensional muon reconstruction maps are shown in Fig. 5.2. Figures 5.3 and 5.4 show examples of the efficiencies versus $q \times \eta$ in different p_T slices and versus p_T in different $q \times \eta$ slices respectively. The structure in Fig. 5.3 shows the transition region between barrel and end-cap ($1 < |\eta| < 1.2$), gap region of two barrel components ($|\eta| = 0$), and the asymmetric behavior is due to the structure of the magnetic field[2] which are well described in MC. The rest of the plots for different slices are shown in Appendix A.

[2]The positive (negative) charged muons are bent towards larger (smaller) η.

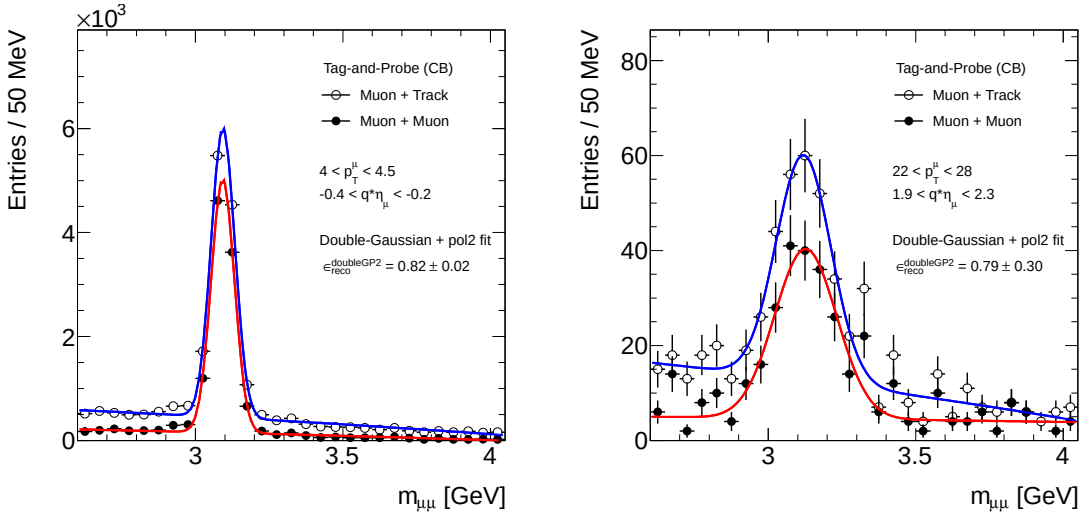

(a) (b)

Figure 5.1: Examples of di-muon mass fits for (a) low-p_T muons in the barrel region, and (b) high-p_T muons in the end-cap region. The blue line is the fit for *tagged muon* and ID track pairs, while the red line is for pairs where the ID track also passes the combined muon requirements.

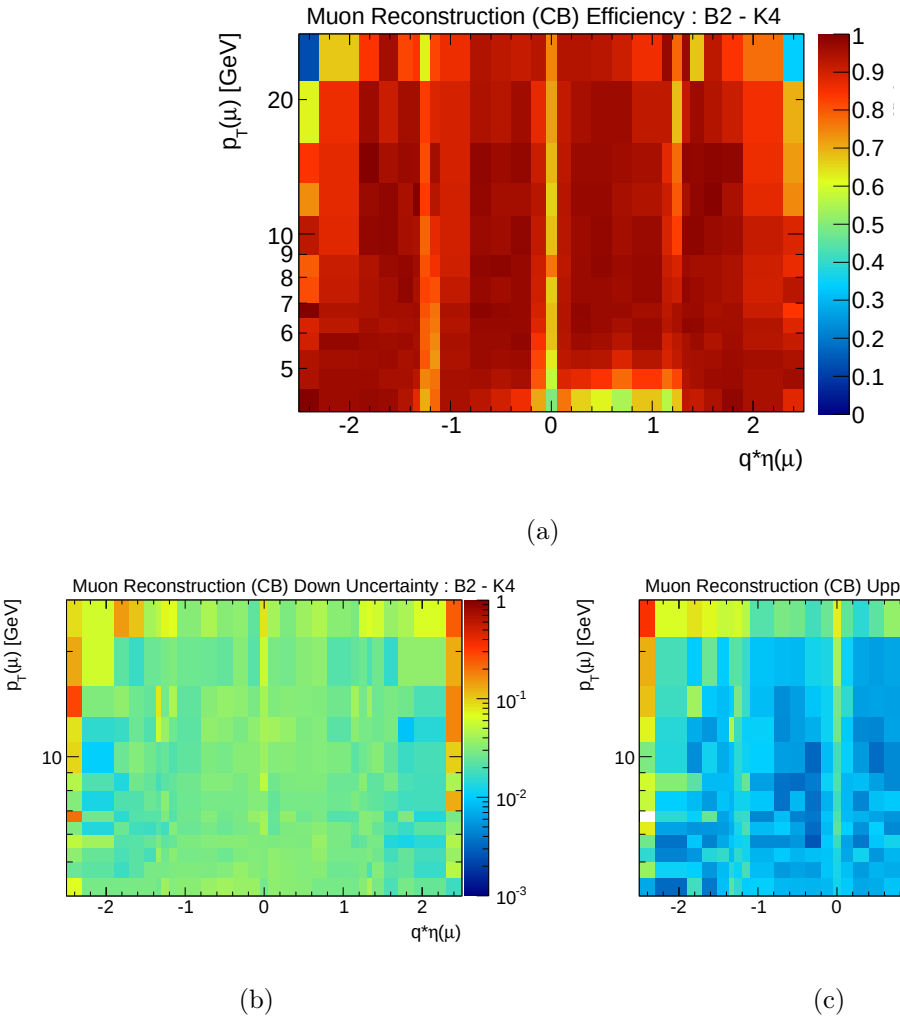

Figure 5.2: The two-dimensional, p_T versus $q \times \eta$, for (a) muon reconstruction efficiency, (b) with downward uncertainties of the efficiency, and (c) with upward uncertainties of the efficiency.

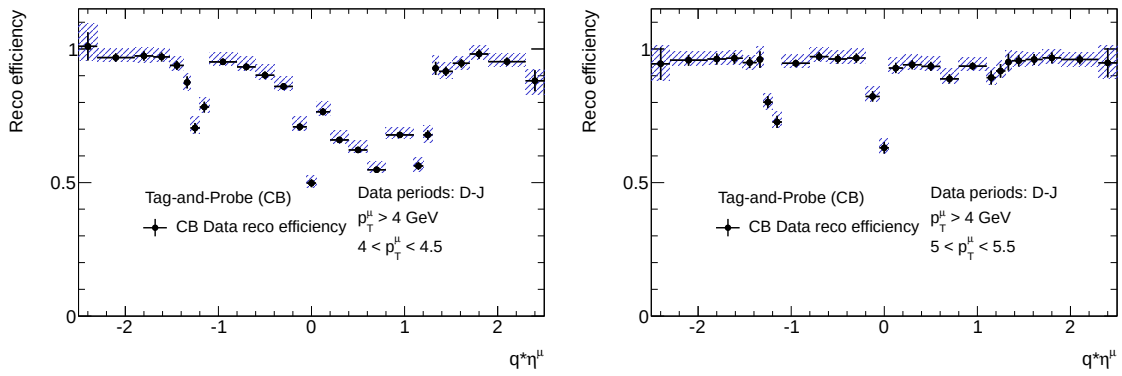

(a) (b)

Figure 5.3: The muon reconstruction efficiencies versus $q \times \eta$ in different probe muon p_T slices.

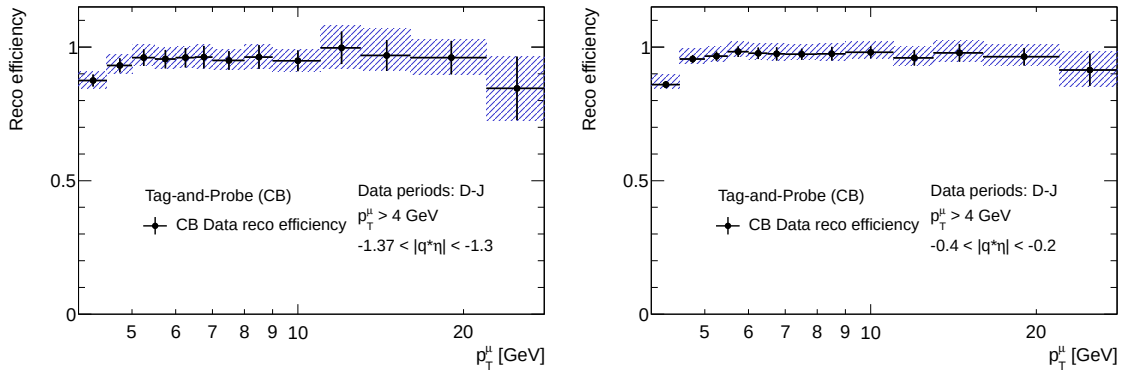

(a) (b)

Figure 5.4: The muon reconstruction efficiencies versus probe muon p_T in different $q \times \eta$ slices.

5.2 B-Physics Di-Muon Trigger

The trigger used in this thesis, for both the Υ cross-section measurements and the CP-odd Higgs search, is the B-physics di-muon trigger (EF_2mu4_DiMu) that requires two Level-1 muon Regions of Interest (RoI) with no p_T requirement confirmed by High Level Trigger (HLT) objects, which require a 4 GeV p_T cut. The other quality cuts are described in Section 4.1. The efficiency of this trigger is calculated with respect to offline selected di-muon candidates (see Section 5.1). The most important ingredients for determining the efficiency of this trigger are p_T, charge and η of each muon; the spatial separation between the two muons, ΔR, and the extra cuts on vertex quality (χ^2) and opposite sign (OS) for the di-muon pair. The trigger efficiency can be factorized into three parts:

$$\varepsilon_{\text{trig.}} = \varepsilon^{+}_{\text{EF\_mu4}}(p_T^{+}, \eta^{+}) \cdot \varepsilon^{-}_{\text{EF\_mu4}}(p_T^{-}, \eta^{-}) \cdot \mathcal{C}_{\mu\mu}^{\Delta\text{R,VTX\_OS}} \tag{5.1}$$

where $\varepsilon^{\pm}_{\text{EF\_mu4}}$ is the efficiency for the single-muon (EF_mu4) trigger where $\pm$ indicates positive and negative muons, while $\mathcal{C}_{\mu\mu}$ takes into account inefficiencies related to the di-muon requirements. Since the B-physics di-muon trigger efficiency changes rapidly when the muons are near the edge of the trigger system, muons are required to have $|\eta| < 2.3$, instead of 2.4, the physical coverage of the muon trigger system.

5.2.1 Closure Test

A Monte Carlo based closure test is performed to verify that the formula in Eq. 5.1 does not result in a biased estimate of the di-muon trigger efficiency. In this closure test, all three components are driven from the $\Upsilon(1S)$ MC except the $C_{\mu\mu}$ in the small ΔR region where J/ψ MC has been used. Experience in the J/ψ analysis [97] indicates that the charge dependence of the muon efficiency is a non-negligible effect. The charge dependence comes from the not-perfect-symmetric detector geometry and

different bending directions for positively and negatively charged muons. Figure 5.5 gives the single muon trigger, EF_mu4, efficiency maps for positive and negative muons from MC.

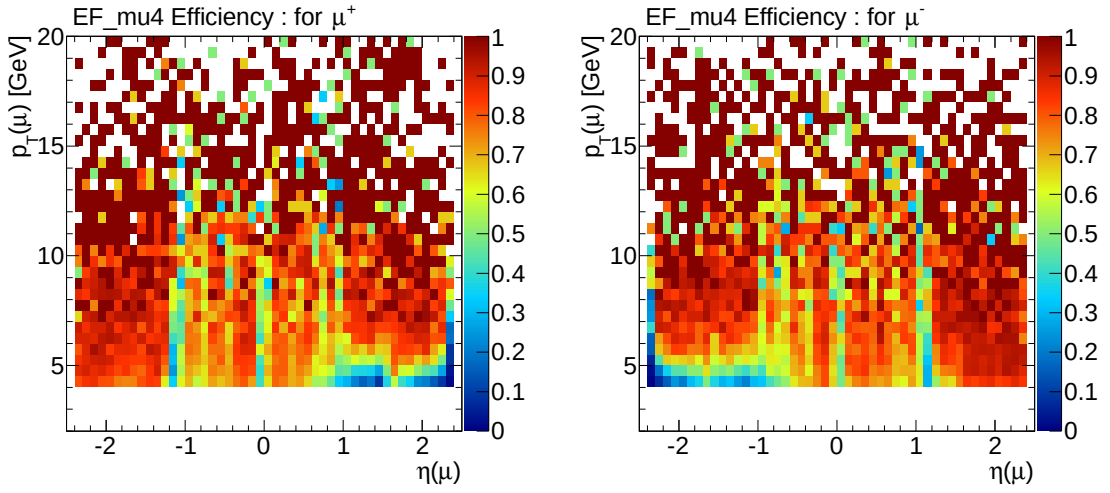

(a) (b)

Figure 5.5: The EF_mu4 trigger efficiency from $\Upsilon(1S)$ MC for (a) positively charged muons and for (b) negatively charged muons.

The efficiency for vertex quality and opposite-charge requirement is calculated using the EF_2mu4 trigger which is identical to EF_2mu4_DiMu except without vertex, opposite-charge requirements, and invariant mass cut. To decouple the momentum dependence, only muons that have $p_T > 8$ GeV are used for this ΔR correction study. The efficiency reaches a plateau value as shown in Fig. 5.6(a). The correction factor for $\Delta R_{\mu\mu}$ are shown in Fig. 5.6(b), the red and blue plots are extracted from J/ψ and $\Upsilon(1S)$ MC, while the black plots are the results from Muon-independent data (JetTauEtmiss stream). The plateau value in Fig. 5.6(b) contains the efficien-

cies of single muon trigger, vertex and opposite-charge requirements. Therefore, the pure ΔR correction can be extracted from the fit function. This plot shows that MC describes the ΔR correlation very well indicating that no large di-muon correlations are neglected in our efficiency calculation.

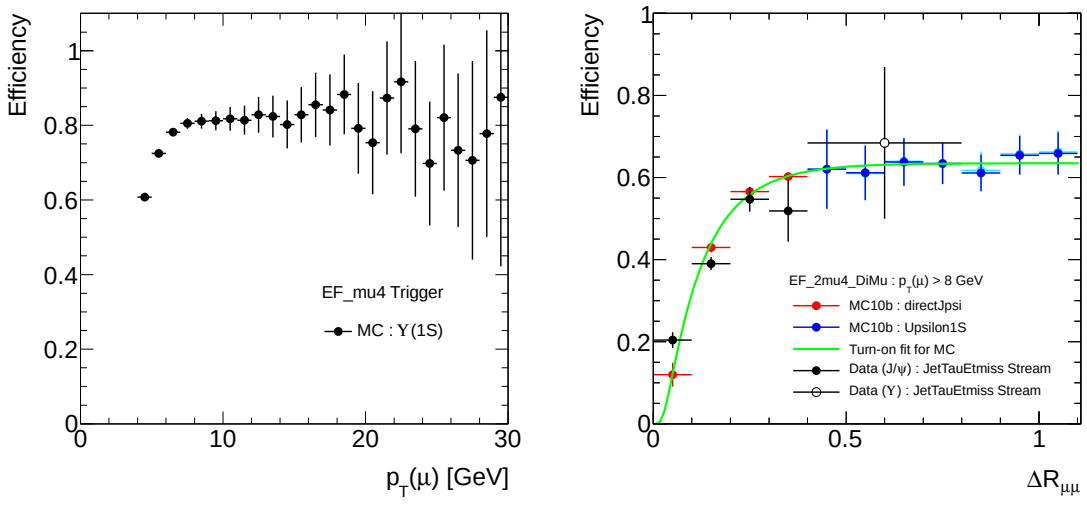

(a) (b)

Figure 5.6: (a) EF_mu4 efficiency versus p_T from MC, and (b) the trigger correction versus ΔR.

The closure test is performed by comparing two numbers: (1) $N_{reco.}^{before\ trigger}$ that is the number of reconstructed $\Upsilon(1S)$ candidates before applying trigger requirements and (2) $N_{corrected\ reco.}^{after\ trigger}$ which is the number of reconstructed $\Upsilon(1S)$ after applying trigger corrected for the EF_2mu4_DiMu trigger efficiency. The ratio of these two numbers should be close to unity if the formula is correct. The closure test is done as a function of $p_T^{\Upsilon(1S)}$ in two rapidity regions, $|y| < 1.2$ and $1.2 < |y| < 2.4$, and as a function of the rapidity of the $\Upsilon(1S)$. Results are shown in Figures 5.7(a), 5.7(b)

and 5.7(c) respectively. The full closure test is shown in the blue plots and they are fitted by a zeroth-order polynomial function (green line). Note that the fitted results are all close to unity.

5.2.2 Data-driven Correction Factor ($C_{\mu\mu}$)

The data-driven correction factor, $C_{\mu\mu}$, is built from two components: (a) the asymptotic value, C_a, from the vertex quality and opposite-charge requirement which is almost independent of the spatial separation of the two muons, $\Delta R_{\mu\mu}$, and (b) all other effects that vary with $\Delta R_{\mu\mu}$, including the requirement of having two distinct trigger RoIs.

I Asymptotic Correction C_a

This correction factor is measured by using $J/\psi \rightarrow \mu^+\mu^-$ candidates, and a special control trigger called EF_2mu4_Dimu_noVtx_noOS, which is equivalent to the EF_2mu4_DiMu trigger but excluding for the vertex quality and opposite-charge requirement[3].

The value of the correction is determined from the ratio of the J/ψ signal in events passing this control trigger to the J/ψ in events passing the EF_2mu4_DiMu trigger:

$$C_a(|y_{\mu\mu}|) = \frac{N_{J/\psi}^{EF\_2mu4\_DiMu}}{N_{J/\psi}^{EF\_2mu4\_DiMu\_noVtx\_noOS}}. \tag{5.2}$$

In this ratio, all other effects (such as single muon efficiency, spatial separation, etc.) cancel out except the vertex-quality and opposite-charge requirements.

This correction factor is measured in three regions: (a) barrel ($0.0 < |y_{\mu\mu}| < 1.0$); (b) transition ($1.0 < |y_{\mu\mu}| < 1.2$); and (c) end-cap ($1.0 < |y_{\mu\mu}| < 2.3$). Figures 5.8

[3]EF_2mu4_DiMu_noVtx_noOS is also equivalent to EF_2mu4 trigger but excluding the mass cut on di-muon candidates.

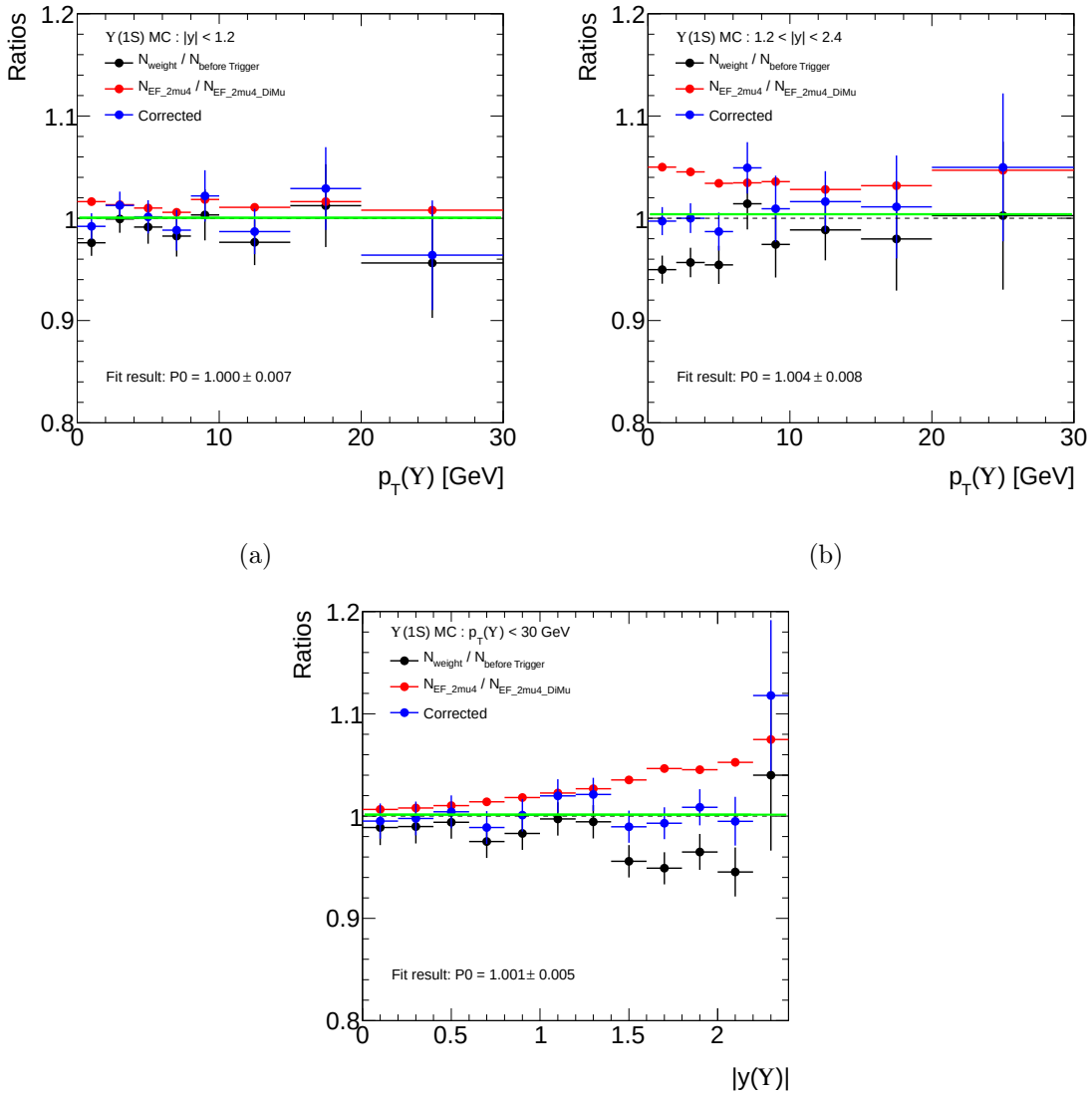

(a) (b)

(c)

Figure 5.7: The closure test for EF_2mu4_DiMu trigger efficiency from $\Upsilon(1S)$ MC versus p_T in (a) central region, and (b) forward region; and (c) versus rapidity of Υ.

and 5.9 show the variation of C_a for di-muon pairs with $\Delta R > 0.3$ is small, and that the plateau values are different in the three regions.

The uncertainties on these correction factors are dominated by the statistics of the control samples. We have verified that the systematic uncertainty from changing the J/ψ signal model (from single to double Gaussian) in fits used to extract the number of J/ψs is negligible.

II The ΔR Correction $C_{\Delta R}$

The correction for changes in trigger selection efficiency with the spatial separation of two muons, $\Delta R_{\mu\mu}$, is driven primarily by cases where the two muon RoIs overlap leading to only a single RoI being reconstructed by the trigger. This is measured in the same three detector regions as C_a. Di-muon events that are collected using the EF_mu18 single muon trigger with the standard muon selection cuts are used for this correction factor. Three additional conditions are also required:

- $2 < m_{\mu\mu} < 8$ GeV (excluding the J/ψ region, $2.9 - 3.3$ GeV)
- a muon with $p_T^{\mu_1} > 18$ GeV matched to the EF_mu18 trigger object
- a second muon with $p_T^{mu_2} > 8$ GeV

The requirement of $p_T^{\mu_2} > 8$ GeV decouples this correction from single-muon low-p_T turn-on behavior as shown in Fig. 5.6(a).

The values of the correction are calculated from the ratio (ρ_{2-8}) of number of di-muon events passing both EF_mu18 and EF_2mu4_Dimu and the number of events passing only EF_mu18:

$$\rho_{2-8}(\Delta R_{\mu\mu}, |y_{\mu\mu}|) = \frac{N_{2-8}^{EF\_mu18\ and\ EF\_2mu4\_DiMu}}{N_{2-8}^{EF\_mu18}}. \tag{5.3}$$

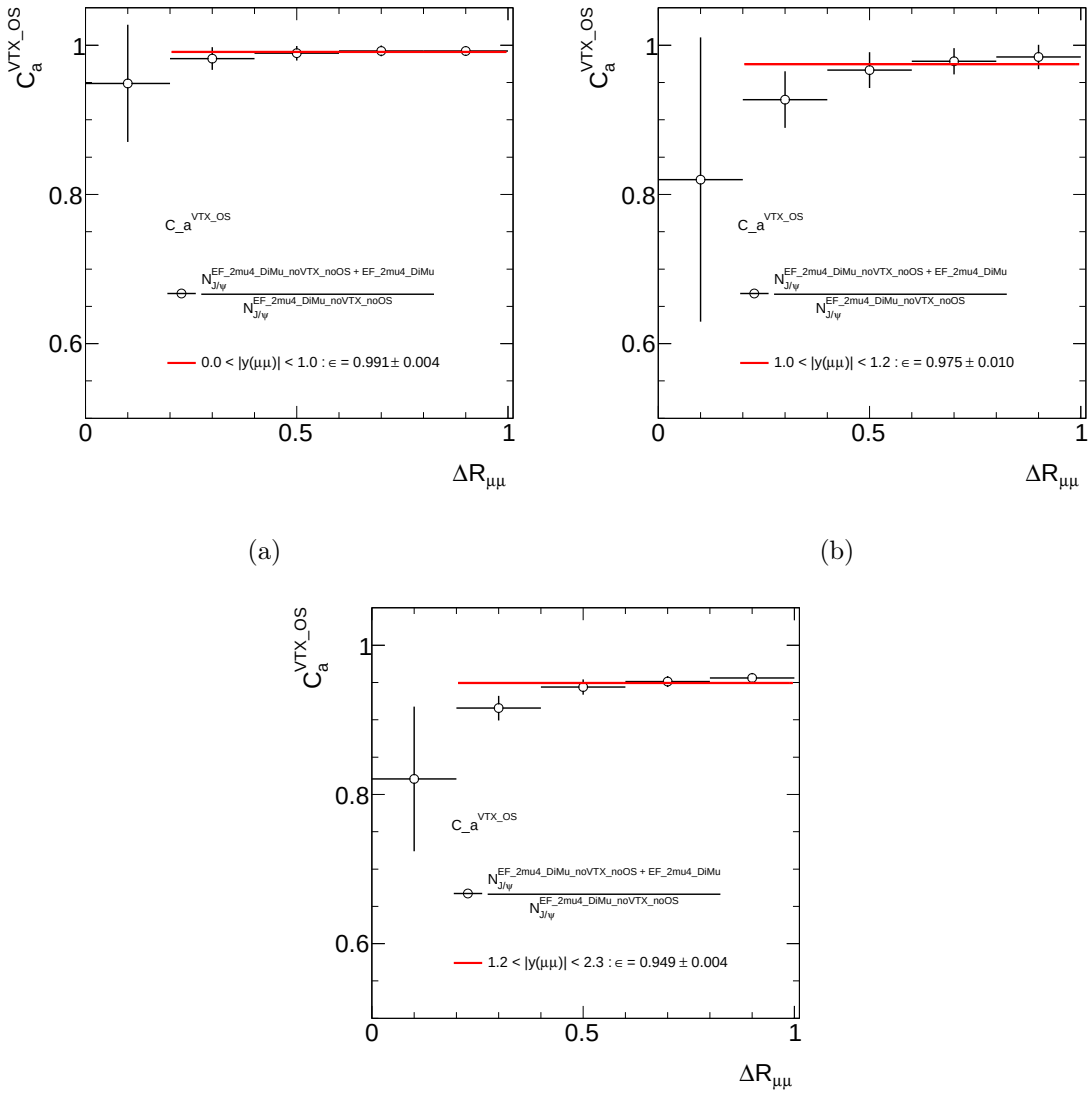

(a) (b)

(c)

Figure 5.8: The vertex and opposite-sign correction, C_a, in three detector regions: (a) $0.0 < |y_{\mu\mu}| < 1.0$; (b) $1.0 < |y_{\mu\mu}| < 1.2$; and (c) $1.0 < |y_{\mu\mu}| < 2.3$.

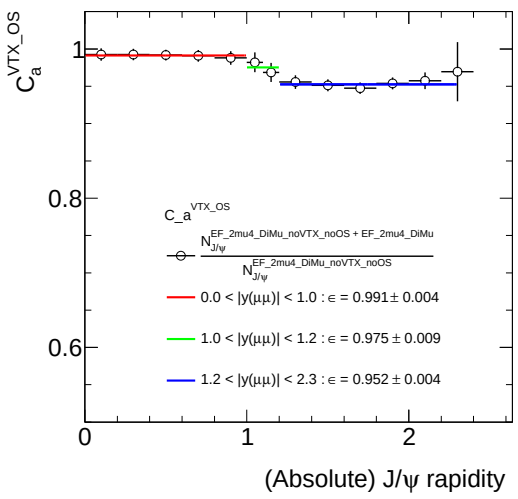

Figure 5.9: The vertex and opposite-sign correction, C_a, versus $|y_{\mu\mu}|$.

The distributions of the ratios in three regions are shown in Fig. 5.10. Each distribution is fitted with a function composed of an error function (describing the shape of the ΔR turn-on) and a normalization (corresponding to the plateau value of the data).

Since the normalization contains contributions from C_a and from the single muon trigger efficiency, the pure spatial separation (ΔR) dependence comes only from the fitted error function. The ΔR correction, $C_{\Delta R}(\Delta R, |y_{\mu\mu}|)$, is extracted from the fitted result of the error function as shown in Fig. 5.11.

III Final Di-muon Correction

The final di-muon correction factor is the combination of the two components, $C_a(|y_{\mu\mu}|)$ and $C_{\Delta R}(\Delta R, |y_{\mu\mu}|)$,

$$C_{\mu\mu}(\Delta R_{\mu\mu}, |y_{\mu\mu}|) = C_a(|y_{\mu\mu}|) \times C_{\Delta R}(\Delta R_{\mu\mu}, |y_{\mu\mu}|) \tag{5.4}$$

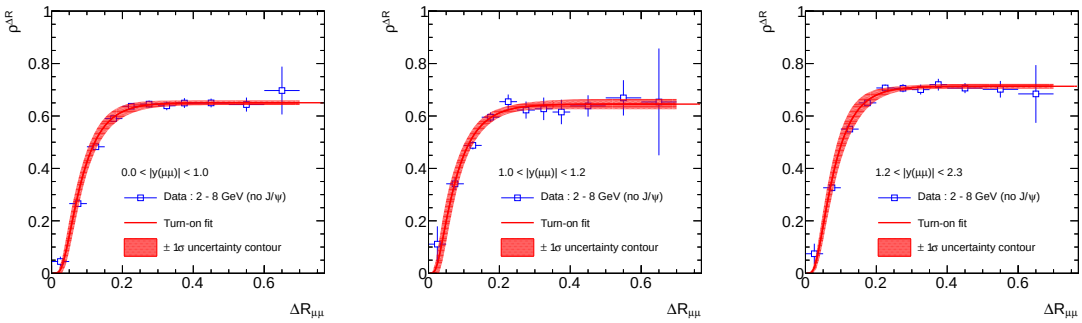

(a) (b) (c)

Figure 5.10: The ρ for ΔR correction in three detector regions.

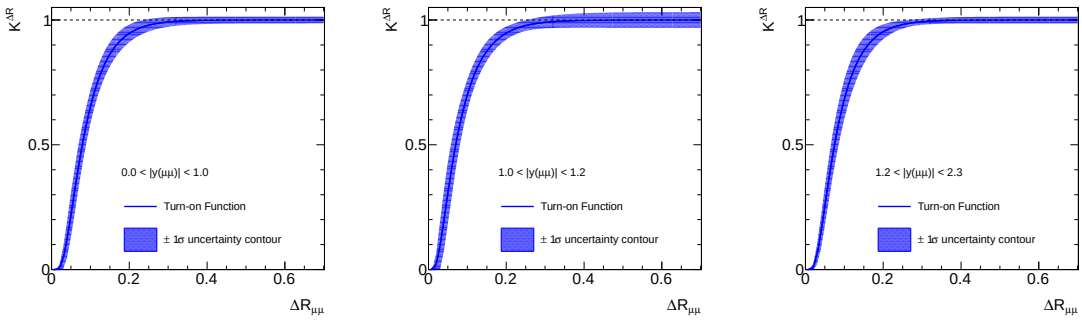

(a) (b) (c)

Figure 5.11: The pure shape of the ΔR correction in three detector regions.

Figure 5.12 shows the final correction factor in the three regions and also the uncertainty band on the correction derived from the uncertainties on C_a and $C_{\Delta R}$, arising from the statistics of the control samples used to obtain them.

5.2.3 Data-driven EF_mu4 Efficiency

The low-p_T single muon trigger, for example EF_mu4, was heavily prescaled in the 2011 ATLAS data-taking, so it is impossible[4] to measure the efficiency by using the standard method (tag-and-probe) which was used in 2010 [98].

The basic method of measuring the EF_mu4 efficiency in 2011 data is based on the tag-and-probe technique, but the details are slightly different[5]. A similar control sample (collected with the EF_mu18 trigger) as for the $C_{\Delta R}$ measurement is used. Additional selection on the candidates are also applied:

- $J/\psi \to \mu^+\mu^-$ candidate in $2.6 < m_{\mu\mu} < 4.1$ GeV (excluding the $\psi(2S)$ region, $3.5 - 3.75$ GeV)
- $p_T^{\mu_1} > 18$ GeV and matched to the EF_mu18 trigger object

The ratio ($\rho_{J/\psi}$) of number of fitted $J/\psi \to \mu^+\mu^-$ decays passing both the EF_mu18 and the EF_2mu4_Dimu and number of $J/\psi \to \mu^+\mu^-$ passing only EF_mu18 is calculated. Combining with Eq. 5.1, $\rho_{J/\psi}$ can be written as:

$$\begin{aligned}
\rho_{J/\psi}(p_T^{\mu_2}, q \times \eta^{\mu_2}, \Delta R_{\mu\mu}, |y_{\mu\mu}|) &= \frac{N_{J/\psi}^{EF_mu18\ and\ EF_2mu4_DiMu}}{N_{J/\psi}^{EF_mu18}} \\
&= \frac{N_{J/\psi} \times \varepsilon_{EF_mu18}^{\mu_1} \times \varepsilon_{EF_mu4}^{\mu_2} \times C_{\mu\mu}}{N_{J/\psi} \times \varepsilon_{EF_mu18}^{\mu_1}} \\
&= \varepsilon_{EF_mu4}^{\mu_2} \times C_{\mu\mu}(\Delta R, |y_{\mu\mu}|).
\end{aligned} \tag{5.5}$$

[4]The low statistics does not allow us to build a two-dimensional efficiency map.

[5]The idea came originally from the author.

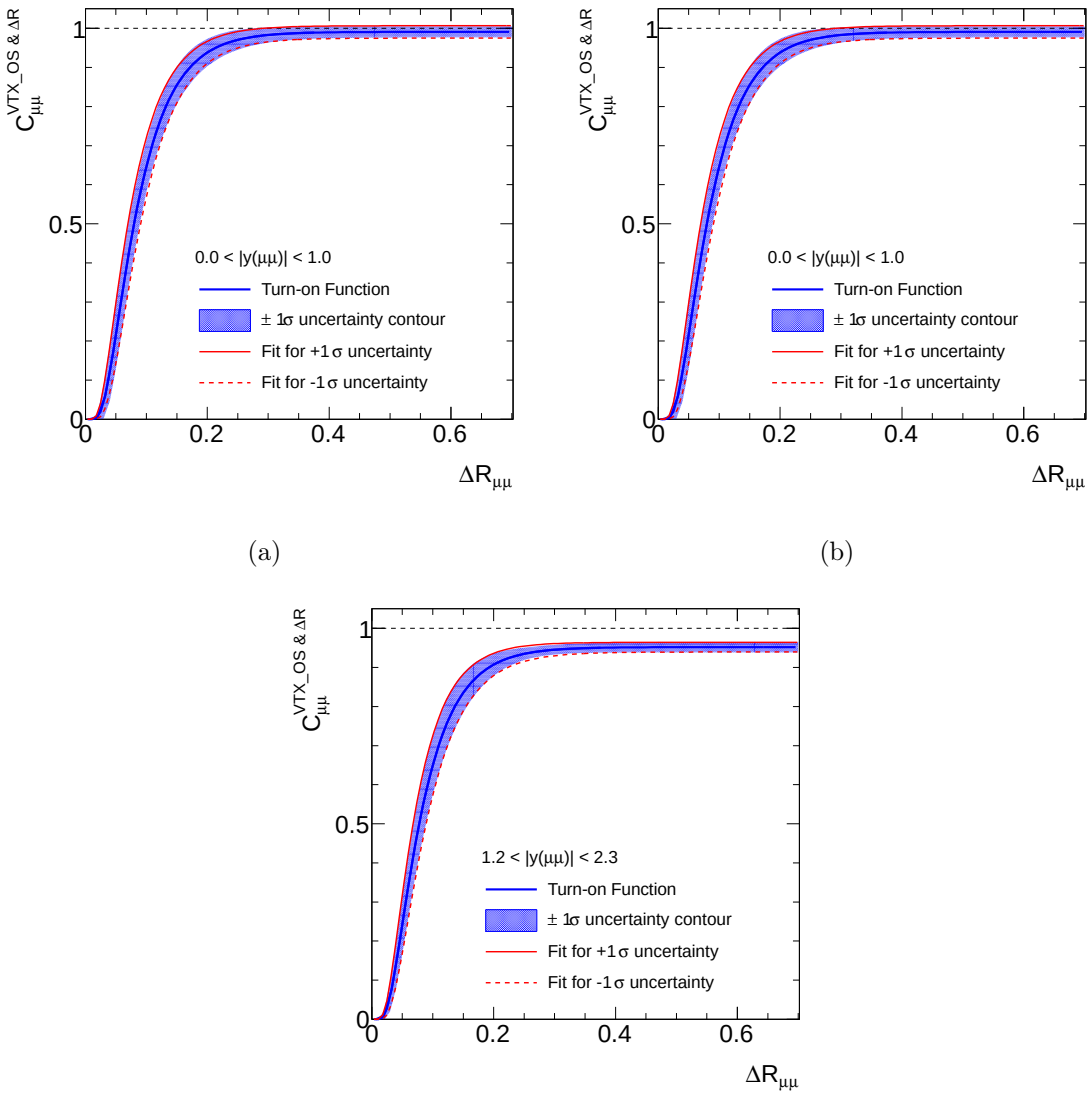

Figure 5.12: The final $C_{\mu\mu}$ in three detector regions.

where we have assumed that EF_mu18 is a subset of EF_mu4. This assumption is validated by using a special trigger chain, EF_mu4_All, which saves the EF_mu4 chain information for the event fired by other trigger as shown in Fig. 5.13.

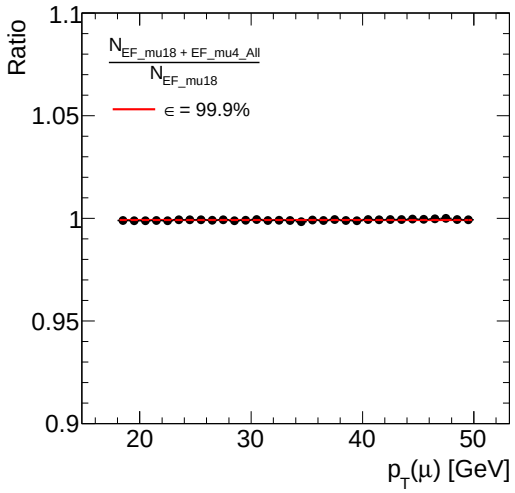

Figure 5.13: The ratio of number of events passing both the EF_mu18 and EF_mu4_All triggers and numbers of event passing the EF_mu18 trigger.

The efficiency of EF_mu4 can then be written down as the following by rearranging Eq. 5.6:

$$\varepsilon_{EF\_mu4}(p_T^{\mu_2}, q \times \eta^{\mu_2}) = \frac{\rho_{J/\psi}(p_T^{\mu_2}, q \times \eta^{\mu_2}, \Delta R_{\mu\mu}, |y_{\mu\mu}|)}{C_{\mu\mu}(\Delta R_{\mu\mu}, |y_{\mu\mu}|)}. \tag{5.6}$$

The EF_mu4 efficiency is measured in bins of p_T and $q \times \eta$ by applying the candidate-by-candidate correction, $C_{\mu\mu}$, to $\rho_{J/\psi}$. Figure 5.14 shows examples of the J/ψ mass fits used to extract the signal in different p_T and $q \times \eta$ region. As with the C_a correction, the systematic uncertainty from J/ψ fitting is negligible compared to the statistical uncertainty of the EF_mu18 and EF_2mu4_DiMu samples.

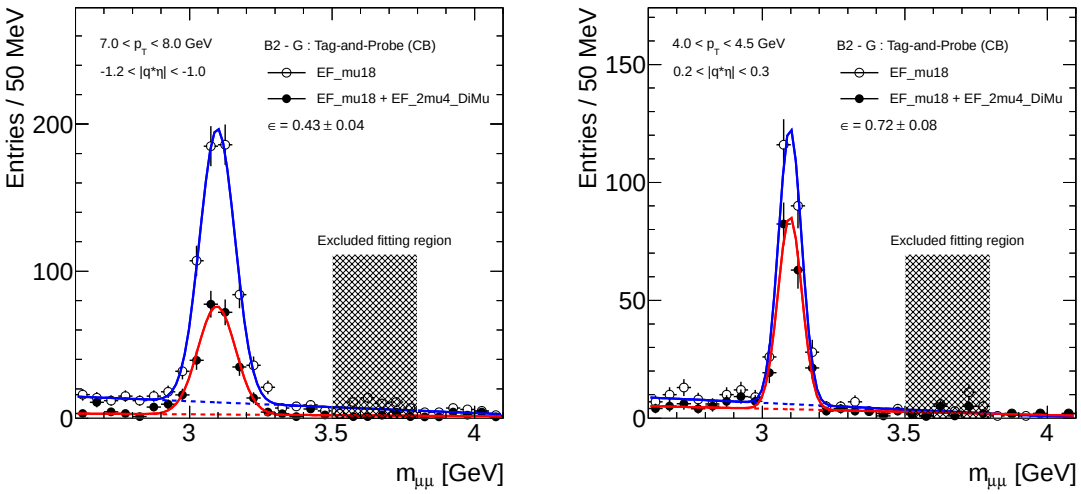

(a) (b)

Figure 5.14: Example J/ψ mass fits used for EF_mu4 efficiency determination.

Separate two-dimensional maps are constructed for periods B2 - G and H - J because the HLT algorithm (muComb) for trigger matching criteria changed in period H. The resulting efficiency maps are shown in Fig. 5.15, and the efficiencies in different p_T slices (before period H) are shown in Fig. 5.16 that have a similar structure in the muon reconstruction efficiency.

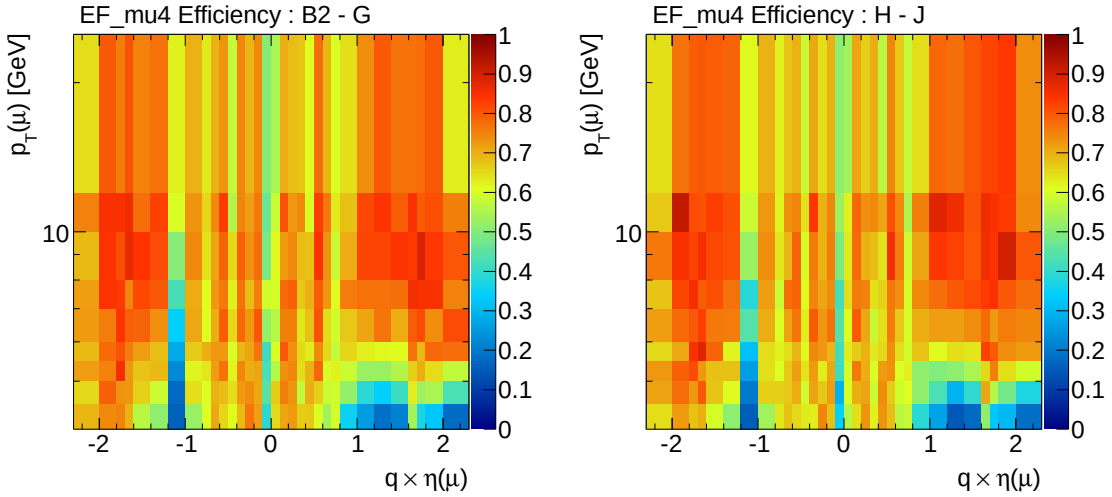

(a) (b)

Figure 5.15: The final two-dimensional EF_mu4 efficiency maps for (a) period B2 - G and (b) period H - J.

5.2.4 Trigger Matching

The trigger matching requirement helps us with only selecting the di-muon pairs associated with the trigger objects that fired the trigger. Trigger matching for single muon triggers is straightforward and without ambiguity. For di-muon triggers, the selected di-muon candidates are required to match to the corresponding trigger objects

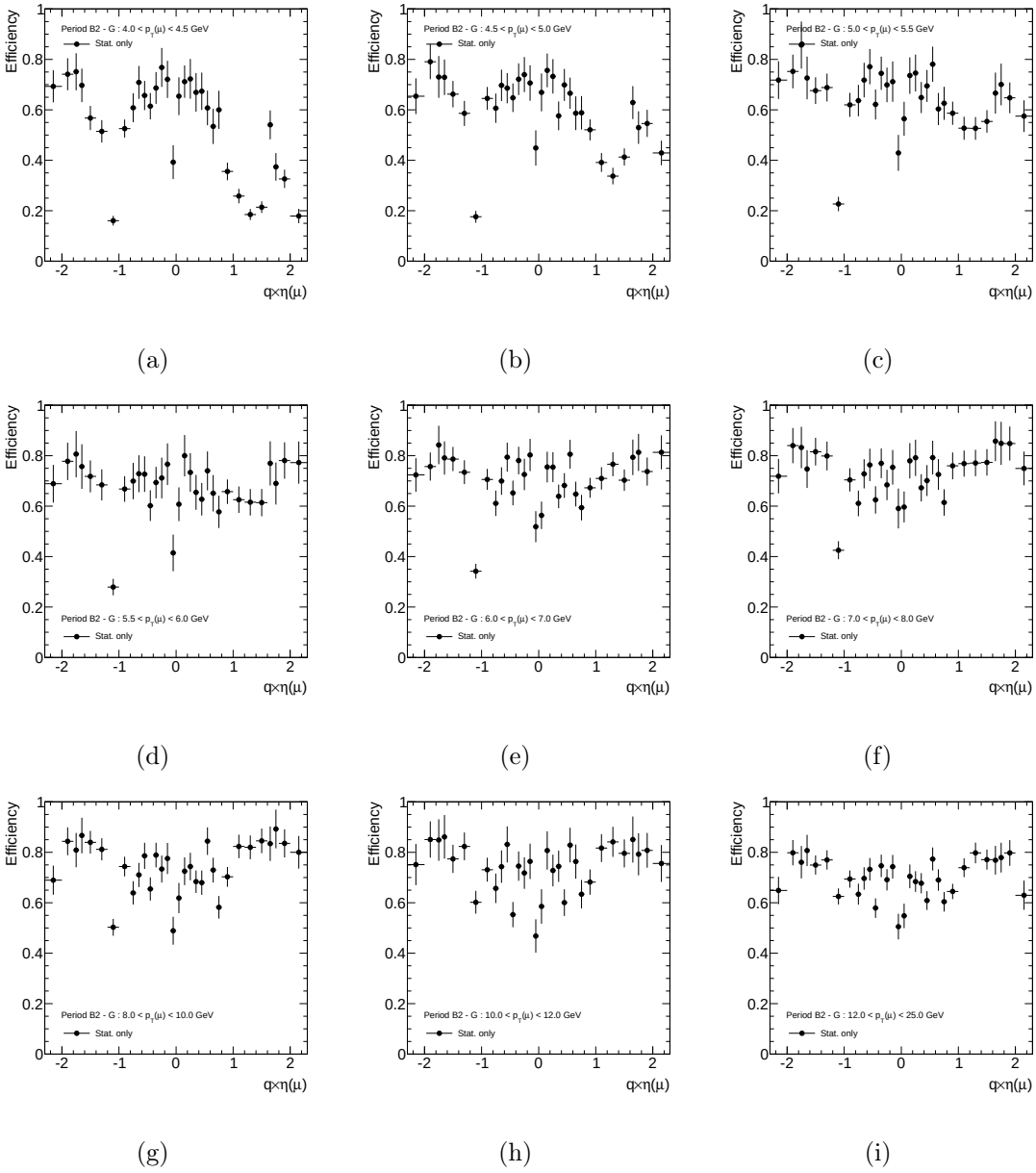

Figure 5.16: The EF_mu4 efficiencies for period B2 - G in different p_T slices.

that caused the events to be recorded. The spatial separation between muon and RoI, $\Delta R(\mu, RoI)$, is required to be less then 0.01.

Two simple examples, the first, if there are three reconstructed muons ($\mu_{1,2,3}$) and one di-muon trigger object which means two RoIs ($\mathrm{RoI}_{1,2}$) as illustrated in Fig. 5.17(a). Since only μ_1 and μ_3 are matched to different RoIs with $\Delta R < 0.01$, then di-muon pair $\mu_1\mu_3$ is selected.

The second example, if there are still three reconstructed muons ($\mu_{1,2,3}$), but two di-muon trigger objects A and B ($\mathrm{RoI}^A_{1,2}$ and $\mathrm{RoI}^B_{1,2}$) as demonstrated in Fig. 5.17(b). In this case, μ_1 and μ_3 are matched to the trigger object A, and μ_2 and μ_3 are matched to the trigger object B. Hence, only di-muon pairs $\mu_1\mu_3$ and $\mu_2\mu_3$ are selected.

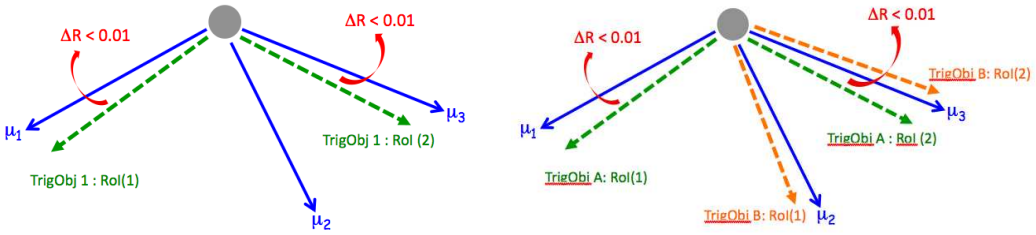

(a) (b)

Figure 5.17: An illustration of the di-muon trigger matching algorithm.

5.3 Di-Muon Candidates Selections

The di-muon candidate selections used in this thesis, for both the Υ cross-section measurement and the search for a light CP-odd Higgs, are summarized in Table. 5.1.

Figure 5.18 shows the di-muon mass distribution obtained from 2.3 fb^{-1} ATLAS

Variable	Cut value
Good Run Lists	Muon GRLs
Trigger	EF_2mu4_DiMu
Trigger matching	$\Delta R(\mu, RoI) < 0.01$
Good primary vertex	3 tracks associated
Muon type	2 combined muons
Standard cuts from ATALS	
Muon Combined Performance Group	Section 5.1.1
SCT hits	≥ 6
Pixel hits	≥ 1
p_T^{μ}	> 4 GeV
$\lvert\eta^{\mu}\rvert$	< 2.3

Table 5.1: The selection cuts for di-muon candidates.

data using a collection of single and di-muon triggers. Figure 5.18(a) shows clear mass resonances from the ω meson to the Z boson, while Figure 5.18(b) zooms into the B-physics area from the J/ψ to the Υ.

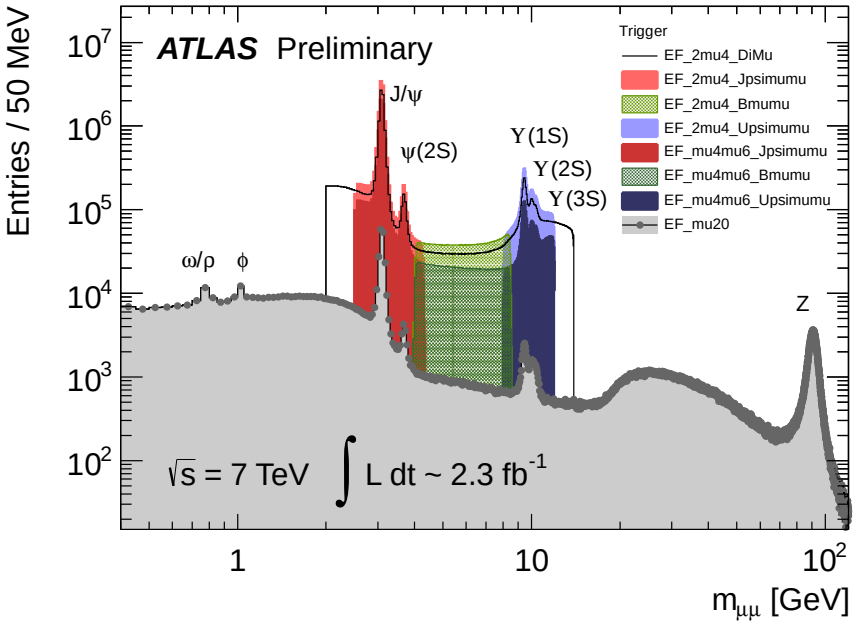

(a)

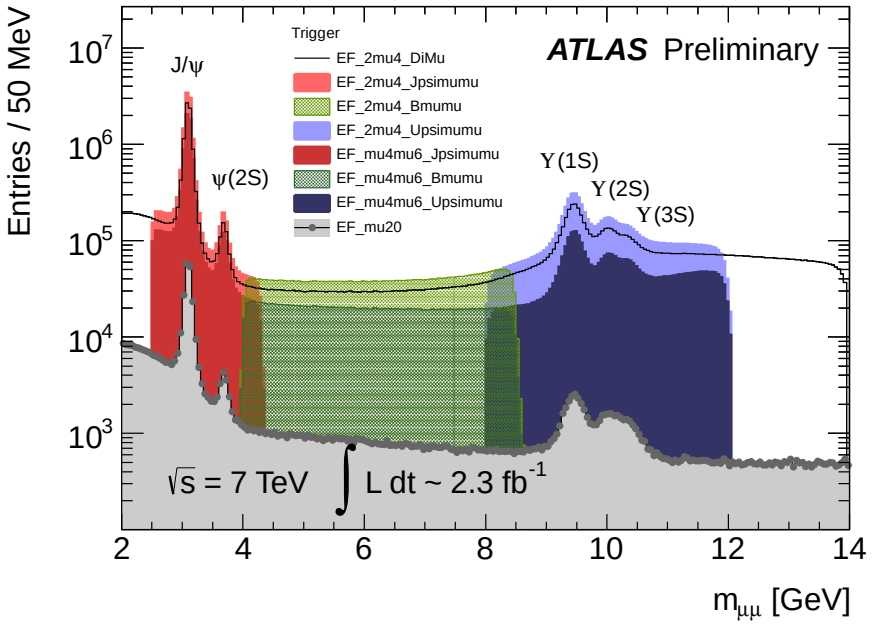

(b)

Figure 5.18: The di-muon mass distribution with various B-physics triggers (a) from the ρ meson to the Z boson; (b) when zoomed-in to the J/ψ to Υ region.

Chapter 6

ϒ Cross-Section Measurements

"It doesn't matter how beautiful your theory is, it doesn't matter how smart you are. If it doesn't agree with experiment, it's wrong."

– **R.P. Feynman**

ATLAS has already measured[1] the $\Upsilon(1S)$ production cross-section using 1.3 pb^{-1} of data collected in 2010 [99].

The cross-section measurements in this chapter expand upon that early work by (a) adding measurements of the $\Upsilon(2S)$ and $\Upsilon(3S)$ states, (b) allowing finer binning, especially at low p_T of the Υ meson, and (c) extending the measurements to the highest $\Upsilon(p_T)$ ever probed. The analysis also aims to build a foundation for future Υ polarization measurements in ATLAS. The results shown here are currently under ATLAS collaboration review, and are planned to be submitted for publication to Physical Review D.

6.1 Υ Fiducial Cross-Sections

As mentioned in Chapter 2 the polarization of the Υ is still not well understood, and huge variations of the cross-section prediction can come from different polarization assumptions. In order to reduce the uncertainty coming from the polarization assumption, cross-sections that are restricted to a particular phase space, i.e., fiducial cross-sections, are measured. This is done instead of measuring cross-sections corrected for acceptance (i.e., the inclusive cross-sections, described in Section 6.2). In this analysis, the fiducial cross-sections are measured for events with two muons with $p_T^\mu > 4$ GeV and $|\eta^\mu| < 2.3$[2]. They are measured as a function of the p_T of the Υ in two rapidity (y) bins and as a function of the rapidity of the Υ. The cross-sections are defined as the following:

$$\frac{d^2\sigma(\Upsilon)}{dp_T d|y|} \times Br(\Upsilon \to \mu^+\mu^-) = \frac{N^\Upsilon_{corr}}{\mathcal{L} \cdot \Delta p_T \Delta|y|}, \tag{6.1}$$

$$\frac{d\sigma(\Upsilon)}{d|y|} \times Br(\Upsilon \to \mu^+\mu^-) = \frac{N^\Upsilon_{corr}}{\mathcal{L} \cdot \Delta|y|}, \tag{6.2}$$

[1] The author contributed to this analysis as well.

[2] As mentioned in Section 5.2, we only used muons with $|\eta^\mu| < 2.3$.

where N^{Υ}_{corr} is the $\Upsilon \to \mu^+\mu^-$ yield in a given p_T and rapidity bin after the correction for all detector efficiencies and bin migration effects are taken into account; $\mathcal{L}$ is the integrated luminosity of the data sample; and Δp_T and Δy are the p_T and rapidity bin widths. To recover the true number of N^{Υ}_{corr} of such decays produced in the collisions, a weight w is applied to each observed $\Upsilon \to \mu^+\mu^-$ candidate, defined as the inverse of the efficiency to detect that candidate:

$$w^{-1} = \mathcal{M} \cdot \varepsilon^2_{\rm trk} \cdot \varepsilon^+_\mu(p^+_T, \eta^+) \cdot \varepsilon^-_\mu(p^-_T, \eta^-) \cdot \varepsilon_{\rm trig} \tag{6.3}$$

where $\mathcal{M}$ is a correction factor for bin migration due to finite detector resolution, $\varepsilon_{\rm trk}$ is the ID tracking efficiency[3], ε_μ is the single-muon offline reconstruction efficiency and $\varepsilon_{\rm trig}$ is the B-physics trigger efficiency. All of these effects are described in Chapter 5. Here $p^\pm_T$ and $\eta^\pm$ are the transverse momenta and pseudorapidities of the positive and negative muons from the Υ decay.

Figure 6.1 shows the unweighted and weighted mass distributions in two rapidity regions and Fig. 6.2 shows the average weights versus the p_T of the Υ.

6.1.1 Extraction of N^{Υ}_{corr}

After making a candidate-by-candidate correction for all efficiencies, the corrected Υ yields, N^{Υ}_{corr}, are determined by using χ^2 binned fits in the ROOT framework [100]. The definition of the χ^2 is

$$\chi^2 = \sum_{i=m_{\mu\mu}-bin} \left(\frac{n_i^{data} - n_i^{pred}}{\sigma_i} \right)^2 , \tag{6.4}$$

where, $n_i^{data} = \sum_{j=N_i} w_j$, and $\sigma_i^2 = \sum_{j=N_i} w_j^2$. N_i represents the number of Υ candidates in bin i.

[3] An overall efficiency of $(99 \pm 0.5)\%$ from ATLAS Muon Performance Group is used.

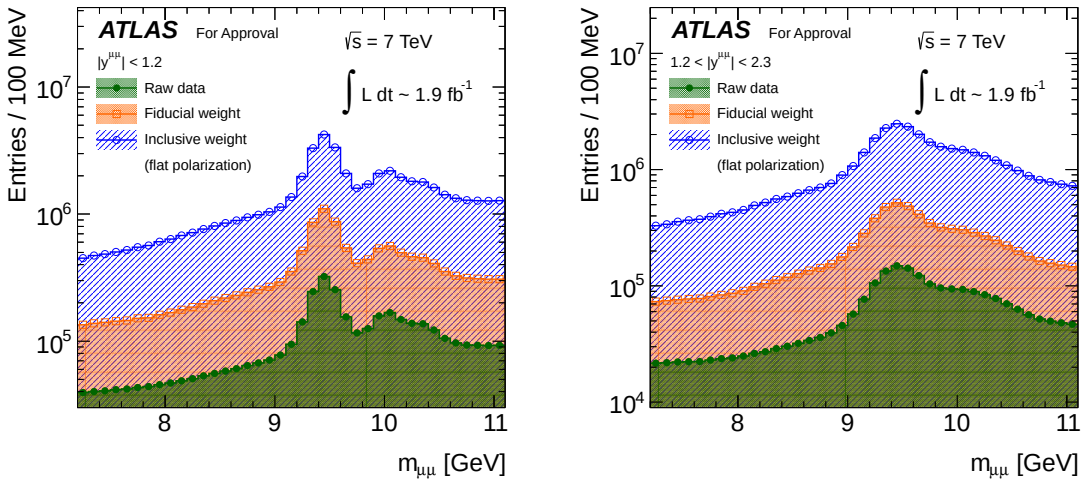

(a) (b)

Figure 6.1: Di-muon mass distributions in two rapidity regions, (a) $|y_{\mu\mu}| < 1.2$ and (b) $1.2 < |y_{\mu\mu}| < 2.3$: The green histograms are the raw di-muon mass; and the orange ones are the weighted mass distributions for the fiducial cross-section; and the blue ones are for the $\Upsilon(1S)$ inclusive cross-section (described in Sec. 6.2).

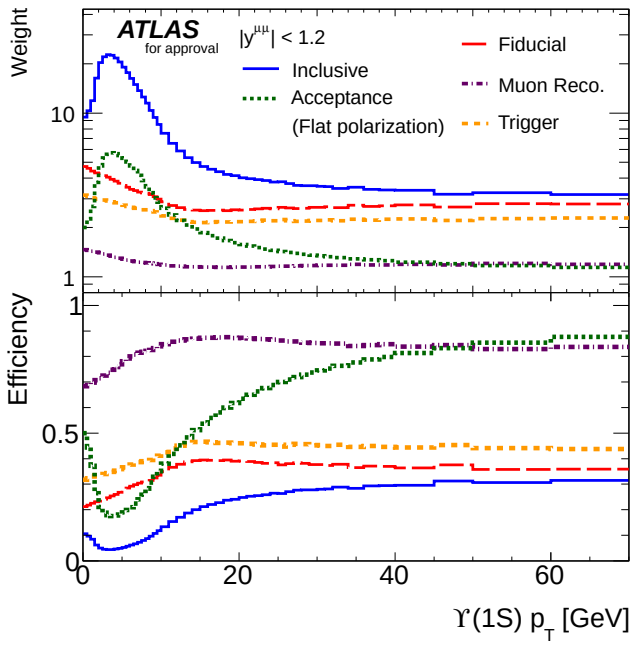
ATLAS
for approval
|y^μμ| < 1.2
Inclusive
Acceptance
(Flat polarization)
Fiducial
Muon Reco.
Trigger
Weight
Efficiency
ϒ(1S) p_T [GeV]

(a)

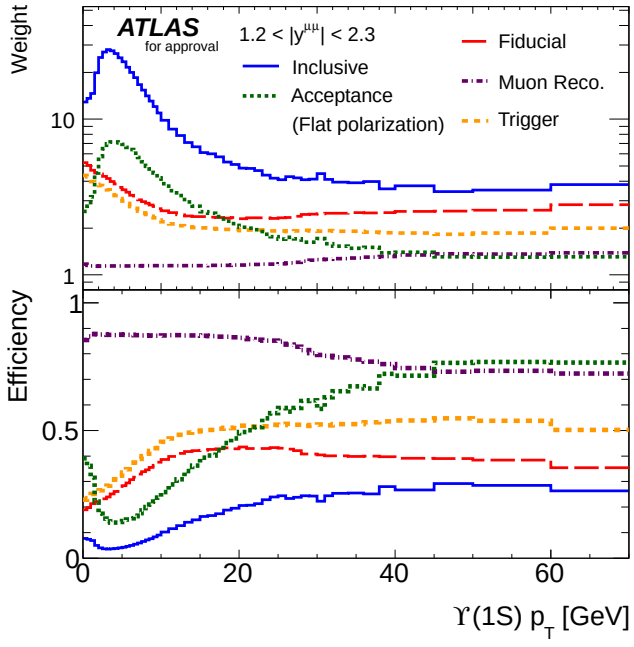
ATLAS
for approval
1.2 < |y^μμ| < 2.3
Inclusive
Acceptance
(Flat polarization)
Fiducial
Muon Reco.
Trigger
Weight
Efficiency
ϒ(1S) p_T [GeV]

(b)

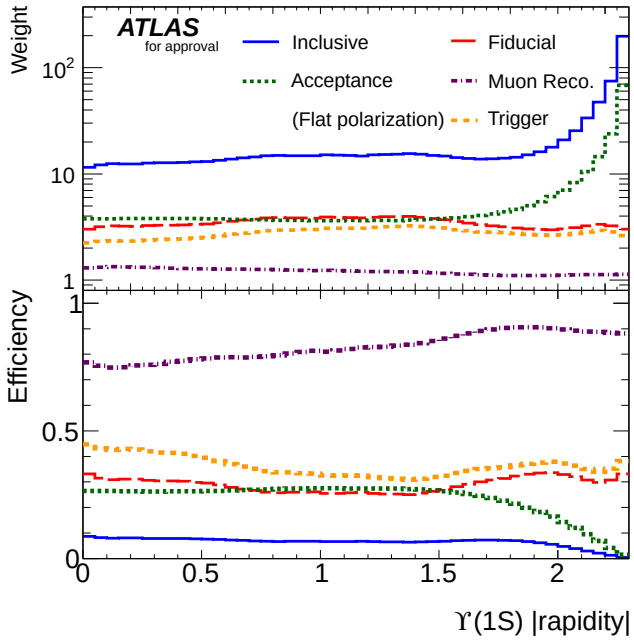

(c)

Figure 6.2: Average weight (upper pane) and average efficiency (lower pane) distributions for (a) and (b) versus $p_T^{\mu\mu}$ in the two rapidity bins, and for (c) versus rapidity.

The total number of di-muon candidates from four sources, three $\Upsilon(1,2,3S)$ peaks and a background component, is determined by:

$$N_{\mu\mu}^{fit} = N_{1S}\cdot f_{1S}(m,p_T,y)+N_{2S}\cdot f_{2S}(m,p_T,y)+N_{3S}\cdot f_{3S}(m,p_T,y)+N_{bkgd}\cdot f_{bkgd}(m,p_T,y) \tag{6.5}$$

To avoid potential bias from the particular choice of fit model (for both signal and background), several different signal and background models are used in this measurement. We use three different functions to model the Υ signal: a single Gaussian (SG), a double Gaussian (DG), and a Crystal-Ball (CB) function [101]. Due to finite detector resolution in the ATLAS detector, the three Υ states are not clearly separated. To get stable fitting results, the relative mass positions, ΔM^{mS-nS} with $m > n$ and m, n = 1, 2 and 3, are fixed to the PDG values [14]. The mass of $\Upsilon(1S)$ is a free parameter in the fit. Also, the mass resolution for higher states, $\Upsilon(2S)$ and $\Upsilon(3S)$, are fixed to the resolution of the $\Upsilon(1S)$ with a linear scaling factor which is determined by the mass ratio, $\frac{M^{nS}}{M^{1S}}$ with n = 2 and 3[4].

Since the background shape changes with the di-muon kinematics we use different background parameterizations in the low, medium, and high-p_T regions. For low-p_T ($0 < p_T^{\mu\mu} < 5$ GeV), an error function multiplied by a second-order polynomial or multiplied by a second-order polynomial with an extra exponential function added is used for describing the background turn-on behavior; at medium ($5 < p_T^{\mu\mu} < 20$ GeV) and high-p_T ($20 < p_T^{\mu\mu} < 70$ GeV), a simple first- or second-order polynomial function or a polynomial function with an extra exponential term is used. In total, there are six combinations of signal and background models that are summarized in Table 6.1. Some examples of mass fits in different regions with different fit models are shown in in Fig. 6.3, Fig. 6.4 and Fig. 6.5 for low-p_T, medium-p_T and high-p_T, respectively.

[4]This is validated using a MC study.

Signal	Background		
	Low-p_T	Med-p_T	High-p_T
Single Gaussian	(0.0 – 5.0 GeV)	(5.0 – 20.0 GeV)	(20.0 – 70.0 GeV)
Double Gaussian	Erf $\times$ 2^{nd}-order Poly.	2^{nd}-order Poly.	1^{st}-order Poly.
Crystal-Ball	Erf $\times$ (2^{nd} Poly. + Expo.)	2^{nd} Poly. + Expo.	1^{st} Poly. + Expo.

Table 6.1: Summary of fit models for the signals and backgrounds for different p_T^{Υ} regions.

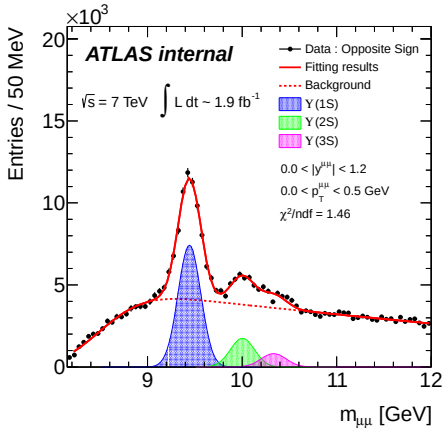
ATLAS internal
Data : Opposite Sign
Fitting results
Background
Υ(1S)
Υ(2S)
Υ(3S)
√s = 7 TeV ∫ L dt ~ 1.9 fb⁻¹
0.0 < |y^μμ| < 1.2
0.0 < p_T^μμ < 0.5 GeV
χ²/ndf = 1.46
Entries / 50 MeV
m_μμ [GeV]

(a)

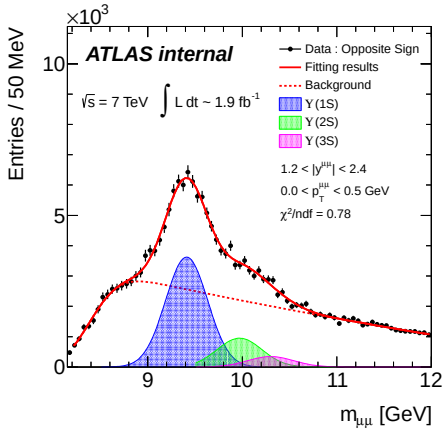
ATLAS internal
Data : Opposite Sign
Fitting results
Background
Υ(1S)
Υ(2S)
Υ(3S)
√s = 7 TeV ∫ L dt ~ 1.9 fb⁻¹
1.2 < |y^μμ| < 2.4
0.0 < p_T^μμ < 0.5 GeV
χ²/ndf = 0.78
Entries / 50 MeV
m_μμ [GeV]

(b)

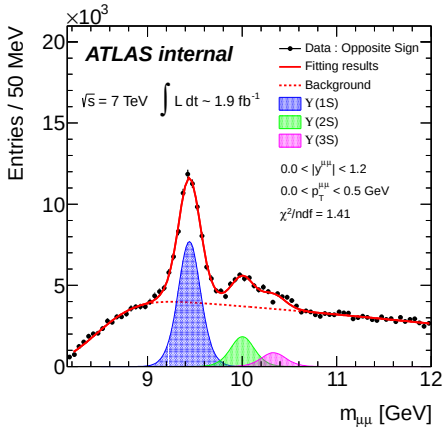
ATLAS internal
Data : Opposite Sign
Fitting results
Background
Υ(1S)
Υ(2S)
Υ(3S)
√s = 7 TeV ∫ L dt ~ 1.9 fb⁻¹
0.0 < |y^μμ| < 1.2
0.0 < p_T^μμ < 0.5 GeV
χ²/ndf = 1.41
Entries / 50 MeV
m_μμ [GeV]

(c)

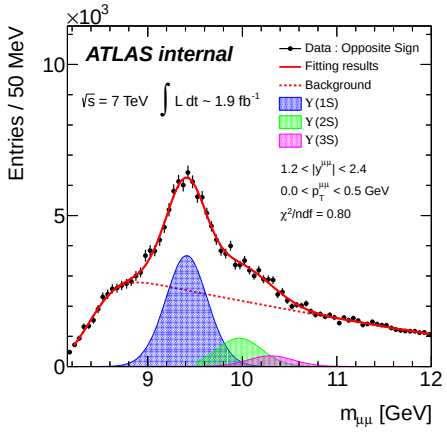
ATLAS internal
Data : Opposite Sign
Fitting results
Background
Υ(1S)
Υ(2S)
Υ(3S)
√s = 7 TeV ∫ L dt ~ 1.9 fb⁻¹
1.2 < |y^μμ| < 2.4
0.0 < p_T^μμ < 0.5 GeV
χ²/ndf = 0.80
Entries / 50 MeV
m_μμ [GeV]

(d)

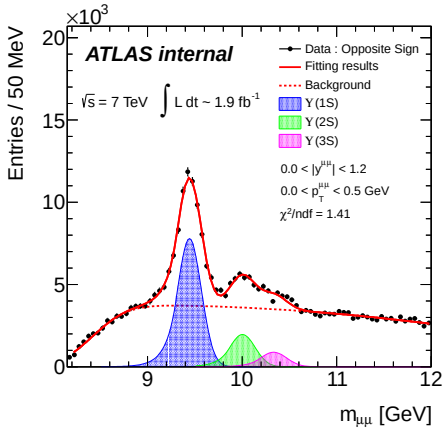
ATLAS internal
Data : Opposite Sign
Fitting results
Background
Υ(1S)
Υ(2S)
Υ(3S)
√s = 7 TeV ∫ L dt ~ 1.9 fb⁻¹
0.0 < |y^μμ| < 1.2
0.0 < p_T^μμ < 0.5 GeV
χ²/ndf = 1.41
Entries / 50 MeV
m_μμ [GeV]

(e)

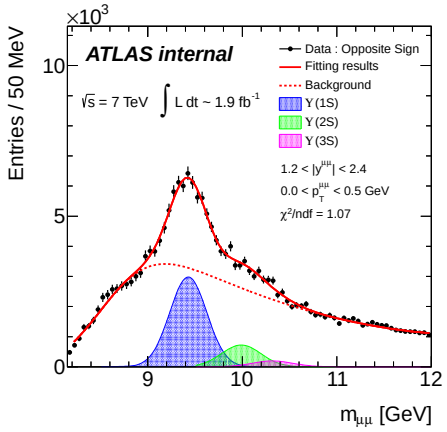
ATLAS internal
Data : Opposite Sign
Fitting results
Background
Υ(1S)
Υ(2S)
Υ(3S)
√s = 7 TeV ∫ L dt ~ 1.9 fb⁻¹
1.2 < |y^μμ| < 2.4
0.0 < p_T^μμ < 0.5 GeV
χ²/ndf = 1.07
Entries / 50 MeV
m_μμ [GeV]

(f)

Figure 6.3: Examples of di-muon mass fits in the low-p_T region ($0.0 - 0.5$ GeV): (a),(c) and (e) for central rapidity and (b), (d) and (f) for forward rapidity. The signal models used in the fit are SG, DG and CB from top to bottom plots.

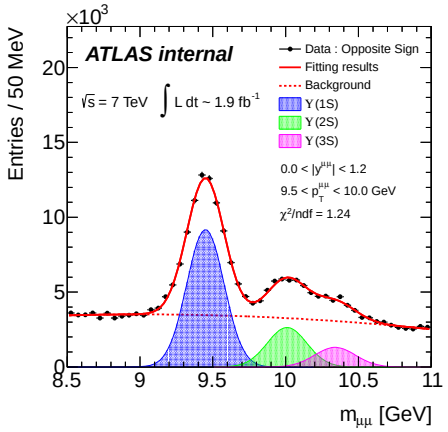
×10^3
ATLAS internal
Data : Opposite Sign
Fitting results
Background
Υ(1S)
Υ(2S)
Υ(3S)
√s = 7 TeV ∫ L dt ~ 1.9 fb^-1
0.0 < |y^μμ| < 1.2
9.5 < p_T^μμ < 10.0 GeV
χ²/ndf = 1.24
Entries / 50 MeV
m_μμ [GeV]

(a)

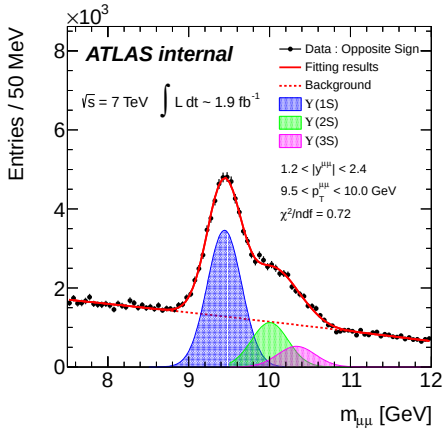
×10^3
ATLAS internal
Data : Opposite Sign
Fitting results
Background
Υ(1S)
Υ(2S)
Υ(3S)
√s = 7 TeV ∫ L dt ~ 1.9 fb^-1
1.2 < |y^μμ| < 2.4
9.5 < p_T^μμ < 10.0 GeV
χ²/ndf = 0.72
Entries / 50 MeV
m_μμ [GeV]

(b)

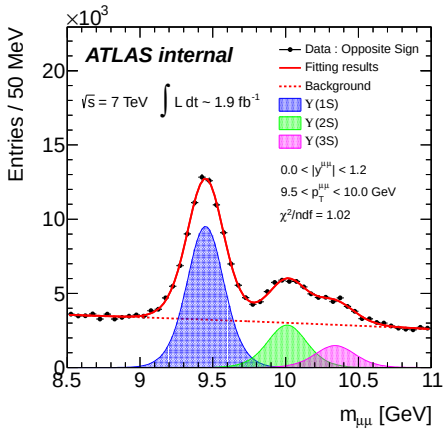
×10^3
ATLAS internal
Data : Opposite Sign
Fitting results
Background
Υ(1S)
Υ(2S)
Υ(3S)
√s = 7 TeV ∫ L dt ~ 1.9 fb^-1
0.0 < |y^μμ| < 1.2
9.5 < p_T^μμ < 10.0 GeV
χ²/ndf = 1.02
Entries / 50 MeV
m_μμ [GeV]

(c)

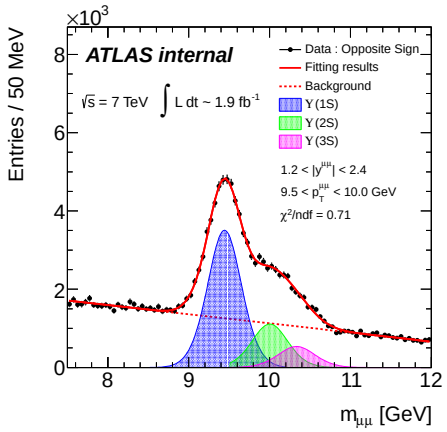
×10^3
ATLAS internal
Data : Opposite Sign
Fitting results
Background
Υ(1S)
Υ(2S)
Υ(3S)
√s = 7 TeV ∫ L dt ~ 1.9 fb^-1
1.2 < |y^μμ| < 2.4
9.5 < p_T^μμ < 10.0 GeV
χ²/ndf = 0.71
Entries / 50 MeV
m_μμ [GeV]

(d)

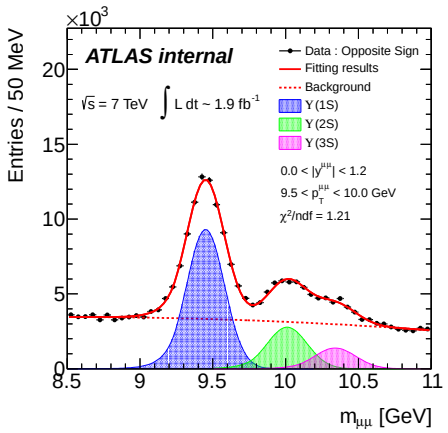
×10^3
ATLAS internal
Data : Opposite Sign
Fitting results
Background
Υ(1S)
Υ(2S)
Υ(3S)
√s = 7 TeV ∫ L dt ~ 1.9 fb^-1
0.0 < |y^μμ| < 1.2
9.5 < p_T^μμ < 10.0 GeV
χ²/ndf = 1.21
Entries / 50 MeV
m_μμ [GeV]

(e)

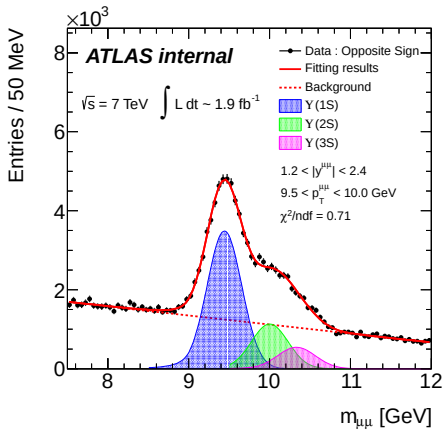
×10^3
ATLAS internal
Data : Opposite Sign
Fitting results
Background
Υ(1S)
Υ(2S)
Υ(3S)
√s = 7 TeV ∫ L dt ~ 1.9 fb^-1
1.2 < |y^μμ| < 2.4
9.5 < p_T^μμ < 10.0 GeV
χ²/ndf = 0.71
Entries / 50 MeV
m_μμ [GeV]

(f)

Figure 6.4: Examples of di-muon mass fits in the medium-p_T region ($9.5 - 10.0$ GeV): (a), (c), and (e) for central rapidity and (b), (d), and (f) for forward rapidity. The signal models used in the fits are SG, DG and CB from top to bottom plots.

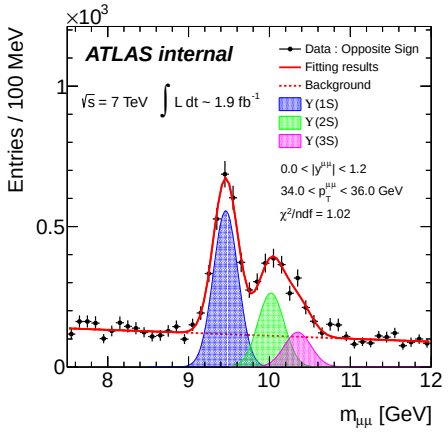
×10^3
Entries / 100 MeV
ATLAS internal
√s = 7 TeV ∫ L dt ~ 1.9 fb^-1
Data : Opposite Sign
Fitting results
Background
Υ(1S)
Υ(2S)
Υ(3S)
0.0 < |y^μμ| < 1.2
34.0 < p_T^μμ < 36.0 GeV
χ^2/ndf = 1.02
m_μμ [GeV]

(a)

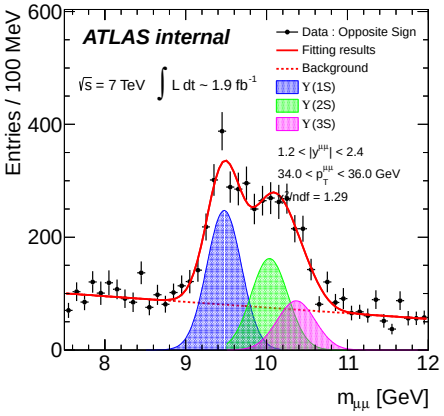
Entries / 100 MeV
ATLAS internal
√s = 7 TeV ∫ L dt ~ 1.9 fb^-1
Data : Opposite Sign
Fitting results
Background
Υ(1S)
Υ(2S)
Υ(3S)
1.2 < |y^μμ| < 2.4
34.0 < p_T^μμ < 36.0 GeV
χ^2/ndf = 1.29
m_μμ [GeV]

(b)

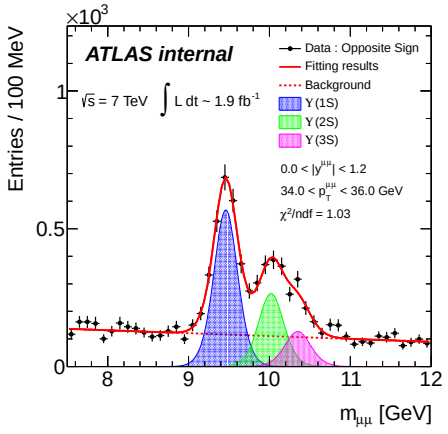
×10^3
Entries / 100 MeV
ATLAS internal
√s = 7 TeV ∫ L dt ~ 1.9 fb^-1
Data : Opposite Sign
Fitting results
Background
Υ(1S)
Υ(2S)
Υ(3S)
0.0 < |y^μμ| < 1.2
34.0 < p_T^μμ < 36.0 GeV
χ^2/ndf = 1.03
m_μμ [GeV]

(c)

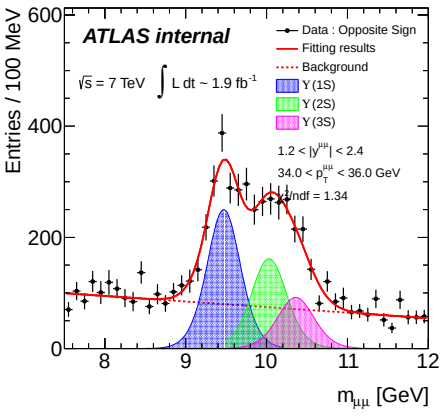
Entries / 100 MeV
ATLAS internal
√s = 7 TeV ∫ L dt ~ 1.9 fb^-1
Data : Opposite Sign
Fitting results
Background
Υ(1S)
Υ(2S)
Υ(3S)
1.2 < |y^μμ| < 2.4
34.0 < p_T^μμ < 36.0 GeV
χ^2/ndf = 1.34
m_μμ [GeV]

(d)

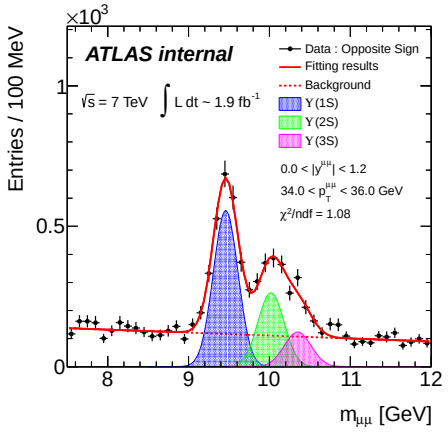
×10^3
Entries / 100 MeV
ATLAS internal
√s = 7 TeV ∫ L dt ~ 1.9 fb^-1
Data : Opposite Sign
Fitting results
Background
Υ(1S)
Υ(2S)
Υ(3S)
0.0 < |y^μμ| < 1.2
34.0 < p_T^μμ < 36.0 GeV
χ^2/ndf = 1.08
m_μμ [GeV]

(e)

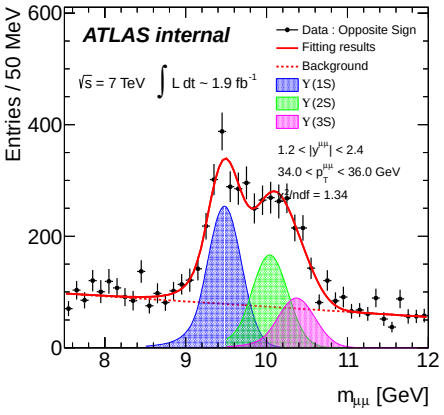
Entries / 50 MeV
ATLAS internal
√s = 7 TeV ∫ L dt ~ 1.9 fb^-1
Data : Opposite Sign
Fitting results
Background
Υ(1S)
Υ(2S)
Υ(3S)
1.2 < |y^μμ| < 2.4
34.0 < p_T^μμ < 36.0 GeV
χ^2/ndf = 1.34
m_μμ [GeV]

(f)

Figure 6.5: Examples of di-muon mass fits in the high-p_T region (34.0−36.0 GeV): (a), (c), and (e) for central rapidity and (b), (d), and (f) for forward rapidity. The signal models used in the fits are SG, DG and CB from top to bottom plots.

The averaged numbers for $\Upsilon(1,2,3S)$ candidates taken over all six fit models are used for the cross-section calculation, and the maximum deviation of any fit result from the average is used as an estimate of the fit model systematic uncertainty.

All the fits on the di-muon mass are required to be convergent and to have a goodness-of-fit quality $\chi^2/\text{n.d.f} < 2$. If not, the fitter will then try different initial values for the fit parameters until convergence is achieved.

6.1.2 Systematic Uncertainties

Several sources of systematic uncertainties are considered in this cross-section measurement. These include:

- **Luminosity:** The official ATLAS luminosity uncertainty of 3.7% is used [102].

- **ID-track reconstruction efficiency:** An overall uncertainty of 0.5%, from the ATLAS Muon Performance Group recommendation, is applied.

- **Muon reconstruction efficiency:** Hundreds of pseudo-experiments are performed using different efficiency maps derived by randomly fluctuating the binned efficiencies within their uncertainties. The distributions of the yields of Υ candidates are binned in the same p_T and rapidity bins as the cross-section measurements. The fitted Υ yields are distributed as a Gaussian distribution, and the systematic uncertainty is determined from the width of this Gaussian distribution. Figure 6.6 shows a example of low p_T bin in the forward region. The systematic uncertainties on the muon reconstruction efficiency are at the level of a few percent. More details are shown in the Appendix C.1.

- **Trigger efficiency:** There are two components to the total di-muon trigger efficiency:

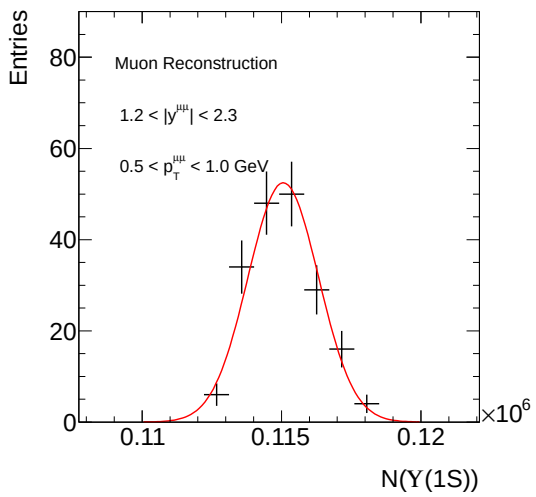

Figure 6.6: Example of determining the systematic uncertainty on the muon reconstruction efficiency.

- **EF_mu4 map**: We use the same pseudo-experiment based method as for the muon reconstruction efficiency systematic to estimate the size of this component.
- **Di-muon correction factors ($C_{\mu\mu}$)**: We use a similar procedure as used before by randomly varying the $C_{\mu\mu}$ correction factor within its uncertainty from the fit so as to rebuild the EF_mu4 maps and to recalculate the final di-muon trigger efficiency.

The combined systematic uncertainties from the trigger efficiency are at the percent level across all p_T and rapidity bins. Details are given in Appendix C.2

- **Bin migration:** When varying the p_T resolution function by a factor of two, we find that the cross-sections shift less then 1%.

- **Fit Model:** As described in Section. 6.1.1, the systematic uncertainty from modeling of the signal and the background is determined by using the maximum deviation of any fit result from the average. Figure 6.7 shows the example of a fit model systematic uncertainties for $\sigma^{\Upsilon(1S)}$ vs p_T. Other distributions are shown in Appendix C.3.

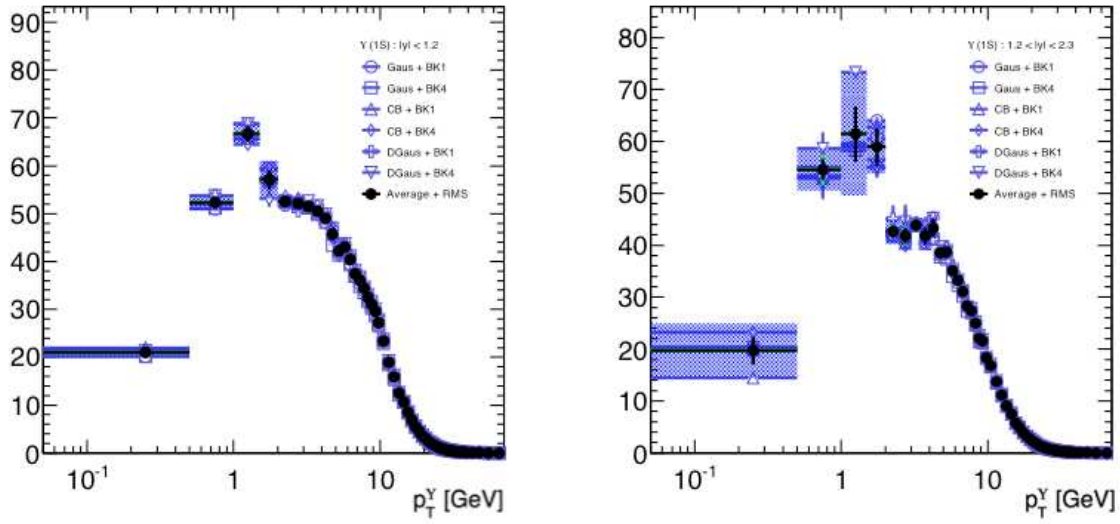

Figure 6.7: Example of the systematic uncertainties on the fit model for $\Upsilon(1S)$.

6.1.3 Results

The measured $\Upsilon(1,2,3S)$ fiducial cross-sections integrated over p_T and rapidity in the fiducial volume $p_T^\mu > 4$ GeV and $|\eta^\mu| < 2.3$ are summarized in Table 6.2. The results for the differential Υ fiducial cross-sections times $\Upsilon \to \mu^+\mu^-$ branching fraction, $\frac{d^2\sigma}{dp_T d|y|} \times Br(\Upsilon \to \mu^+\mu^-)$ and $\frac{d\sigma}{d|y|} \times Br(\Upsilon \to \mu^+\mu^-)$, are summarized below.[5]

[5]Tables with all details are listed in Appendix E.1.

State	$\sigma^{fiducial}_{p_T^\mu>4\ GeV;\|\eta^\mu\|<2.3}(pp \to \Upsilon;\ \|y^\Upsilon\|<2.3) \times Br(\Upsilon \to \mu^+\mu^-)$
$\Upsilon(1S)$	2.331 ± 0.007 (stat.) ± 0.116 (syst.) ± 0.086 (lumi.) nb
$\Upsilon(2S)$	0.747 ± 0.004 (stat.) ± 0.041 (syst.) ± 0.028 (lumi.) nb
$\Upsilon(3S)$	0.379 ± 0.004 (stat.) ± 0.030 (syst.) ± 0.014 (lumi.) nb

Table 6.2: Fiducial cross-section measurements.

The differential cross-sections versus p_T are calculated in two rapidity bins, $|y^\Upsilon| < 1.2$ and $1.2 < |y^\Upsilon| < 2.3$. The cross-sections and uncertainties for $\Upsilon(1S)$, $\Upsilon(2S)$ and $\Upsilon(3S)$ are shown in Fig. 6.8 and 6.9. Due to the lower statistics of the $\Upsilon(2S)$ and $\Upsilon(3S)$ samples, a coarser binning is used for them. $\Upsilon(1S)$ results are consistent with our previous measurement [99][6]. Comparisons are also shown in Appendix E.1. In low-p_T regions, the uncertainties are dominated by the fit model; while for higher p_T, the uncertainties are dominated by the statistics.

Figure 6.10(a) shows the fiducial cross-sections within $p_T^\Upsilon < 70$ GeV versus the absolute rapidity of the Υ with a very fine binning (0.05). Figure 6.10(b) shows the corresponding uncertainties for each bin.

In our previous measurements [99], we found NLO Color Singlet predictions [104] underestimated the production rates by approximately an order of magnitude. This is not surprising as we have already mentioned in Section 2.3.1 that higher-order contributions (NNLO) are large. The three models we considered, NNLO Color Singlet, Color Evaporation and Color Octet, do not provide predictions within a restricted muon acceptance. At this time, there are very few predictions available for this fiducial cross-section on the market. However, the fiducial cross-sections presented here are precise and independent of any assumptions on the Υ polarization, and these will

[6] They are shown in Appendix E.1.

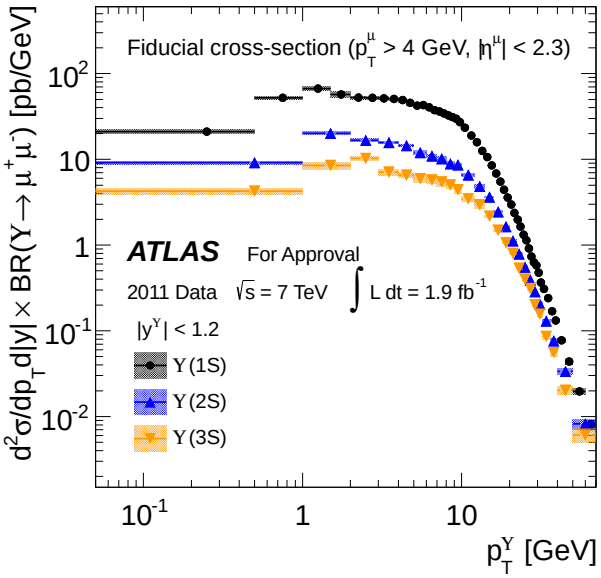

(a)

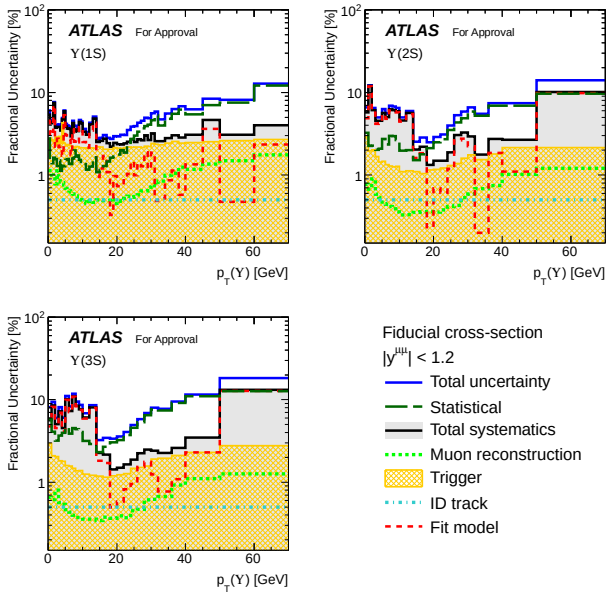

(b)

Figure 6.8: (a) Fiducial cross-section versus p_T in the central rapidity region ($|y^\Upsilon| < 1.2$), and (b) corresponding uncertainties versus p_T.

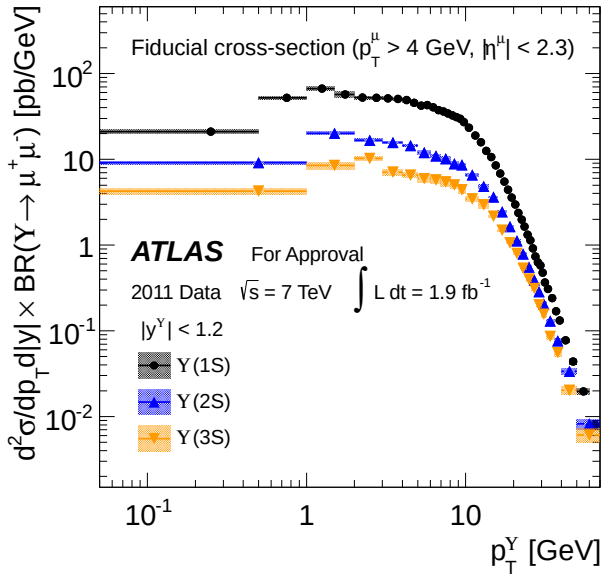

(a)

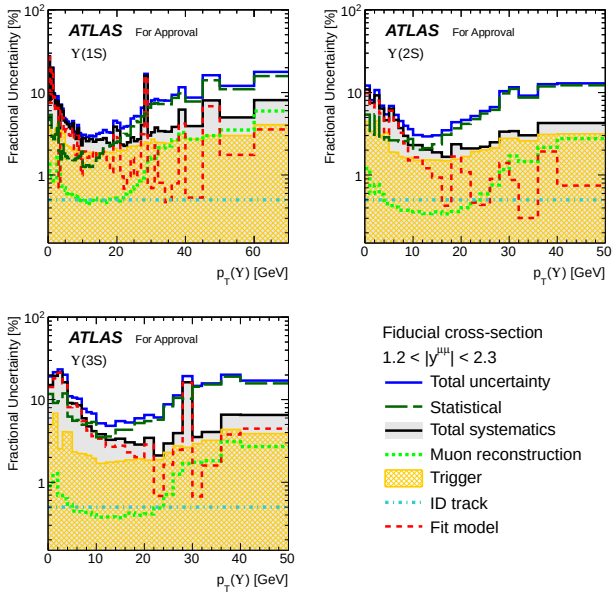

(b)

Figure 6.9: (a) Fiducial cross-section versus p_T in the forward rapidity region ($1.2 < |y^\Upsilon| < 2.3$), and (b) corresponding uncertainties versus p_T.

be useful for understanding the Υ production mechanism when the polarization of the Υ is determined.

6.2 Υ Inclusive Cross-Sections

To access the full phase space of Υ production in the ATLAS detector, a correction for those Υ decays falling outside of the kinematic region $p_T^\mu > 4$ GeV and $|\eta^\mu| < 2.3$ is needed. The cross-sections with full acceptance correction are usually referred as the "inclusive cross-sections". Because the variation of the inclusive cross-sections under different polarization assumptions is very large, they provide information on the polarization of Υ, and will also allow us to make direct comparisons with theoretical predictions and with other experiments such as CMS and LHCb.

6.2.1 Acceptance Correction

The kinematic acceptance $\mathcal{A}(p_T, y)$ is the probability that the muons from an $\Upsilon(1S)$ with transverse momentum p_T and rapidity y have $p_T^\mu > 4$ GeV and $|\eta^\mu| < 2.3$. This probability is calculated using the analytic equation:

$$\frac{d^2N}{d\cos\theta^\star d\phi^\star} \propto 1 + \lambda_\theta \cos^2\theta^\star + \lambda_\phi \sin^2\theta^\star \cos 2\phi^\star + \lambda_{\theta\phi} \sin 2\theta^\star \cos\phi^\star, \tag{6.6}$$

as discussed in Section 2.3.2.

The candidate weighting formula now has a new acceptance map term ($\mathcal{A}$) for the inclusive cross-section measurement,

$$w^{-1} \;=\; \mathcal{A} \cdot \mathcal{M} \cdot \varepsilon^2_{\rm trk} \cdot \varepsilon^+_\mu(p_T^+, \eta^+) \cdot \varepsilon^-_\mu(p_T^-, \eta^-) \cdot \varepsilon_{\rm trig}. \tag{6.7}$$

A large number of possible combinations of the coefficients $\lambda_\theta, \lambda_\phi, \lambda_{\theta\phi}$ have been studied [57], including some with $\lambda_{\theta\phi} \neq 0$ which is the correlation term between $\theta^\star$ and $\phi^\star$. From the ATLAS J/ψ analysis [50], five extreme cases have been identified

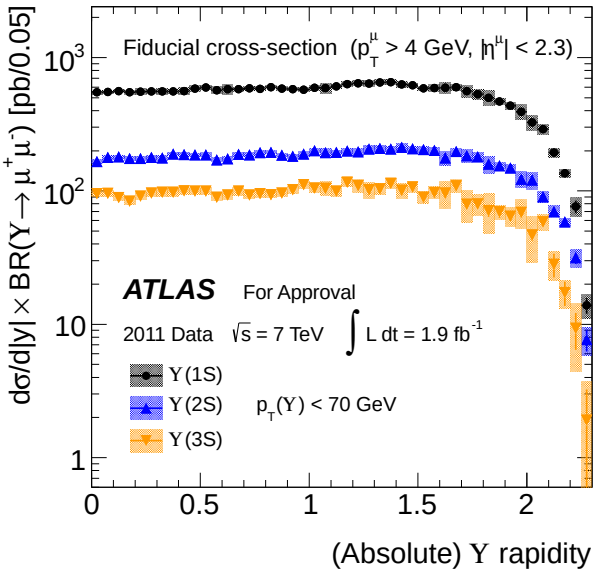

(a)

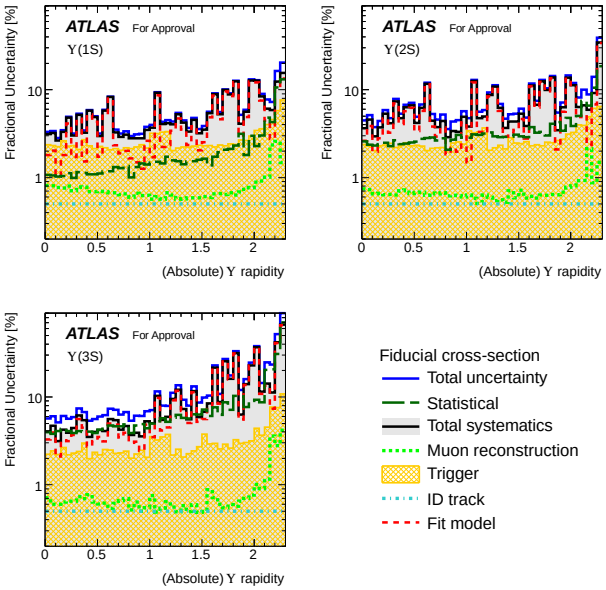

(b)

Figure 6.10: (a) Fiducial cross-section versus ϒ rapidity, and (b) corresponding uncertainties versus ϒ rapidity.

that lead to the largest variation of acceptance within the kinematics of the ATLAS detector:

1. Unpolarized, independent of $\theta^\star$ and $\phi^\star$, with $\lambda_\theta = \lambda_\phi = \lambda_{\theta\phi} = 0$, labelled as "FLAT". This is used as the main (central) hypothesis.

2. Full longitudinal polarization with $\lambda_\theta = -1, \lambda_\phi = \lambda_{\theta\phi} = 0$, labelled as "LONG".

3. Transverse polarization with $\lambda_\theta = +1, \lambda_\phi = \lambda_{\theta\phi} = 0$, labelled as T_{+0}.

4. Transverse polarization with $\lambda_\theta = +1, \lambda_\phi = +1, \lambda_{\theta\phi} = 0$, labelled as T_{++}.

5. Transverse polarization with $\lambda_\theta = +1, \lambda_\phi = -1, \lambda_{\theta\phi} = 0$, labelled as T_{+-}.

A toy-MC based acceptance map generator "Onia Gun" is used for generating extremely high statistics maps with an overall 0.4% statistical uncertainty. Two-dimensional acceptance maps are produced in bins of p_T and y of the $\Upsilon(1S)$, for each of these five scenarios, and they are illustrated in Fig. 6.11. The acceptance maps for $\Upsilon(2S)$ and $\Upsilon(3S)$ are shown in the Appendix D.

The impact of vertex spread along the z-axis on the acceptance has been studied. The average z-spread is ± 62 mm [103] which corresponds to an $\sim$0.02 shift in η. The systematic uncertainty due to this effect is about 2% in the high rapidity region. Details are shown in Appendix C.4.1.

6.2.2 Polarization Envelope

The central values for the cross-section measurements are obtained by using the unpolarized hypothesis. Measurements using the other scenarios are used to construct an envelope of maximum variation so as to demonstrate the effect from different Υ polarization assumptions.

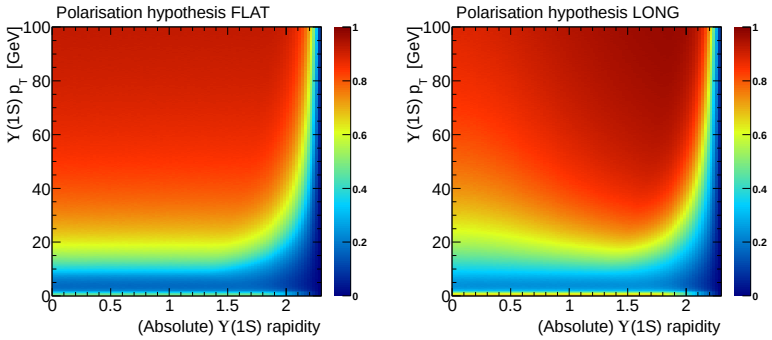

(a)

(b)

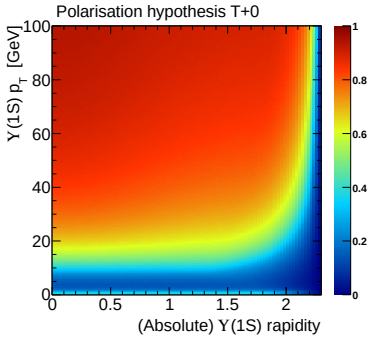

(c)

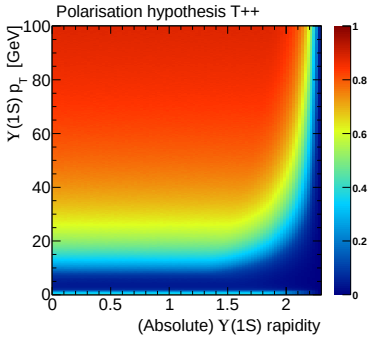

(d)

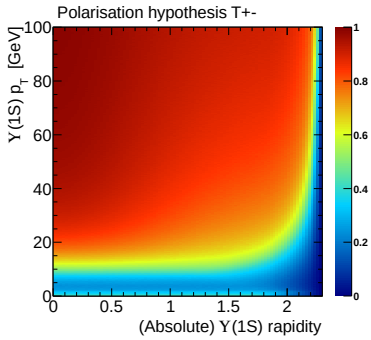

(e)

Figure 6.11: The acceptance maps $\mathcal{A}$ for $\Upsilon(1S)$ with the polarization assumptions of (a) FLAT; (b) LONG; (c) T_{+0}; (d) T_{++}; and (e) T_{+-}.

6.2.3 Results

Figure 6.12 shows a summary of the inclusive cross-sections for three Υ states as a function of $\Upsilon(p_T)$ and rapidity, and the integrated Υ inclusive cross-sections with $|y^{\Upsilon}|$ < 2.3 are summarized in Table 6.3. The details of $\sigma^{\Upsilon}_{inc} \times BR(\Upsilon \to \mu^+\mu^-)$ versus p_T and rapidity are discussed in the following.[7]

State	$\sigma^{inclusive}(pp \to \Upsilon;\ \|y^{\Upsilon}\| < 2.3) \times Br(\Upsilon \to \mu^+\mu^-)$
$\Upsilon(1S)$	9.96 $\pm$ 0.03 (stat.) $\pm$ 0.52 (syst.) $\pm$ 0.37 (lumi.) nb
$\Upsilon(2S)$	2.59 $\pm$ 0.02 (stat.) $\pm$ 0.15 (syst.) $\pm$ 0.10 (lumi.) nb
$\Upsilon(3S)$	1.16 $\pm$ 0.01 (stat.) $\pm$ 0.11 (syst.) $\pm$ 0.04 (lumi.) nb

Table 6.3: Inclusive cross-section measurements.

The double-differential inclusive cross-sections are calculated with the same binning as the fiducial cross-sections. The final results are shown in Fig. 6.13, Fig. 6.14 and Fig. 6.15 for $\Upsilon(1S)$, $\Upsilon(2S)$ and $\Upsilon(3S)$ respectively, and the corresponding uncertainties are shown in Fig. 6.16. The maximal variations due to the polarization assumptions, bounded by the polarization envelopes, are shown as a blue band in each plot. Different line-shapes in the lower pane indicate the contributions from different polarization scenarios. The upper bound of the polarization envelope is set by the T_{++} ($\lambda_\theta = +1, \lambda_\phi = +1, \lambda_{\theta\phi} = 0$) scenario. At very low p_T (< 4 GeV), the lower bound is determined by fully longitudinal polarization, and above about 4 GeV it is determined by the T_{+-} ($\lambda_\theta = +1, \lambda_\phi = -1, \lambda_{\theta\phi} = 0$) scenario. In the high Υ p_T region ($p_T > 45$ GeV), the variation due to the unknown polarization of the Υ is within $\pm$10%. The results are compared to CMS measurements [105] and found to

[7] Tables with the details are given in Appendix E.2.

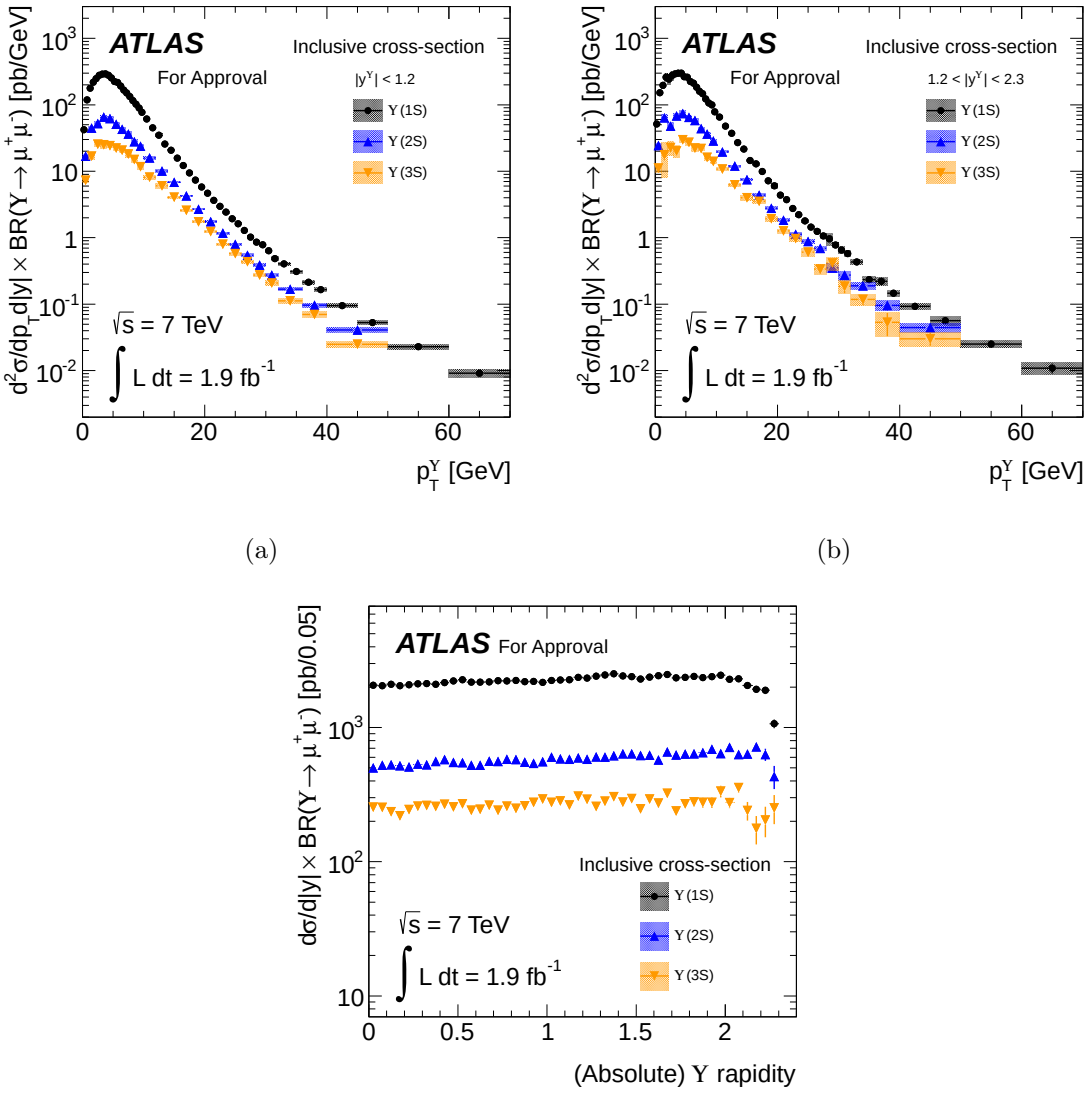

Figure 6.12: Inclusive cross-sections for $\Upsilon(1S)$, $\Upsilon(2S)$ and $\Upsilon(3S)$ as a function of $p_T(\Upsilon)$ for (a) $|y^{\Upsilon}| < 1.2$ and (b) $1.2 < |y^{\Upsilon}| < 2.3$. (c) Inclusive cross-sections integrated over p_T as a function of Υ rapidity.

be in good agreement. They are also compared to theoretical predictions of the Color Singlet Model (CSM) with NNLO* contribution [49, 43], and the Color Evaporation Model (CEM) [51]. Due to the technical details (soft and collinear divergences) on higher-order calculations, the NNLO* CSM only provides predictions above certain Υ p_T. Similar to the CSM, the CEM predictions also have a limitation on the low threshold of Υ p_T.

Higher-order (NLO or NNLO*) CSM calculations predict the polarization of direct Υ to be largely longitudinally polarized, especially at high p_T, with large uncertainties from the feed-down contribution. On the other hand, the CEM has no explicit prediction of the polarization.

Since the predictions from CSM do not take into account the feed-down contribution from the production of higher Υ states or from radiative decays of the $\chi_{bJ}(nP)$, we corrected the CSM $\Upsilon(1S)$ prediction for direct Υ production by applying a scaling factor of 1.5 from the previous measurement [107]. Similar feed-down contributions to $\Upsilon(2S)$ production are expected, but due to the fact that there is no measurement or reliable prediction for them we did not apply a correction to the direct $\Upsilon(2S)$ CSM predictions. There is no feed-down contribution for $\Upsilon(3S)$ from higher Υ states[8]. However, since the recent discovery of $\chi_{bJ}(3P)$ states below the $B\bar{B}$ threshold at ATLAS [108] may introduce some contributions from radiative decays $\chi_{bJ}(3P) \rightarrow \Upsilon(3S)+\gamma$ to $\Upsilon(3S)$ production (and other Υ states). For the same reason as $\Upsilon(2S)$, no correction is applied on the direct $\Upsilon(3S)$ predictions.

The NNLO* CSM predictions give us good agreement in the moderate Υ p_T region, but slightly underestimates the data at high p_T. The CEM calculations provide a better agreement at high p_T, but underestimates the measured cross-sections at lower p_T.

[8] $\Upsilon(4S)$ is above the $B\bar{B}$ threshold.

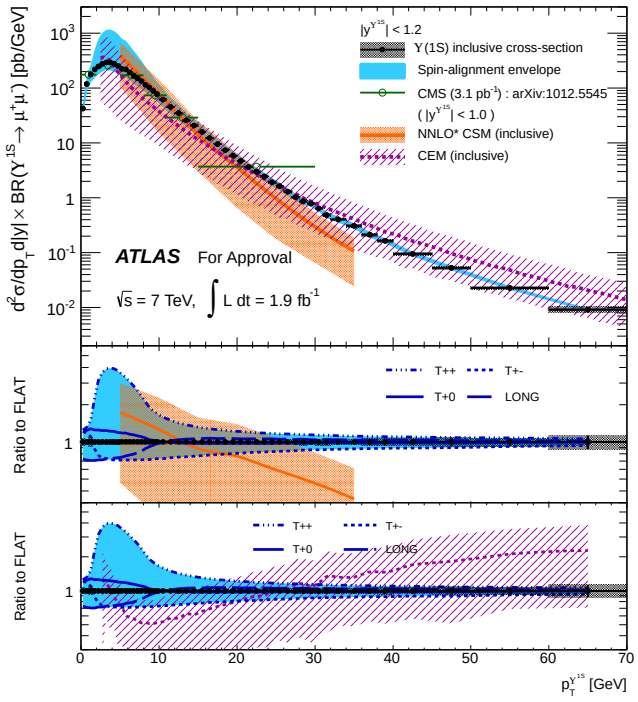
|y^Υ1S| < 1.2
Υ(1S) inclusive cross-section
Spin-alignment envelope
CMS (3.1 pb-1) : arXiv:1012.5545
(|y^Υ1S| < 1.0)
NNLO* CSM (inclusive)
CEM (inclusive)
ATLAS For Approval
√s = 7 TeV, ∫ L dt = 1.9 fb-1
d2σ/dpT d|y| × BR(Υ1S→ μ+μ-) [pb/GeV]
Ratio to FLAT
T++ T+-
T+0 LONG
pT^Υ1S [GeV]

(a)

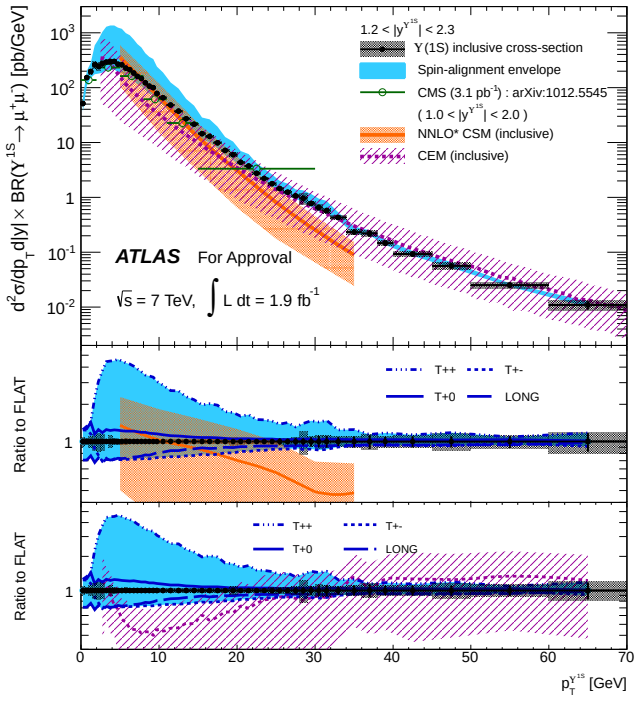
1.2 < |y^Υ1S| < 2.3
Υ(1S) inclusive cross-section
Spin-alignment envelope
CMS (3.1 pb-1) : arXiv:1012.5545
(1.0 < |y^Υ1S| < 2.0)
NNLO* CSM (inclusive)
CEM (inclusive)
ATLAS For Approval
√s = 7 TeV, ∫ L dt = 1.9 fb-1
d2σ/dpT d|y| × BR(Υ1S→ μ+μ-) [pb/GeV]
Ratio to FLAT
T++ T+-
T+0 LONG
pT^Υ1S [GeV]

(b)

Figure 6.13: Inclusive cross-section versus p_T for $\Upsilon(1S)$ in (a) central rapidity region ($|y^{\Upsilon}| < 1.2$), and (b) forward rapidity region ($1.2 < |y^{\Upsilon}| < 2.3$). The maximal envelope of variation of the result due to the polarization assumption is indicated by the solid blue band. The NNLO* CSM prediction is shown as an orange solid line and band multiplying by a correction factor 1.5 for the feed-down contribution. The CEM predictions is shown as a purple dashed line and band. The measurements from CMS [105] are shown in green open circles.

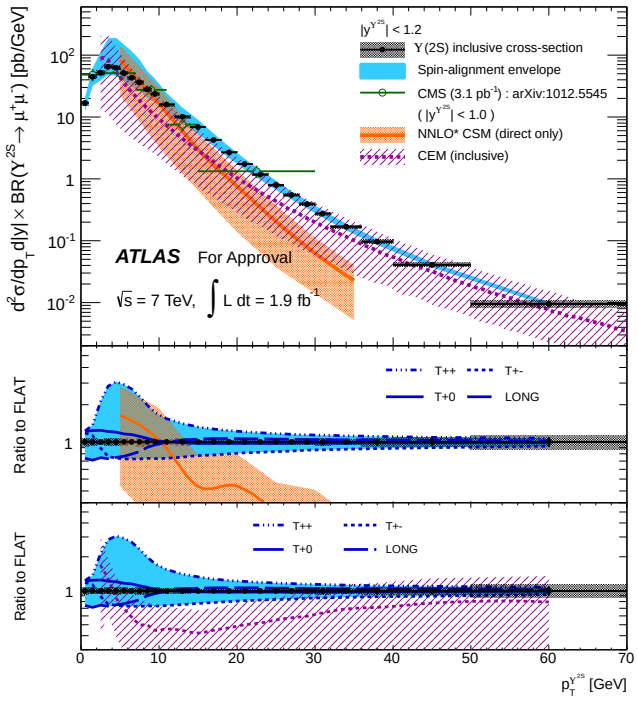
|y^2S| < 1.2
Υ(2S) inclusive cross-section
Spin-alignment envelope
CMS (3.1 pb-1) : arXiv:1012.5545
(|y^2S| < 1.0)
NNLO* CSM (direct only)
CEM (inclusive)
ATLAS For Approval
√s = 7 TeV, ∫ L dt = 1.9 fb-1
d2σ/dpT d|y| × BR(ϒ2S→ μ+μ-) [pb/GeV]
T++ T+-
T+0 LONG
Ratio to FLAT
p_T^2S [GeV]

(a)

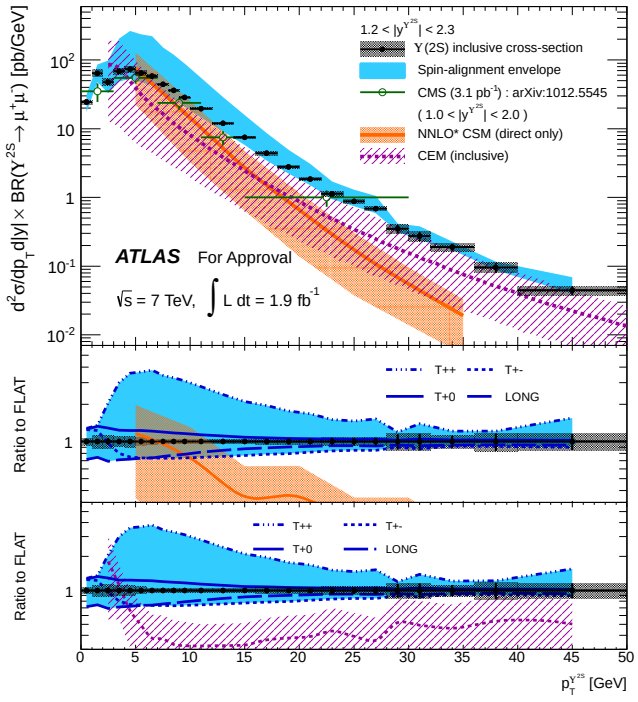
1.2 < |y^2S| < 2.3
Υ(2S) inclusive cross-section
Spin-alignment envelope
CMS (3.1 pb-1) : arXiv:1012.5545
(1.0 < |y^2S| < 2.0)
NNLO* CSM (direct only)
CEM (inclusive)
ATLAS For Approval
√s = 7 TeV, ∫ L dt = 1.9 fb-1
d2σ/dpT d|y| × BR(ϒ2S→ μ+μ-) [pb/GeV]
T++ T+-
T+0 LONG
Ratio to FLAT
p_T^2S [GeV]

(b)

Figure 6.14: Inclusive cross-section versus p_T for $\Upsilon(2S)$ in (a) central rapidity region ($|y^{\Upsilon}| < 1.2$), and (b) forward rapidity region ($1.2 < |y^{\Upsilon}| < 2.3$). The maximal envelope of variation of the result due to the polarization assumption is indicated by the solid blue band. The NNLO* CSM prediction is shown as an orange solid line and band. The CEM predictions are shown as the purple dashed line and band. The measurements from CMS [105] are shown in green open circles.

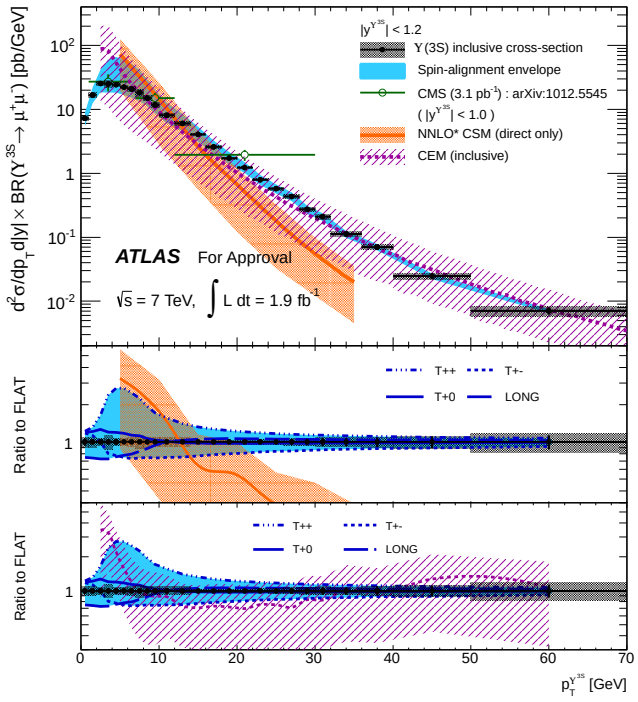
|y^3S| < 1.2
Υ(3S) inclusive cross-section
Spin-alignment envelope
CMS (3.1 pb-1) : arXiv:1012.5545
(|y^3S| < 1.0)
NNLO* CSM (direct only)
CEM (inclusive)
ATLAS For Approval
√s = 7 TeV, ∫ L dt = 1.9 fb-1
d2σ/dpT d|y| × BR(ϒ3S→ μ+μ-) [pb/GeV]
Ratio to FLAT
T++
T+-
T+0
LONG
p_T^3S [GeV]

(a)

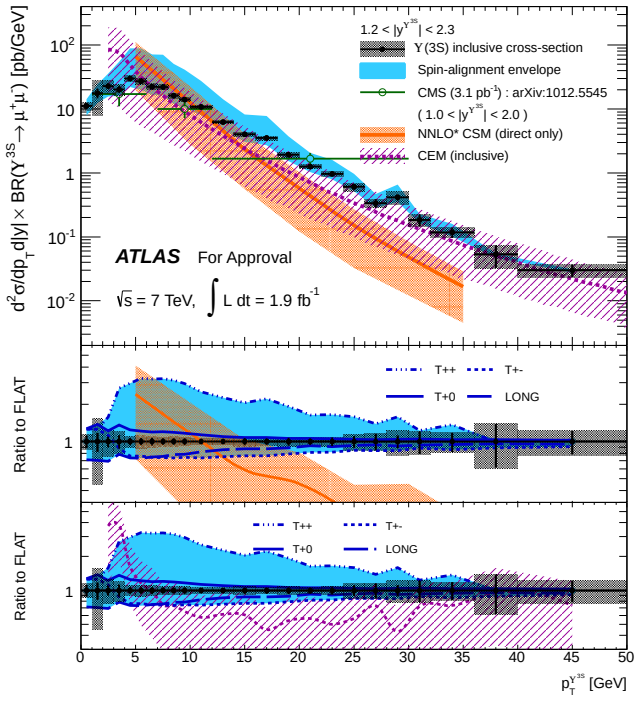
1.2 < |y^3S| < 2.3
Υ(3S) inclusive cross-section
Spin-alignment envelope
CMS (3.1 pb-1) : arXiv:1012.5545
(1.0 < |y^3S| < 2.0)
NNLO* CSM (direct only)
CEM (inclusive)
ATLAS For Approval
√s = 7 TeV, ∫ L dt = 1.9 fb-1
d2σ/dpT d|y| × BR(ϒ3S→ μ+μ-) [pb/GeV]
Ratio to FLAT
T++
T+-
T+0
LONG
p_T^3S [GeV]

(b)

Figure 6.15: Inclusive cross-section versus p_T for $\Upsilon(3S)$ in (a) central rapidity region ($|y^{\Upsilon}| < 1.2$), and (b) forward rapidity region ($1.2 < |y^{\Upsilon}| < 2.3$). The maximal envelope of variation of the result due to the polarization assumption is indicated by the solid blue band. The NNLO* CSM prediction is shown as an orange solid line and band. The CEM predictions are shown as the purple dashed line and band. The measurements from CMS [105] are shown in green open circles.

Results for the differential inclusive cross-sections as a function of absolute Υ rapidity (integrated Υ p_T) are shown in Fig. 6.17, and are, in general, in good agreement with the measurements from the CMS [105] and LHCb [106] experiments. The dependence on rapidity is relatively flat across the whole rapidity interval. Different polarization scenarios basically only give an overall effect on normalization of the distributions with the exception that at high rapidity ($|y| > 1.7$) the T_{++} scenario pulls the cross-sections up by about a factor of 3 and the fully longitudinally polarized scenario pulls them down by about 20%.

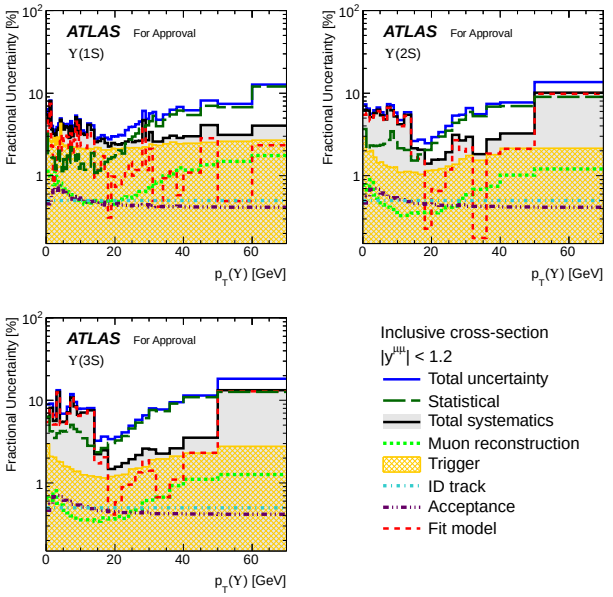

(a)

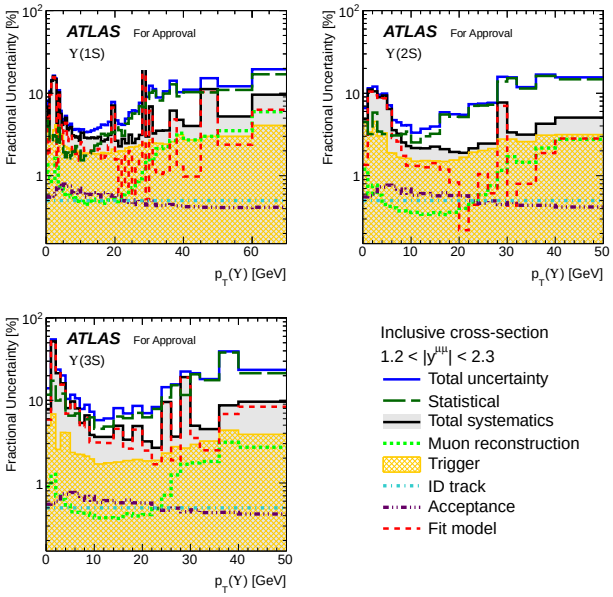

(b)

Figure 6.16: Corresponding uncertainties for $\Upsilon(nS)$ $(n = 1, 2, 3)$ in (a) central rapidity region $(|y^{\Upsilon}| < 1.2)$, and (b) forward rapidity region $(1.2 < |y^{\Upsilon}| < 2.3)$.

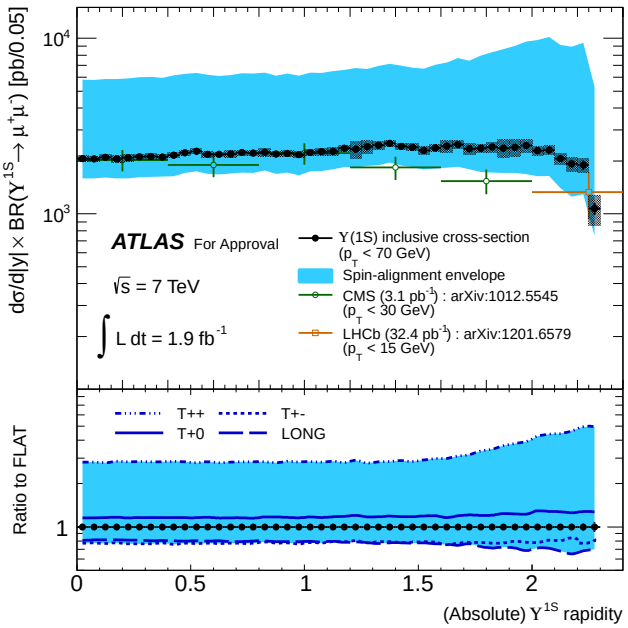
dσ/d|y| × BR(Υ^1S → μ+μ-) [pb/0.05]
ATLAS For Approval
√s = 7 TeV
∫ L dt = 1.9 fb-1
Υ(1S) inclusive cross-section
(pT < 70 GeV)
Spin-alignment envelope
CMS (3.1 pb-1) : arXiv:1012.5545
(pT < 30 GeV)
LHCb (32.4 pb-1) : arXiv:1201.6579
(pT < 15 GeV)
T++
T+-
T+0
LONG
Ratio to FLAT
(Absolute) Υ^1S rapidity

(a)

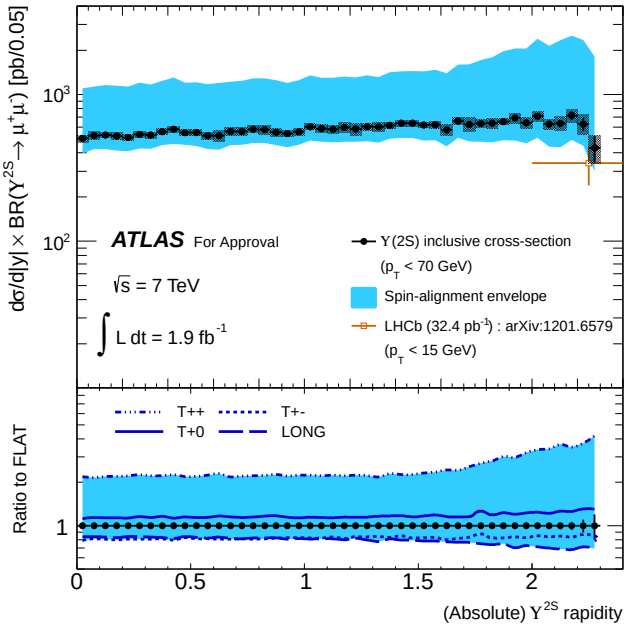
dσ/d|y| × BR(Υ^2S → μ+μ-) [pb/0.05]
ATLAS For Approval
√s = 7 TeV
∫ L dt = 1.9 fb-1
Υ(2S) inclusive cross-section
(pT < 70 GeV)
Spin-alignment envelope
LHCb (32.4 pb-1) : arXiv:1201.6579
(pT < 15 GeV)
T++
T+-
T+0
LONG
Ratio to FLAT
(Absolute) Υ^2S rapidity

(b)

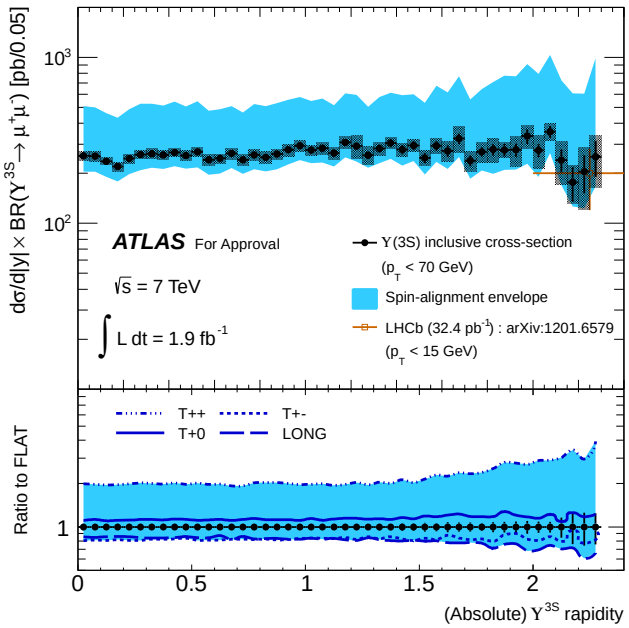
ATLAS For Approval
√s = 7 TeV
∫ L dt = 1.9 fb-1
ϒ(3S) inclusive cross-section
(pT < 70 GeV)
Spin-alignment envelope
LHCb (32.4 pb-1) : arXiv:1201.6579
(pT < 15 GeV)
dσ/d|y| × BR(ϒ3S→ μ+μ-) [pb/0.05]
T++
T+-
T+0
LONG
Ratio to FLAT
(Absolute) ϒ3S rapidity

(c)

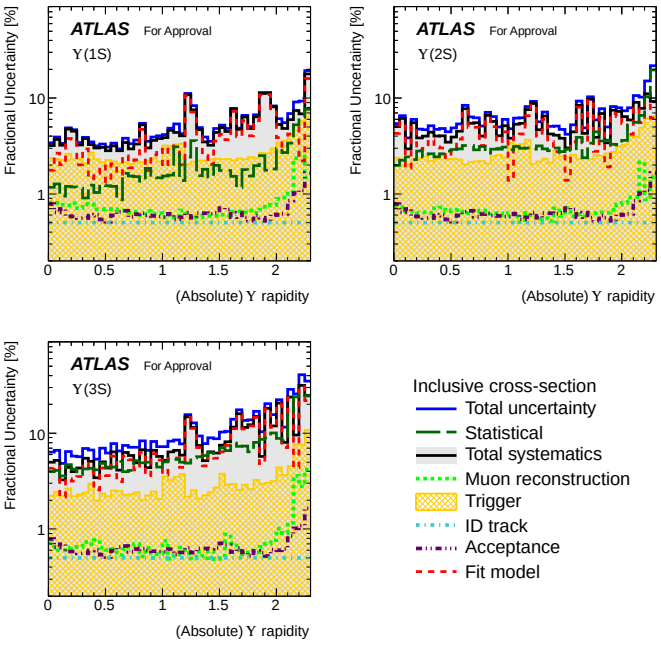
ATLAS For Approval
ϒ(1S)
ϒ(2S)
ϒ(3S)
Fractional Uncertainty [%]
(Absolute) ϒ rapidity
Inclusive cross-section
Total uncertainty
Statistical
Total systematics
Muon reconstruction
Trigger
ID track
Acceptance
Fit model

(d)

Figure 6.17: Inclusive cross-section versus rapidty for (a) $\Upsilon(1S)$; (b) $\Upsilon(2S)$; and (c) $\Upsilon(3S)$. The maximal envelope of variation of the result due to the polarization assumption is indicated by the solid blue band. The measurements from CMS [105] are shown as a green open circle, and the orange open circle is measurement from LHCb [106]. (d) Corresponding uncertainties for $\Upsilon(nS)$, n = 1, 2, 3.

6.2.4 The ratios $\sigma(\Upsilon^{2S})/\sigma(\Upsilon^{1S})$ and $\sigma(\Upsilon^{3S})/\sigma(\Upsilon^{1S})$

The ratios of $\sigma(\Upsilon^{2,3S})$ to $\sigma(\Upsilon^{1S})$, are not calculated directly from the average cross-section numbers. They are calculated from each fit model separately, and then averaged over all these models. In this way, the correlation of yields between $\Upsilon^{2,3S}$ and Υ^{1S} are included.

Systematic uncertainties from the efficiencies (muon reconstruction, trigger and acceptance) on the ratios are reduced because the number of Υ mesons shift coherently when the efficiency fluctuates. Figure 6.18 shows the ratios versus Υ p_T in two rapidity regions. At low p_T ($0-5$ GeV), the ratios to the $\Upsilon(1S)$ are relatively constant at $\sim$20% and $\sim$7% for the $\Upsilon(2S)$ and $\Upsilon(3S)$, respectively. At higher p_T the production rates of higher Υ states increase significantly and steadily with Υ p_T. The results agree very well with the previous measurements from CMS [105] and LHCb [106]. However, our results extend to a significantly higher p_T, and the ratios seem to be saturated above 30 GeV. The ratios versus Υ rapidity are quite flat across the full $|y| < 2.3$ rapidity interval as shown in Fig. 6.18(c).[9]. Currently there is no prediction from higher-order CSM calculations available due to the significant feed-down contributions.

[9]Tables with details are given in Appendix E.3.

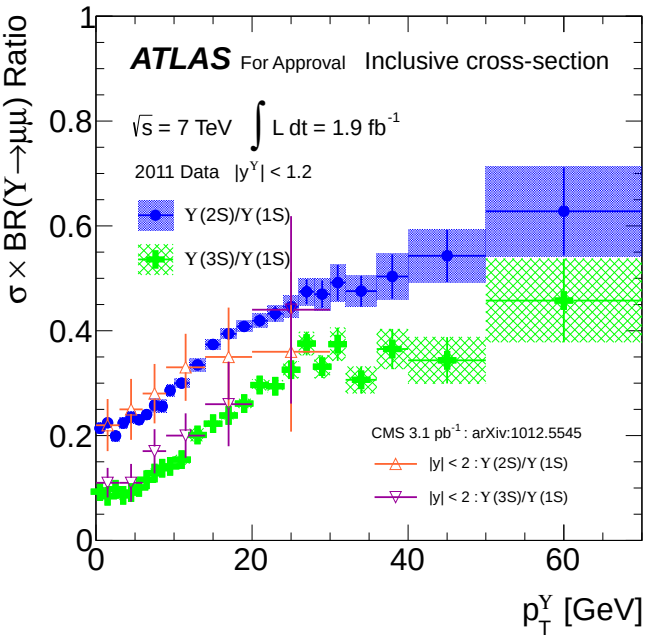
ATLAS For Approval Inclusive cross-section
√s = 7 TeV ∫ L dt = 1.9 fb-1
2011 Data |yϒ| < 1.2
ϒ(2S)/ϒ(1S)
ϒ(3S)/ϒ(1S)
CMS 3.1 pb-1 : arXiv:1012.5545
|y| < 2 : ϒ(2S)/ϒ(1S)
|y| < 2 : ϒ(3S)/ϒ(1S)
σ × BR(ϒ→μμ) Ratio
pTϒ [GeV]

(a)

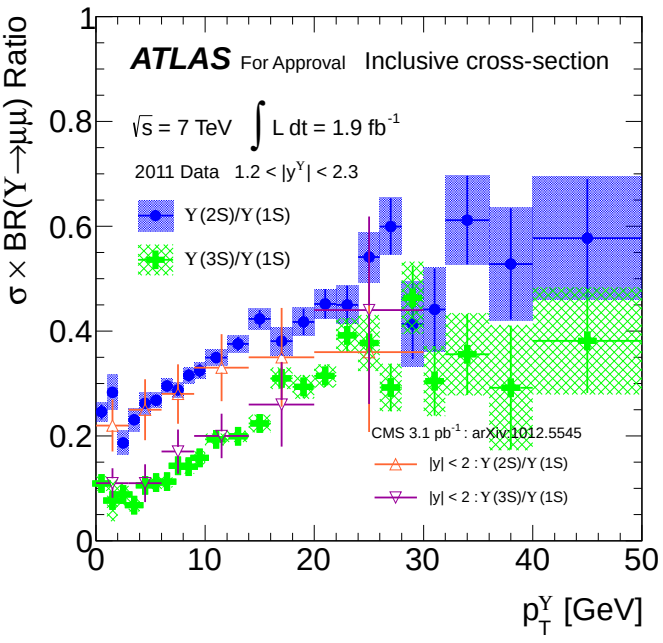
ATLAS For Approval Inclusive cross-section
√s = 7 TeV ∫ L dt = 1.9 fb-1
2011 Data 1.2 < |yϒ| < 2.3
ϒ(2S)/ϒ(1S)
ϒ(3S)/ϒ(1S)
CMS 3.1 pb-1 : arXiv:1012.5545
|y| < 2 : ϒ(2S)/ϒ(1S)
|y| < 2 : ϒ(3S)/ϒ(1S)
σ × BR(ϒ→μμ) Ratio
pTϒ [GeV]

(b)

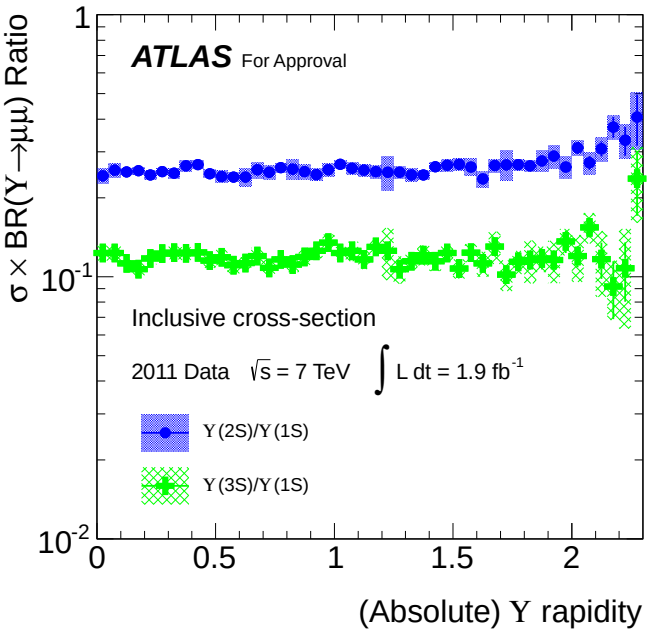

(c)

Figure 6.18: The ratios of inclusive cross-section versus p_T in (a) central rapidity region ($|y^{\Upsilon}| < 1.2$), and (b) forward rapidity region ($1.2 < |y^{\Upsilon}| < 2.3$). (c) Ratios of inclusive cross-section versus rapidity of ϒ. The open triangles are measurements from CMS [105].

Chapter 7

The Search for Light CP-odd Higgs a_1

"A theory with mathematical beauty is more likely to be correct then an ugly one that fits some experimental data."

– **P.A.M. Dirac**

The search for a light CP-odd Higgs particle a_1 decaying into a di-muon pair is very similar to selecting $\Upsilon \to \mu^+\mu^-$ decays. We search for this narrow resonance in a di-muon mass region ranging from 6 to 12 GeV. The mass region containing the Υ resonances is excluded, since there is no easy way to distinguish an a_1 signal from an Υ if they overlap. Observing no anomalous resonances, we set upper limits on the production cross-section $gg \to a_1$ times $a_1 \to \mu^+\mu^-$ branching ratio as a function of m_{a_1}.

A search using the full 2010 dataset, 39 pb^{-1}, was performed by the author in early 2011. This analysis was approved by the ATLAS collaboration [109] as a preliminary result. This was the first limit on the light NMSSM CP-odd Higgs from the LHC. In this chapter, details of the analysis will be described in Sec. 7.1 – 7.4. At the end of the chapter, prospective results using 1.9 fb^{-1} of data collected by ATLAS in 2011[1] are shown.

7.1 Advanced Event Selection

The basic selection cuts for the muon and di-muon candidates are identical to those used in the Υ analysis and summarized in Table 5.1. However, in order to increase the significance of the a_1 signal, a multivariate selection called the Likelihood Ratio (LR) is added to the basic criteria. In the LR method, the discriminating variable R is

$$R \equiv \frac{1-Y}{1+Y}, \tag{7.1}$$

where $Y \equiv \prod y_i$ with $y_i = \frac{f_{bkgd}(x_i)}{f_{sig}(x_i)}$, the ratio of background and signal probability density functions (PDFs) coming from the variable x_i. The value of this discriminating variable tends to 1 for signal-like events, and to -1 for background events. The

[1] The updated results are aimed for a publication in the near future.

variables x_i used here are the following:

- The di-muon vertex fit quality χ^2/n.d.f.
- The isolation, $E_T cone20/p_T(\mu)$, for each muon. The variable $E_T cone20$ is the transverse energy which is measured in the calorimeters in a cone size $\Delta R = 0.2$ centered on the direction of the muon. For this calculation, the expected muon energy loss in the calorimeters is subtracted from $E_T cone20$.

The LR selection here is essentially selecting high quality di-muon candidates with a common vertex.

7.1.1 Data-driven PDFs

The PDFs, for both signal and background, that are used in the Likelihood Ratio (LR) selection are derived from data. The background PDFs come from distributions of the variables in the $m_{\mu\mu}$ sideband regions $4.5-5.5$ GeV and $12.5-14.0$ GeV which are away from the potential signal region (6.0 – 12.0 GeV).

The signal PDFs are constructed from distributions of the variables under the $\Upsilon(1S)$ resonance (9.0 – 10.0 GeV) with sideband subtraction (the sideband regions are 7.0 – 8.5 GeV and 11.0 – 12.0 GeV). A fit is performed in the $m_{\mu\mu}$ region (7.0 – 12.0 GeV) with double-Gaussian functions for the three Υ states (no a_1 assumption) and a fourth-order polynomial for the background shape as described in Eq. 6.5. The distributions in the sideband regions are normalized to the number of background events under the signal region, and then the distributions from normalized background distributions are subtracted from the signal region distributions to obtain pure $\Upsilon(1S)$ PDFs. Figure 7.1(a) shows the signal and sideband regions in the $m_{\mu\mu}$ distribution.

As mentioned before, the LR selection here is used to select high quality di-muon resonances and is insensitive to the details of the resonance production mechanism.

Figure 7.1(b) and 7.1(c) show the generally good agreement in signal PDFs between the pure $\Upsilon(1S)$ obtained from data, and the Monte Carlo predictions for $\Upsilon(1S)$ and a_1 (8 GeV) signal.

The ratios for vertex χ^2/n.d.f and $E_T cone20/p_T(\mu_{1,2})$ are calculated by comparing the background and signal PDFs, and are parametrized by simple polynomials that are shown in Fig. 7.2. The signal-background separation power of the LR selection is shown in Fig. 7.3(a).

7.1.2 Cut Optimization

To enhance the sensitivity of a possible a_1 signal, the cut on the discriminating variable R is optimized by using the metric $\varepsilon_{LR}(a_1)/\sqrt{N_{bkgd}}$. The a_1 MC with 7.5 GeV mass is used for determining the Likelihood Ratio efficiency ($\varepsilon_{LR}(a_1)$). The number of background events (N_{bkgd}) under a potential signal is estimated by extrapolating a fourth-order polynomial fit to the data in the sideband regions within a mass window of $\pm 3\sigma$ of the mass resolution at 7.5 GeV.

Figure 7.3(b) shows the relation of $\varepsilon_{LR}(a_1)/\sqrt{N_{bkgd}}$ with the discriminating variable R. The optimized value of the R cut is also shown. The final di-muon mass distribution after the Likelihood Ratio selection with several simulated a_1 signals superimposed is shown in Fig. 7.3(c).

7.2 Cross-section Limits

Since there is no evidence of a non-Υ resonance in the final data sample, limits on the a_1 production cross-section via gluon fusion times $a_1 \to \mu^+\mu^-$ branching fraction are set using:

$$\sigma(gg \to a_1) \times Br(a_1 \to \mu^+\mu^-) = \frac{N_{sig}^{95\%}}{\mathcal{L} \cdot \varepsilon}, \tag{7.2}$$

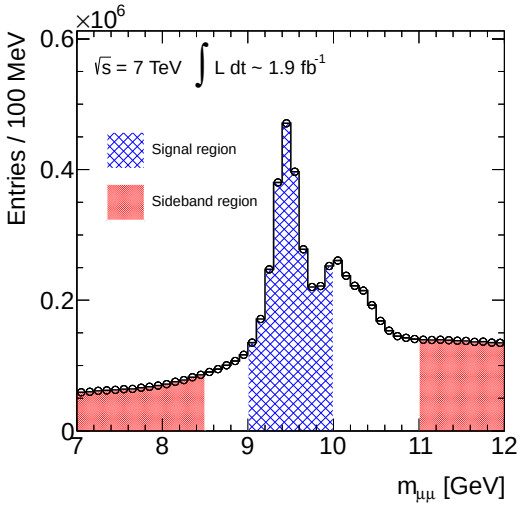

(a)

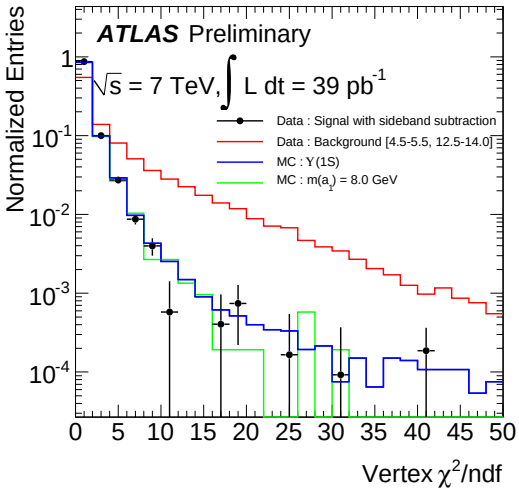

(b)

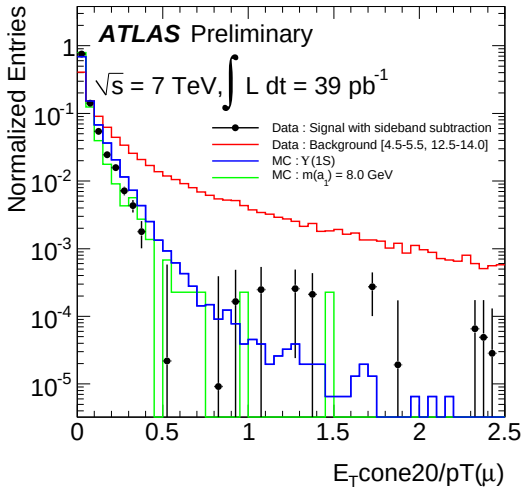

(c)

Figure 7.1: (a) Di-muon mass distribution from $7 - 12$ GeV. The variables for the Likelihood Ratio: (b) vertex χ^2/n.d.f; (c) $E_T cone20/p_T(\mu)$

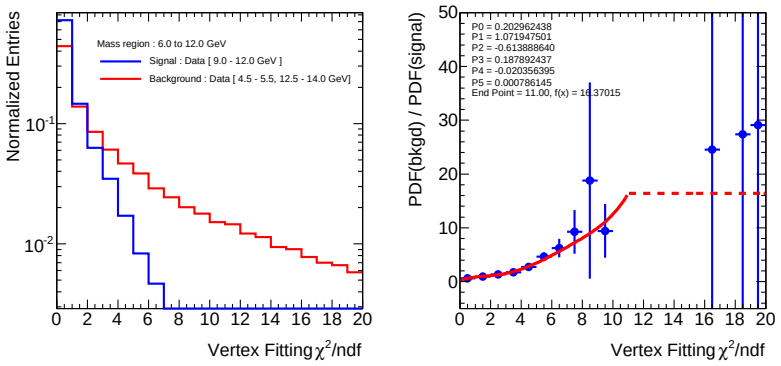

(a)

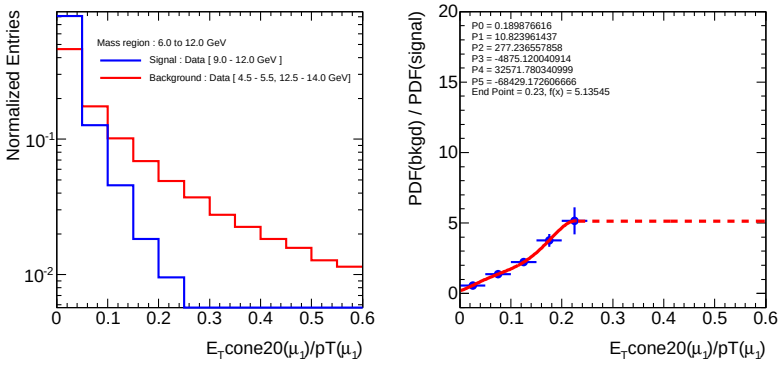

(b)

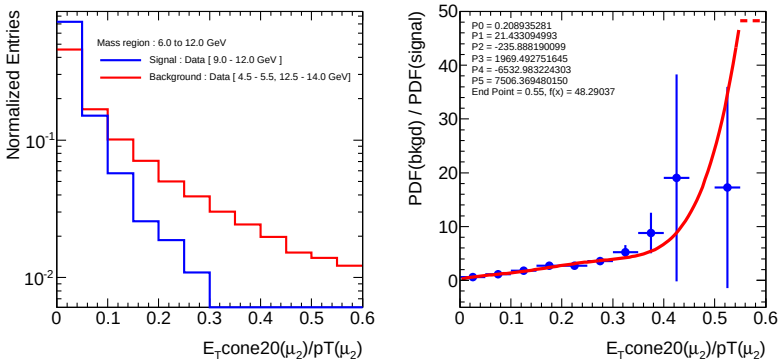

(c)

Figure 7.2: The ratios of background to signal PDFs for (a) vertex χ^2/n.d.f; (b) $E_T cone20/p_T(\mu_1)$; (c) $E_T cone20/p_T(\mu_2)$.

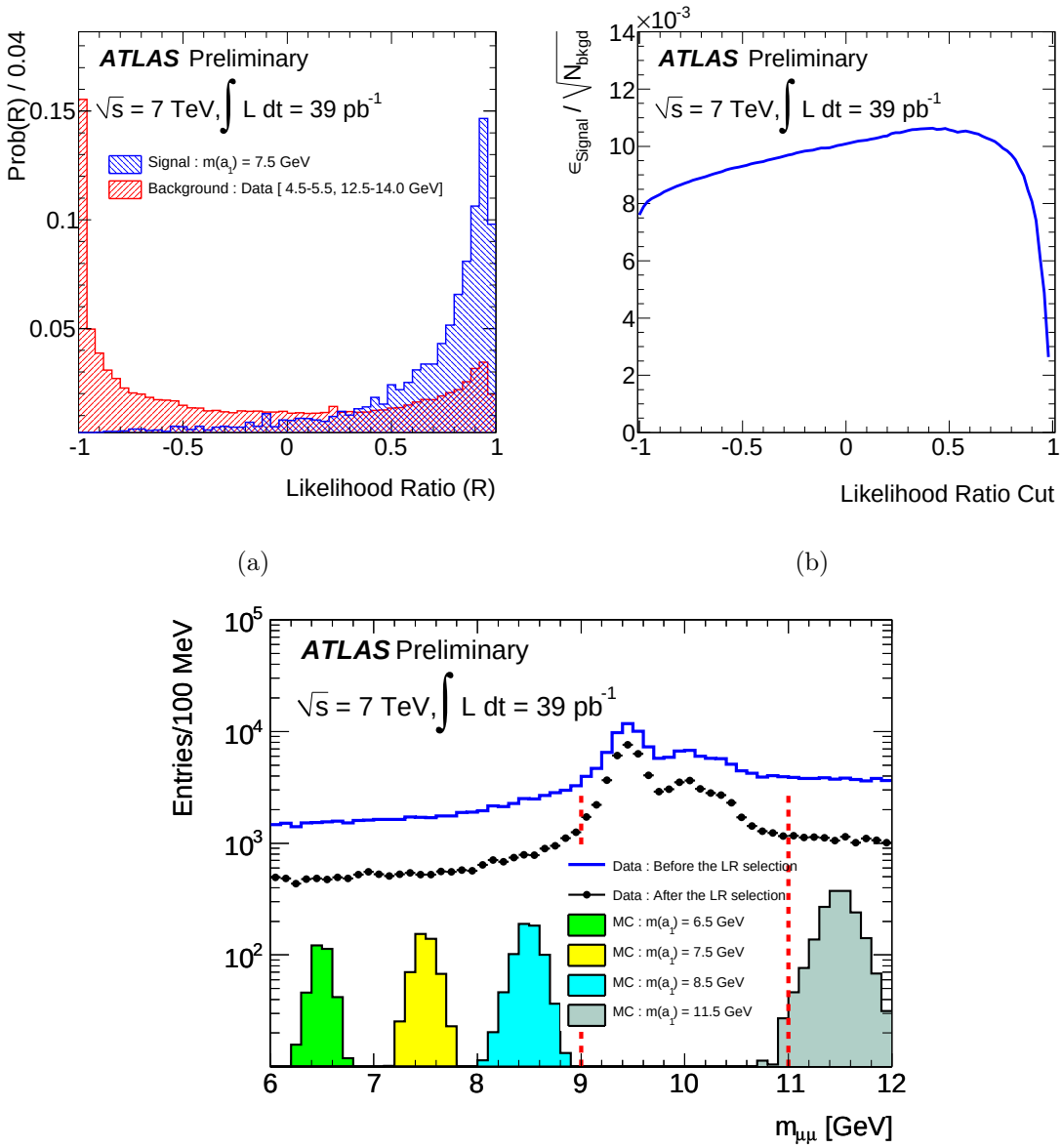

Figure 7.3: (a) Separation power of the Likelihood Ratio distributions, (b) optimization of the Likelihood Ratio cut, and (c) final di-muon mass distribution with Likelihood Ratio selection and some a_1 mass points.

where $N_{sig}^{95\%}$ is the 95% confidence level limit on the number of $a_1 \to \mu^+\mu^-$ signal events for a given m_{a_1}, and $\mathcal{L}$ is the integrated luminosity (here it is 39 pb^{-1} for the 2010 ATLAS data), and ε is the total efficiency for all selection cuts.

7.2.1 Efficiencies

The total efficiency is factorized into four components,

$$\varepsilon = \varepsilon_{acc} \cdot \varepsilon_{\mu\mu} \cdot \varepsilon_{trig} \cdot \varepsilon_{LR}, \tag{7.3}$$

where, similar to the Υ analysis, ε_{acc} is the kinematic acceptance for the a_1 signal, $\varepsilon_{\mu\mu}$ is the reconstruction efficiency for di-muon pairs, ε_{trig} is the efficiency of the di-muon trigger (EF_2mu4_DiMu), and ε_{LR} is the efficiency of the Likelihood Ratio selection. The efficiency for each component is calculated relative to all the previous selections. The di-muon ($\varepsilon_{\mu\mu}$) efficiency is calculated by using the muon kinematic distributions (p_T, η and q) in MC combined with the data-driven efficiencies from the ATLAS Muon Combined Performance group [110, 111].

Due to the low statistics of the di-muon sample collected during 2010 data-taking, we also included segment tagged-muons as described in Sec. 5.1 to increase sensitivity to a potential a_1 signal. The di-muon efficiency for tagged-combined and combined-combined combinations can be written:

$$\varepsilon_{\mu\mu} = \varepsilon_C(\mu^+) \cdot \varepsilon_{CT}(\mu^-) + \varepsilon_C(\mu^-) \cdot \varepsilon_{CT}(\mu^+) - \varepsilon_C(\mu^+) \cdot \varepsilon_C(\mu^-) \tag{7.4}$$

where ε_C and ε_{CT} are the muon reconstruction efficiencies for combined muon and for either tagged or combined muon, respectively.

The trigger efficiency is calculated from the $\Upsilon(1S)$ MC [2]. We use muon-independent data (JetTauEtmiss) to estimate the systematic uncertainty due to modeling the ΔR

[2] At that time, our data-driven method which we described in Chapter 5, was not available.

correction in MC. Figure 7.10 shows a summary of all efficiencies as a function of m_{a_1}.

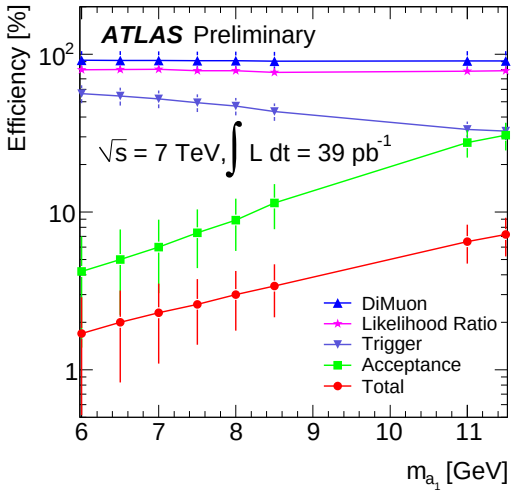

Figure 7.4: Different components of the total efficiency as a function of m_{a_1}.

7.2.2 Extracting Limits

A likelihood function is defined as the product over bins in $m_{\mu\mu}$:

$$L(\mu, \hat{\theta}) = \prod_{i=bin} \frac{\eta_i^{N_i}}{N_i!} e^{-\eta_i} \tag{7.5}$$

where μ is the number of signal events, and θ represents other (nuisance) parameters of the likelihood. N_i is the number of observed events in bin i, and η_i is the predicted number of events in that bin as determined by:

$$\eta_i = \mu \cdot \underbrace{f_{s,i}(m, \sigma_m)}_{\text{the potential } a_1 \text{ signal}} + \underbrace{\sum_{n=1}^{3} n_{nS} \cdot f_{nS,i}(m, \sigma_m)}_{\text{the } \Upsilon \text{ peaks}} + \underbrace{n_{bk} \cdot f_{bk,i}(m)}_{\text{continuum background}} \tag{7.6}$$

The functions $f_{s,i}$, $f_{nS,i}$ and $f_{bk,i}$ are probability density functions (PDFs) for the a_1 signal, the $\Upsilon(nS)$ and the continuum background, respectively, in each bin. The total background PDF is a combination of three double-Gaussians (for the three Υs) with the same setting on the relative masses and widths as we described in Sec. 6.1.1 and a fourth-order polynomial function (for continuum background). The signal PDF for the a_1 is a double-Gaussian function with width (σ_m) scaled linearly from the width of the $\Upsilon(1S)$ as we described in Sec. 6.1.1.

To obtain stable fits result, we divide the data into two regions: low mass (6 – 11 GeV) and high mass (9 – 12 GeV) and perform separate fit in each region, as shown in Fig. 7.5.

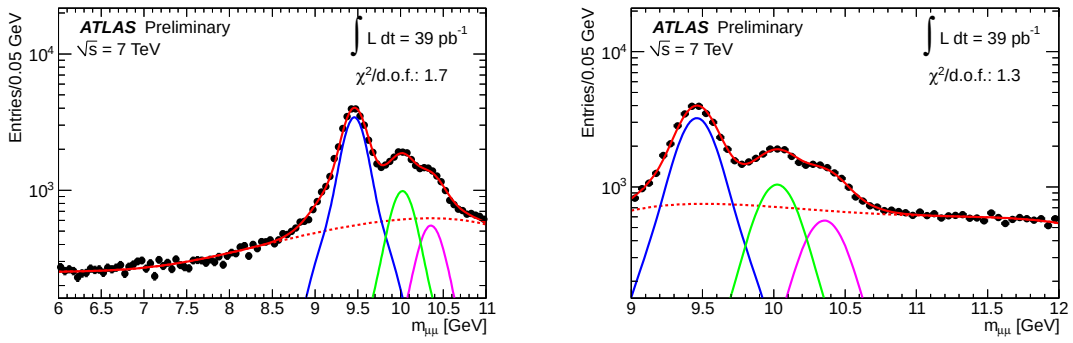

(a) (b)

Figure 7.5: The mass fits (no a_1 assumption) for (a) low mass and (b) high mass regions. The red solid line is the total fitting result; The blue, green and pink lines are fit results for the $\Upsilon(1S)$, $\Upsilon(2S)$ and $\Upsilon(3S)$, respectively. The red dashed line is the continuum background.

After building the likelihood function from the fit results, we use the Profile Like-

lihood Ratio (PLR) method[3] that is implemented in RooStats package in [112] to extract limits on the number of signal events. A test statistic:

$$q_\mu \equiv 2\ln\lambda(\mu) = -2\ln\frac{L(\mu,\hat{\hat{\theta}})}{L(\hat{\mu},\hat{\theta})} \tag{7.7}$$

is used, where the likelihood function in the numerator is calculated at the value $\hat{\hat{\theta}}$, that maximizes it for a given μ. The likelihood function in the denominator is the global maximum with parameters $(\hat{\mu},\hat{\theta})$. This technique allows systematic uncertainties on the nuisance parameters to be included automatically in limits derived on μ.

7.3 Systematic Uncertainties

We consider several sources of systematic uncertainties that affect our limits.

- **Luminosity:** The official ATLAS luminosity uncertainty of 3.4% [113] for 2010 data-taking is used.

- **Acceptance:** Low-mass particles (like a_1), especially those that have mass less than 8 GeV, need substantial p_T to provide their daughter muons enough transverse momentum to pass the $p_T^\mu > 4$ GeV requirement. Acceptance of the a_1 candidate can therefore be affected by several sources, such as modeling of initial and final state radiation (ISR/FSR), the choice of parton density function, the choice of α_s, and contributions from beyond Next-to-Leading Order (NLO) calculations of a_1 production. The magnitudes of the first three items are -5 to 9%, -2.8 to 2.1% and -1.4 to 0.7%, respectively, by comparing the acceptances from different ISR/FSR models, different PDFs[4], and varying the nominal value

[3] This is the recommended method in ATLAS.

[4] We used three different NLO parametrization: MRSTW2008nlo, NNPDF2.0 and CTEQ6.6.

of α_s by ± 0.002. We found a huge difference in acceptance between PYTHIA simulation and MC@NLO simulation as shown in Fig. 7.6 which shows the p_T of leading and subleading muons at the parton level predicted by these two generators. Obviously, the muons from the PYTHIA prediction have a much softer p_T spectrum, and this is the reason that PYTHIA has a dramatically lower acceptance than MC@NLO. PYTHIA generates hard scattering events at leading-order level with a parton shower to model gluon radiation. MC@NLO, as we mentioned in Sec. 4.3.2, uses the full NLO matrix elements. They also use different ISR/FSR models, different PDFs, and different values of α_s. Although we expect the true difference between NLO and Next-to-NLO to be significantly smaller than the difference between LO and NLO, there exists no generator yet to do this comparison. Here we quote a conservative upper bound on the true uncertainty which is half of the difference between the acceptances that are calculated from MC@NLO and from PYTHIA.

- **Di-muon reconstruction efficiency:** This systematic uncertainty is dominated by the statistics of the efficiency maps in their p_T and η bins. The efficiency $\varepsilon_{\mu\mu}$ is recalculated using the efficiency maps with coherent variations of $+1\sigma$ and -1σ across all bins. The size of this systematic uncertainty is determined from the difference between the original $\varepsilon_{\mu\mu}$ and recalculated $\varepsilon_{\mu\mu}$.

- **Trigger efficiency:** There are two parts in the systematic uncertainty on the trigger efficiency determination. The first part is similar to the di-muon efficiency. The systematic uncertainty is driven by the statistics of the MC samples used to build the efficiency maps. The second part comes from the uncertainty on the data-driven correction factors obtained from muon-independent sample as shown in Fig 7.7.

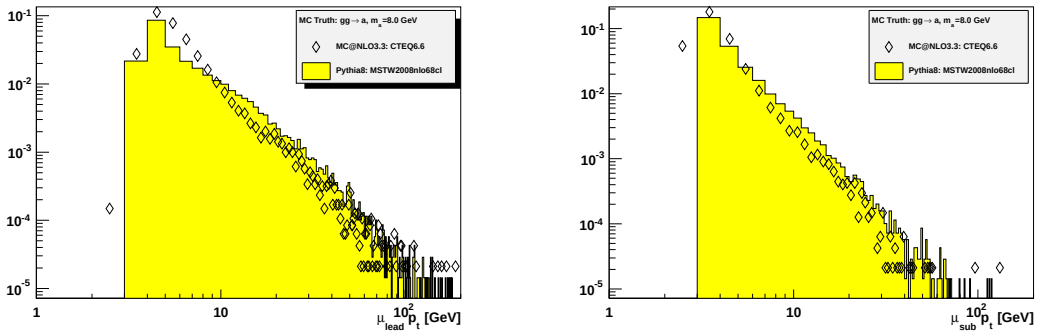

(a) (b)

Figure 7.6: The muon p_T distributions (a) for leading muon and (b) for subleading muon at generator level. The open diamond points are the predictions from MC@NLO; and the yellow histogram is the prediction from PYTHIA.

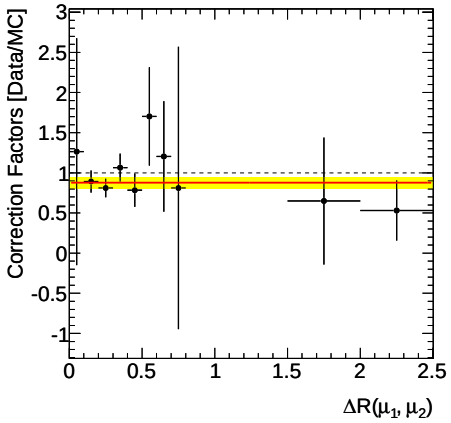

Figure 7.7: The ratio of ΔR correction from Data and MC.

- **Likelihood Ratio selection:** We considered several possible sources of the systematic uncertainty on the Likelihood Ratio selection. There are three negligible (<1%) components: (a) the statistics of the data-driven PDFs, estimated by using toy-MC experiments; (b) differences in shape of the Likelihood Ratio variables between $\Upsilon(1S)$ and a_1 MCs; and (c) the statistics of the a_1 MC for calculating the efficiency of the Likelihood Ratio selection.

  A larger uncertainty, about 3%, comes from comparing the efficiencies that are calculated from $\Upsilon(1S)$ MC and from the data (extracting the number of $\Upsilon(1S)$ events before and after Likelihood Ratio selection).

Table 7.1 shows the magnitudes of each of these uncertainties for different a_1 masses.

	Relative Uncertainty (%) at m_{a_1} (GeV)							
Source	6.0	6.5	7.0	7.5	8.0	8.5	11.0	11.5
Luminosity	± 3							
Acceptance	± 67	± 55	± 49	± 40	± 36	± 32	± 20	± 20
Muon Efficiency	$^{+14}_{-13}$	$^{+14}_{-13}$	$^{+14}_{-13}$	$^{+14}_{-13}$	$^{+14}_{-13}$	$^{+14}_{-13}$	$^{+15}_{-14}$	$^{+15}_{-14}$
Trigger Efficiency	± 13	± 13	± 13	± 13	± 13	± 13	± 12	± 12
Likelihood Ratio Modeling	± 3							
Total	± 70	± 59	± 53	± 45	± 41	± 37	± 28	± 28

Table 7.1: Summary of systematic uncertainties used in the limit setting.

7.4 Results

The final upper limit on $\sigma(gg \to a_1 \to \mu^+\mu^-)$ is shown in Fig. 7.8. The observed limit (black solid line) is translated from the limit on μ which is set as a 16% power constrained limit (PCL) [114][5] and uses an asymptotic expression for q_μ [115]. The systematic uncertainties described in Sec. 7.3 are included.

The expected limit (red dashed line) and its $\pm 1\sigma$ and $+2\sigma$ bands are calculated by using 500 statistically independent pseudo-experiments. The -2σ band is not displayed because it systematically goes to zero in this method. Deviations of the observed limit from its expected values are consistent with statistical fluctuations arising from a null-signal $m_{\mu\mu}$ distribution taking into account "Look-Elsewhere effects" [116]. Using the techniques described in Ref. [116], probabilities of observing a given fluctuation are increased by factors of 70 – 90 (depending on the precise mass at which the fluctuation occurs) over what would be calculated were an a_1 particle to exist at known mass due to the fact that the fluctuation could occur anywhere in the mass range.

7.5 Prospects for the 2011 dataset

By using the same dataset as the Υ cross-section measurements in Chapter 6 (1.9 fb^{-1}, almost 50 times larger than 2010 dataset), we will be able to set a significantly better upper limit on the a_1 production cross-section times branching fraction. We use the same reconstruction, trigger efficiencies, and basic selection cuts for the muon and di-muon candidates as summarized in Table 5.1. However, we are incorporating several improvements that will be described in the following subsections.

[5] This 16% is recommended from the ATLAS statistics working group.

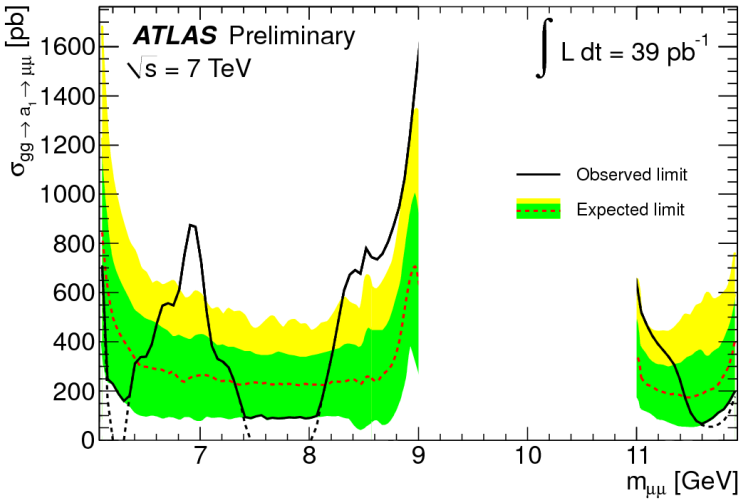

Figure 7.8: Upper limit on $\sigma(gg \to a_1) \times Br(a_1 \to \mu^+\mu^-)$ at 95% confidence level as a function of m_{a_1}. The black solid line is the observed upper limit, presented as a 16% power constrained limit using an asymptotic formula; the dashed red line is the expected limit, assuming absence of a signal. The green and yellow bands are the $\pm 1\sigma$ and $+2\sigma$ uncertainties on the expected limit. The -2σ band is not displayed since it systematically goes to zero in this method.

7.5.1 Likelihood Ratio Selection

The same three variables of the Likelihood Ratio selection will be used. Our studies indicate (all details are shown in Appendix H) that this selection will exhibit similar performance on 2011 data as it did in 2010. Figure 7.9 shows the final di-muon mass spectrum for the 2011 dataset.

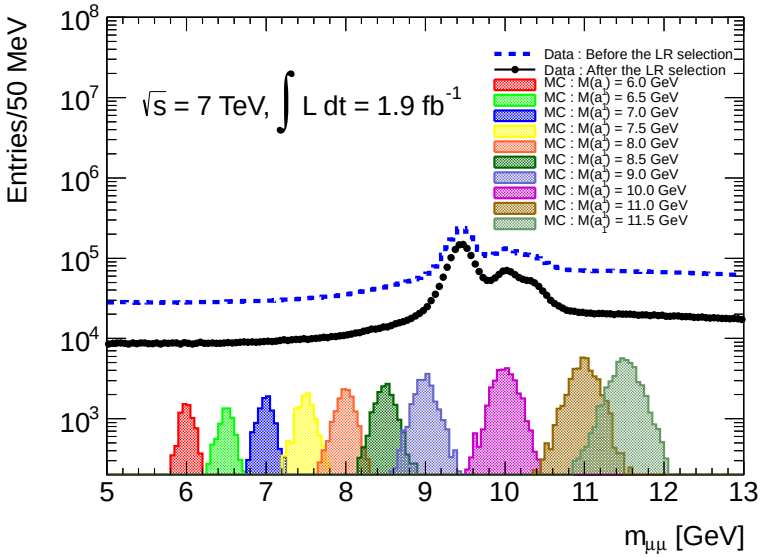

Figure 7.9: The di-muon mass distribution of the 2011 ATLAS 1.9 fb^{-1} data: the blue dashed line is the result obtained before using Likelihood Ratio Selection, and the black points are the results obtained after using the Likelihood Ratio selection, and the color histograms are the a_1 signal distributions with different masses.

7.5.2 Efficiencies

An alternative way[6] to determine the total efficiency is by using the candidate-based correction method as described in Eq. 6.7 to correct for muon reconstruction and trigger efficiencies. Acceptances and Likelihood Ratio efficiencies are calculated using the signal MCs. The formula for limit setting can then be re-written as:

$$\sigma(gg \to a_1) \times Br(a_1 \to \mu^+\mu^-) = \frac{N_{corr}^{95\%}}{\mathcal{L} \cdot \varepsilon_{acc} \cdot \varepsilon_{LR}}, \tag{7.8}$$

where $N_{corr}^{95\%}$ is the 95% confidence level limit on the number of signal events corrected for muon reconstruction and trigger efficiencies.

Table 7.2 and Fig. 7.10 summarize the average acceptances and the efficiencies of the Likelihood Ratio selection as a function of m_{a_1}.

	Efficiency (%) at m_{a_1} (GeV)									
	6.0	6.5	7.0	7.5	8.0	8.5	9.0	10.0	11.0	11.5
$\varepsilon_{\text{filter}}$	23.8	28.7	33.5	37.5	40.7	44.0	47.9	52.8	56.3	57.8
$\varepsilon_{\text{pT>4GeV;}\lvert\eta\rvert\text{<2.3}}$	17.6	16.9	17.3	18.6	20.5	24.5	29.8	38.2	45.5	48.5
$\varepsilon_{\text{acc.}}$	4.2	4.9	5.8	7.0	8.3	10.8	14.3	20.2	25.6	28.0
ε_{LR}	82.3	81.0	78.3	77.9	79.5	77.9	76.5	77.1	77.3	76.7
$\varepsilon_{\text{LR}} \cdot \varepsilon_{\text{acc.}}$	3.5	4.0	4.5	5.5	6.6	8.4	10.9	15.6	19.8	21.5

Table 7.2: The acceptance and the efficiency of Likelihood Ratio selection as a function of a_1 mass.

7.5.3 Limit Setting

Similar to the description in Sec. 7.2.2, the signal PDF is modelled using a double-Gaussian function. Here, we divide the mass distribution into three regions, with

[6] In this way, we might be able to set model-independent upper limits.

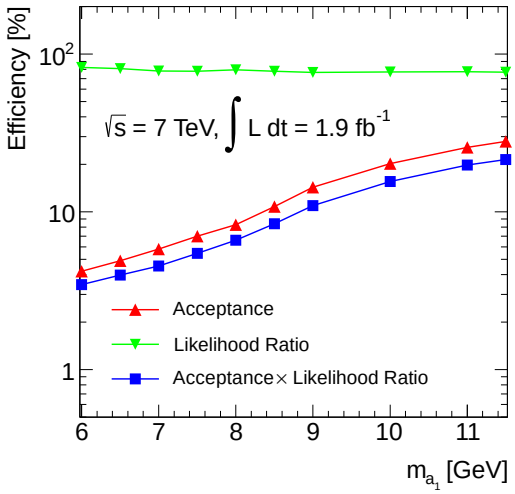

Figure 7.10: The acceptance and the efficiency of Likelihood Ratio selection as a function of a_1 mass.

background PDFs derived separately in each region:

- **Low (5 - 8.5 GeV) and high (11 - 12 GeV) mass regions:** Since the di-muon mass distribution is smooth in these two regions, a simple fourth order polynomial function is used.

- **Υ peaks region (8.5 - 11 GeV):** In this region, the three Υ states contribute to the background determination. The total background PDF is modelled using three double-Gaussian functions (for the three Υs) and a 4^{th} order polynomial function (for the continuum background). The total number of background events is estimated by:

$$N_{bkgd} = \sum_{n=1}^{3} n_{nS} \cdot f_{nS}(m, \sigma_m) + n_{cont.} \cdot f_{cont.}(m). \tag{7.9}$$

  As we have mentioned at the beginning of this chapter, we have excluded this region for the limit setting.

Figure 7.11(a) shows the mass distribution for these three regions; and Fig. 7.11(b) shows the signal PDF for $m_{a_1} = 7$ GeV; and Fig. 7.11(c) and 7.11(d) are the background-only PDFs for the low and high mass sideband regions.

7.5.4 Systematic Uncertainties

By using the muon reconstruction, trigger efficiency maps and the pseudo-experiment method employed in the Υ cross-section measurements (see Section 6.1.2), the systematic uncertainties from these two components are reduced significantly. For each varied efficiency map, we determine the weighted number of events within ± 5 GeV ($\sim 3\ \sigma$) of the a_1 mass under consideration. The size of the systematics uncertainty is taken to be the RMS of the distribution of those numbers over all trials. For the di-muon reconstruction efficiency this is about 0.5%, while the trigger efficiency, including the EF_mu4 and $C_{\mu\mu}$ components, is 2%. These uncertainties are summarized as a function of m_{a_1} in Table 7.3.

	Systematic Uncertainty (%) at m_{a_1} (GeV)							
	6.0	6.5	7.0	7.5	8.0	8.5	11.0	11.5
Di-muon efficiency	± 0.5	± 0.5	± 0.5	± 0.5	± 0.6	± 0.5	± 0.5	± 0.4
Trigger (EF_mu4)	± 1.4	± 1.4	± 1.4	± 1.6	± 2.1	± 2.0	± 1.3	± 1.4
Trigger ($C_{\mu\mu}$)	± 1.8	± 1.8	± 1.8	± 1.8	± 1.8	± 1.8	± 2.0	± 1.9
Trigger (Total)	± 2.3	± 2.3	± 2.2	± 2.4	± 2.7	± 2.7	± 2.4	± 2.4
Total	± 2.4	± 2.3	± 2.3	± 2.4	± 2.8	± 2.7	± 2.4	± 2.4

Table 7.3: The systematic uncertainties for di-muon and trigger efficiency as a function of m_{a_1}.

The systematic uncertainties for acceptance, due to the Next-to-NLO prediction are still not available. We have used the values from the previous study (half the

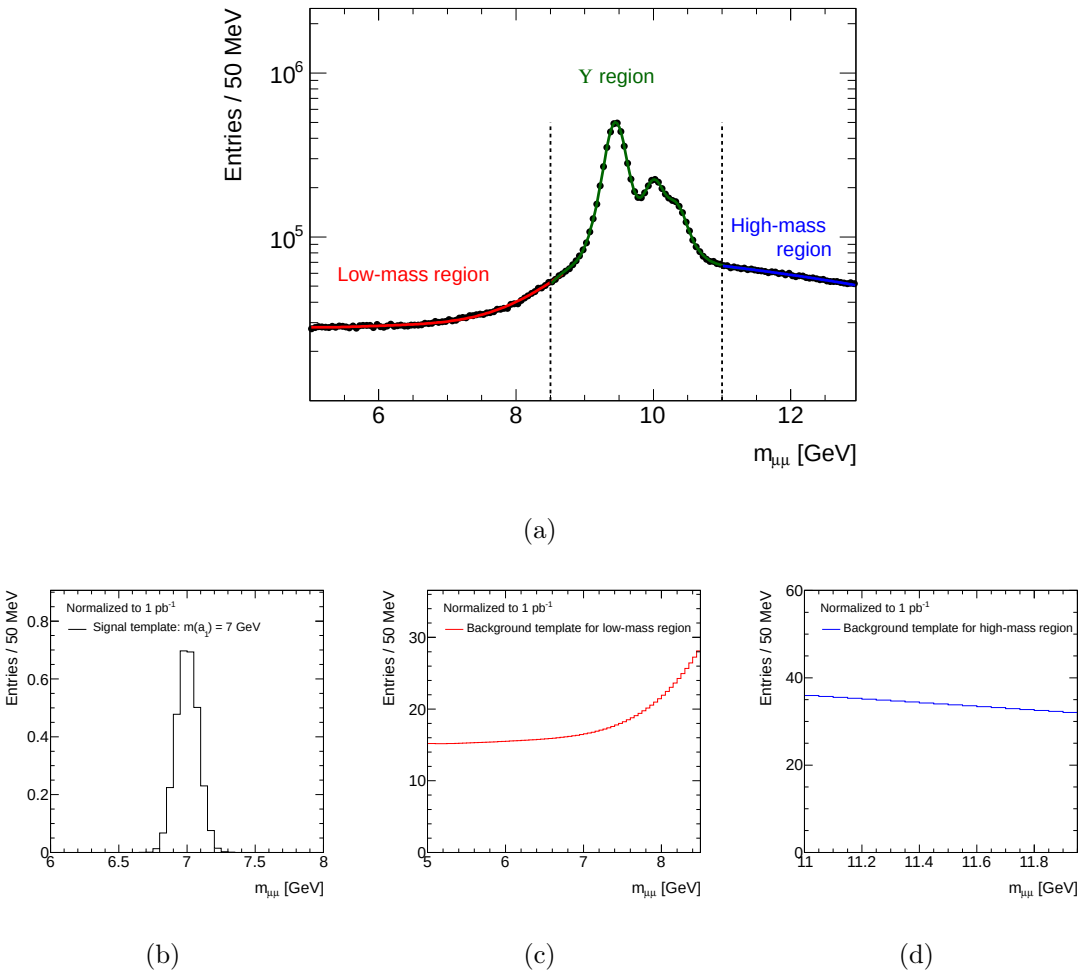

Figure 7.11: (a) Three mass regions for the background PDFs. (b) Signal template for $m_{a_1} = 7$ GeV, (c) and (d) respective background templates for low and high mass regions.

difference between MC@NLO and PYTHIA). We have also used the old values ($\pm$ 3%) for the systematic uncertainties due to the Likelihood Ratio selection as quoted at Table. 7.1.

7.5.5 Results

Figure 7.12 shows the prospective expected limits on a_1 production via gluon fusion times $a_1 \rightarrow \mu^+\mu^-$ branching ratio using 1.9 fb^{-1} ATLAS date from the 2011 run. These limits are a factor of 20 more stringent than those from our previous result.

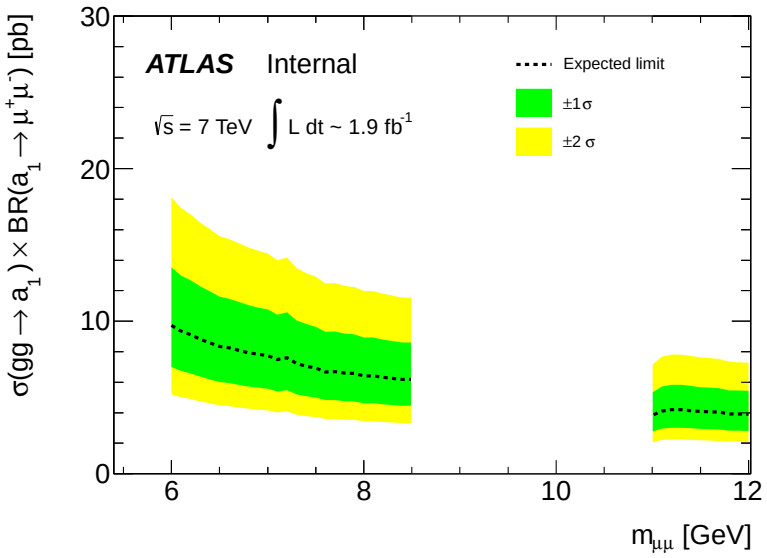

Figure 7.12: The prospective expected limits by using 1.9 fb^{-1} of data from 2011.

Chapter 8

Conclusions

"I don't know, I don't care, and it doesn't make any difference!"

– **A. Einstein**

In this thesis, a new method to determine the di-muon trigger efficiency was presented in Chapter 5. Two analyses covering three important and interesting topics in particle physics were also presented: QCD, Supersymmetry and searches for the Higgs boson. These were described in Chapter 6 and 7.

With increasing instantaneous luminosity in 2011 and finite data storage ability, single muon triggers with low-p_T thresholds were no longer feasible as a means of acquiring Υ and a_1 candidates. Di-muon triggers were required, and therefore their efficiencies determination became important. The di-muon trigger efficiency is factorized into three components, the first two are single muon efficiencies for two muons, while the third part corresponds to correction factors for the extra di-muon requirements. One of the major issues here is to obtain the single muon trigger efficiency. The low-p_T single muon trigger was heavily prescaled in 2011 data-taking, hence it is impossible to get this efficiency from the old method we used in 2010. We developed a new method using a modified tag-and-probe technique to calculate the low-p_T signal muon trigger efficiency. Combining with the correction factors, the di-muon trigger efficiency can be determined. This efficiency determination is not only useful in our analyses, but also will be very important for almost all analyses in the ATLAS B-Physics Group.

The production mechanism of Υ mesons and their polarizations are still significant puzzles to physicists. To obtain a clearer picture, we first need to measure the production cross-sections. After having this foundation, we can move on to the next step – understanding the Υ polarization. In this thesis, we measure the Υ production cross-sections in the di-muon final state in pp collision at $\sqrt{s} = 7$ TeV using 1.9 fb^{-1} ATLAS data from the 2011 runs. The cross-section measurements reach the highest Υ p_T values (70 GeV) ever probed, and both the fiducial cross-sections which are measured in a restricted phase-space of Υ production, and also the inclusive cross-sections, corrected for kinematic acceptance are presented. The fiducial cross-sections

are consistent with our previous measurement [99], and the inclusive cross-sections are in good agreement with the results measured by the CMS [105] and LHCb [106] Collaborations. We also compared the inclusive cross-sections to theoretical predictions of the NNLO* Color Singlet Mechanism (CSM) [48] and the Color Evaporation Model (CEM) [51]. Both of these models agree with our data reasonably well: certainly much better than had previously been the case of predictions of quarkonium production at new energies. However, despite the fact that uncertainties are large on both predictions and our measurements (due to unknown spin-alignment effects) discrepancies between models and data are apparent. Neither the NNLO* CSM or the CEM predictions agree with the data over the full p_T range of the measurements. The next step in the process will be to reduce experimental uncertainties by measuring Υ polarizations at LHC energies. Armed with these new measurements, model builders will be able to determine more clearly where the weakness in their theories lie.

Additionally, we also reported the relative production rates for $\Upsilon(1S)$, $\Upsilon(2S)$ and $\Upsilon(3S)$. Our results again agree very well with the measurements by CMS [105], and it is the first time that we see saturation of these ratios in the high p_T region. Theoretical predictions of these ratios are complicated by the presence of feed-down from higher (2, 3S) to lower (1S) states, and have not yet been completed. Nevertheless, our measurements will provide valuable input for eventual calculations.

The second analysis covered two of the hottest topics in particle physics: Searches for the Higgs bosons and Supersymmetry. The Next-to-Minimal-Supersymmetric Standard Model (NMSSM) [64, 65] is one of the most attractive supersymmetric extension models, it provides a solution for the μ-term problem in the Minimal-Supersymmetric Standard Model (MSSM). The NMSSM predicts richer Higgs phenomena by containing seven Higgs bosons: three neutral CP-even (h_1, h_2, h_3), two neutral CP-odd (a_1, a_2), and two charged (H^+, H^-) Higgs bosons. Results using the

2010 ATLAS dataset (39 pb^{-1}) on a search for the lightest CP-odd Higgs boson a_1 decaying to a di-muon pair in the mass window $6-12$ GeV (excluding three Υ states) are reported. No obvious evidence of a new resonance was found, so the limits on production cross-section $gg \to a_1$ times branching ratio $a_1 \to \mu^+\mu^-$ as a function of m_{a_1} were set. Following that, prospective results using 1.9 fb^{-1} data collected by ATLAS in 2011 are shown. We expect that the upper limit on the production cross-section times branch fraction will be improved by roughly a factor of 20 over the 2010 limit.

Conventionally, the low-mass region is not considered to be the most interesting area in current high energy particle physics. Many theories for the physics beyond the Standard Model on the market concentrate on new phenomena at high-p_T and at high-mass. However, many unknown problems and fascinating physics exist below the $B\bar{B}$ threshold, and this region might help build a bridge to new physics. On the other hand, analyses in the low-mass region have a number of challenges, such as understanding the behaviors of low-p_T muons, dealing with huge and complicated QCD background, etc. Meeting these challenges will continue to lead us into a better understanding of the ATLAS detector.

Bibliography

[1] P. A. M. Dirac, Proc. R. Soc. A **117**, 767 (1929).

[2] E. Fermi, Z. Physik **88**, 161 (1934).

[3] S. Tomonaga, Prog. of Theo. Phys. **1**, 2 (1946).

[4] J. Schwinger, Phys. Rev. **73**, 4 (1948).

[5] J. Schwinger, Phys. Rev. **74**, 10 (1948).

[6] R. P. Feynman, Phys. Rev. **76**, 6: 749 (1949).

[7] R. P. Feynman, Phys. Rev. **76**, 6: 769 (1949).

[8] R. P. Feynman, Phys. Rev. **80**, 3 (1950).

[9] F. Dyson, Phys. Rev. **75**, 3 (1949).

[10] F. Dyson, Phys. Rev. **75**, 11 (1949).

[11] D. J. Gross and F. Wilczek, Phys. Rev. **D 8**, 3633 (1973)

[12] C. D. Anderson, Phys. Rev. **43**, 491 (1933).

[13] E. Braaten, S. Fleming and A.K. Leibovich, Phys. Rev. **D 63**, 094006 (2001).

[14] K. Nakamura *et al.* (Particle Data Group), J. Phys. **G 37**, 075021 (2010).

[15] F. Halzen and A. D. Martin, "Quarks and Leptons: An Introductory Course in Modern Particle Physics", Wiley, ISBN-10: 0471887412 (1984).

[16] W. N. Cottingham and D. A. Greenwood, "An Introduction to the Standard Model of Particle Physics", Cambridge University Press, ISBN-10: 0521852498 (2007).

[17] Y. Nambu, Phys. Rev. Lett. **4**, 380 (1960).

[18] P. W. Higgs, Phys. Rev. Lett. **13**, 508 (1964).

[19] P. W. Higgs, Phys. Lett. **12**, 132 (1964).

[20] S. Weinberg, Phys. Rev. Lett. **19**, 1264 (1967).

[21] A. Salam, Proceedings of 8th Nobel Symposium, Lerum, Sweden, 19-25 May (1968).

[22] G. 't Hooft, Nucl. Phys. **B 35**, 167 (1971); G. 't Hooft and M. J. G. Veltman, Nucl. Phys. **B 44**, 189 (1972).

[23] B. W. Lee and J. Zinn-Justin, Phys. Rev. **D 5**, 3121 (1972); Phys. Rev. **D 5**, 3137 (1972) [Erratum-ibid. **D 8** (1973) 4654]. [Erratum-ibid. **D 8** (1973) 4654]; Phys. Rev. **D 5**, 3155 (1972); Phys. Rev. **D 7**, 1049 (1973).

[24] K. Fujikawa, B. W. Lee and A. I. Sanda, Phys. Rev. **D 6**, 2923 (1972).

[25] UA1 Collab., Phys. Lett. **B 122** 103 (1983); Phys. Lett. **B 126**, 398 (1983).

[26] J. Ellis, M. K. Gaillard, D. V. Nanopoulos, arXiv:1201.6045 (2012).

[27] L. H. Ryder, "Quantum Field Theory", Cambridge University Press, ISBN-10: 0521478146 (1996).

[28] ATLAS Collab., ATLAS-CONF-2012-019 (2012).

[29] CMS Collab., CMS-HIG-11-032, CERN-PH-EP-2012-023, arXiv:1202.1488 (submitted to Physics Letters B) (2012).

[30] CDF Collab. and DØ Collab., arXiv:1203.3774 (2012).

[31] R. P. Feynman, "The Behavior of Hadron Collisions at Extreme Energies", Gordon & Breach, ISBN 978-0677139500 (1969)

[32] http://imperialhep.blogspot.com/2011/08/strangeness-at-lhcb.html.

[33] J. Pumplin, D. R. Stump, J. Huston, H. L. Lai, P. Nadolsky and W. K. Tung, JHEP **07** 012 [arXiv:hep-ph/0201195v3] (2002).

[34] B. Andersson *et al.*, Phys. Rep. **97** (2 & 3), 31 (1983).

[35] G. Marchesini *et al.*, Comp. Phys. Commun. **67**, 465 (1992).

[36] B.R. Webber, Int. J. Mod. Phys. **A 15S1** [arXiv:hep-ph/9912292] (2000).

[37] E598 Collab., Phys. Rev. Lett. **33**, 1404 (1974).

[38] SLAC-SP-017 Collab., Phys. Rev. Lett. **33**, 1406 (1974).

[39] E288 Collab., Phys. Rev. Lett. **39**, 252 (1977).

[40] N. Brambilla *et al* CERN Yellow Report, CERN-2005-005 [arXiv:hep-ph/0412158] (2005).

[41] M. Beneke arXiv:hep-ph/9703429 (1997).

[42] M. Kramer, Prog. Part. Nucl. Phys. **47**, 141 [arXiv:hep-ph/0106120] (2001).

[43] C-H. Chang, Nucl. Phys. **B 172**, 425 (1980); R. Baier and R. Ru ÌĹckl, Phys. Lett. **B 102**, 364 (1981); Z. Phys. **C 19**, 251 (1983); E. L. Berger, D. L. Jones, Phys. Rev. **D 23**, 1521 (1981).

[44] UA1 Collab., Phys. Lett. **B 256**, 112 (1991).

[45] Phys. Lett. **B 370**, 239 (1996).

[46] CDF Collab., Phys. Rev. Lett. **69**, 3704 (1992).

[47] E. Braaten and S. Fleming, Phys. Rev. Lett. **74**, 3327 [arXiv:hep-ph/9411365] (1995).

[48] P. Artoisenet, J. Campbell, J. P. Lansberg, F. Maltoni and F. Tramontano, Phys. Rev. Lett. **101**, 152001[arXiv:0806.3282 [hep-ph]] (2008).

[49] P. Artoisenet, J. P. Lansberg and F. Maltoni, Phys. Lett, **B 653**, 60 (2007); P. Artoisenet, J. M. Camp- bell, J. P. Lansberg, F. Maltoni and F. Tramontano, Phys. Rev. Lett. **101**, 152001 (2008) [arXiv:0806.3282 [hep-ph]]; J. P. Lansberg, Eur. Phys. J. **C 61**, 693 (2009) [arXiv:0811.4005 [hep- ph]].

[50] ATLAS Collab., Nucl. Phys. **B 850**, 3 [arXiv:1104.3038] (2011).

[51] H. Fritzsch, Phys. Lett. **B 67**, 217 (1977); F. Halzen, Phys. Lett. **B 69**, 105 (1977); M. Gluck, J. F. Owens, and E. Reya, Phys. Rev. **D 17**, 2324 (1978); V. D. Barger, W. Y. Keung, and R. J. N. Phillips, Phys. Lett. **B 91**, 253 (1980); J. F. Amundson, O. J. P. Eboli, E. M. Gregores and F. Halzen, Phys. Lett. **B 372**, 127 (1996); J. F. Amundson, O. J. P. Eboli, E. M. Gregores and F. Halzen, Phys. Lett. **B 390**, 323 (1997).

[52] G. T. Bodwin, E. Braaten, and G. P. Lepage, Phys. Rev. **D 51**, 1125 (1995).

[53] M. Kramer, Prog. Part. Nucl. Phys. **47**, 141 [arXiv:hep-ph/0106120] (2001).

[54] CDF Collab., Phys. Rev. Lett. **99**, 132001 [arXiv:0704.0638] (2007).

[55] CDF Collab., CDF public note 9966 (2009).

[56] DØ Collab., Phys. Rev. Lett. **101** 182004 [arXiv:0804.2799] (2008).

[57] P. Faccioli, C. Lourenco, J. Seixas, H. K. Woehri, arXiv:1006.2738 (2010).

[58] CDF Collab., CDF public note 10665 (2011).

[59] D. I. Kazakov, arXiv:hep-ph/0012288 (2001).

[60] S. P. Martin, arXiv:hep-ph/9709356v6 (2011).

[61] H. Haber, G. Kane, and T. Sterling, Nucl. Phys. **B 161**, 493 (1979).

[62] I. J. R. Aitchison, arXiv:hep-ph/0505105 (2005).

[63] N. Polonsky, arXiv:hep-ph/9911329 (1999).

[64] R. Dermisek and J. Gunion, Phys. Rev. **D 79**, 055014 [arXiv:0811.3537] (2009).

[65] F. Mahmoudi, J. Rathsman, O. Stal and L. Zeune, Eur. Phys. J. **C 71**, 1608 [arXiv:1012.4490] (2011).

[66] J. Gunion, D. Hooper and B. McElrath, Phys. Rev. **D 73**, 015011 [arXiv:hep-ph/0509024] (2005).

[67] R. Dermisek and J. Gunion, Phys. Rev. **D 79**, 055014, [arXiv:hep-ph/0811.3537] (2008).

[68] A, Akeroyd, A. Arhrib and Q.-S. Yan, Eur. Phys. J. **C 55**, 653 [arXiv:hep-ph/0712.3933] (2008).

[69] R. Dermisek and J. Gunion, Phys. Rev. **D 76**, 095006 [arXiv:hep-ph/0705.4387] (2007).

[70] G. Abbiendi, *et al.* (the ALEPH Collaboration, the DELPHI Collaboration, the L3 Collaboration and the OPAL Collaboration, The LEP Working Group for Higgs Boson Searches) Phys. Lett. **B 565**, 61 [arXiv:hep-ex/0306033v1] (2003).

[71] Babar Collab., Phys. Rev. Lett. **103**, 081803 [arXiv:0905.4539] (2009).

[72] DØ Collab., Phys. Rev. Lett. **103**, 061801 [arXiv:0905.3381] (2009).

[73] R. Dermisek and J. Gunion, Phys. Rev. **D 81**, 075003 [arXiv:hep-ph/1002.1971] (2010).

[74] A. Belyaev, J. Pivarski, S.Senkin, and A. Tatarinov, Phys. Rev. **D 81**, 075021, [arXiv:hep-ph/1002.1956] (2010).

[75] ALEPH Collab., JHEP **1005**, 049 [arXiv:1003.0705] (2010).

[76] CDF Collab., Phys. Rev. Lett. **107**, 031801 [arXiv:1104.5701] (2011).

[77] R. Dermisek and J. Gunion, Phys. Rev. **D 81**, 055001 [arXiv:hep-ph/0911.2460] (2007).

[78] E. Fullana and M.-A. Sanchis-Lozano, Phys. Lett. **B 653**, 67 [arXiv:hep-ph/0702190] (2007).

[79] F. Domingo, U. Ellwanger, E. Fullana, C. Hugonie and M.-A. Sanchis-Lozano, JHEP **0901**, 061 [arXiv:hep-ph/0810.4736] (2009).

[80] M.-A. Sanchis-Lozano, arXiv:1003.0312 (2010).

[81] J. Gunion, JHEP **0908**, 032 [arXiv:hep-ph/0808.2509v1] (2008).

[82] M.A. Sanchis-Lozano, Mod. Phys. Lett. **A 17**, 2265 [arXiv:hep-ph/0206156] (2002).

[83] M.A. Sanchis-Lozano, Int. J. Mod. Phys. **A 19**, 2183 [arXiv:hep-ph/0307313] (2004).

[84] Y.-J. Zhang and H.-S. Shao [arXiv:0911.1766] (2009).

[85] BaBar Collab., Phys. Rev. Lett. **104**, 191801 [arXiv:1002.4358] (2010).

[86] L. Evans and P. Bryant, "LHC Machine" JINST **3**, S08001 (2008).

[87] http://public.web.cern.ch/public/Objects/Research/AccComplex0700829.gif.

[88] https://espace.cern.ch/acc-tec-sector/Chamonix/ Chamx2011/papers/BM_4_01.pdf.

[89] ATLAS Collab., JINST **3**, S08003 (2008).

[90] http://atlas.web.cern.ch/Atlas/GROUPS/SOFT-WARE/OO/ architecture/General/index.html.

[91] T. Sjostrand, S. Mrenna, and P. Skands, PYTHIA 6.4 Physics and Manual, JHEP 05 026 [arXiv:hep-ph/0603175] (2006).

[92] S. Frixione and B. Webber, JHEP **0206**, 029 [arXiv:hep-ph/0204244] (2002) .

[93] G. Corcella *et al.*, HERWIG 6.5, JHEP **0101**, 010 [arXiv:hep-ph/0011363]; arXiv:hep-ph/0210213 (2001).

[94] S. Agostinelli *et al.*, Instrum. Meth. **A 506**, 3 (2003).

[95] Y. Liao, Eur. Phys. J. **C 55**, 483 (2008).

[96] P. Nadolsky *et al.*, Phys. Rev. **D 78**, 013004 [arXiv:hep-ph/0802.0007] (2008).

[97] E. Braaten, S. Fleming and A.K. Leibovich, Phys. Rev. **D 63**, 094006 (2001).

[98] ATLAS Collab., ATLAS-CONF-2011-021 (2011).

[99] ATLAS Collab., Phys. Lett. **B 705**, 9 (2011).

[100] http://root.cern.ch/.

[101] http://en.wikipedia.org/wiki/Crystal_Ball_function.

[102] ATLAS Collab., Eur. Phys. J. **C 71**, 1630 (2011); ATLAS-CONF-2011-116 (2011).

[103] https://twiki.cern.ch/twiki/bin/view/AtlasPublic/OnlineBeamSpotPublicResults.

[104] J. M. Campbell, F. Maltoni, and F. Tramontano, Phys. Rev. Lett. **98**, 252002 (2007).

[105] CMS Collab., Phys. Rev. **D 83**, 112004 (2011).

[106] LHCb Collab., LHCb-PAPER-2011-036; arXiv:1202.6579 (2012).

[107] CDF Collab., Phys. Rev. Lett. **84**, 2094 [hep-ex/9910025] (2000).

[108] ATLAS Collab., Phys. Rev. Lett. **108**, 152001 [arXiv:1112.5154] (2012).

[109] ATLAS Collab., ATLAS-CONF-2011-020 (2011).

[110] ATLAS Collab., ATLAS-CONF-2011-008 (2011).

[111] ATLAS Collab., ATLAS-BPHYS-2010-01-002 (2011).

[112] https://twiki.cern.ch/twiki/bin/view/RooStats/WebHome.

[113] ATLAS Collab., ATLAS-CONF-2011-011 (2011).

[114] G. Cowan, K. Cranmer, E. Gross, and O. Vitells, arXiv:1105.3166v1 (2011).

[115] G. Cowan, K. Cranmer, E. Gross, and O. Vitells, Eur. Phys. J. **C 71**, 1554 [arXiv:1007.1727] (2002).

[116] E. Gross and O. Vitells, Eur. Phys. J. **C 70**, 525 [arXiv:1005.1891] (2010).

Appendix A

Muon Reconstruction

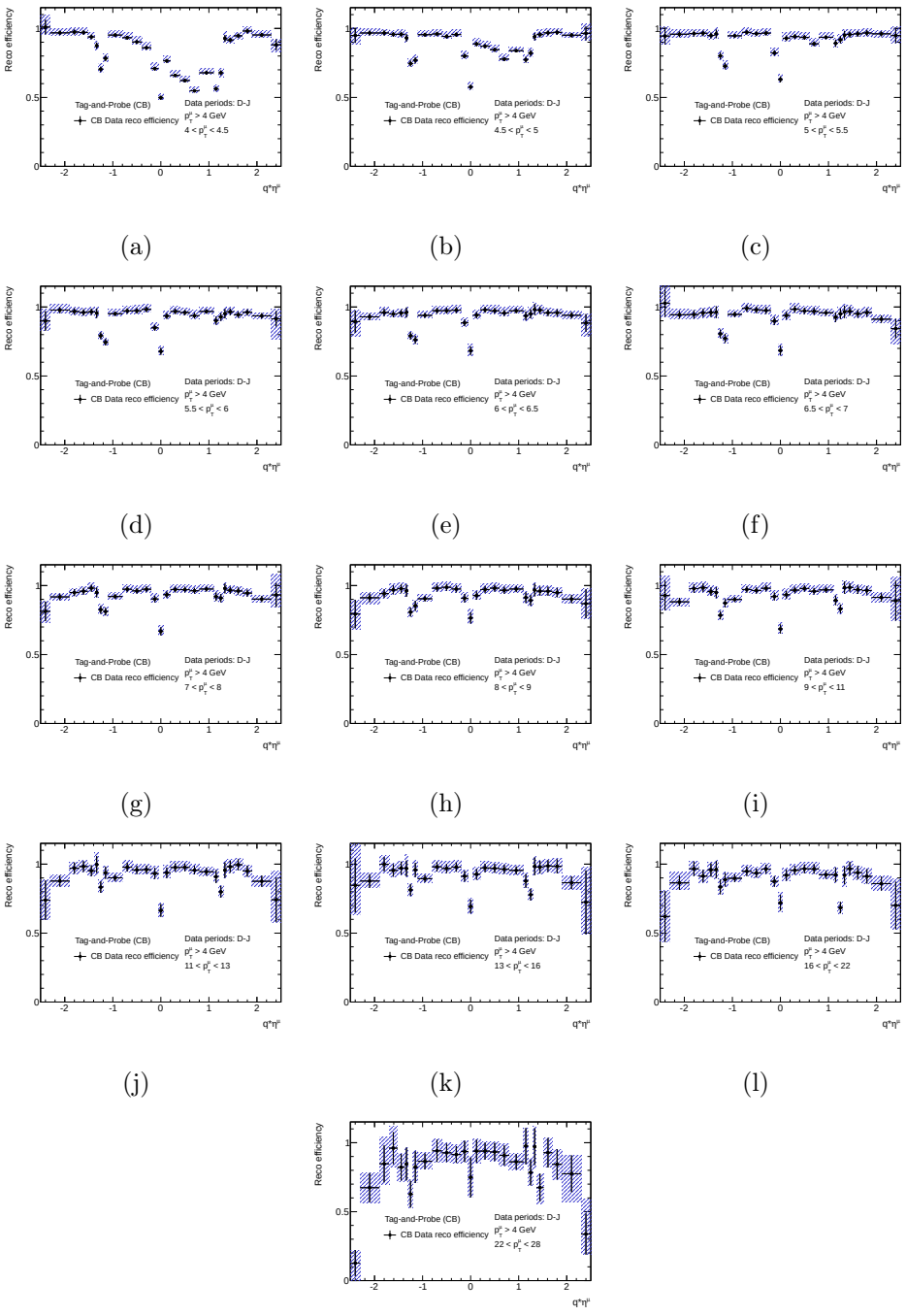

Figure A.1: The muon reconstruction efficiencies versus $q \times \eta$ in different p_T slices.

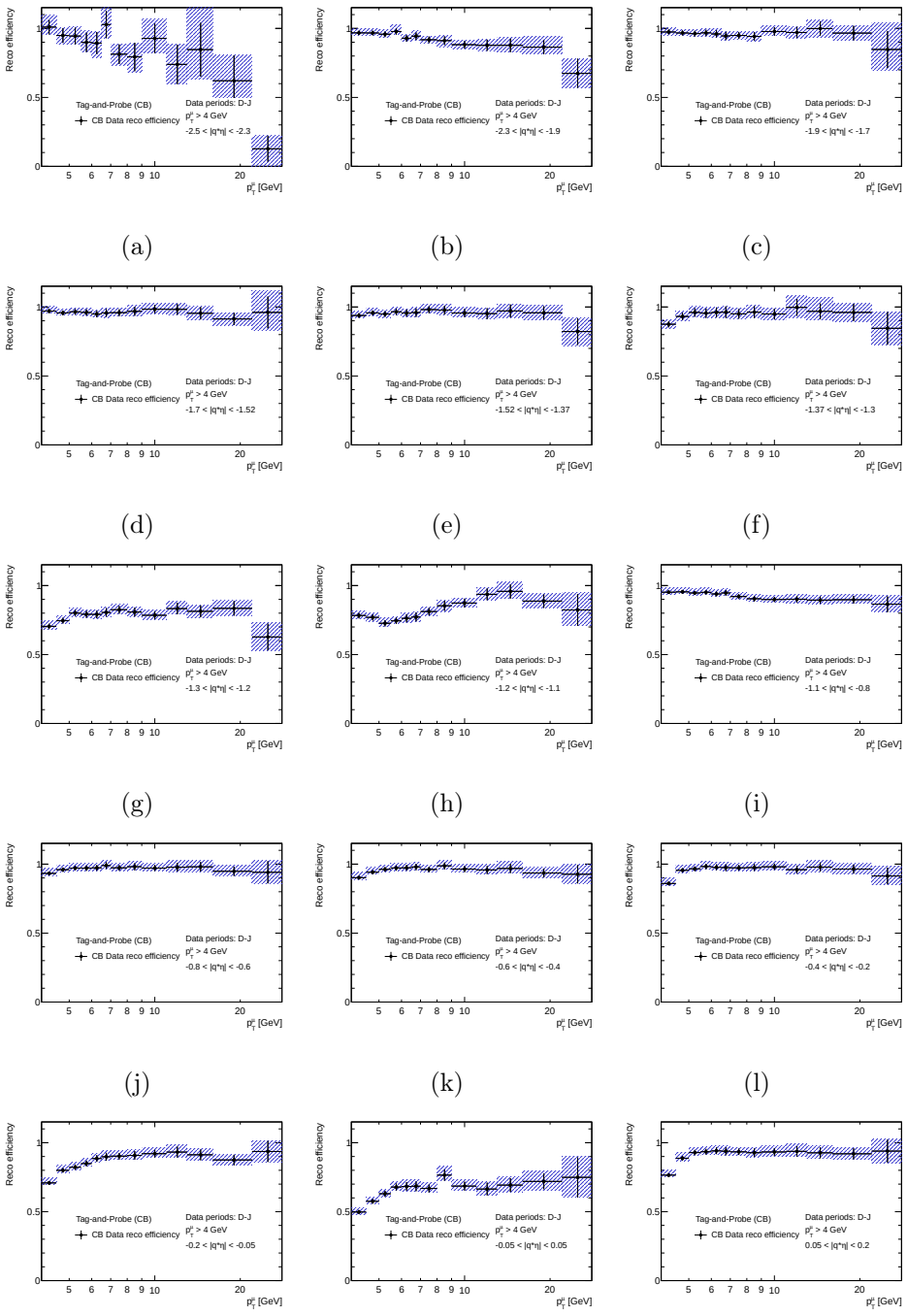

Figure A.2: The muon reconstruction efficiencies versus p_T in different $q \times \eta$ slices.

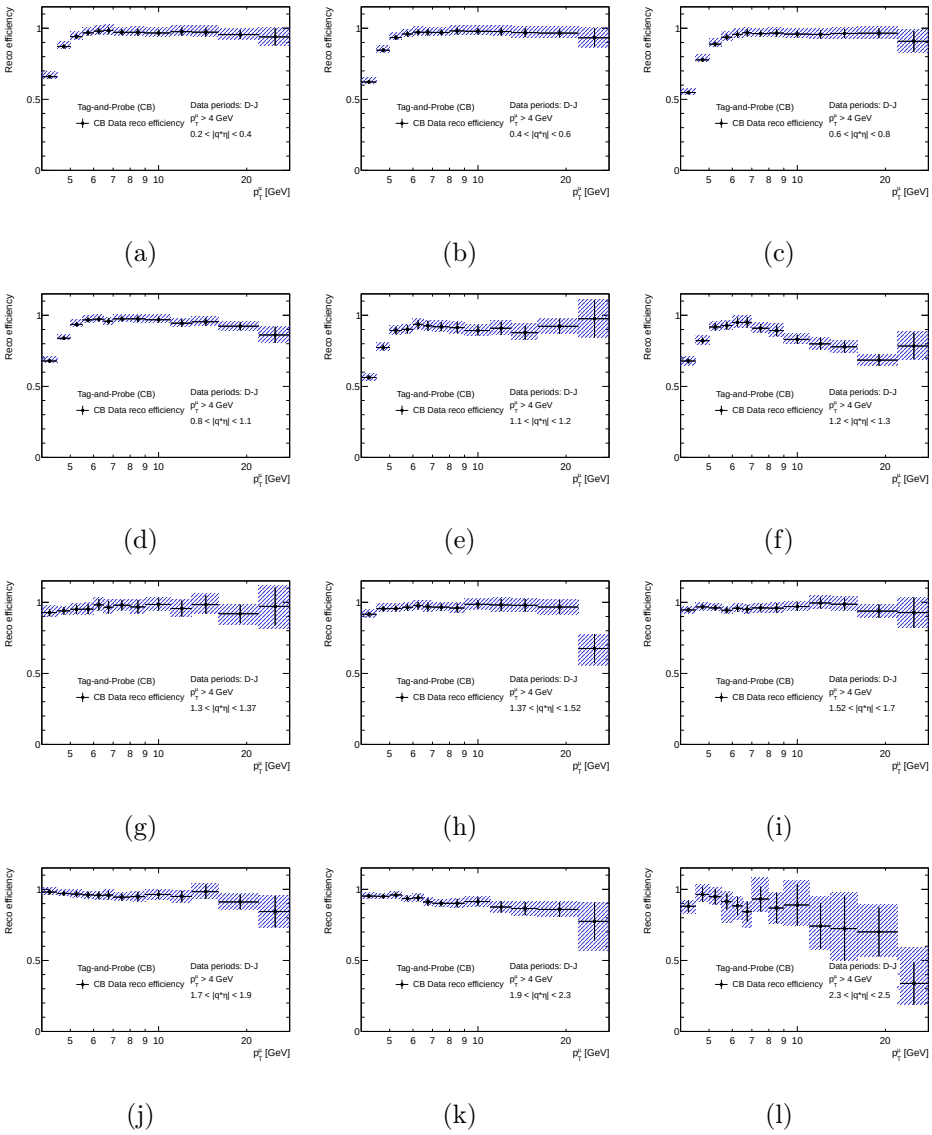

Figure A.3: The muon reconstruction efficiencies versus p_T in different $q \times \eta$ slices (continue).

Appendix B

B-Physics Trigger

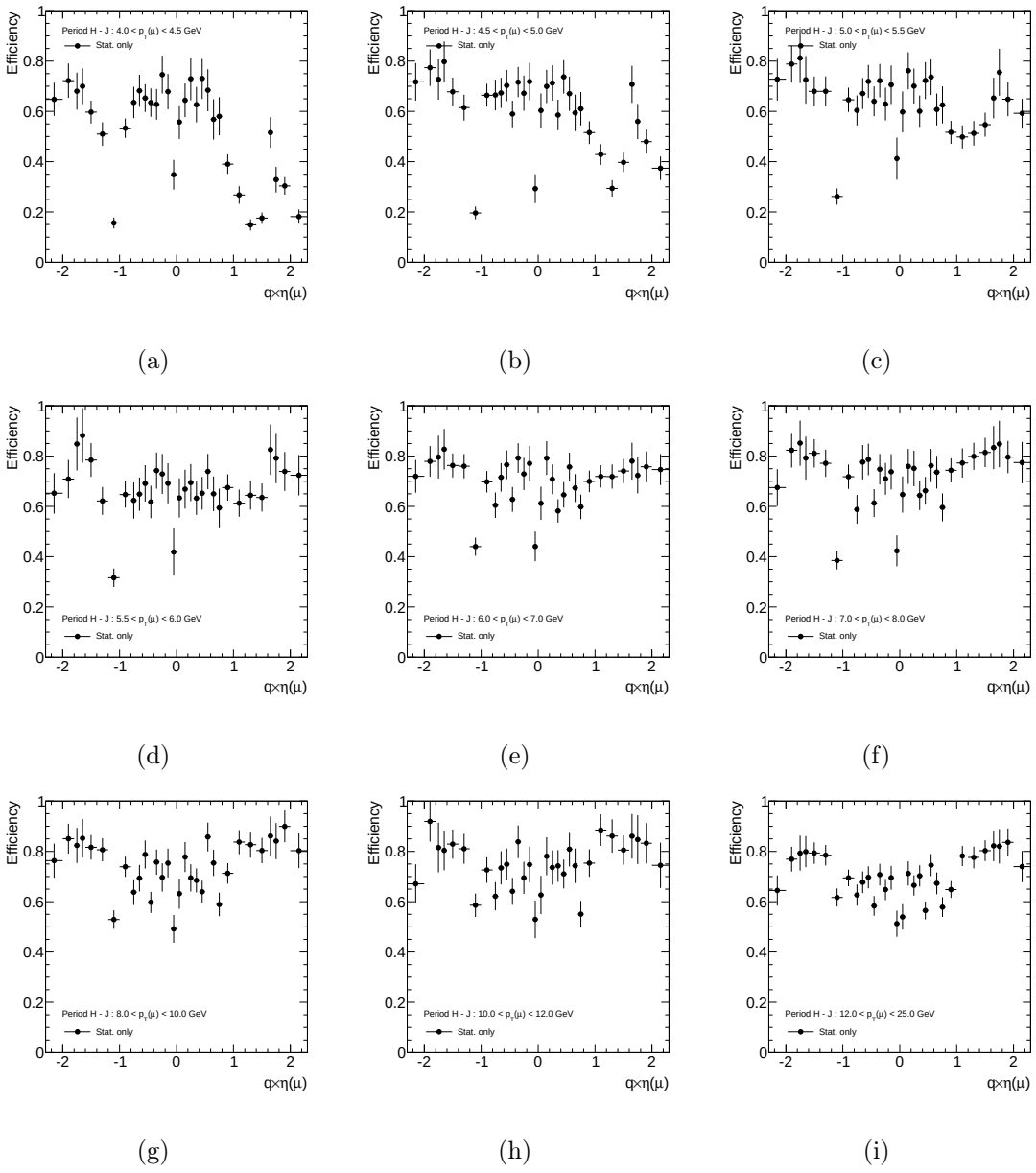

Figure B.1: The EF_mu4 efficiencies for period H - K4 in different p_T slices

Appendix C

Systematic Uncertainties

C.1 Muon Reconstruction

To avoid repetitiveness, we only show here the example of the systematic uncertainty for reconstruction efficiency for $\Upsilon(1S)$ versus p_T in central rapidity region in Fig. C.1.

C.2 Trigger Efficiency

An example of the systematic of trigger efficiency of EF_mu4 component for $\Upsilon(1S)$ versus p_T in central rapidity region is shown in Fig. C.2, and the $C_{\mu\mu}$ correction is shown in Fig. C.3.

C.3 Fit Model

Figures C.4 and C.5 show the fit model uncertainties for the fiducial cross-sections, and Figures C.6 and C.7 correspond to the inclusive cross-sections.

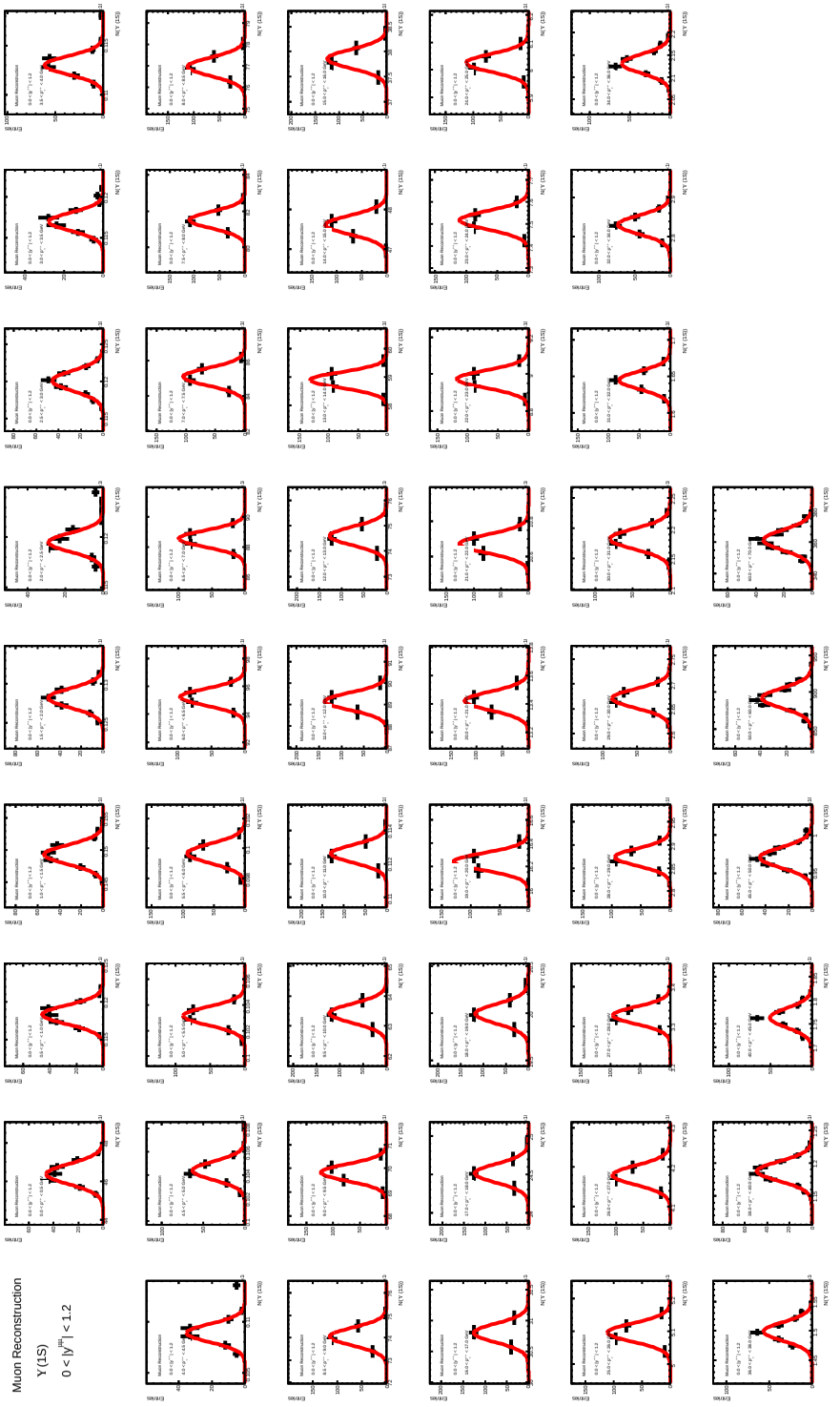

Figure C.1: The systematic uncertainty for reconstruction efficiency.

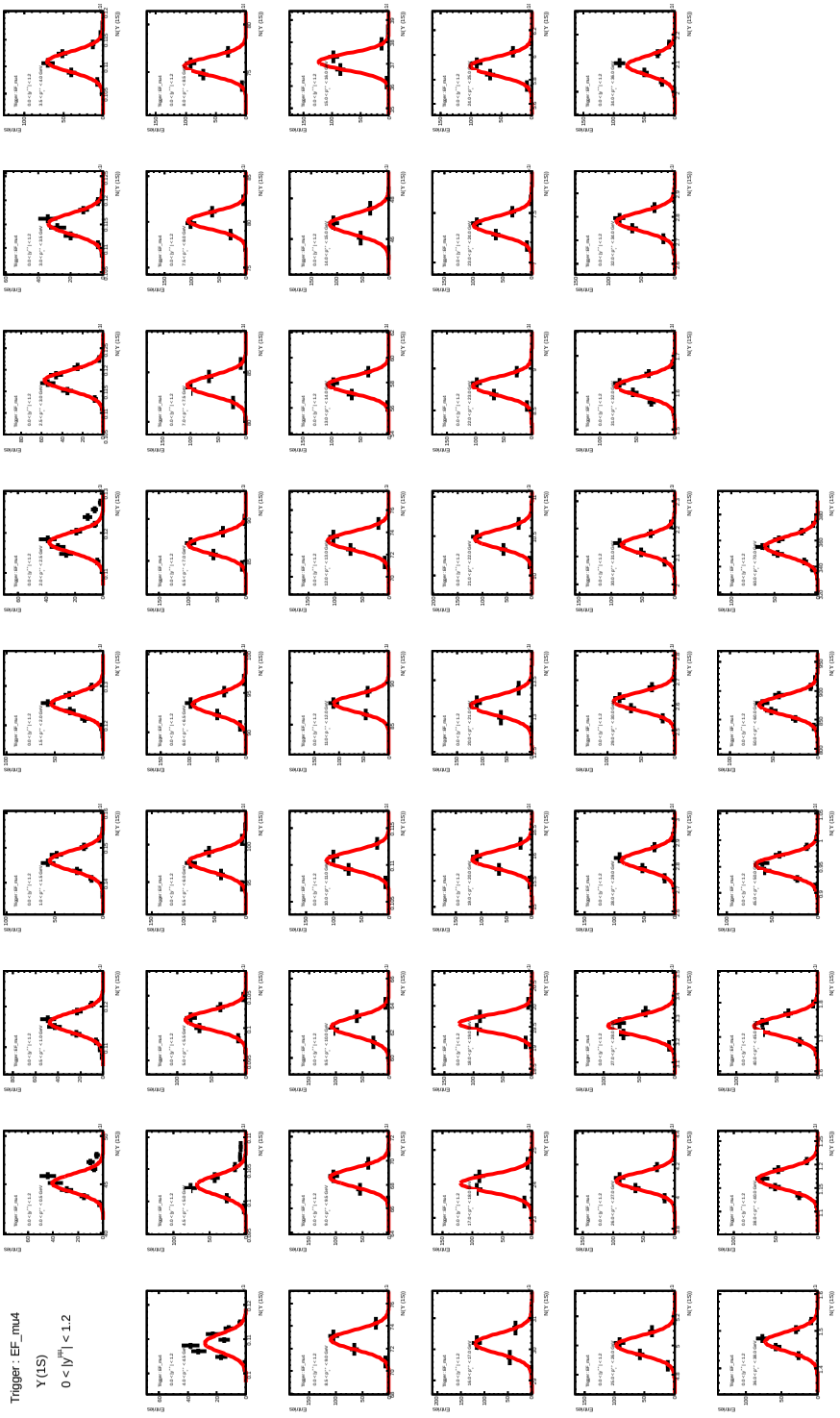

Figure C.2: The systematic of trigger efficiency of EF_mu4 component.

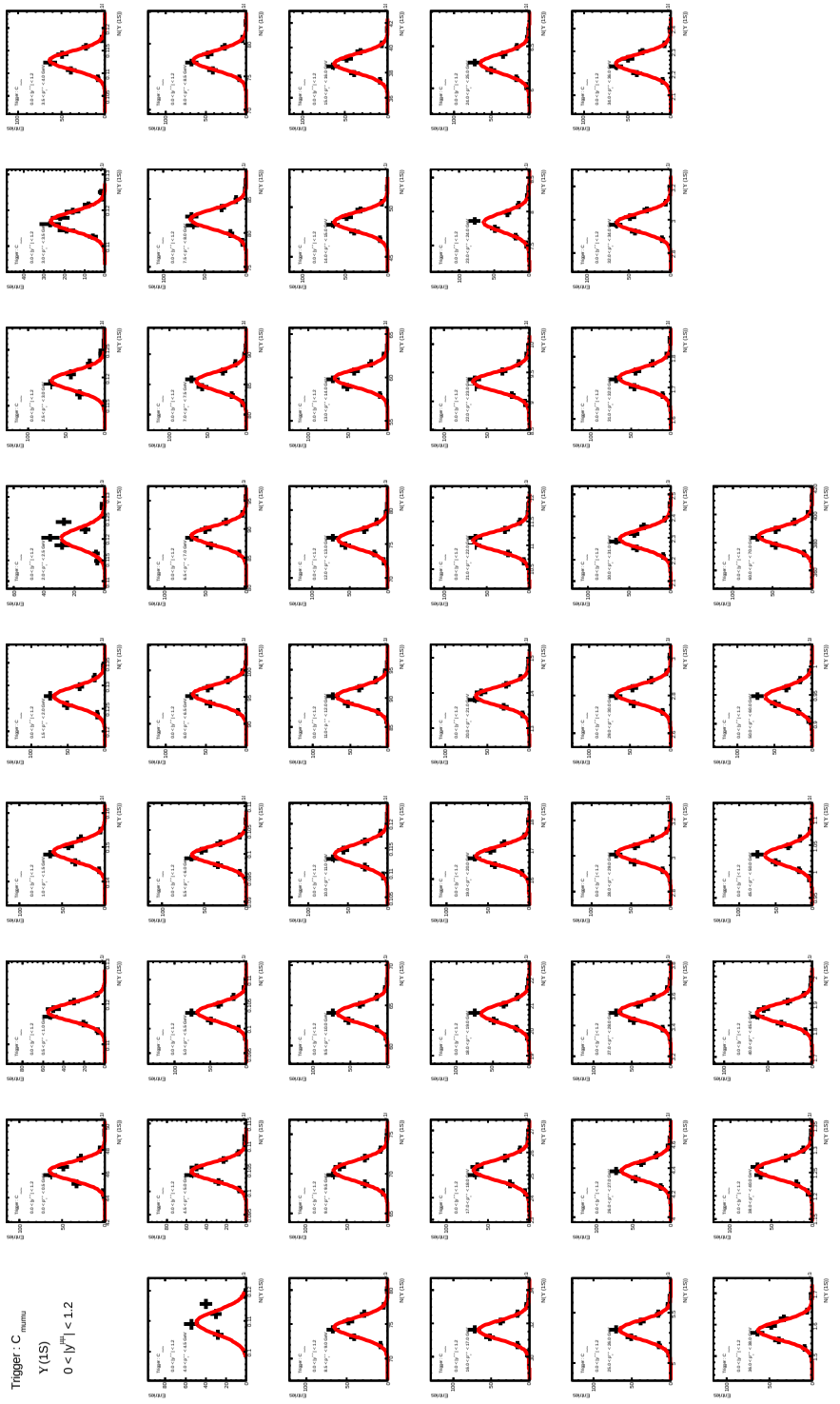

Figure C.3: The systematic of trigger efficiency of $C_{\mu\mu}$ correction.

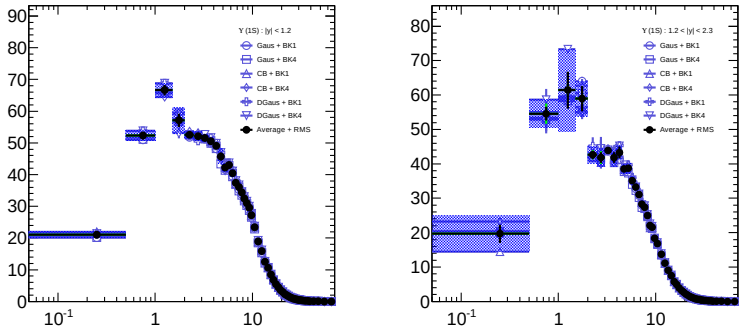

(a)

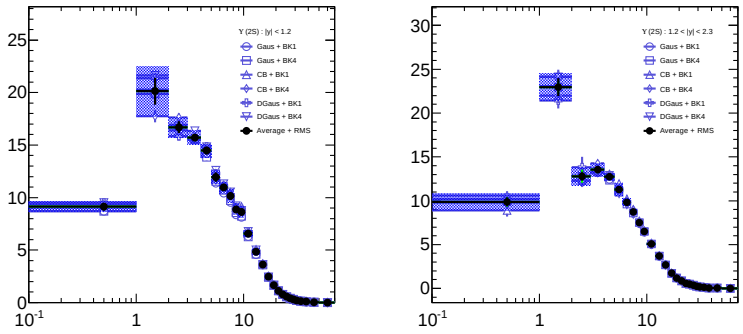

(b)

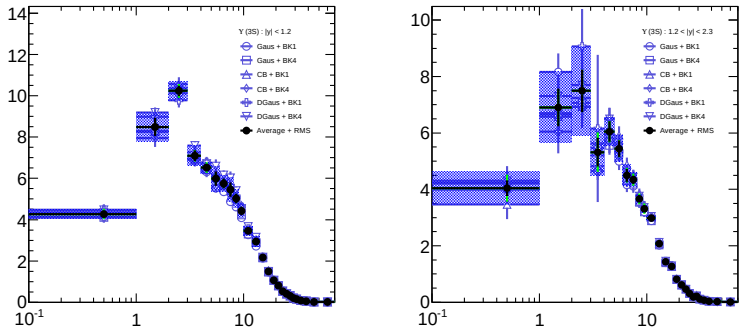

(c)

Figure C.4: The fit model systematic uncertainties for fiducial cross-sections versus p_T for (a) $\Upsilon(1S)$, (b) $\Upsilon(2S)$, and (c) $\Upsilon(3S)$.

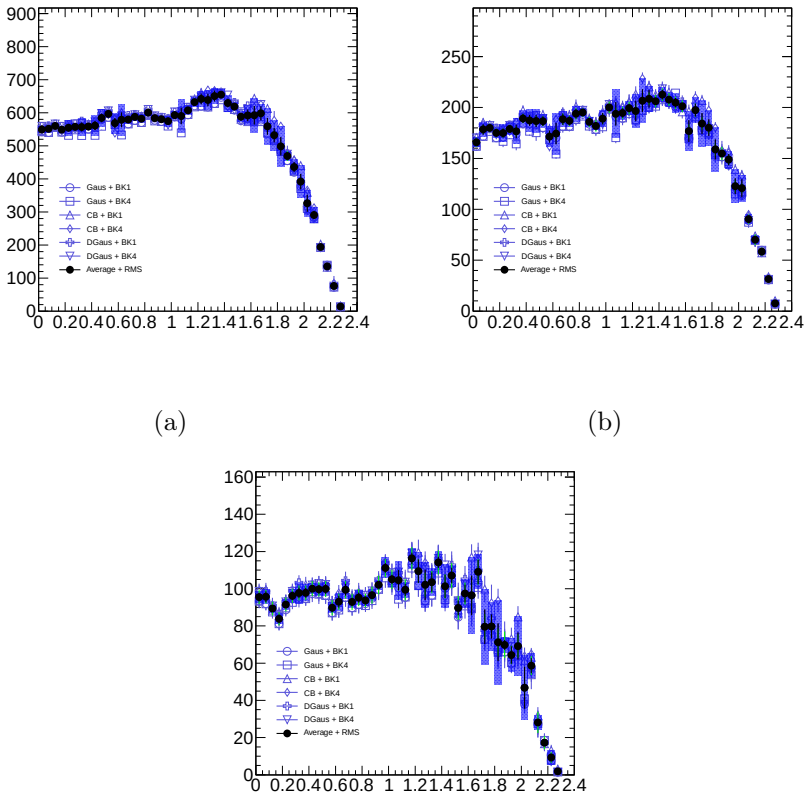

Figure C.5: The fit model systematic uncertainties for fiducial cross-sections versus y for (a) $\Upsilon(1S)$, (b) $\Upsilon(2S)$, and (c) $\Upsilon(3S)$.

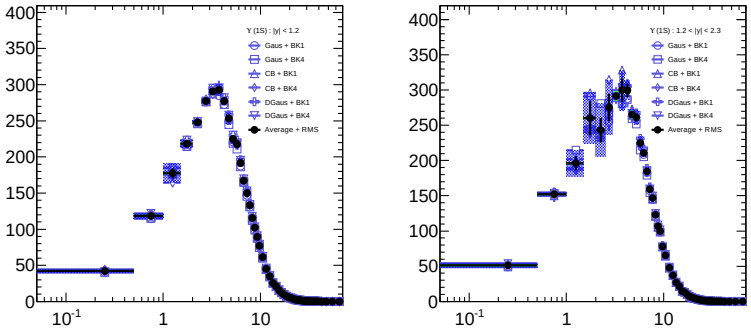

(a)

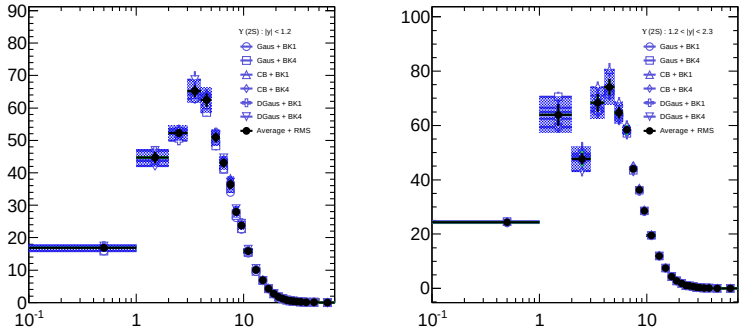

(b)

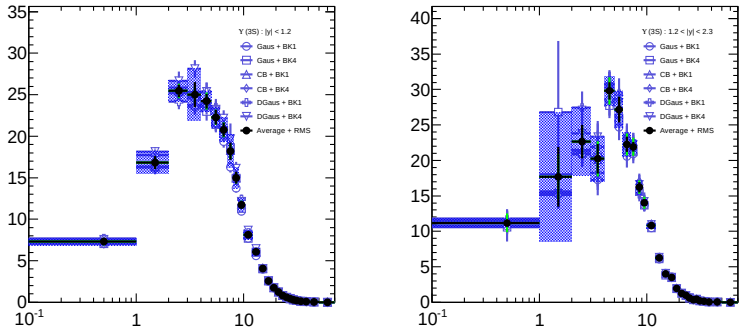

(c)

Figure C.6: The fit model systematic uncertainties for inclusive cross-sections versus p_T for (a) $\Upsilon(1S)$, (b) $\Upsilon(2S)$, and (c) $\Upsilon(3S)$.

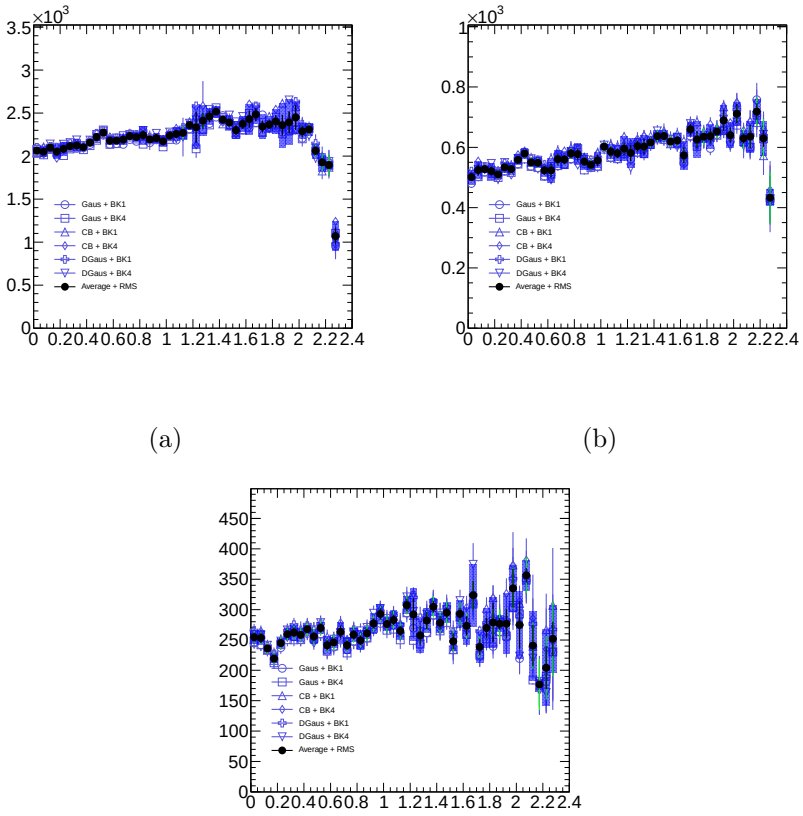

(a) (b)

(c)

Figure C.7: The fit model systematic uncertainties for inclusive cross-sections versus y for (a) $\Upsilon(1S)$, (b) $\Upsilon(2S)$, and (c) $\Upsilon(3S)$.

C.4 Bin Migration

A Monte Carlo study was performed by comparing the Υ p_T (or rapidity) in truth and in reconstructed levels. As shown in Fig. C.8, the overall correction is at the 1 – 2% level, but due to the limited statistics the error bars are large in the high-p_T region.

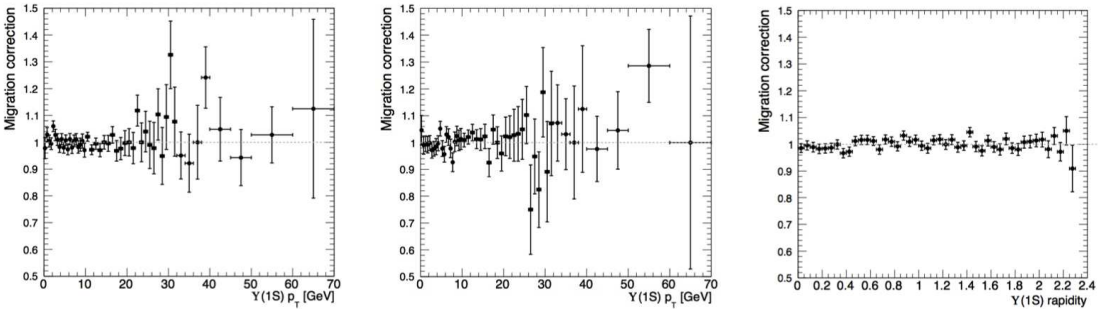

(a) (b) (c)

Figure C.8: Bin migration in MC versus p_T in (a) central rapidity (b) forward rapidity; and (c) versus rapidity.

The other approach is using the data-driven method (this is the same method which used in ATLAS J/ψ publication [50]). For example, the bin migration of p_T, first, use the relation between p_T resolution and mass resolution that is written in Eq. C.1 to build a functional form of p_T resolution versus p_T, see Fig. C.9(a).

$$\sigma_{p_T} = \frac{\sigma_M}{M} \cdot \sqrt{2} \cdot p_T, \tag{C.1}$$

Then, Using Hermite-quadrature numerical integration of this fitted function with the p_T resolution function at each p_T or rapidity bin obtains an unsmeared fit function. Then taking the ratio of the unsmeared fit function to the smeared function gives a

correction for the resolution effect Fig. C.9(b). The bin migration corrections from this data-driven method are shown in Fig. C.9. The results are similar as the MC study.

C.4.1 Dependence of acceptance corrections on vertex position

Acceptance corrections are derived assuming that Υ are produced at the centre of the detector: $(x, y, z) = (0, 0, 0)$. In the ATLAS detector the proton-proton collision does not perfectly occur at $(0, 0, 0)$ but instead is Gaussian distributed about this position with some characteristic resolution. Any variation from the central vertex can modify the acceptance, particularly near the edges of the fiducial volume since for a shifted interaction point the pseudorapidity in the collision frame is slightly modified to that in the detector frame. Typical beam spreads in 2011 data considered in this analysis are 0.05 mm in x and y, and 62 mm in z[1]. Vertex spreads in x, y are too small to impact the acceptance corrections.

The impact of a spread of ± 62 mm in z on acceptance corrections is considered by first (conservatively) assuming the spread in z is uniform across ± 62 mm instead of Gaussian. This maximal z spread is converted into a maximal shift in muon pseudorapidity. The shifts in pseudorapidity are ± 0.02 units at the edge of pseudorapidity acceptance. There is some (negligible) η-dependence to this η-variation, but the variation is greatest at high pseudorapidity so we use this variation across the full η region as a conservative estimate of the impact of the vertex spread.

New acceptance maps are built with an appropriate shift in the pseudorapidities of the muons, and the relative change in the acceptance corrections at fixed Υ rapidity between the nominal and shifted maps is calculated (see Figure C.10). A shift upward

[1] https://twiki.cern.ch/twiki/bin/view/AtlasPublic/OnlineBeamSpotPublicResults

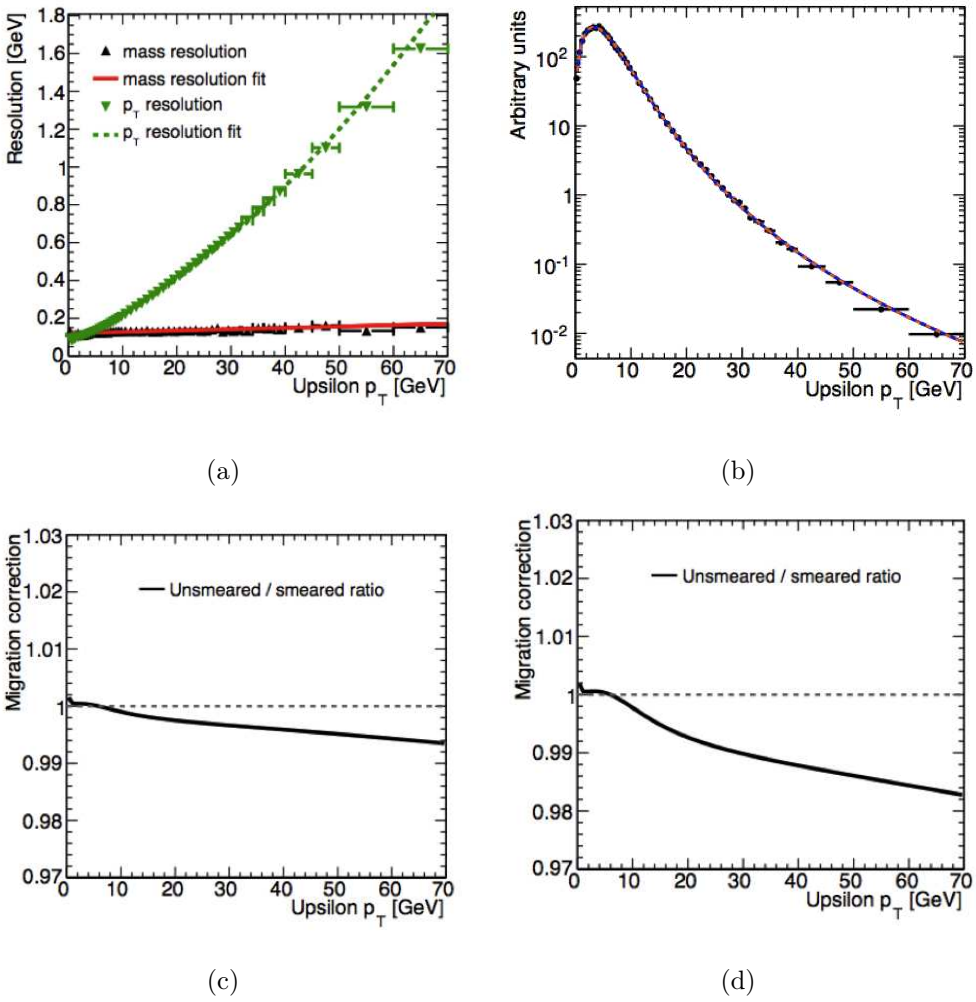

Figure C.9: (a) The data-driven p_T resolution, and (b) the smeared and unsmeared p_T distribution. Data-driven bin migration of p_T in (c) central rapidity and (d) forward rapidity.

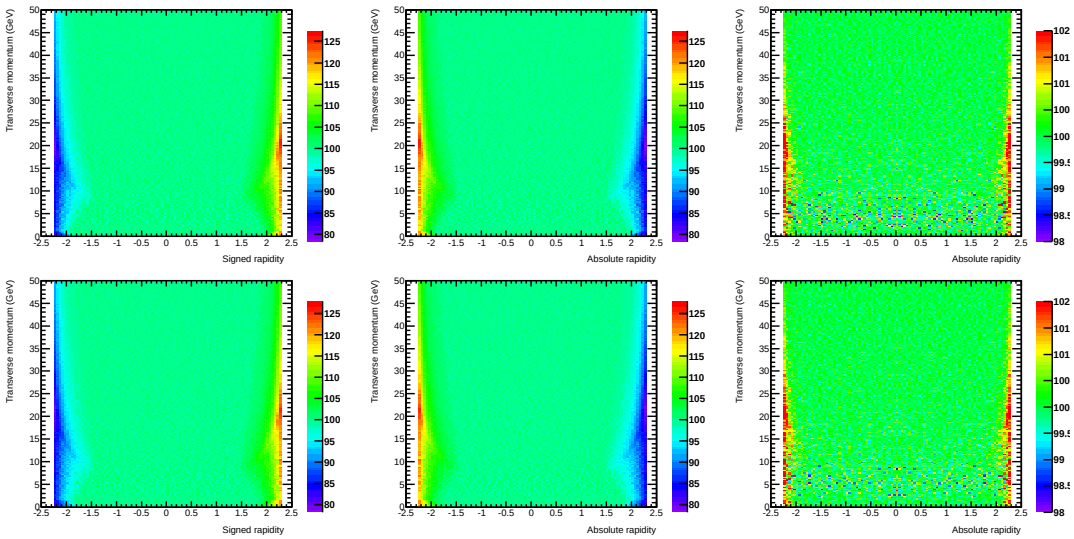

Figure C.10: **Top:** Impact of vertex z co-ordinate shift by ± 62 mm on acceptance corrections. *Left:* Relative change in acceptance due to negative z shift, *Middle:* Relative change in acceptance due to positive z shift, *Right:* Relative change in acceptance on *absolute* rapidity (symmetrised) due to positive and negative z shifts on $\Upsilon(1S)$ acceptance. **Bottom:** As for $\Upsilon(1S)$ (top) but for $\Upsilon(2S)$ No significant variation with invariant mass is seen in the acceptance uncertainty due to vertex z spread. A common uncertainty is used for each of the three Υ resonances.

to maximal z spread results in relative acceptance gains in positive rapidities of +5% across the bulk of the distribution, rising to as high as 20% at the very edge of acceptance near $y = +2.25$. Equivalently in negative rapidities, acceptance losses of -5% are observed, increasing to -20% near $y = -2.25$. As all results considered in this paper only consider absolute Υ rapidities, we are not sensitive to gains or losses in signed rapidity but only in the resultant overall gain or loss at a given $|y|$ value. To determine this, the negative rapidity shifts are averaged with positive rapidity shifts (given symmetric dimuon production across rapidity) to arrive at a relative uncertainty on the acceptance correction. This is shown in Figure C.10. Across the bulk of the phase space, uncertainties due to vertex z position are below 0.7%, rising to near $\pm 2\%$ at very large rapidity $y \sim 2.25$. This uncertainty is propagated to the final results on a candidate-by-candidate basis. The direct influence on the weights in the analysis bins can be seen in Figure C.11. No dependence of this uncertainty on invariant mass was observed outside of the statistical fluctuations on the corrections, so a common relative uncertainty is used for all three Υ resonances.

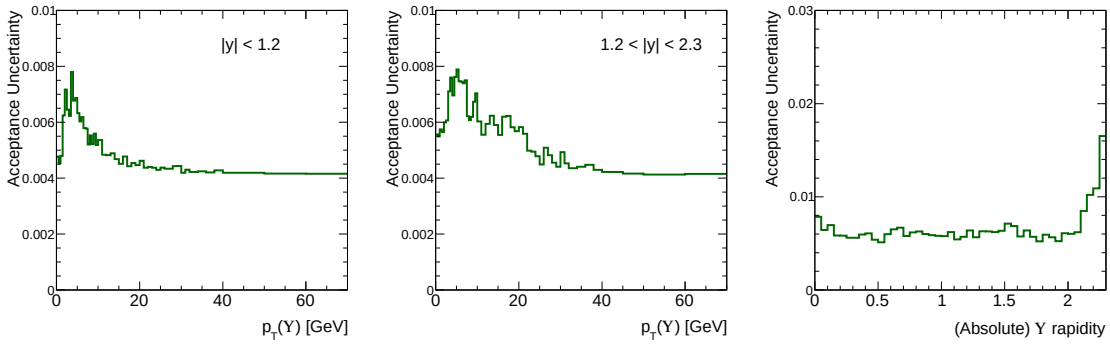

Figure C.11: Fractional impact of vertex z co-ordinate shift by ± 62 mm on measured cross-section added in quadrature with statistical uncertainties ($\sim$0.5%) on the maps, as a function of p_T for (left) central rapidities and (middle) forward rapidities, and also as a function of absolute rapidity (right).

Appendix D

Acceptance Maps for $\Upsilon(2S)$ and $\Upsilon(3S)$

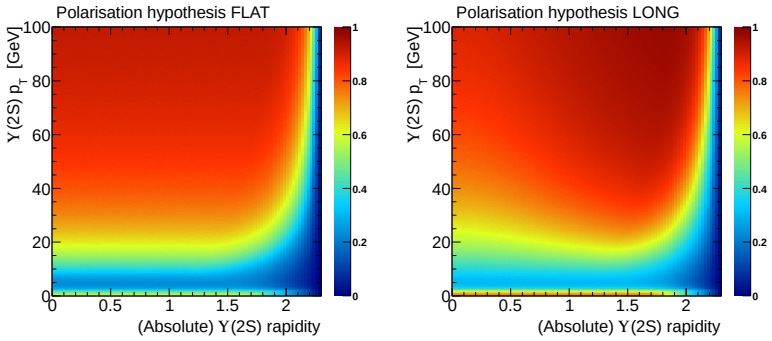

(a)

(b)

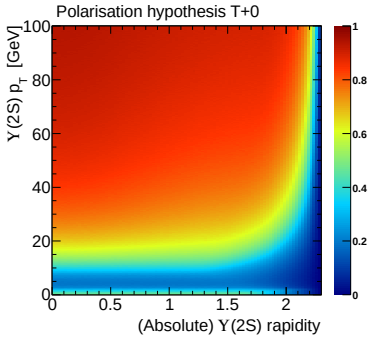

(c)

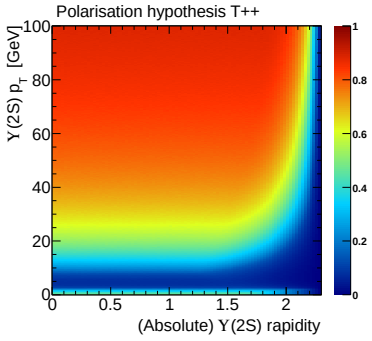

(d)

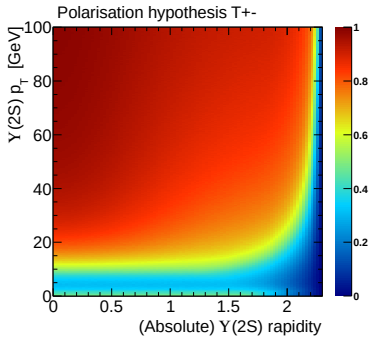

(e)

Figure D.1: The acceptance maps $\mathcal{A}$ for $\Upsilon(2S)$ with the polarization assumptions of (a) FLAT; (b) LONG; (c) T_{+0}; (d) T_{++}; and (e) T_{+-}.

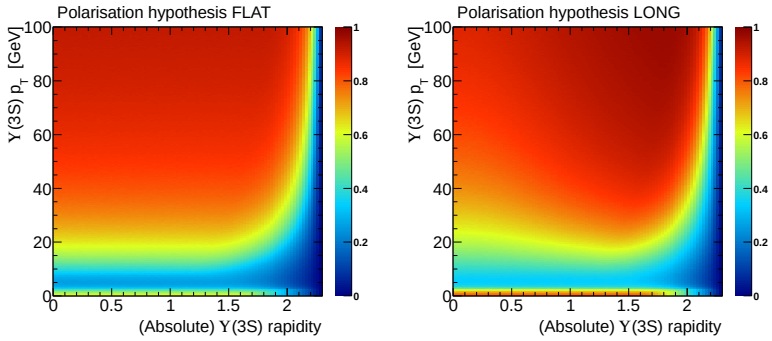

(a)

(b)

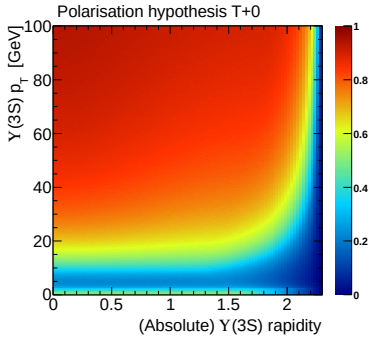

(c)

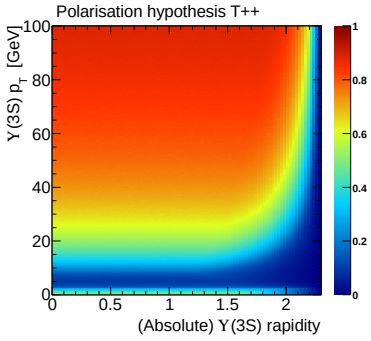

(d)

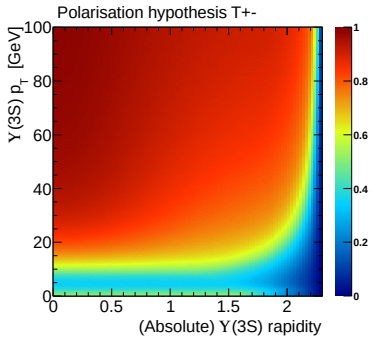

(e)

Figure D.2: The acceptance maps $\mathcal{A}$ for $\Upsilon(3S)$ with the polarization assumptions of (a) FLAT; (b) LONG; (c) T_{+0}; (d) T_{++}; and (e) T_{+-}.

Appendix E

ϒ Cross-sections

E.1 Fiducial Cross-sections

E.1.1 Comparisons to previous results

Figure E.1 shows the comparison to previous ATLAS results [99] (red points), and the green point is the average over the first four bins in our measurement.

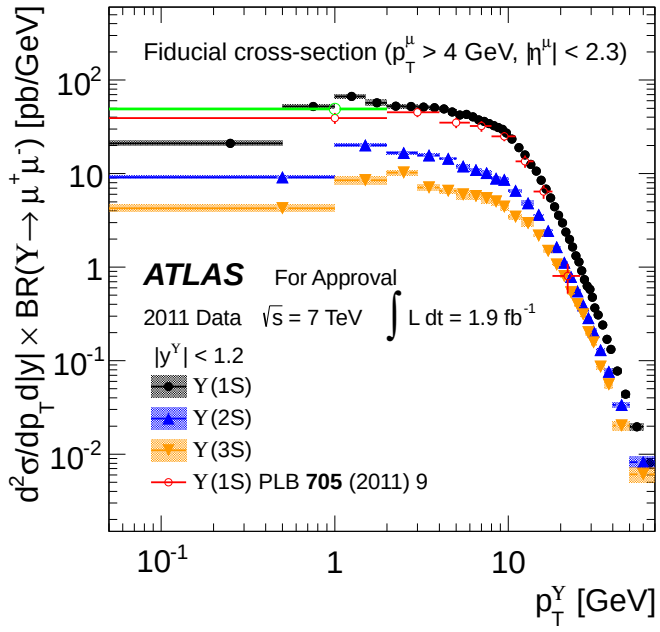

(a)

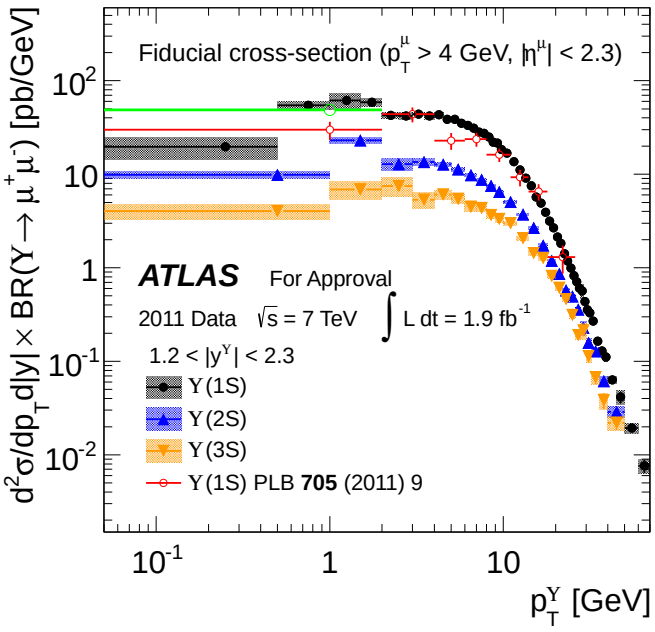

(b)

Figure E.1: Fiducial cross-section versus $p_T^{\Upsilon(1S)}$ for (a) $|y^\Upsilon| < 1.2$ and (b) $1.2 < |y^\Upsilon| < 2.3$.

E.1.2 Tables for cross-section versus p_T

Table E.1: The $\Upsilon(1S)$ fiducial cross-section.

$p_T^{\Upsilon(1S)}$ (GeV)	$d^2\sigma/dp_T dy$ (pb)	$\delta_{stat.}$ (%)	$\delta_{sys.}$ (%)	δ_{total} (%)	$d^2\sigma/dp_T dy$ (pb)	$\delta_{stat.}$ (%)	$\delta_{sys.}$ (%)	δ_{total} (%)
	$\|y\| < 1.2$				$1.2 < \|y\| < 2.3$			
0.00 - 0.50	21.11	2.77	5.36	6.03	19.68	4.66	27.17	27.57
0.50 - 1.00	52.33	1.46	4.20	4.45	54.61	5.35	8.33	9.90
1.00 - 1.50	66.69	1.39	4.39	4.61	61.45	2.91	19.75	19.96
1.50 - 2.00	57.19	1.62	7.47	7.64	58.99	2.71	9.26	9.65
2.00 - 2.50	52.57	1.56	3.71	4.02	42.67	3.09	6.91	7.57
2.50 - 3.00	52.12	1.29	3.80	4.02	41.85	4.37	7.86	9.00
3.00 - 3.50	51.61	1.50	3.78	4.07	43.91	1.98	3.14	3.71
3.50 - 4.00	50.60	1.12	3.42	3.60	41.84	1.54	6.98	7.15
4.00 - 4.50	49.10	1.29	4.69	4.87	43.34	2.34	5.89	6.34
4.50 - 5.00	45.76	1.27	5.89	6.03	38.53	1.82	4.55	4.90
5.00 - 5.50	42.29	1.52	3.86	4.15	38.72	1.69	4.32	4.64
5.50 - 6.00	42.98	1.56	3.63	3.95	35.11	1.60	4.09	4.39
6.00 - 6.50	40.40	1.36	3.57	3.83	33.22	1.65	3.79	4.13
6.50 - 7.00	37.40	1.36	2.90	3.20	31.04	1.62	3.62	3.96
7.00 - 7.50	36.06	1.59	4.24	4.53	28.22	1.52	4.20	4.46
7.50 - 8.00	34.32	1.99	3.35	3.89	27.32	1.52	2.96	3.33
8.00 - 8.50	32.48	1.68	3.52	3.90	24.93	1.59	2.68	3.12
8.50 - 9.00	31.00	1.73	3.36	3.77	22.04	1.63	3.65	4.00
9.00 - 9.50	29.57	1.53	4.38	4.64	21.48	1.70	2.70	3.19
9.50 - 10.00	27.15	1.34	4.20	4.40	18.27	1.91	2.24	2.94
10.00 - 11.00	23.33	1.36	3.32	3.59	16.75	1.26	2.75	3.02
11.00 - 12.00	18.83	1.17	3.03	3.25	13.62	1.32	2.53	2.85
12.00 - 13.00	15.80	1.27	4.08	4.27	11.09	1.26	2.70	2.97
13.00 - 14.00	12.47	1.65	4.82	5.09	9.02	1.49	2.49	2.90
14.00 - 15.00	10.59	1.08	2.45	2.68	7.51	1.62	2.65	3.10
15.00 - 16.00	8.46	1.16	2.54	2.79	5.69	1.84	2.63	3.20
16.00 - 17.00	6.82	1.29	2.71	3.00	4.87	2.12	2.75	3.46
17.00 - 18.00	5.49	1.46	2.38	2.79	3.91	2.22	2.40	3.26
18.00 - 19.00	4.40	1.63	2.14	2.69	3.14	2.34	2.22	3.21
19.00 - 20.00	3.57	1.68	2.40	2.93	2.65	2.46	3.81	4.53
20.00 - 21.00	2.95	1.77	2.30	2.90	2.12	2.58	3.43	4.28
21.00 - 22.00	2.35	2.02	2.28	3.04	1.81	2.85	2.29	3.63
22.00 - 23.00	1.96	1.87	2.37	3.02	1.40	3.17	2.19	3.83
23.00 - 24.00	1.64	2.47	2.47	3.48	1.17	3.03	2.45	3.88
24.00 - 25.00	1.32	2.76	2.67	3.83	0.98	3.91	2.83	4.80
25.00 - 26.00	1.13	3.03	2.45	3.89	0.82	4.56	2.52	5.17
26.00 - 27.00	0.91	3.37	2.66	4.28	0.70	4.42	2.67	5.13
27.00 - 28.00	0.73	3.71	2.58	4.50	0.60	5.19	4.02	6.52
28.00 - 29.00	0.63	3.95	2.99	4.93	0.56	5.59	15.88	16.81
29.00 - 30.00	0.58	4.09	2.61	4.83	0.43	6.63	2.96	7.20
30.00 - 31.00	0.47	4.63	3.15	5.57	0.35	7.38	3.25	7.99
31.00 - 32.00	0.36	5.32	2.51	5.85	0.33	7.51	3.73	8.31
32.00 - 34.00	0.31	4.00	2.53	4.71	0.27	7.32	3.37	7.98

Continued on next page

Table E.1: The $\Upsilon(1S)$ fiducial cross-section.

$p_T^{\Upsilon(1S)}$ (GeV)	$d^2\sigma/dp_T dy$ (pb)	$\delta_{stat.}$ (%)	$\delta_{sys.}$ (%)	δ_{total} (%)	$d^2\sigma/dp_T dy$ (pb)	$\delta_{stat.}$ (%)	$\delta_{sys.}$ (%)	δ_{total} (%)
	$\|y\| < 1.2$				$1.2 < \|y\| < 2.3$			
34.00 - 36.00	0.24	4.82	2.76	5.53	0.16	7.30	3.32	7.94
36.00 - 38.00	0.17	5.58	2.98	6.28	0.13	8.70	3.80	9.40
38.00 - 40.00	0.13	6.27	2.79	6.81	0.11	9.89	6.17	11.54
40.00 - 45.00	0.08	5.47	3.04	6.22	0.06	7.89	3.88	8.69
45.00 - 50.00	0.04	7.10	4.62	8.41	0.04	14.27	8.04	16.19
50.00 - 60.00	0.02	7.64	3.04	8.14	0.02	11.12	4.94	11.99
60.00 - 70.00	0.01	12.31	3.98	12.78	0.01	16.14	8.05	17.75

Table E.2: The $\Upsilon(2S)$ fiducial cross-section.

$p_T^{\Upsilon(2S)}$ (GeV)	$d^2\sigma/dp_T dy$ (pb)	$\delta_{stat.}$ (%)	$\delta_{sys.}$ (%)	δ_{total} (%)	$d^2\sigma/dp_T dy$ (pb)	$\delta_{stat.}$ (%)	$\delta_{sys.}$ (%)	δ_{total} (%)
	$\|y\| < 1.2$				$1.2 < \|y\| < 2.3$			
0.00 - 1.00	9.14	3.25	5.73	6.59	9.87	5.38	10.85	12.11
1.00 - 2.00	20.15	2.24	12.02	12.22	22.97	3.09	7.44	8.06
2.00 - 3.00	16.71	2.27	6.09	6.50	12.81	5.43	9.19	10.67
3.00 - 4.00	15.73	2.01	4.52	4.95	13.55	2.68	6.37	6.92
4.00 - 5.00	14.49	2.09	4.51	4.97	12.74	2.87	4.58	5.41
5.00 - 6.00	11.96	2.74	5.64	6.27	11.28	2.63	6.33	6.86
6.00 - 7.00	10.96	2.34	5.02	5.53	9.81	2.64	4.64	5.34
7.00 - 8.00	10.15	2.99	6.22	6.90	8.72	2.54	3.68	4.47
8.00 - 9.00	8.87	2.96	6.07	6.76	7.51	2.58	2.94	3.91
9.00 - 10.00	8.62	2.66	5.89	6.46	6.48	2.75	2.24	3.55
10.00 - 12.00	6.54	1.98	4.57	4.98	5.06	2.03	2.25	3.02
12.00 - 14.00	4.82	2.01	5.61	5.96	3.69	2.12	1.97	2.89
14.00 - 16.00	3.62	1.51	1.98	2.49	2.67	2.37	1.81	2.98
16.00 - 18.00	2.44	1.79	2.15	2.79	1.72	3.09	1.59	3.46
18.00 - 20.00	1.64	2.12	1.23	2.44	1.18	3.71	2.31	4.35
20.00 - 22.00	1.12	2.50	1.40	2.85	0.85	4.20	2.04	4.64
22.00 - 24.00	0.78	2.72	1.41	3.05	0.57	4.78	2.04	5.16
24.00 - 26.00	0.55	3.52	1.81	3.94	0.49	5.61	2.15	5.96
26.00 - 28.00	0.39	4.38	3.00	5.29	0.36	6.23	2.43	6.63
28.00 - 30.00	0.28	4.89	3.23	5.83	0.23	9.89	3.32	10.34
30.00 - 32.00	0.20	5.94	2.89	6.57	0.16	11.17	3.37	11.54
32.00 - 36.00	0.13	5.26	1.70	5.49	0.13	8.75	2.99	9.15
36.00 - 40.00	0.08	6.98	2.68	7.42	0.06	12.00	4.25	12.58
40.00 - 50.00	0.03	7.02	2.62	7.43	0.03	12.39	4.25	12.92
50.00 - 70.00	0.01	9.78	10.12	14.02	0.00	279.77	376.46	466.58

Table E.3: The $\Upsilon(3S)$ fiducial cross-section.

$p_T^{\Upsilon(3S)}$ (GeV)	$d^2\sigma/dp_T dy$ (pb)	$\delta_{stat.}$ (%)	$\delta_{sys.}$ (%)	δ_{total} (%)	$d^2\sigma/dp_T dy$ (pb)	$\delta_{stat.}$ (%)	$\delta_{sys.}$ (%)	δ_{total} (%)
	$\|y\| < 1.2$				$1.2 < \|y\| < 2.3$			
0.00 - 1.00	4.28	5.82	5.63	8.10	4.04	11.75	15.08	19.12
1.00 - 2.00	8.50	4.10	8.49	9.43	6.91	9.15	19.43	21.48
2.00 - 3.00	10.24	3.20	5.03	5.96	7.49	9.60	21.31	23.37
3.00 - 4.00	7.10	3.68	7.20	8.08	5.32	11.89	16.25	20.14
4.00 - 5.00	6.52	3.96	4.52	6.01	6.05	6.22	9.12	11.04
5.00 - 6.00	5.99	4.60	10.13	11.12	5.45	5.56	9.02	10.60
6.00 - 7.00	5.75	3.88	7.25	8.22	4.50	5.66	8.57	10.27
7.00 - 8.00	5.45	4.54	10.92	11.83	4.34	4.97	5.94	7.75
8.00 - 9.00	5.02	4.39	8.42	9.50	3.67	5.20	4.74	7.04
9.00 - 10.00	4.42	4.05	7.64	8.65	3.31	5.36	4.12	6.76
10.00 - 12.00	3.45	3.18	6.05	6.83	2.98	3.50	3.79	5.15
12.00 - 14.00	2.94	2.90	8.03	8.54	2.07	3.58	3.22	4.81
14.00 - 16.00	2.16	2.32	2.20	3.20	1.43	4.35	3.33	5.46
16.00 - 18.00	1.48	2.69	2.09	3.40	1.27	4.34	3.00	5.26
18.00 - 20.00	1.06	3.05	1.34	3.32	0.81	5.25	2.81	5.92
20.00 - 22.00	0.79	3.26	1.42	3.54	0.60	5.56	3.42	6.49
22.00 - 24.00	0.53	3.74	1.56	4.03	0.46	5.75	2.05	6.06
24.00 - 26.00	0.40	4.59	1.81	4.91	0.31	8.37	2.91	8.79
26.00 - 28.00	0.31	5.38	2.20	5.78	0.19	10.65	3.90	11.24
28.00 - 30.00	0.20	6.50	2.44	6.91	0.21	10.40	16.30	19.27
30.00 - 32.00	0.16	7.67	2.36	7.98	0.11	14.50	3.48	14.74
32.00 - 36.00	0.09	7.48	2.21	7.74	0.07	15.49	4.02	15.80
36.00 - 40.00	0.06	9.20	2.55	9.47	0.04	19.23	6.55	20.05
40.00 - 50.00	0.02	11.11	3.44	11.52	0.02	16.04	6.51	17.05
50.00 - 70.00	0.01	12.78	13.14	18.25	0.01	14.42	14.37	20.18

E.1.3 Tables for cross-section versus rapidity

Table E.4: The $\Upsilon(nS)$ fiducial cross-section versus rapidity.

y^{Υ}	$d\sigma/dy$ (pb)	$\delta_{stat.}$ (%)	$\delta_{sys.}$ (%)	δ_{total} (%)	$d\sigma/dy$ (pb)	$\delta_{stat.}$ (%)	$\delta_{sys.}$ (%)	δ_{total} (%)	$d\sigma/dy$ (pb)	$\delta_{stat.}$ (%)	$\delta_{sys.}$ (%)	δ_{total} (%)
	$\Upsilon(1S)$				$\Upsilon(2S)$				$\Upsilon(3S)$			
0.00 - 0.05	549.23	1.07	3.09	3.27	165.86	2.59	3.62	4.45	95.50	3.97	4.02	5.65
0.05 - 0.10	551.64	1.06	3.19	3.36	178.48	2.36	4.55	5.12	95.69	3.80	4.67	6.02
0.10 - 0.15	560.42	1.03	2.59	2.79	179.96	2.31	2.91	3.72	89.36	4.08	3.11	5.13
0.15 - 0.20	549.16	1.05	3.27	3.43	175.10	2.40	3.69	4.40	83.85	4.35	4.21	6.06
0.20 - 0.25	554.61	1.12	4.78	4.91	174.88	2.50	5.31	5.87	91.53	4.09	3.89	5.64
0.25 - 0.30	557.36	0.99	2.97	3.13	178.99	2.29	4.13	4.73	96.18	3.88	4.40	5.86
0.30 - 0.35	557.25	1.15	5.17	5.30	176.57	2.67	7.37	7.84	97.74	4.10	6.16	7.40
0.35 - 0.40	558.82	1.13	3.20	3.40	189.28	2.40	4.74	5.31	97.83	3.99	5.42	6.73
0.40 - 0.45	561.27	1.09	5.76	5.87	187.36	2.44	6.28	6.74	100.02	4.04	3.47	5.33
0.45 - 0.50	584.39	1.09	4.86	4.98	186.78	2.51	6.66	7.12	99.67	3.89	3.99	5.57
0.50 - 0.55	596.55	1.12	2.94	3.14	186.52	2.56	4.18	4.90	99.87	4.23	4.19	5.96
0.55 - 0.60	568.92	1.18	5.76	5.88	171.39	2.77	6.22	6.81	89.81	4.65	4.07	6.18
0.60 - 0.65	578.81	1.18	8.25	8.33	174.38	2.82	11.71	12.05	93.04	4.74	5.59	7.33
0.65 - 0.70	579.78	1.32	3.23	3.49	188.51	2.87	4.43	5.27	99.46	4.64	5.41	7.12
0.70 - 0.75	587.79	1.28	2.87	3.14	186.87	2.65	3.72	4.57	92.97	4.65	4.21	6.27
0.75 - 0.80	582.15	1.36	3.05	3.34	193.86	2.81	4.38	5.20	95.24	4.88	4.65	6.73
0.80 - 0.85	600.43	1.00	2.76	2.94	195.09	2.08	2.85	3.53	93.66	3.89	3.65	5.34
0.85 - 0.90	583.80	1.32	2.77	3.06	185.84	2.70	3.37	4.32	96.55	4.73	3.88	6.12
0.90 - 0.95	580.80	1.45	2.75	3.11	181.88	3.07	3.28	4.50	102.07	4.92	3.52	6.05
0.95 - 1.00	574.88	1.41	3.46	3.74	188.98	2.84	4.92	5.68	111.16	4.42	5.27	6.88
1.00 - 1.05	592.86	1.48	3.68	3.96	200.07	2.84	3.79	4.74	105.01	5.00	5.01	7.08
1.05 - 1.10	590.38	1.51	9.24	9.36	193.80	3.11	12.58	12.95	104.58	5.28	10.32	11.59
1.10 - 1.15	607.33	1.45	4.03	4.28	194.60	3.06	4.72	5.62	99.41	5.75	5.47	7.93
1.15 - 1.20	632.52	1.73	4.14	4.49	199.33	3.18	4.94	5.87	116.33	5.21	5.90	7.87
1.20 - 1.25	642.04	1.57	4.02	4.32	196.60	3.27	8.70	9.29	109.49	5.83	9.46	11.12
1.25 - 1.30	638.70	1.54	5.22	5.44	206.74	2.95	10.85	11.25	102.09	6.25	12.06	13.58
1.30 - 1.35	650.74	1.42	4.21	4.44	208.46	2.89	6.23	6.86	103.57	5.77	7.28	9.29
1.35 - 1.40	654.87	1.52	3.30	3.63	206.17	2.91	3.65	4.67	114.16	5.69	5.55	7.95
1.40 - 1.45	629.51	1.54	4.51	4.76	212.60	2.93	4.33	5.23	101.29	6.34	11.63	13.25
1.45 - 1.50	618.84	1.59	3.16	3.54	207.77	3.08	4.32	5.30	107.02	6.32	5.88	8.63
1.50 - 1.55	588.43	1.64	3.47	3.84	204.71	2.94	5.30	6.06	89.71	7.18	6.76	9.87
1.55 - 1.60	592.05	1.37	5.41	5.58	201.25	2.90	3.84	4.81	97.41	6.07	8.44	10.40
1.60 - 1.65	592.45	1.73	8.93	9.09	176.78	3.74	11.20	11.81	96.44	7.61	21.56	22.87
1.65 - 1.70	598.23	1.94	5.23	5.58	197.42	3.25	6.72	7.46	109.03	6.27	8.78	10.79
1.70 - 1.75	559.04	2.07	9.91	10.13	184.20	3.32	12.52	12.95	79.57	8.68	25.56	27.00
1.75 - 1.80	532.29	2.12	8.86	9.11	180.20	3.02	9.92	10.37	79.74	7.16	16.12	17.64
1.80 - 1.85	498.64	2.33	12.48	12.69	158.79	4.09	13.80	14.39	71.23	10.28	31.64	33.27
1.85 - 1.90	469.28	3.15	4.08	5.16	154.80	4.28	3.44	5.49	69.81	10.19	6.29	11.97
1.90 - 1.95	436.04	1.81	5.62	5.90	148.80	3.41	6.29	7.15	64.39	7.68	14.02	15.98
1.95 - 2.00	391.83	2.99	12.80	13.15	122.69	4.77	13.72	14.52	69.18	9.00	22.90	24.60
2.00 - 2.05	326.25	2.29	12.66	12.86	120.71	3.88	11.28	11.92	46.78	9.30	36.86	38.01
2.05 - 2.10	290.71	3.02	8.42	8.95	90.43	5.05	6.37	8.13	58.66	8.70	11.45	14.38
2.10 - 2.15	194.04	4.82	6.06	7.74	70.06	7.48	6.62	9.99	28.13	20.35	14.24	24.84

Continued on next page

Table E.4: The $\Upsilon(nS)$ fiducial cross-section versus rapidity.

y^{Υ}	$d\sigma/dy$ (pb)	$\delta_{stat.}$ (%)	$\delta_{sys.}$ (%)	δ_{total} (%)	$d\sigma/dy$ (pb)	$\delta_{stat.}$ (%)	$\delta_{sys.}$ (%)	δ_{total} (%)	$d\sigma/dy$ (pb)	$\delta_{stat.}$ (%)	$\delta_{sys.}$ (%)	δ_{total} (%)
	$\Upsilon(1S)$				$\Upsilon(2S)$				$\Upsilon(3S)$			
2.15 - 2.20	135.60	4.28	5.83	7.24	58.50	6.63	5.88	8.86	17.27	20.61	11.22	23.47
2.20 - 2.25	76.27	10.67	12.40	16.36	31.63	10.59	9.20	14.03	9.32	30.84	42.05	52.15
2.25 - 2.30	13.84	13.19	15.54	20.38	7.68	18.49	34.68	39.30	1.90	70.71	66.84	97.30

E.2 Inclusive Cross-sections

E.2.1 Tables for cross-section versus p_T

Table E.5: The $\Upsilon(1S)$ inclusive cross-section.

$p_T^{\Upsilon(1S)}$ (GeV)	$d^2\sigma/dp_T dy$ (pb)	$\delta_{stat.}$ (%)	$\delta_{sys.}$ (%)	δ_{total} (%)	$d^2\sigma/dp_T dy$ (pb)	$\delta_{stat.}$ (%)	$\delta_{sys.}$ (%)	δ_{total} (%)
	$\|y\| < 1.2$				$1.2 < \|y\| < 2.3$			
0.00 - 0.50	42.20	3.21	5.52	6.39	51.54	4.66	6.68	8.15
0.50 - 1.00	118.45	1.79	4.41	4.76	152.57	3.91	4.10	5.67
1.00 - 1.50	177.54	1.69	8.00	8.17	196.11	2.77	10.22	10.59
1.50 - 2.00	218.49	1.67	3.65	4.01	260.17	2.59	14.20	14.44
2.00 - 2.50	248.01	1.63	3.22	3.61	243.11	3.10	15.99	16.28
2.50 - 3.00	277.39	1.21	2.97	3.21	275.66	2.99	14.77	15.07
3.00 - 3.50	290.57	1.43	3.60	3.88	291.90	2.55	3.42	4.27
3.50 - 4.00	292.51	2.00	3.79	4.29	300.04	3.79	10.18	10.86
4.00 - 4.50	277.35	1.35	4.77	4.96	299.87	2.39	5.62	6.11
4.50 - 5.00	253.25	1.13	4.18	4.33	265.50	2.27	4.14	4.72
5.00 - 5.50	224.53	1.59	3.62	3.96	261.20	1.93	4.39	4.80
5.50 - 6.00	217.81	1.21	3.98	4.16	224.89	1.68	5.04	5.31
6.00 - 6.50	191.85	1.76	3.87	4.25	210.93	1.92	3.58	4.06
6.50 - 7.00	166.93	1.43	2.87	3.21	184.47	1.63	3.78	4.12
7.00 - 7.50	150.13	2.23	4.02	4.59	159.27	1.77	3.89	4.27
7.50 - 8.00	132.97	1.82	3.00	3.51	146.55	1.94	3.07	3.63
8.00 - 8.50	115.26	1.76	3.64	4.04	122.67	1.96	3.03	3.61
8.50 - 9.00	102.15	1.52	5.11	5.33	106.54	2.28	2.90	3.69
9.00 - 9.50	89.24	1.81	3.25	3.72	99.62	2.17	2.98	3.68
9.50 - 10.00	77.13	1.22	4.67	4.83	77.99	2.20	2.66	3.45
10.00 - 11.00	61.39	1.40	3.24	3.53	65.33	1.54	3.31	3.65
11.00 - 12.00	45.01	1.18	3.12	3.33	47.74	1.76	2.89	3.38
12.00 - 13.00	34.96	1.20	4.12	4.29	36.98	1.87	2.83	3.39
13.00 - 14.00	25.66	1.89	3.61	4.07	26.94	2.02	2.91	3.53
14.00 - 15.00	20.75	1.08	2.55	2.77	21.47	2.33	2.85	3.67
15.00 - 16.00	15.79	1.15	2.64	2.88	14.40	2.45	2.96	3.83
16.00 - 17.00	12.21	1.30	2.81	3.09	12.89	3.26	2.62	4.16
17.00 - 18.00	9.46	1.47	2.50	2.90	9.82	3.10	2.73	4.12
18.00 - 19.00	7.35	1.60	2.25	2.76	7.12	3.25	3.12	4.49
19.00 - 20.00	5.79	1.68	2.49	3.00	5.98	3.39	7.10	7.86
20.00 - 21.00	4.66	1.77	2.40	2.98	4.33	3.88	2.66	4.67
21.00 - 22.00	3.63	2.02	2.37	3.11	3.70	3.61	2.27	4.24
22.00 - 23.00	2.97	1.86	2.47	3.09	2.74	3.08	2.79	4.14
23.00 - 24.00	2.43	2.46	2.59	3.57	2.19	4.30	2.47	4.92
24.00 - 25.00	1.92	2.74	2.75	3.88	1.77	5.00	3.14	5.87
25.00 - 26.00	1.62	2.98	2.55	3.91	1.44	5.76	2.49	6.22
26.00 - 27.00	1.28	3.27	2.63	4.19	1.24	5.36	2.81	6.00
27.00 - 28.00	1.02	3.71	2.65	4.55	1.05	7.06	3.13	7.65
28.00 - 29.00	0.86	3.92	4.71	6.12	0.95	6.81	20.44	21.52
29.00 - 30.00	0.78	4.09	2.69	4.88	0.77	8.63	2.99	9.04

Continued on next page

Table E.5: The $\Upsilon(1S)$ inclusive cross-section.

$p_T^{\Upsilon(1S)}$ (GeV)	$d^2\sigma/dp_T dy$ (pb)	$\delta_{stat.}$ (%)	$\delta_{sys.}$ (%)	δ_{total} (%)	$d^2\sigma/dp_T dy$ (pb)	$\delta_{stat.}$ (%)	$\delta_{sys.}$ (%)	δ_{total} (%)
	$\|y\| < 1.2$				$1.2 < \|y\| < 2.3$			
30.00 - 31.00	0.64	4.61	3.37	5.70	0.65	10.24	6.94	12.27
31.00 - 32.00	0.48	5.33	2.60	5.92	0.57	10.85	3.25	11.21
32.00 - 34.00	0.40	3.98	2.59	4.74	0.43	8.24	3.50	8.86
34.00 - 36.00	0.31	4.76	2.86	5.54	0.23	10.02	3.53	10.51
36.00 - 38.00	0.21	5.56	3.05	6.32	0.22	13.00	6.15	14.23
38.00 - 40.00	0.16	6.19	2.87	6.80	0.14	9.28	4.75	10.32
40.00 - 45.00	0.09	5.46	3.01	6.22	0.09	10.45	4.02	11.06
45.00 - 50.00	0.05	7.09	4.10	8.16	0.06	10.41	11.20	15.18
50.00 - 60.00	0.02	6.78	3.12	7.43	0.02	11.11	5.24	12.11
60.00 - 70.00	0.01	12.14	4.03	12.72	0.01	17.26	9.62	19.46

Table E.6: The $\Upsilon(2S)$ inclusive cross-section.

$p_T^{\Upsilon(2S)}$ (GeV)	$d^2\sigma/dp_T dy$ (pb)	$\delta_{stat.}$ (%)	$\delta_{sys.}$ (%)	δ_{total} (%)	$d^2\sigma/dp_T dy$ (pb)	$\delta_{stat.}$ (%)	$\delta_{sys.}$ (%)	δ_{total} (%)
	$\|y\| < 1.2$				$1.2 < \|y\| < 2.3$			
0.00 - 1.00	16.81	3.67	6.28	7.28	24.39	4.47	4.84	6.59
1.00 - 2.00	44.68	2.08	6.15	6.49	63.91	3.19	11.05	11.50
2.00 - 3.00	52.27	2.33	5.15	5.65	47.72	5.82	10.56	12.06
3.00 - 4.00	65.19	2.29	5.76	6.20	68.40	3.43	8.98	9.61
4.00 - 5.00	62.46	2.30	6.31	6.72	74.15	3.21	9.34	9.88
5.00 - 6.00	50.93	2.36	5.39	5.89	64.70	3.05	6.47	7.16
6.00 - 7.00	43.03	2.44	4.79	5.37	58.35	3.06	3.57	4.71
7.00 - 8.00	36.42	2.71	6.84	7.35	44.05	3.07	3.22	4.44
8.00 - 9.00	27.89	3.47	6.22	7.12	36.21	3.20	2.54	4.08
9.00 - 10.00	23.74	2.55	5.23	5.82	28.49	3.43	2.29	4.12
10.00 - 12.00	15.84	2.16	4.19	4.71	19.53	2.53	2.17	3.33
12.00 - 14.00	10.09	2.06	5.49	5.86	11.95	3.02	2.16	3.70
14.00 - 16.00	6.83	1.52	2.15	2.63	7.46	3.25	2.24	3.93
16.00 - 18.00	4.26	1.81	2.06	2.74	4.36	5.54	2.10	5.90
18.00 - 20.00	2.67	2.05	1.40	2.48	2.76	5.24	1.94	5.56
20.00 - 22.00	1.74	2.50	1.56	2.94	1.83	5.17	1.90	5.47
22.00 - 24.00	1.17	3.00	1.58	3.38	1.12	7.11	2.15	7.37
24.00 - 26.00	0.79	3.51	1.93	4.00	0.87	7.12	2.45	7.47
26.00 - 28.00	0.54	4.37	3.12	5.36	0.68	7.35	2.44	7.68
28.00 - 30.00	0.39	4.78	2.66	5.46	0.35	14.00	7.69	15.85
30.00 - 32.00	0.27	5.94	2.95	6.61	0.27	15.42	3.36	15.61
32.00 - 36.00	0.17	5.27	1.82	5.56	0.19	11.53	3.16	11.82
36.00 - 40.00	0.10	6.91	2.76	7.42	0.09	16.46	4.28	16.80
40.00 - 50.00	0.04	7.00	3.25	7.69	0.04	14.97	5.08	15.60
50.00 - 70.00	0.01	9.07	10.17	13.60	0.00	97.50	115.76	150.43

Table E.7: The $\Upsilon(3S)$ inclusive cross-section.

$p_T^{\Upsilon(3S)}$ (GeV)	$d^2\sigma/dp_T dy$ (pb)	$\delta_{stat.}$ (%)	$\delta_{sys.}$ (%)	δ_{total} (%)	$d^2\sigma/dp_T dy$ (pb)	$\delta_{stat.}$ (%)	$\delta_{sys.}$ (%)	δ_{total} (%)
	$\|y\| < 1.2$				$1.2 < \|y\| < 2.3$			
0.00 - 1.00	7.30	6.35	6.30	8.94	11.18	11.74	7.75	14.07
1.00 - 2.00	16.83	4.22	8.11	9.14	17.70	17.30	52.04	54.84
2.00 - 3.00	25.47	3.50	5.62	6.62	22.66	9.98	21.39	23.60
3.00 - 4.00	25.02	4.00	12.64	13.26	20.23	12.06	16.09	20.12
4.00 - 5.00	24.23	4.25	5.44	6.91	29.82	6.52	8.09	10.39
5.00 - 6.00	22.29	4.18	5.52	6.93	27.19	6.53	9.70	11.70
6.00 - 7.00	20.79	4.29	7.18	8.37	22.27	6.95	7.99	10.59
7.00 - 8.00	18.20	5.05	10.81	11.94	21.92	5.82	5.33	7.89
8.00 - 9.00	15.00	4.51	8.43	9.56	16.21	5.90	6.56	8.83
9.00 - 10.00	11.73	4.17	6.70	7.89	14.02	6.24	3.80	7.30
10.00 - 12.00	8.12	3.48	7.11	7.92	10.80	4.52	3.62	5.79
12.00 - 14.00	6.05	2.82	7.58	8.09	6.23	4.85	3.63	6.04
14.00 - 16.00	4.04	2.35	2.23	3.24	3.99	6.39	4.95	8.06
16.00 - 18.00	2.57	2.66	2.48	3.63	3.50	6.14	3.33	6.95
18.00 - 20.00	1.73	3.06	1.48	3.39	1.92	7.11	4.91	8.60
20.00 - 22.00	1.23	3.26	1.57	3.61	1.25	6.30	3.19	7.03
22.00 - 24.00	0.79	3.72	1.73	4.09	0.96	7.93	2.66	8.30
24.00 - 26.00	0.57	4.57	1.93	4.95	0.60	10.96	9.57	14.47
26.00 - 28.00	0.43	5.41	2.17	5.81	0.33	15.39	3.63	15.66
28.00 - 30.00	0.27	6.09	2.61	6.61	0.41	11.77	19.19	22.44
30.00 - 32.00	0.21	7.64	2.53	8.02	0.18	20.98	4.94	21.31
32.00 - 36.00	0.11	7.46	2.27	7.77	0.12	17.82	4.50	18.15
36.00 - 40.00	0.07	9.20	2.63	9.53	0.05	38.71	8.70	39.12
40.00 - 50.00	0.02	10.99	3.52	11.48	0.03	21.72	9.65	23.43
50.00 - 70.00	0.01	12.74	13.27	18.35	0.01	16.64	17.58	24.01

E.2.2 Tables for cross-section versus rapidity

Table E.8: The $\Upsilon(nS)$ inclusive cross-section versus rapidity.

y^{Υ}	$d\sigma/dp_T$ (pb)	$\delta_{stat.}$ (%)	$\delta_{sys.}$ (%)	δ_{total} (%)	$d\sigma/dp_T$ (pb)	$\delta_{stat.}$ (%)	$\delta_{sys.}$ (%)	δ_{total} (%)	$d\sigma/dp_T$ (pb)	$\delta_{stat.}$ (%)	$\delta_{sys.}$ (%)	δ_{total} (%)
	$\Upsilon(1S)$				$\Upsilon(2S)$				$\Upsilon(3S)$			
0.00 - 0.05	2064.99	1.18	3.20	3.41	501.25	1.99	5.04	5.42	254.72	3.96	4.99	6.38
0.05 - 0.10	2052.78	1.27	3.71	3.92	524.72	2.25	6.14	6.54	253.36	4.09	5.20	6.62
0.10 - 0.15	2098.47	0.95	3.23	3.37	527.65	2.43	2.95	3.83	236.22	3.59	3.26	4.85
0.15 - 0.20	2052.42	1.19	4.74	4.89	520.74	2.28	5.55	6.00	219.55	4.69	4.40	6.43
0.20 - 0.25	2085.00	1.18	4.52	4.67	510.17	2.80	3.84	4.75	245.00	4.21	3.98	5.80
0.25 - 0.30	2115.14	1.15	3.24	3.44	533.76	2.43	4.00	4.68	259.56	3.72	4.33	5.70
0.30 - 0.35	2125.13	0.91	3.78	3.89	528.04	2.63	4.40	5.13	262.48	4.24	5.50	6.94
0.35 - 0.40	2103.87	1.23	3.26	3.48	558.36	2.45	4.01	4.70	258.43	4.30	5.10	6.67
0.40 - 0.45	2157.60	1.03	3.01	3.18	578.85	2.63	4.05	4.83	267.64	4.15	3.43	5.38
0.45 - 0.50	2221.92	1.25	3.07	3.31	550.01	2.80	3.46	4.45	255.89	4.84	5.04	6.98
0.50 - 0.55	2273.71	1.21	2.82	3.07	548.68	2.91	3.92	4.88	269.66	4.44	4.33	6.20
0.55 - 0.60	2180.85	1.20	3.18	3.40	523.73	2.95	4.50	5.38	241.30	4.45	6.40	7.79
0.60 - 0.65	2179.81	0.87	2.83	2.96	523.50	3.21	7.77	8.41	245.97	5.08	4.12	6.54
0.65 - 0.70	2192.03	1.64	3.45	3.82	560.73	3.21	5.48	6.35	263.24	3.97	6.31	7.45
0.70 - 0.75	2234.33	1.54	2.95	3.33	559.37	2.90	5.53	6.24	241.39	4.11	5.86	7.16
0.75 - 0.80	2221.26	1.51	3.32	3.65	579.68	3.13	4.02	5.10	258.69	5.18	4.93	7.15
0.80 - 0.85	2243.43	1.36	5.28	5.45	577.52	2.65	6.59	7.11	249.46	4.92	6.72	8.32
0.85 - 0.90	2193.66	1.84	3.02	3.54	552.73	2.94	5.69	6.40	261.15	4.99	4.37	6.63
0.90 - 0.95	2208.35	1.57	3.61	3.94	541.78	2.94	4.05	5.01	277.08	4.83	6.66	8.23
0.95 - 1.00	2171.42	1.47	3.77	4.05	556.74	3.08	5.14	5.99	292.91	4.42	5.73	7.24
1.00 - 1.05	2238.44	1.53	3.87	4.16	601.93	2.88	3.83	4.79	276.21	5.01	5.23	7.24
1.05 - 1.10	2257.71	1.57	4.60	4.86	585.61	3.13	5.33	6.18	283.12	5.21	6.40	8.25
1.10 - 1.15	2270.62	3.11	4.39	5.38	580.24	2.99	5.45	6.21	264.79	5.31	6.62	8.49
1.15 - 1.20	2360.30	1.38	4.03	4.26	595.58	3.02	7.58	8.16	307.38	5.00	5.88	7.72
1.20 - 1.25	2334.33	2.42	10.89	11.15	581.31	2.94	8.79	9.27	291.93	4.86	14.81	15.59
1.25 - 1.30	2411.21	3.59	7.55	8.36	604.02	3.18	4.68	5.65	257.58	5.53	11.53	12.79
1.30 - 1.35	2460.45	1.55	4.67	4.92	602.65	2.94	6.53	7.16	281.97	5.70	7.46	9.39
1.35 - 1.40	2516.79	1.80	3.50	3.93	616.01	2.82	4.22	5.08	304.74	5.85	5.18	7.81
1.40 - 1.45	2424.11	1.50	3.21	3.55	637.17	3.01	4.11	5.09	278.20	6.28	6.42	8.98
1.45 - 1.50	2391.45	1.99	4.39	4.82	637.53	2.77	3.80	4.70	294.94	6.19	6.20	8.76
1.50 - 1.55	2302.13	1.76	4.91	5.22	618.92	2.93	3.02	4.21	247.78	7.06	7.49	10.29
1.55 - 1.60	2373.62	1.75	4.48	4.81	622.71	2.82	4.46	5.28	293.05	6.59	8.13	10.47
1.60 - 1.65	2430.13	1.52	7.67	7.82	573.47	3.89	8.43	9.29	273.20	7.93	11.61	14.06
1.65 - 1.70	2483.74	1.16	4.73	4.87	659.74	2.39	4.28	4.90	323.75	7.28	15.97	17.55
1.70 - 1.75	2343.64	1.79	6.36	6.60	625.57	3.40	9.76	10.34	238.53	7.35	11.48	13.62
1.75 - 1.80	2366.21	1.54	4.80	5.04	634.93	4.44	3.89	5.91	269.86	6.39	12.26	13.82
1.80 - 1.85	2403.69	1.97	6.38	6.68	636.63	3.56	6.91	7.77	278.84	8.00	15.01	17.01
1.85 - 1.90	2359.97	2.51	11.16	11.44	652.31	3.65	3.42	5.00	276.59	8.65	5.74	10.39
1.90 - 1.95	2391.96	1.77	11.27	11.41	689.66	3.29	7.50	8.19	276.87	8.94	18.21	20.29
1.95 - 2.00	2450.60	1.82	8.11	8.32	640.68	3.24	7.24	7.94	335.08	10.10	11.95	15.64
2.00 - 2.05	2289.36	2.99	5.32	6.10	711.32	3.61	6.42	7.36	274.92	8.82	20.65	22.46
2.05 - 2.10	2311.09	2.71	4.83	5.54	629.55	5.27	5.91	7.92	356.45	8.32	8.05	11.57
2.10 - 2.15	2061.63	3.40	5.98	6.88	635.57	5.60	9.02	10.62	240.79	15.87	24.01	28.78

Continued on next page

Table E.8: The $\Upsilon(nS)$ inclusive cross-section versus rapidity.

y^{Υ}	$d\sigma/dp_T$ (pb)	$\delta_{stat.}$ (%)	$\delta_{sys.}$ (%)	δ_{total} (%)	$d\sigma/dp_T$ (pb)	$\delta_{stat.}$ (%)	$\delta_{sys.}$ (%)	δ_{total} (%)	$d\sigma/dp_T$ (pb)	$\delta_{stat.}$ (%)	$\delta_{sys.}$ (%)	δ_{total} (%)
	$\Upsilon(1S)$				$\Upsilon(2S)$				$\Upsilon(3S)$			
2.15 - 2.20	1927.12	5.28	7.44	9.12	718.30	6.61	7.80	10.22	176.83	23.97	9.59	25.82
2.20 - 2.25	1897.49	6.32	6.83	9.31	629.54	10.30	11.08	15.13	204.34	25.65	31.70	40.78
2.25 - 2.30	1070.10	7.68	17.84	19.43	432.54	19.69	9.23	21.75	251.84	24.48	24.86	34.89

E.3 Ratios

E.3.1 Tables for ratios versus p_T

Table E.9: The ratio of inclusive cross-sections $\sigma(\Upsilon^{2S})/\sigma(\Upsilon^{1S})$ versus p_T.

p_T^{Υ} (GeV)	$\sigma(\Upsilon^{2S})/\sigma(\Upsilon^{1S})$	$\delta_{stat.}$ (%)	$\delta_{sys.}$ (%)	δ_{total} (%)	$\sigma(\Upsilon^{2S})/\sigma(\Upsilon^{1S})$	$\delta_{stat.}$ (%)	$\delta_{sys.}$ (%)	δ_{total} (%)
	$\lvert y\rvert < 1.2$				$1.2 < \lvert y\rvert < 2.3$			
0.00 - 1.00	0.21	3.78	2.87	4.74	0.25	5.80	5.00	7.66
1.00 - 2.00	0.22	2.06	2.48	3.23	0.28	3.60	11.05	11.63
2.00 - 3.00	0.20	2.32	4.32	4.91	0.19	5.11	11.21	12.32
3.00 - 4.00	0.22	2.45	4.06	4.74	0.23	4.32	8.60	9.62
4.00 - 5.00	0.23	2.52	3.91	4.65	0.26	3.71	7.32	8.21
5.00 - 6.00	0.23	2.69	2.34	3.57	0.27	3.46	4.21	5.45
6.00 - 7.00	0.24	2.43	2.49	3.48	0.30	3.40	3.70	5.02
7.00 - 8.00	0.26	2.43	4.64	5.24	0.29	3.50	3.65	5.06
8.00 - 9.00	0.26	3.27	3.52	4.80	0.32	3.77	3.25	4.98
9.00 - 10.00	0.29	2.62	2.94	3.94	0.32	4.09	2.46	4.78
10.00 - 12.00	0.30	2.23	2.05	3.03	0.35	3.01	3.24	4.42
12.00 - 14.00	0.33	2.19	3.24	3.91	0.38	3.52	2.64	4.40
14.00 - 16.00	0.37	1.72	1.84	2.52	0.42	3.96	2.57	4.72
16.00 - 18.00	0.39	1.98	1.71	2.62	0.38	6.81	1.58	6.99
18.00 - 20.00	0.41	2.38	0.77	2.50	0.42	6.04	2.18	6.42
20.00 - 22.00	0.42	2.89	1.25	3.15	0.45	6.24	0.82	6.30
22.00 - 24.00	0.43	3.44	1.29	3.67	0.45	8.10	0.60	8.12
24.00 - 26.00	0.45	4.11	2.40	4.76	0.54	8.62	1.78	8.81
26.00 - 28.00	0.47	5.02	2.20	5.48	0.60	8.99	0.89	9.04
28.00 - 30.00	0.47	5.54	3.35	6.48	0.41	16.19	11.04	19.59
30.00 - 32.00	0.49	6.90	2.40	7.30	0.44	17.86	3.65	18.23
32.00 - 36.00	0.48	6.14	0.80	6.20	0.61	13.78	0.74	13.80
36.00 - 40.00	0.50	8.44	2.16	8.71	0.53	20.12	2.70	20.30
40.00 - 50.00	0.54	9.17	1.85	9.35	0.58	19.56	5.57	20.34
50.00 - 70.00	0.63	13.40	2.85	13.70				

Table E.10: The ratio of inclusive cross-sections $\sigma(\Upsilon^{3S})/\sigma(\Upsilon^{1S})$ versus p_T.

p_T^{Υ} (GeV)	$\sigma(\Upsilon^{3S})/\sigma(\Upsilon^{1S})$	$\delta_{stat.}$ (%)	$\delta_{sys.}$ (%)	δ_{total} (%)	$\sigma(\Upsilon^{3S})/\sigma(\Upsilon^{1S})$	$\delta_{stat.}$ (%)	$\delta_{sys.}$ (%)	δ_{total} (%)
	$\lvert y\rvert < 1.2$				$1.2 < \lvert y\rvert < 2.3$			
0.00 - 1.00	0.09	6.86	8.91	11.25	0.11	10.98	6.75	12.89
1.00 - 2.00	0.08	3.95	4.97	6.35	0.08	10.25	50.84	51.86
2.00 - 3.00	0.10	3.56	4.84	6.01	0.09	8.99	23.10	24.78
3.00 - 4.00	0.09	4.07	11.07	11.80	0.07	11.06	14.07	17.90
4.00 - 5.00	0.09	4.48	3.26	5.54	0.11	6.35	3.73	7.37
5.00 - 6.00	0.10	4.52	4.22	6.19	0.11	6.67	8.40	10.73
6.00 - 7.00	0.12	4.42	4.90	6.60	0.11	7.03	6.60	9.64
7.00 - 8.00	0.13	4.62	8.75	9.89	0.14	5.77	3.38	6.69
8.00 - 9.00	0.14	4.43	6.25	7.66	0.14	6.04	7.38	9.53
9.00 - 10.00	0.14	4.38	4.44	6.24	0.16	6.53	4.37	7.85
10.00 - 12.00	0.15	3.78	4.95	6.22	0.19	4.75	3.32	5.80
12.00 - 14.00	0.20	2.79	5.44	6.11	0.20	5.00	2.12	5.43
14.00 - 16.00	0.22	2.57	1.23	2.85	0.22	6.77	3.38	7.57
16.00 - 18.00	0.24	2.85	1.39	3.17	0.31	6.55	0.91	6.61
18.00 - 20.00	0.26	3.38	0.59	3.43	0.29	7.45	1.80	7.67
20.00 - 22.00	0.30	3.61	0.25	3.62	0.31	6.77	1.77	7.00
22.00 - 24.00	0.29	3.98	0.31	4.00	0.39	8.45	0.79	8.49
24.00 - 26.00	0.33	4.97	0.36	4.98	0.38	11.49	8.39	14.23
26.00 - 28.00	0.38	6.05	0.65	6.08	0.29	15.47	1.41	15.53
28.00 - 30.00	0.33	6.52	1.32	6.65	0.46	13.08	7.03	14.85
30.00 - 32.00	0.37	8.48	0.38	8.49	0.30	21.58	4.17	21.97
32.00 - 36.00	0.31	8.44	0.18	8.45	0.36	21.66	4.44	22.11
36.00 - 40.00	0.37	10.50	0.44	10.51	0.29	40.61	4.27	40.84
40.00 - 50.00	0.34	12.85	1.77	12.97	0.38	26.08	6.35	26.85
50.00 - 70.00	0.46	17.42	1.11	17.46				

E.3.2 Tables for ratio versus rapidity

Table E.11: The ratio of inclusive cross-sections $\sigma(\Upsilon^{nS})/\sigma(\Upsilon^{1S})$ versus rapidity.

y^{Υ}	$\sigma(\Upsilon^{2S})/\sigma(\Upsilon^{1S})$	$\delta_{stat.}$ (%)	$\delta_{sys.}$ (%)	δ_{total} (%)	$\sigma(\Upsilon^{3S})/\sigma(\Upsilon^{1S})$	$\delta_{stat.}$ (%)	$\delta_{sys.}$ (%)	δ_{total} (%)
0.00 - 0.05	0.24	2.34	5.81	6.27	0.12	4.00	5.33	6.66
0.05 - 0.10	0.26	2.47	5.55	6.07	0.12	4.23	4.31	6.04
0.10 - 0.15	0.25	2.46	1.28	2.77	0.11	3.69	1.11	3.85
0.15 - 0.20	0.25	2.32	2.55	3.45	0.11	4.73	2.59	5.39
0.20 - 0.25	0.24	2.74	2.59	3.77	0.12	4.38	2.69	5.13
0.25 - 0.30	0.25	2.46	1.47	2.87	0.12	3.76	2.04	4.28
0.30 - 0.35	0.25	2.61	3.15	4.09	0.12	4.29	3.57	5.58
0.35 - 0.40	0.27	2.70	3.78	4.64	0.12	4.46	3.36	5.58
0.40 - 0.45	0.27	2.92	1.48	3.28	0.12	4.28	2.24	4.83
0.45 - 0.50	0.25	2.76	2.13	3.49	0.12	4.88	3.74	6.15
0.50 - 0.55	0.24	3.02	4.29	5.25	0.12	4.54	4.90	6.68
0.55 - 0.60	0.24	2.88	2.85	4.05	0.11	4.46	5.13	6.80
0.60 - 0.65	0.24	3.17	7.20	7.86	0.11	4.98	1.54	5.22
0.65 - 0.70	0.26	3.52	5.84	6.82	0.12	4.12	6.05	7.32
0.70 - 0.75	0.25	3.11	4.88	5.78	0.11	4.42	5.88	7.35
0.75 - 0.80	0.26	3.22	2.49	4.07	0.12	5.15	3.18	6.05
0.80 - 0.85	0.26	2.95	8.33	8.83	0.11	5.12	3.81	6.38
0.85 - 0.90	0.25	3.53	5.43	6.48	0.12	5.40	4.02	6.73
0.90 - 0.95	0.25	3.18	4.00	5.11	0.13	4.94	3.50	6.05
0.95 - 1.00	0.26	3.32	4.42	5.52	0.13	4.58	6.02	7.56
1.00 - 1.05	0.27	3.17	1.29	3.42	0.12	5.14	1.78	5.44
1.05 - 1.10	0.26	3.15	4.40	5.42	0.13	5.39	6.57	8.50
1.10 - 1.15	0.26	4.51	2.94	5.39	0.12	6.71	4.76	8.22
1.15 - 1.20	0.25	3.20	4.83	5.80	0.13	5.05	3.50	6.14
1.20 - 1.25	0.25	3.81	14.31	14.81	0.13	5.48	21.84	22.52
1.25 - 1.30	0.25	4.47	2.97	5.37	0.11	6.45	10.02	11.92
1.30 - 1.35	0.24	3.08	5.09	5.95	0.11	5.72	3.81	6.87
1.35 - 1.40	0.24	3.19	2.91	4.32	0.12	6.08	6.30	8.75
1.40 - 1.45	0.26	3.27	1.80	3.73	0.11	6.23	5.59	8.37
1.45 - 1.50	0.27	3.50	4.28	5.53	0.12	5.98	3.74	7.05
1.50 - 1.55	0.27	3.46	3.58	4.98	0.11	7.25	4.29	8.42
1.55 - 1.60	0.26	3.37	6.63	7.44	0.12	6.92	3.74	7.87
1.60 - 1.65	0.24	4.09	5.97	7.24	0.11	7.75	7.71	10.94
1.65 - 1.70	0.27	2.87	4.89	5.67	0.13	7.61	11.88	14.11
1.70 - 1.75	0.27	3.80	12.48	13.05	0.10	7.62	11.06	13.43
1.75 - 1.80	0.27	4.50	1.44	4.72	0.11	6.52	7.63	10.04
1.80 - 1.85	0.26	4.01	3.28	5.18	0.12	8.23	16.62	18.55
1.85 - 1.90	0.28	4.19	8.18	9.19	0.12	9.11	6.50	11.18
1.90 - 1.95	0.29	3.60	9.45	10.11	0.12	9.05	16.08	18.45
1.95 - 2.00	0.26	3.72	8.88	9.63	0.14	9.74	6.19	11.54
2.00 - 2.05	0.31	5.21	3.61	6.34	0.12	9.26	18.15	20.37
2.05 - 2.10	0.27	6.02	7.35	9.50	0.15	8.43	10.29	13.31

Continued on next page

Table E.11: The ratio of inclusive cross-sections $\sigma(\Upsilon^{nS})/\sigma(\Upsilon^{1S})$ versus rapidity.

y^{Υ}	$\sigma(\Upsilon^{2S})/\sigma(\Upsilon^{1S})$	$\delta_{stat.}$ (%)	$\delta_{sys.}$ (%)	δ_{total} (%)	$\sigma(\Upsilon^{3S})/\sigma(\Upsilon^{1S})$	$\delta_{stat.}$ (%)	$\delta_{sys.}$ (%)	δ_{total} (%)
2.10 - 2.15	0.31	6.45	8.34	10.55	0.12	15.76	23.38	28.20
2.15 - 2.20	0.37	9.07	4.90	10.31	0.09	24.80	5.70	25.44
2.20 - 2.25	0.33	12.65	7.80	14.86	0.11	25.59	32.24	41.16
2.25 - 2.30	0.41	22.16	10.69	24.60	0.24	27.83	16.07	32.14

Appendix F

Cross Checks

F.0.3 Luminosity Dependence of the Result

We verify that the result is independent of luminosity-dependent effects (pileup, number of reconstructed vertices, etc.) by dividing the data sample into two parts: before and after period H. The total number of (unweighted) fitted Υ mesons per fb^{-1} is consistent for these two periods as shown in Additionally, no rapidity dependence of the results is observed as can be seen in Fig. F.1.

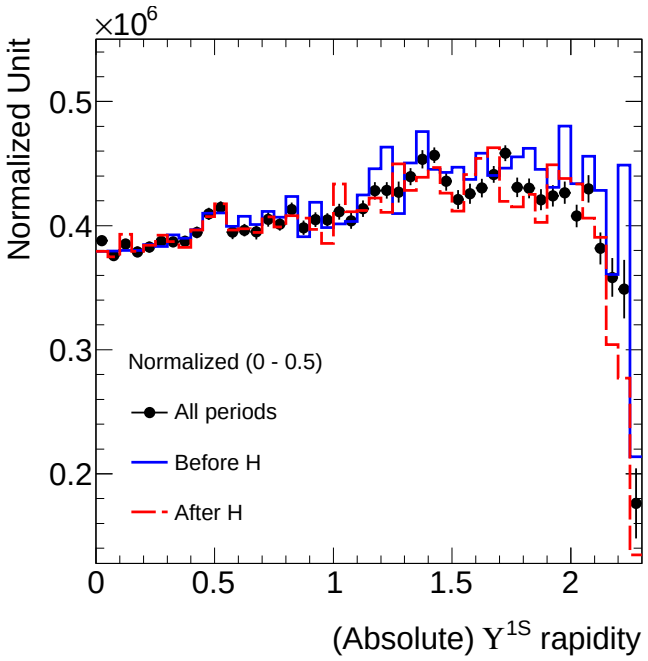

Figure F.1: The total cross-section versus $|y^{\Upsilon}|$ for data split into different periods.

F.0.4 Rapidity Dependence of the Result in p_T slices

There is a rise observed in the rapidity dependence of the cross-section toward forward rapidities. Figure F.2 shows the $\Upsilon(1S)$ cross-section as a function of rapidity for four p_T slices (normalised to the $0-5$ GeV slice). The dependence is greatest at low Υ p_T but is still seen in the high p_T slice.

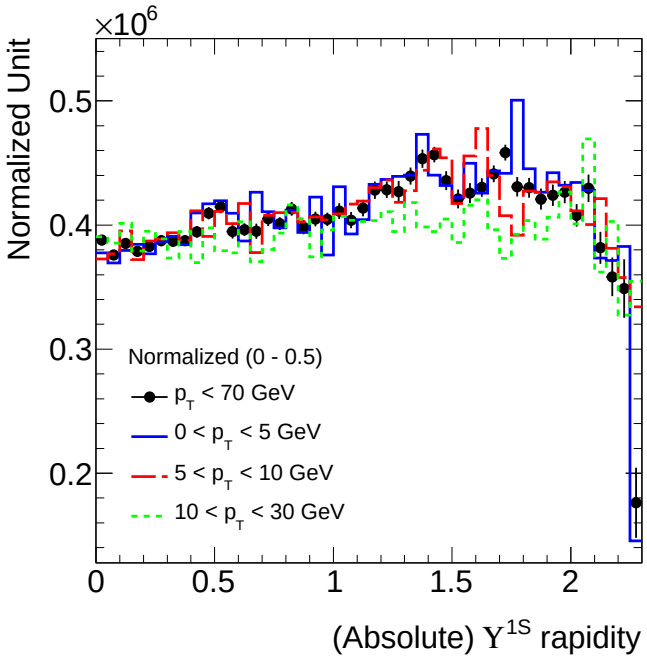

Figure F.2: The total cross-section vs $|y^{\Upsilon}|$ for data split into three p_T intervals: $0 < p_T < 5$ GeV, $5 < p_T < 10$ GeV, $10 < p_T < 30$ GeV.

F.0.5 Rapidity Dependence of the Result for extreme spin-alignment scenario

Figure F.3 shows an example of the $\Upsilon(1S)$ rapidity result recast in terms of a fully longitudinal spin-alignment scenario for the central result.

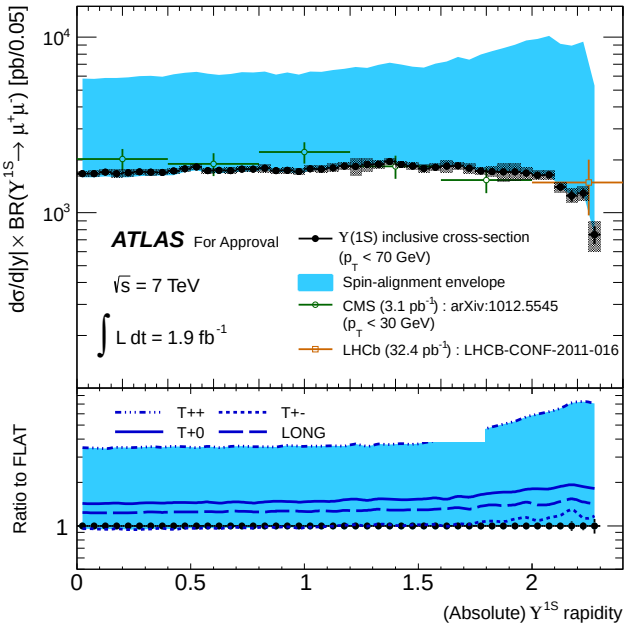

Figure F.3: The total cross-section vs $|y^{\Upsilon}|$ for data under the fully longitudinal hypothesis.

F.0.6 Toy MC checks of possible correlations between $\Upsilon(2S)$ and $\Upsilon(3S)$ states

Toy MC studies were conducted to see if the fitted yields between the $\Upsilon(2S)$ and $\Upsilon(3S)$ states were correlated and whether any bias is observed toward one state or the other. Figure F.4 shows the pull distribution $[\frac{3S}{2S}\text{Fit} - \frac{3S}{2S}\text{Input}]/\sigma\frac{3S}{2S}$ built using 10,000 pseudoexperiments, and where $\sigma\frac{3S}{2S}$ takes into account correlations from the fit, for an example bin in p_T and rapidity where the nominal $\Upsilon(3S)$ yield is larger than that of the $\Upsilon(2S)$. The resultant mean of the distribution is $\mu = -0.052 \pm 0.011$ with fitted sigma of $\sigma = 0.983 \pm 0.007$. Due to the negligibly small effect, suggesting no systematic bias is observed.

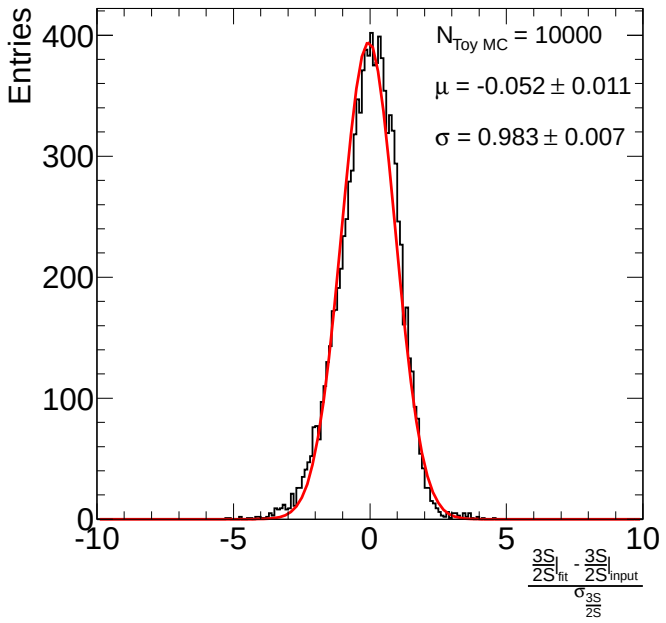

Figure F.4: Pull distribution of the ratio of fitted $\Upsilon(2S)$ and $\Upsilon(3S)$ yields in 10,000 pseudo-experiments.

F.0.7 Mass resolution scaling

A linear invariant mass scaling assumption is used in the combined mass fits to the $\Upsilon(1,2,3S)$ system. The dependence of the mass resolution with invariant mass is shown in Figure F.5 studied using signal Monte Carlo, and shows that the linear scaling assumption is a reasonable one. In addition, we see consistent behaviour in the data-derived mass resolution between the mass point at 3.096 GeV (the J/ψ peak) and the Υ signal region.

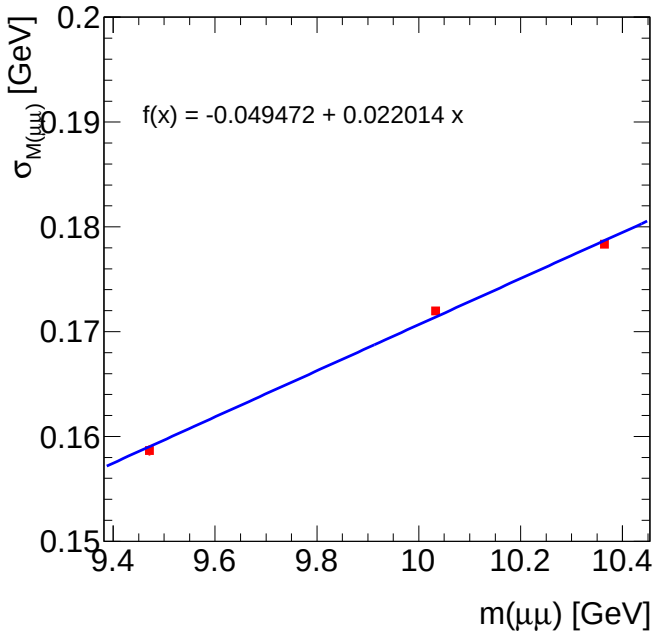

Figure F.5: Check of linear dependence assumption of mass resolution scaling using MC simulated Υ events.

Appendix G

Examples of ϒ Fitting Plots

In the analysis of ϒ cross-section measurements, since we have to deal with about sixteen thousands fits[1], we are not able to show all of them in the thesis. All the plots are saved in the CERN Document Server (CDS), but they are restricted to only ATLAS members. Here, we show a set of fitting plots, for fiducial cross-section in p_T and y bins, as examples in Fig. G.1, Fig. G.2 and Fig. G.3.

Table G.1: ϒ mass fitting plots for fiducial cross-section as a function of p_T in rapidity region $|y| < 1.2$.

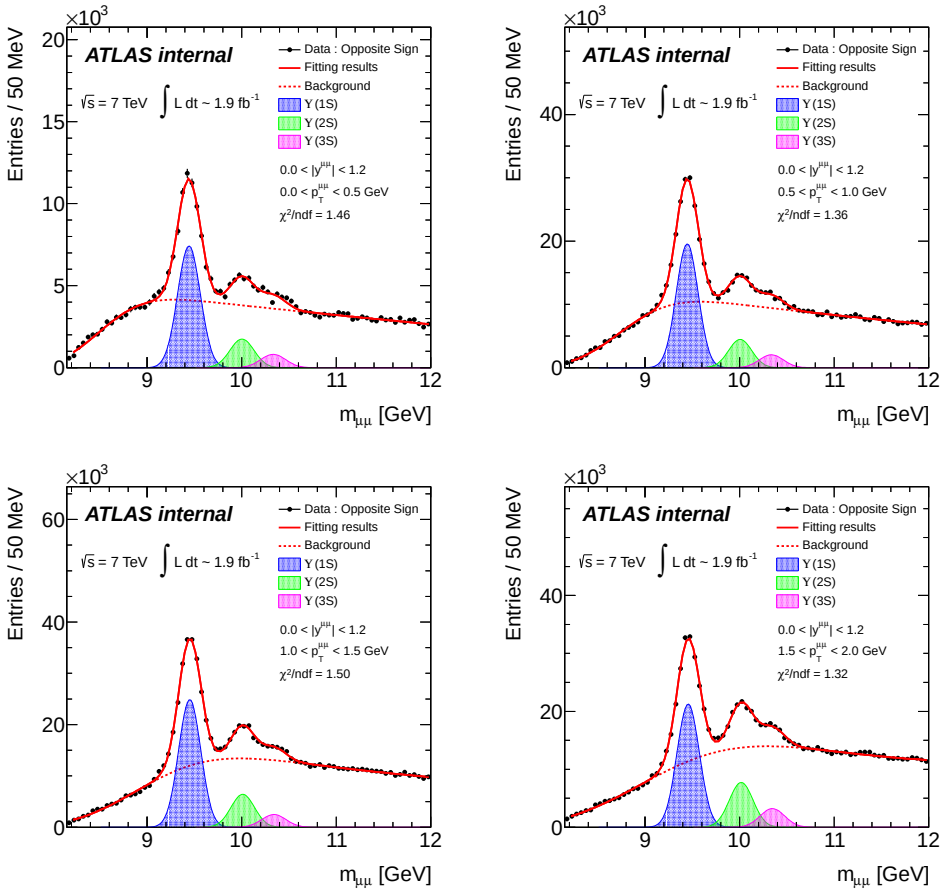

[1] 50(bins) × 3(p_T, y) × 3(3 ϒ states) × 6(fit models) × 6(fid. + incl. with 5 pol.) = 16200 plots.

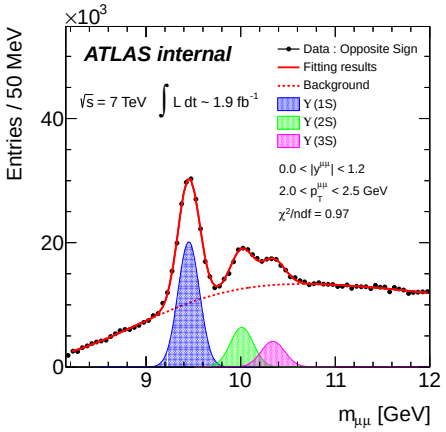
ATLAS internal
Data : Opposite Sign
Fitting results
Background
Υ(1S)
Υ(2S)
Υ(3S)
√s = 7 TeV ∫ L dt ~ 1.9 fb⁻¹
0.0 < |y^μμ| < 1.2
2.0 < p_T^μμ < 2.5 GeV
χ²/ndf = 0.97
Entries / 50 MeV
m_μμ [GeV]

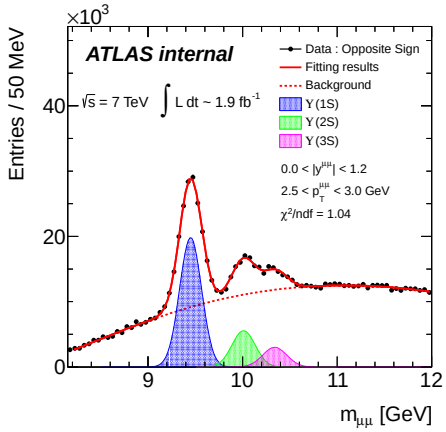
ATLAS internal
Data : Opposite Sign
Fitting results
Background
Υ(1S)
Υ(2S)
Υ(3S)
√s = 7 TeV ∫ L dt ~ 1.9 fb⁻¹
0.0 < |y^μμ| < 1.2
2.5 < p_T^μμ < 3.0 GeV
χ²/ndf = 1.04
Entries / 50 MeV
m_μμ [GeV]

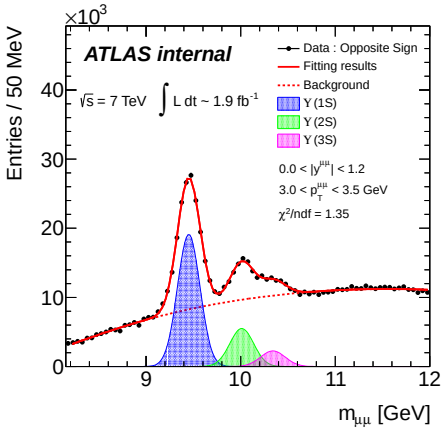
ATLAS internal
Data : Opposite Sign
Fitting results
Background
Υ(1S)
Υ(2S)
Υ(3S)
√s = 7 TeV ∫ L dt ~ 1.9 fb⁻¹
0.0 < |y^μμ| < 1.2
3.0 < p_T^μμ < 3.5 GeV
χ²/ndf = 1.35
Entries / 50 MeV
m_μμ [GeV]

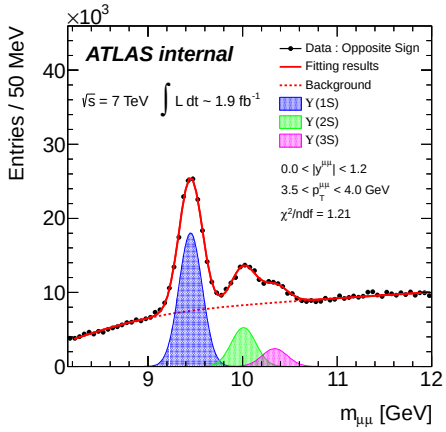
ATLAS internal
Data : Opposite Sign
Fitting results
Background
Υ(1S)
Υ(2S)
Υ(3S)
√s = 7 TeV ∫ L dt ~ 1.9 fb⁻¹
0.0 < |y^μμ| < 1.2
3.5 < p_T^μμ < 4.0 GeV
χ²/ndf = 1.21
Entries / 50 MeV
m_μμ [GeV]

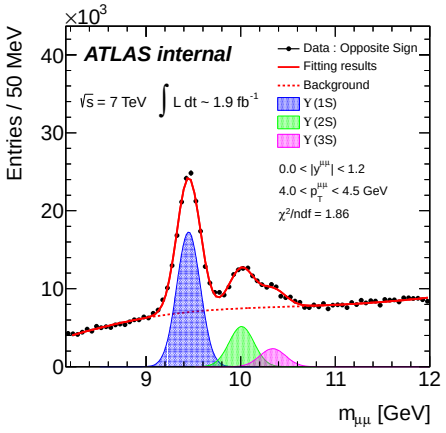
ATLAS internal
Data : Opposite Sign
Fitting results
Background
Υ(1S)
Υ(2S)
Υ(3S)
√s = 7 TeV ∫ L dt ~ 1.9 fb⁻¹
0.0 < |y^μμ| < 1.2
4.0 < p_T^μμ < 4.5 GeV
χ²/ndf = 1.86
Entries / 50 MeV
m_μμ [GeV]

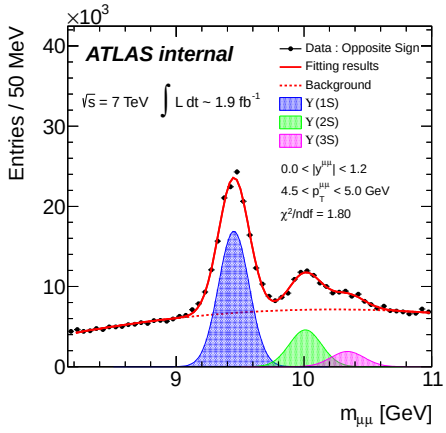
ATLAS internal
Data : Opposite Sign
Fitting results
Background
Υ(1S)
Υ(2S)
Υ(3S)
√s = 7 TeV ∫ L dt ~ 1.9 fb⁻¹
0.0 < |y^μμ| < 1.2
4.5 < p_T^μμ < 5.0 GeV
χ²/ndf = 1.80
Entries / 50 MeV
m_μμ [GeV]

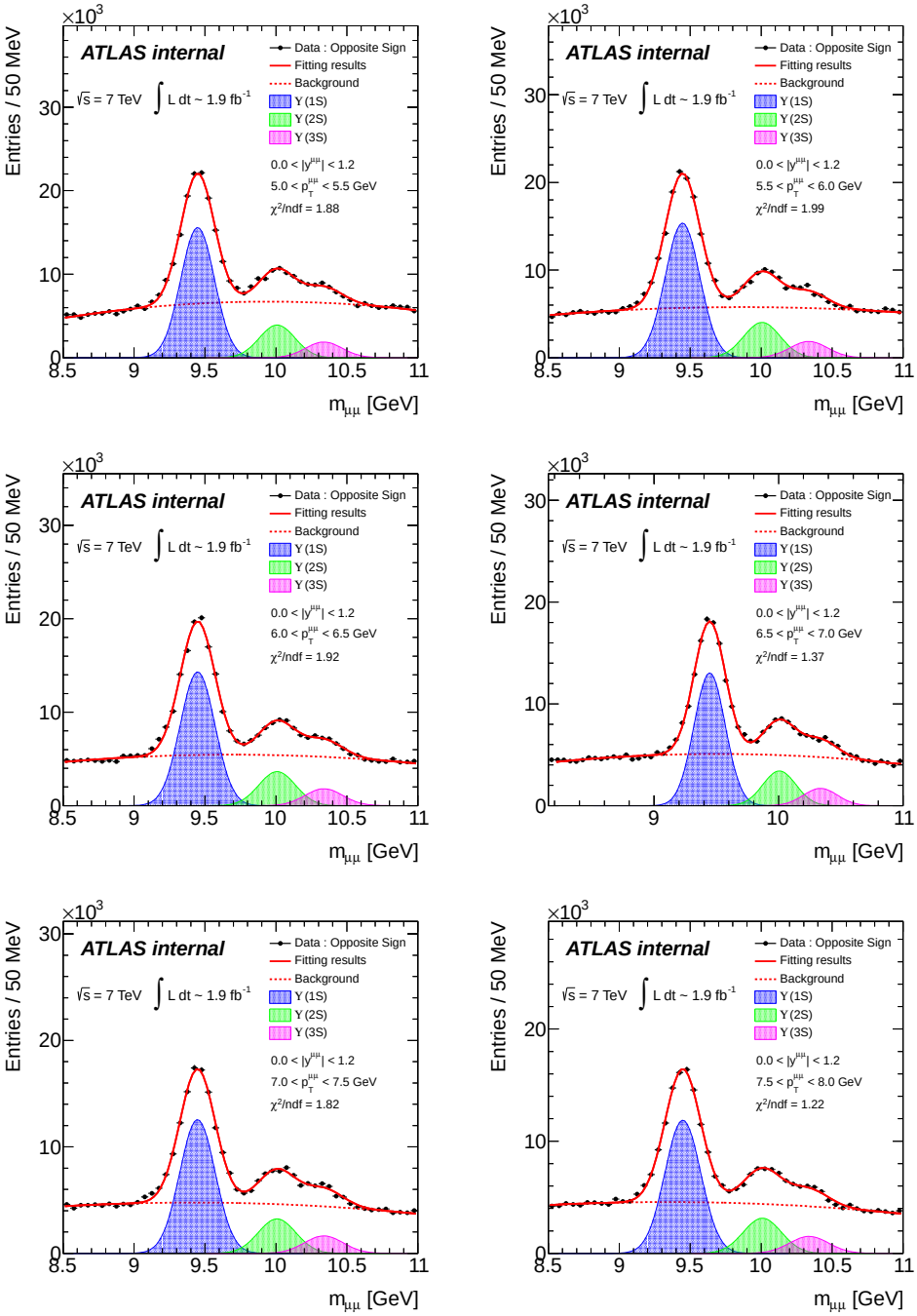
ATLAS internal
Data : Opposite Sign
Fitting results
Background
Y (1S)
Y (2S)
Y (3S)
√s = 7 TeV ∫ L dt ~ 1.9 fb-1
0.0 < |yμμ| < 1.2
5.0 < pTμμ < 5.5 GeV
χ2/ndf = 1.88
5.5 < pTμμ < 6.0 GeV
χ2/ndf = 1.99
6.0 < pTμμ < 6.5 GeV
χ2/ndf = 1.92
6.5 < pTμμ < 7.0 GeV
χ2/ndf = 1.37
7.0 < pTμμ < 7.5 GeV
χ2/ndf = 1.82
7.5 < pTμμ < 8.0 GeV
χ2/ndf = 1.22
Entries / 50 MeV
mμμ [GeV]
×10^3

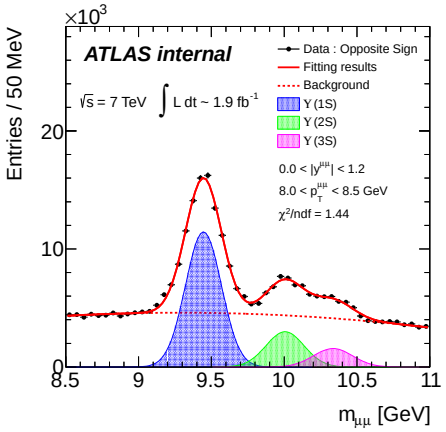
×10^3
ATLAS internal
√s = 7 TeV ∫ L dt ~ 1.9 fb^-1
Data : Opposite Sign
Fitting results
Background
Υ(1S)
Υ(2S)
Υ(3S)
0.0 < |y^μμ| < 1.2
8.0 < p_T^μμ < 8.5 GeV
χ²/ndf = 1.44
Entries / 50 MeV
m_μμ [GeV]

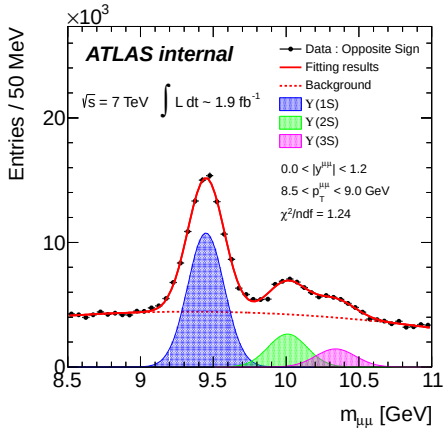
×10^3
ATLAS internal
√s = 7 TeV ∫ L dt ~ 1.9 fb^-1
Data : Opposite Sign
Fitting results
Background
Υ(1S)
Υ(2S)
Υ(3S)
0.0 < |y^μμ| < 1.2
8.5 < p_T^μμ < 9.0 GeV
χ²/ndf = 1.24
Entries / 50 MeV
m_μμ [GeV]

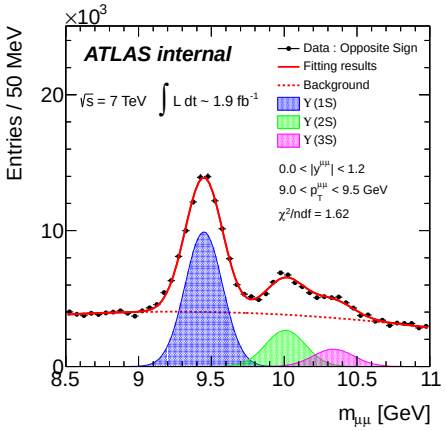
×10^3
ATLAS internal
√s = 7 TeV ∫ L dt ~ 1.9 fb^-1
Data : Opposite Sign
Fitting results
Background
Υ(1S)
Υ(2S)
Υ(3S)
0.0 < |y^μμ| < 1.2
9.0 < p_T^μμ < 9.5 GeV
χ²/ndf = 1.62
Entries / 50 MeV
m_μμ [GeV]

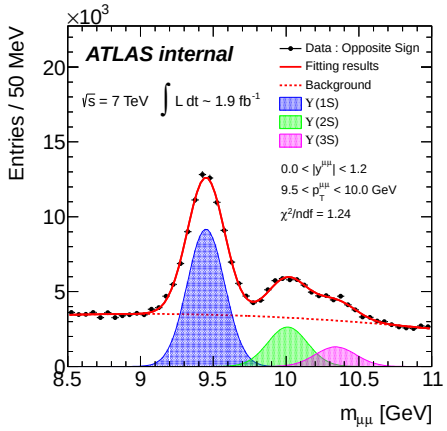
×10^3
ATLAS internal
√s = 7 TeV ∫ L dt ~ 1.9 fb^-1
Data : Opposite Sign
Fitting results
Background
Υ(1S)
Υ(2S)
Υ(3S)
0.0 < |y^μμ| < 1.2
9.5 < p_T^μμ < 10.0 GeV
χ²/ndf = 1.24
Entries / 50 MeV
m_μμ [GeV]

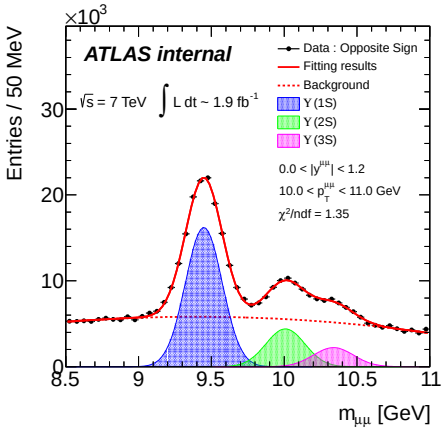
×10^3
ATLAS internal
√s = 7 TeV ∫ L dt ~ 1.9 fb^-1
Data : Opposite Sign
Fitting results
Background
Υ(1S)
Υ(2S)
Υ(3S)
0.0 < |y^μμ| < 1.2
10.0 < p_T^μμ < 11.0 GeV
χ²/ndf = 1.35
Entries / 50 MeV
m_μμ [GeV]

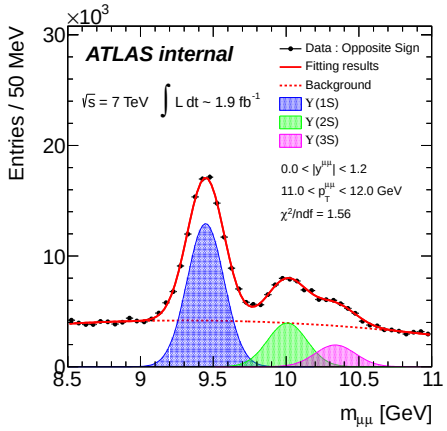
×10^3
ATLAS internal
√s = 7 TeV ∫ L dt ~ 1.9 fb^-1
Data : Opposite Sign
Fitting results
Background
Υ(1S)
Υ(2S)
Υ(3S)
0.0 < |y^μμ| < 1.2
11.0 < p_T^μμ < 12.0 GeV
χ²/ndf = 1.56
Entries / 50 MeV
m_μμ [GeV]

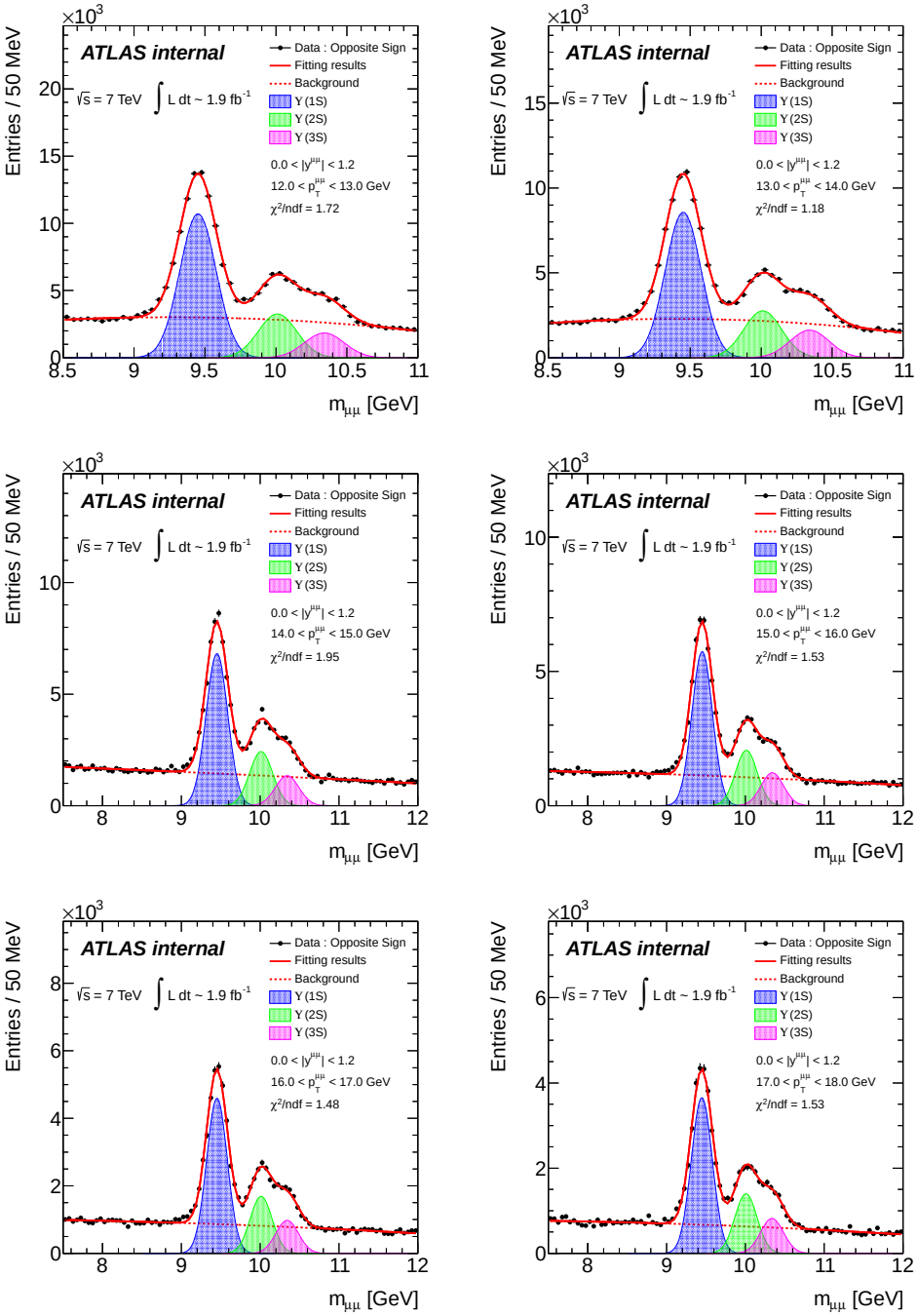
ATLAS internal
√s = 7 TeV ∫ L dt ~ 1.9 fb⁻¹
Data : Opposite Sign
Fitting results
Background
Υ(1S)
Υ(2S)
Υ(3S)
0.0 < |y^μμ| < 1.2
12.0 < p_T^μμ < 13.0 GeV
χ²/ndf = 1.72
13.0 < p_T^μμ < 14.0 GeV
χ²/ndf = 1.18
14.0 < p_T^μμ < 15.0 GeV
χ²/ndf = 1.95
15.0 < p_T^μμ < 16.0 GeV
χ²/ndf = 1.53
16.0 < p_T^μμ < 17.0 GeV
χ²/ndf = 1.48
17.0 < p_T^μμ < 18.0 GeV
χ²/ndf = 1.53
Entries / 50 MeV
×10³
m_μμ [GeV]

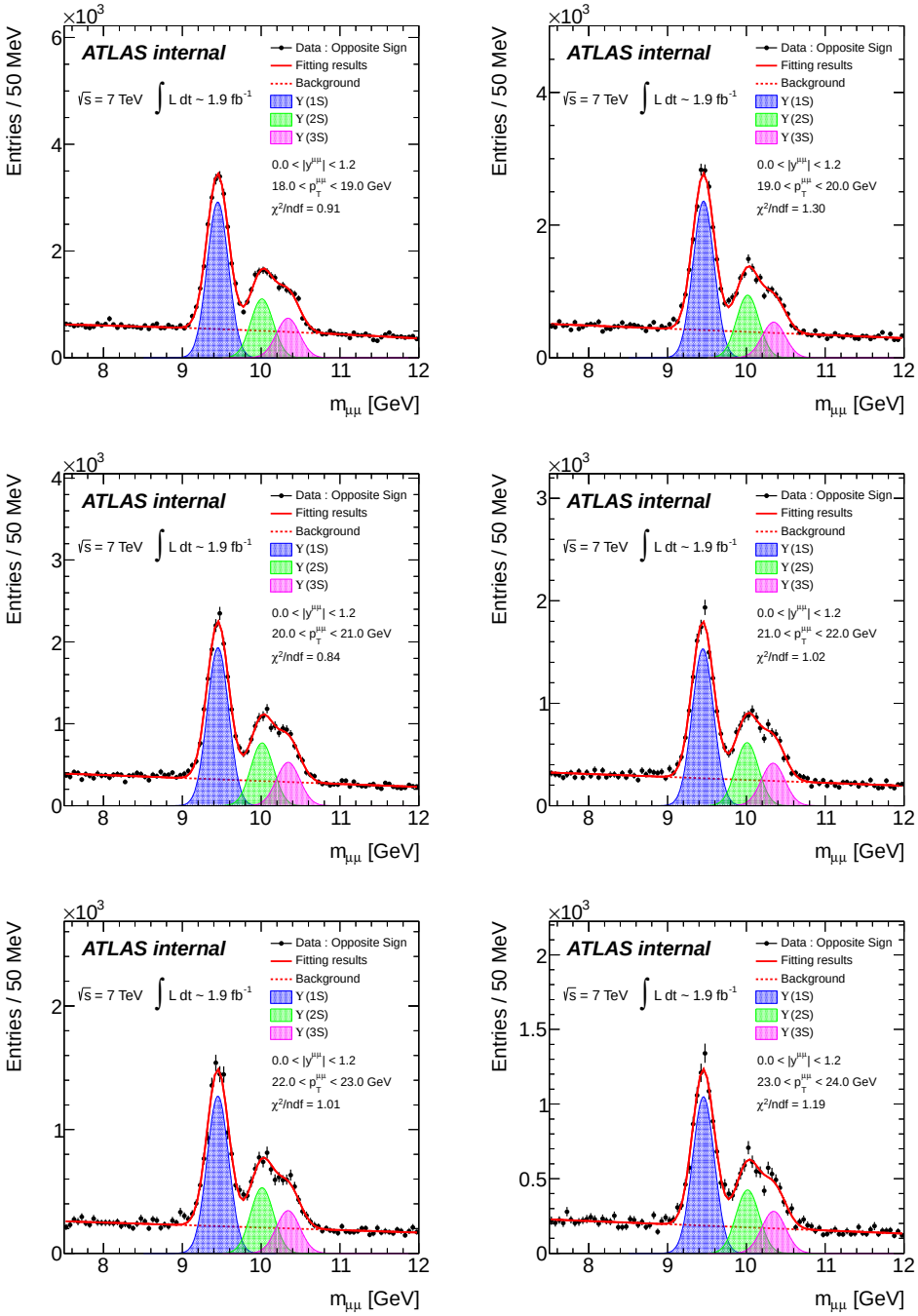
ATLAS internal
√s = 7 TeV ∫ L dt ~ 1.9 fb⁻¹
Data : Opposite Sign
Fitting results
Background
Υ(1S)
Υ(2S)
Υ(3S)
0.0 < |y^μμ| < 1.2
18.0 < p_T^μμ < 19.0 GeV
χ²/ndf = 0.91
19.0 < p_T^μμ < 20.0 GeV
χ²/ndf = 1.30
20.0 < p_T^μμ < 21.0 GeV
χ²/ndf = 0.84
21.0 < p_T^μμ < 22.0 GeV
χ²/ndf = 1.02
22.0 < p_T^μμ < 23.0 GeV
χ²/ndf = 1.01
23.0 < p_T^μμ < 24.0 GeV
χ²/ndf = 1.19
Entries / 50 MeV
m_μμ [GeV]

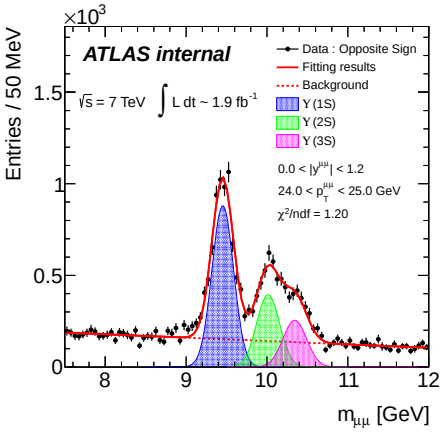
ATLAS internal
Data : Opposite Sign
Fitting results
Background
Υ(1S)
Υ(2S)
Υ(3S)
√s = 7 TeV ∫ L dt ~ 1.9 fb⁻¹
0.0 < |y^μμ| < 1.2
24.0 < p_T^μμ < 25.0 GeV
χ²/ndf = 1.20
Entries / 50 MeV
m_μμ [GeV]

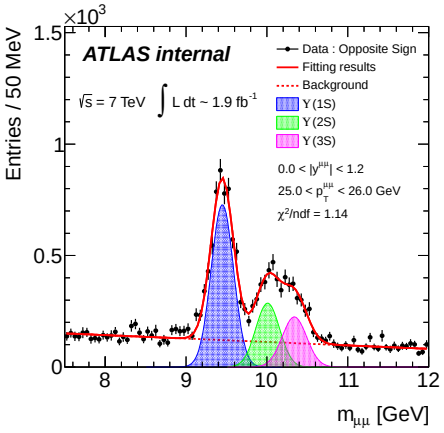
ATLAS internal
Data : Opposite Sign
Fitting results
Background
Υ(1S)
Υ(2S)
Υ(3S)
√s = 7 TeV ∫ L dt ~ 1.9 fb⁻¹
0.0 < |y^μμ| < 1.2
25.0 < p_T^μμ < 26.0 GeV
χ²/ndf = 1.14
Entries / 50 MeV
m_μμ [GeV]

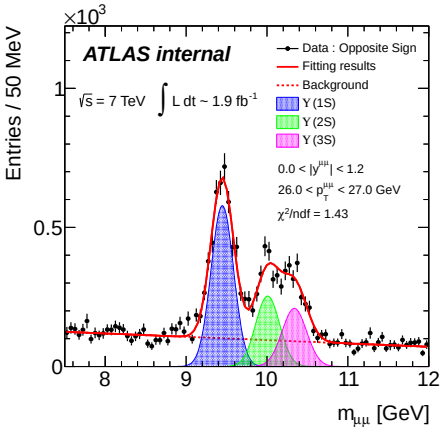
ATLAS internal
Data : Opposite Sign
Fitting results
Background
Υ(1S)
Υ(2S)
Υ(3S)
√s = 7 TeV ∫ L dt ~ 1.9 fb⁻¹
0.0 < |y^μμ| < 1.2
26.0 < p_T^μμ < 27.0 GeV
χ²/ndf = 1.43
Entries / 50 MeV
m_μμ [GeV]

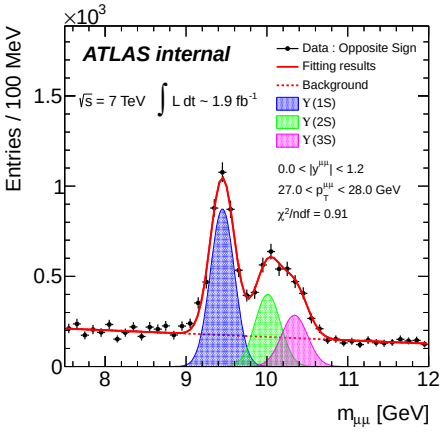
ATLAS internal
Data : Opposite Sign
Fitting results
Background
Υ(1S)
Υ(2S)
Υ(3S)
√s = 7 TeV ∫ L dt ~ 1.9 fb⁻¹
0.0 < |y^μμ| < 1.2
27.0 < p_T^μμ < 28.0 GeV
χ²/ndf = 0.91
Entries / 100 MeV
m_μμ [GeV]

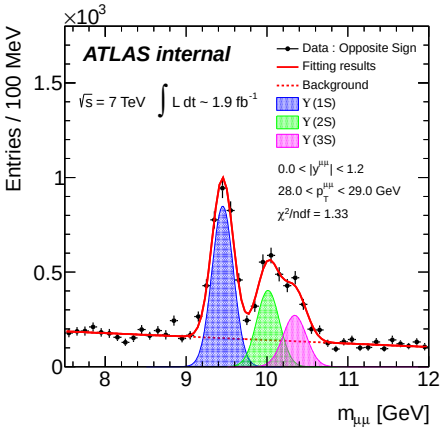
ATLAS internal
Data : Opposite Sign
Fitting results
Background
Υ(1S)
Υ(2S)
Υ(3S)
√s = 7 TeV ∫ L dt ~ 1.9 fb⁻¹
0.0 < |y^μμ| < 1.2
28.0 < p_T^μμ < 29.0 GeV
χ²/ndf = 1.33
Entries / 100 MeV
m_μμ [GeV]

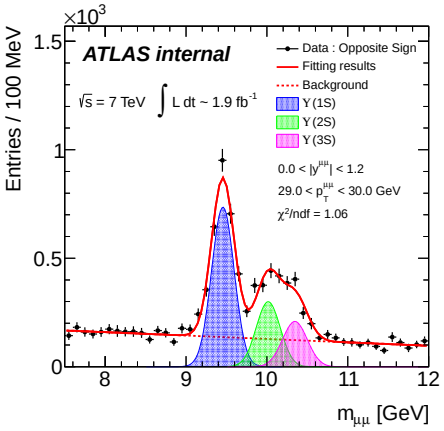
ATLAS internal
Data : Opposite Sign
Fitting results
Background
Υ(1S)
Υ(2S)
Υ(3S)
√s = 7 TeV ∫ L dt ~ 1.9 fb⁻¹
0.0 < |y^μμ| < 1.2
29.0 < p_T^μμ < 30.0 GeV
χ²/ndf = 1.06
Entries / 100 MeV
m_μμ [GeV]

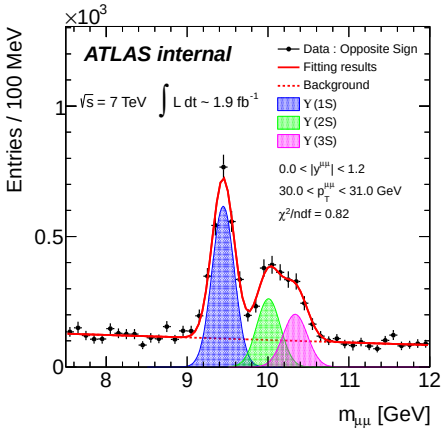
ATLAS internal
√s = 7 TeV ∫ L dt ~ 1.9 fb⁻¹
Data : Opposite Sign
Fitting results
Background
Υ(1S)
Υ(2S)
Υ(3S)
0.0 < |y^μμ| < 1.2
30.0 < p_T^μμ < 31.0 GeV
χ²/ndf = 0.82
Entries / 100 MeV
m_μμ [GeV]

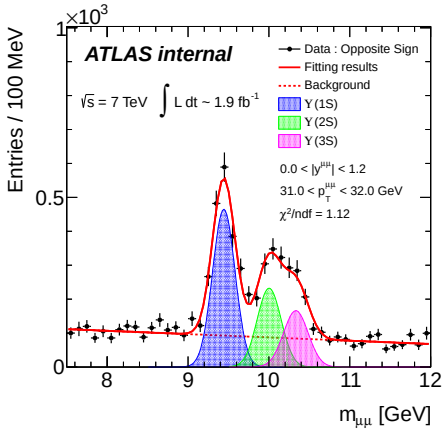
ATLAS internal
√s = 7 TeV ∫ L dt ~ 1.9 fb⁻¹
Data : Opposite Sign
Fitting results
Background
Υ(1S)
Υ(2S)
Υ(3S)
0.0 < |y^μμ| < 1.2
31.0 < p_T^μμ < 32.0 GeV
χ²/ndf = 1.12
Entries / 100 MeV
m_μμ [GeV]

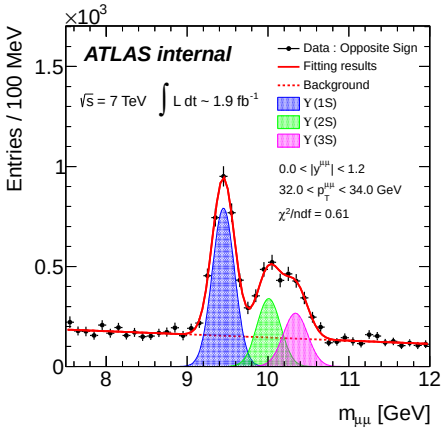
ATLAS internal
√s = 7 TeV ∫ L dt ~ 1.9 fb⁻¹
Data : Opposite Sign
Fitting results
Background
Υ(1S)
Υ(2S)
Υ(3S)
0.0 < |y^μμ| < 1.2
32.0 < p_T^μμ < 34.0 GeV
χ²/ndf = 0.61
Entries / 100 MeV
m_μμ [GeV]

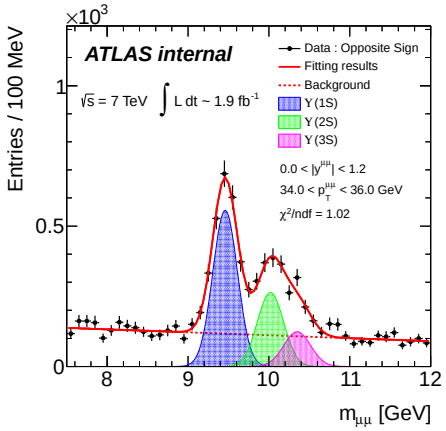
ATLAS internal
√s = 7 TeV ∫ L dt ~ 1.9 fb⁻¹
Data : Opposite Sign
Fitting results
Background
Υ(1S)
Υ(2S)
Υ(3S)
0.0 < |y^μμ| < 1.2
34.0 < p_T^μμ < 36.0 GeV
χ²/ndf = 1.02
Entries / 100 MeV
m_μμ [GeV]

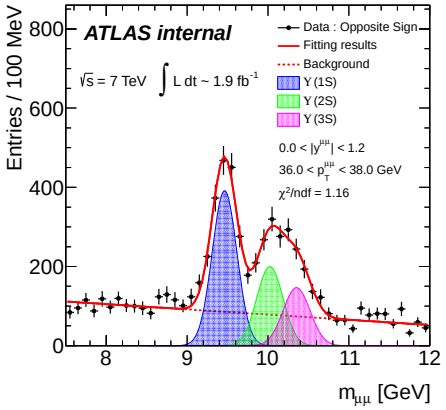
ATLAS internal
√s = 7 TeV ∫ L dt ~ 1.9 fb⁻¹
Data : Opposite Sign
Fitting results
Background
Υ(1S)
Υ(2S)
Υ(3S)
0.0 < |y^μμ| < 1.2
36.0 < p_T^μμ < 38.0 GeV
χ²/ndf = 1.16
Entries / 100 MeV
m_μμ [GeV]

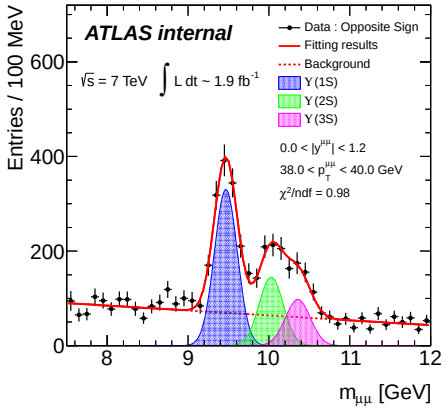
ATLAS internal
√s = 7 TeV ∫ L dt ~ 1.9 fb⁻¹
Data : Opposite Sign
Fitting results
Background
Υ(1S)
Υ(2S)
Υ(3S)
0.0 < |y^μμ| < 1.2
38.0 < p_T^μμ < 40.0 GeV
χ²/ndf = 0.98
Entries / 100 MeV
m_μμ [GeV]

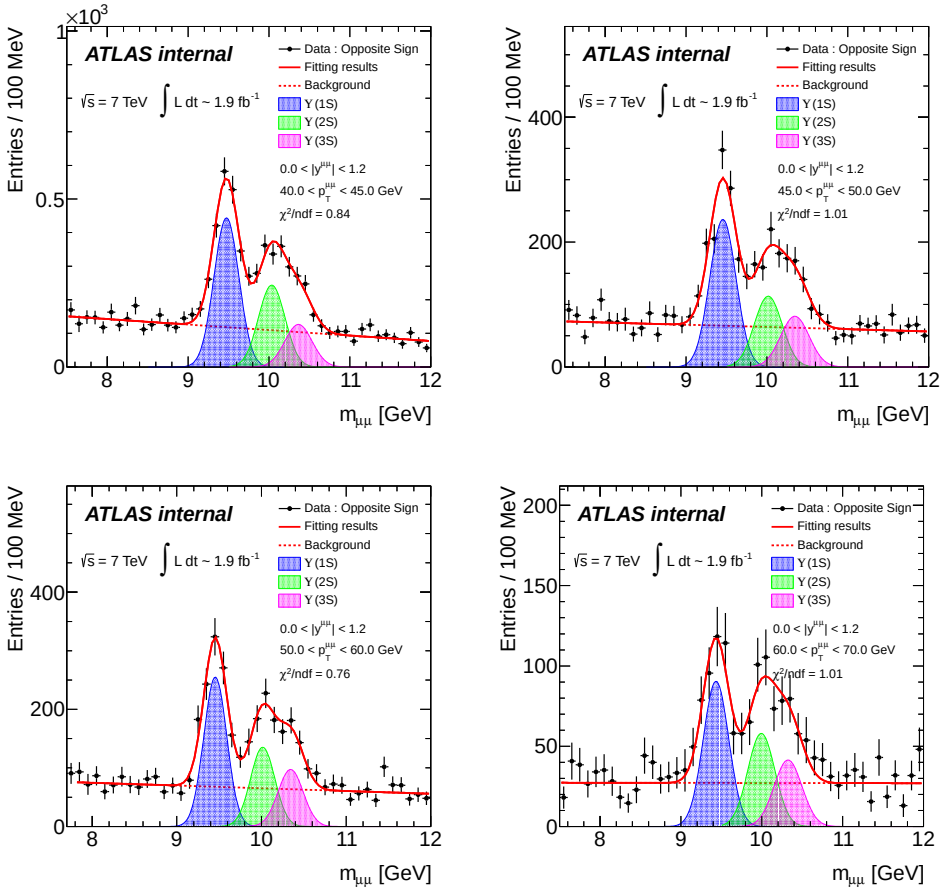
ATLAS internal
Data : Opposite Sign
Fitting results
Background
Υ(1S)
Υ(2S)
Υ(3S)
√s = 7 TeV ∫ L dt ~ 1.9 fb⁻¹
0.0 < |y^μμ| < 1.2
40.0 < p_T^μμ < 45.0 GeV
χ²/ndf = 0.84
45.0 < p_T^μμ < 50.0 GeV
χ²/ndf = 1.01
50.0 < p_T^μμ < 60.0 GeV
χ²/ndf = 0.76
60.0 < p_T^μμ < 70.0 GeV
χ²/ndf = 1.01
Entries / 100 MeV
m_μμ [GeV]
×10³

Table G.2: Υ mass fitting plots for fiducial cross-section as a function of p_T in rapidity region $1.2 < |y| < 2.3$.

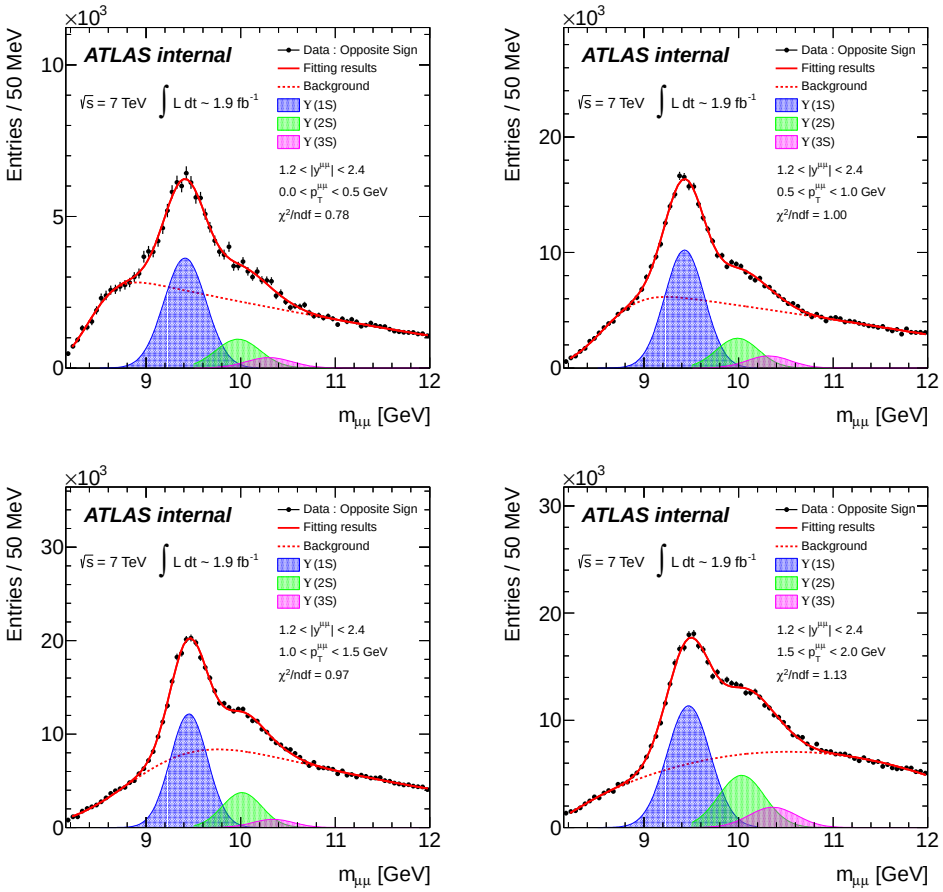

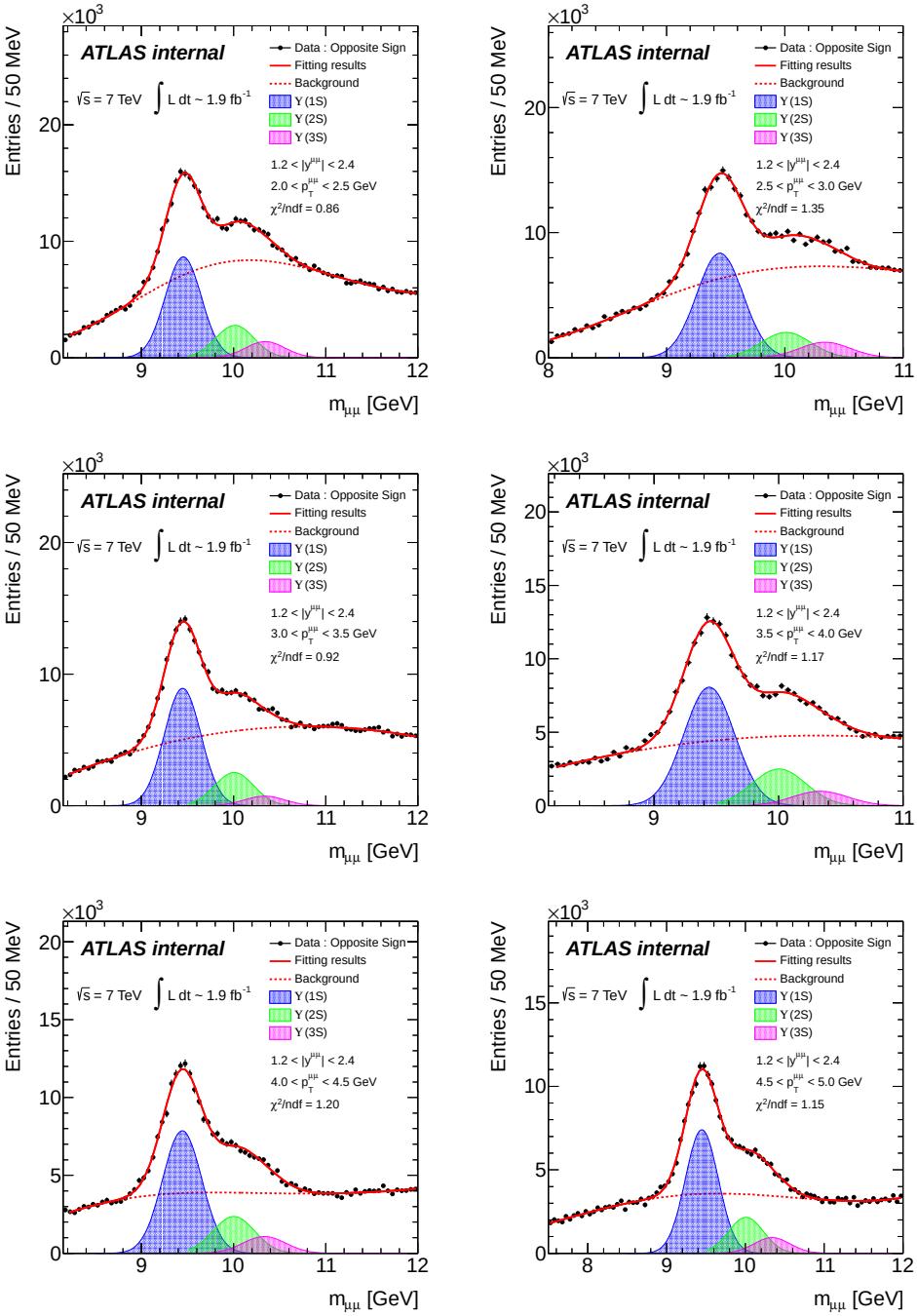
ATLAS internal
√s = 7 TeV ∫ L dt ~ 1.9 fb⁻¹
Data : Opposite Sign
Fitting results
Background
Υ(1S)
Υ(2S)
Υ(3S)
1.2 < |y^μμ| < 2.4
2.0 < p_T^μμ < 2.5 GeV
χ²/ndf = 0.86
2.5 < p_T^μμ < 3.0 GeV
χ²/ndf = 1.35
3.0 < p_T^μμ < 3.5 GeV
χ²/ndf = 0.92
3.5 < p_T^μμ < 4.0 GeV
χ²/ndf = 1.17
4.0 < p_T^μμ < 4.5 GeV
χ²/ndf = 1.20
4.5 < p_T^μμ < 5.0 GeV
χ²/ndf = 1.15
Entries / 50 MeV
×10³
m_μμ [GeV]

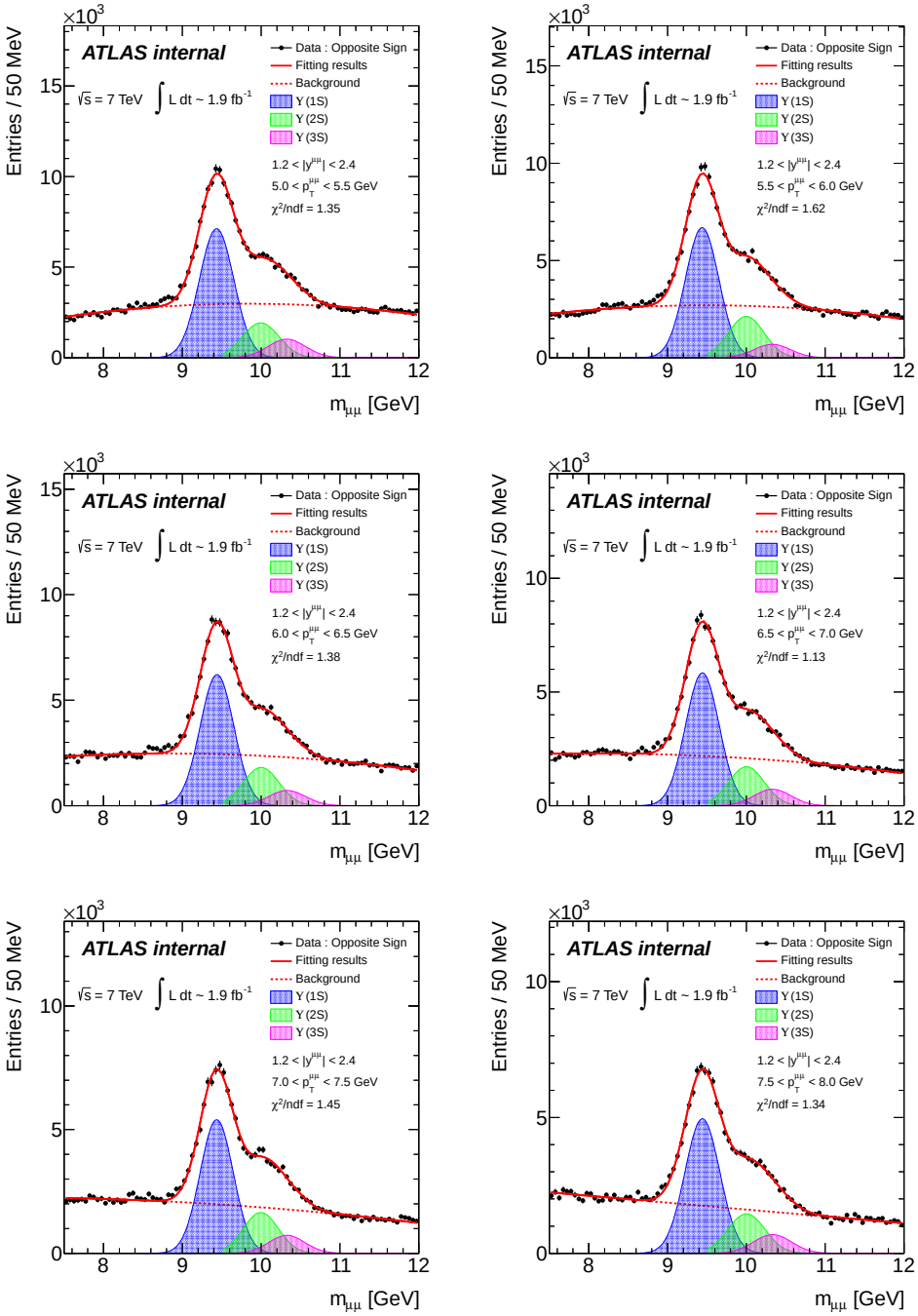
ATLAS internal
√s = 7 TeV ∫ L dt ~ 1.9 fb⁻¹
Data : Opposite Sign
Fitting results
Background
Υ(1S)
Υ(2S)
Υ(3S)
1.2 < |y^μμ| < 2.4
5.0 < p_T^μμ < 5.5 GeV
χ²/ndf = 1.35
5.5 < p_T^μμ < 6.0 GeV
χ²/ndf = 1.62
6.0 < p_T^μμ < 6.5 GeV
χ²/ndf = 1.38
6.5 < p_T^μμ < 7.0 GeV
χ²/ndf = 1.13
7.0 < p_T^μμ < 7.5 GeV
χ²/ndf = 1.45
7.5 < p_T^μμ < 8.0 GeV
χ²/ndf = 1.34
Entries / 50 MeV
×10³
m_μμ [GeV]

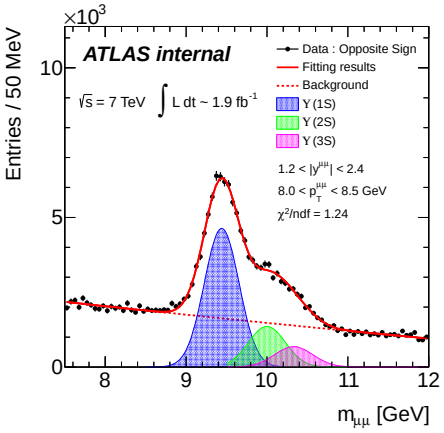
ATLAS internal
Data : Opposite Sign
Fitting results
Background
Υ(1S)
Υ(2S)
Υ(3S)
√s = 7 TeV ∫ L dt ~ 1.9 fb⁻¹
1.2 < |y^μμ| < 2.4
8.0 < p_T^μμ < 8.5 GeV
χ²/ndf = 1.24
Entries / 50 MeV
m_μμ [GeV]

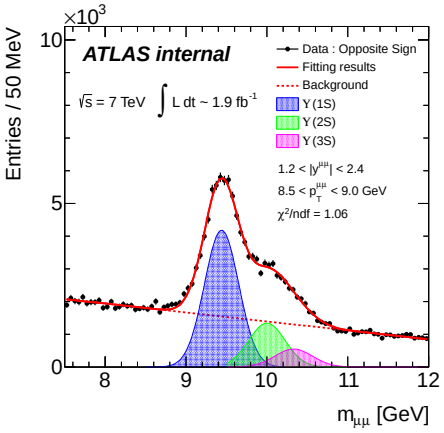
ATLAS internal
Data : Opposite Sign
Fitting results
Background
Υ(1S)
Υ(2S)
Υ(3S)
√s = 7 TeV ∫ L dt ~ 1.9 fb⁻¹
1.2 < |y^μμ| < 2.4
8.5 < p_T^μμ < 9.0 GeV
χ²/ndf = 1.06
Entries / 50 MeV
m_μμ [GeV]

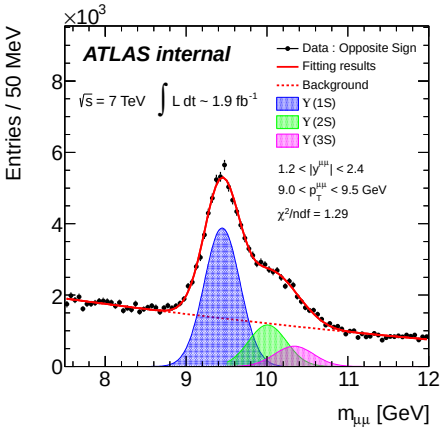
ATLAS internal
Data : Opposite Sign
Fitting results
Background
Υ(1S)
Υ(2S)
Υ(3S)
√s = 7 TeV ∫ L dt ~ 1.9 fb⁻¹
1.2 < |y^μμ| < 2.4
9.0 < p_T^μμ < 9.5 GeV
χ²/ndf = 1.29
Entries / 50 MeV
m_μμ [GeV]

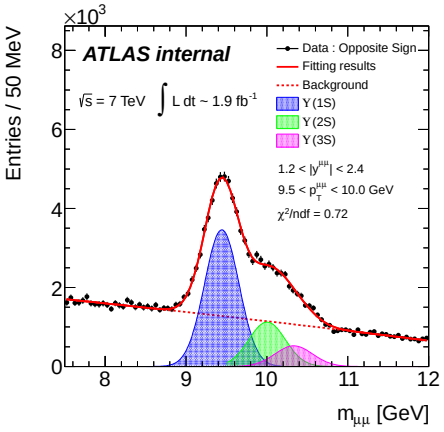
ATLAS internal
Data : Opposite Sign
Fitting results
Background
Υ(1S)
Υ(2S)
Υ(3S)
√s = 7 TeV ∫ L dt ~ 1.9 fb⁻¹
1.2 < |y^μμ| < 2.4
9.5 < p_T^μμ < 10.0 GeV
χ²/ndf = 0.72
Entries / 50 MeV
m_μμ [GeV]

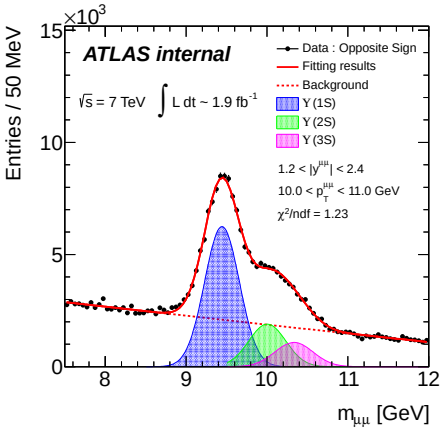
ATLAS internal
Data : Opposite Sign
Fitting results
Background
Υ(1S)
Υ(2S)
Υ(3S)
√s = 7 TeV ∫ L dt ~ 1.9 fb⁻¹
1.2 < |y^μμ| < 2.4
10.0 < p_T^μμ < 11.0 GeV
χ²/ndf = 1.23
Entries / 50 MeV
m_μμ [GeV]

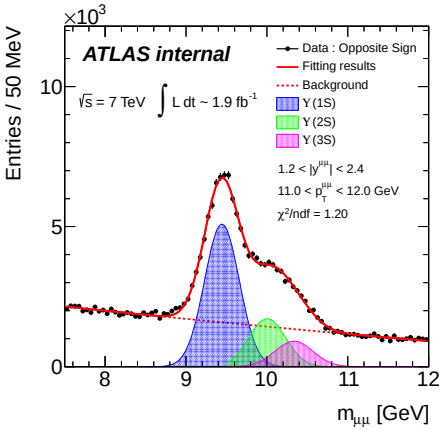
ATLAS internal
Data : Opposite Sign
Fitting results
Background
Υ(1S)
Υ(2S)
Υ(3S)
√s = 7 TeV ∫ L dt ~ 1.9 fb⁻¹
1.2 < |y^μμ| < 2.4
11.0 < p_T^μμ < 12.0 GeV
χ²/ndf = 1.20
Entries / 50 MeV
m_μμ [GeV]

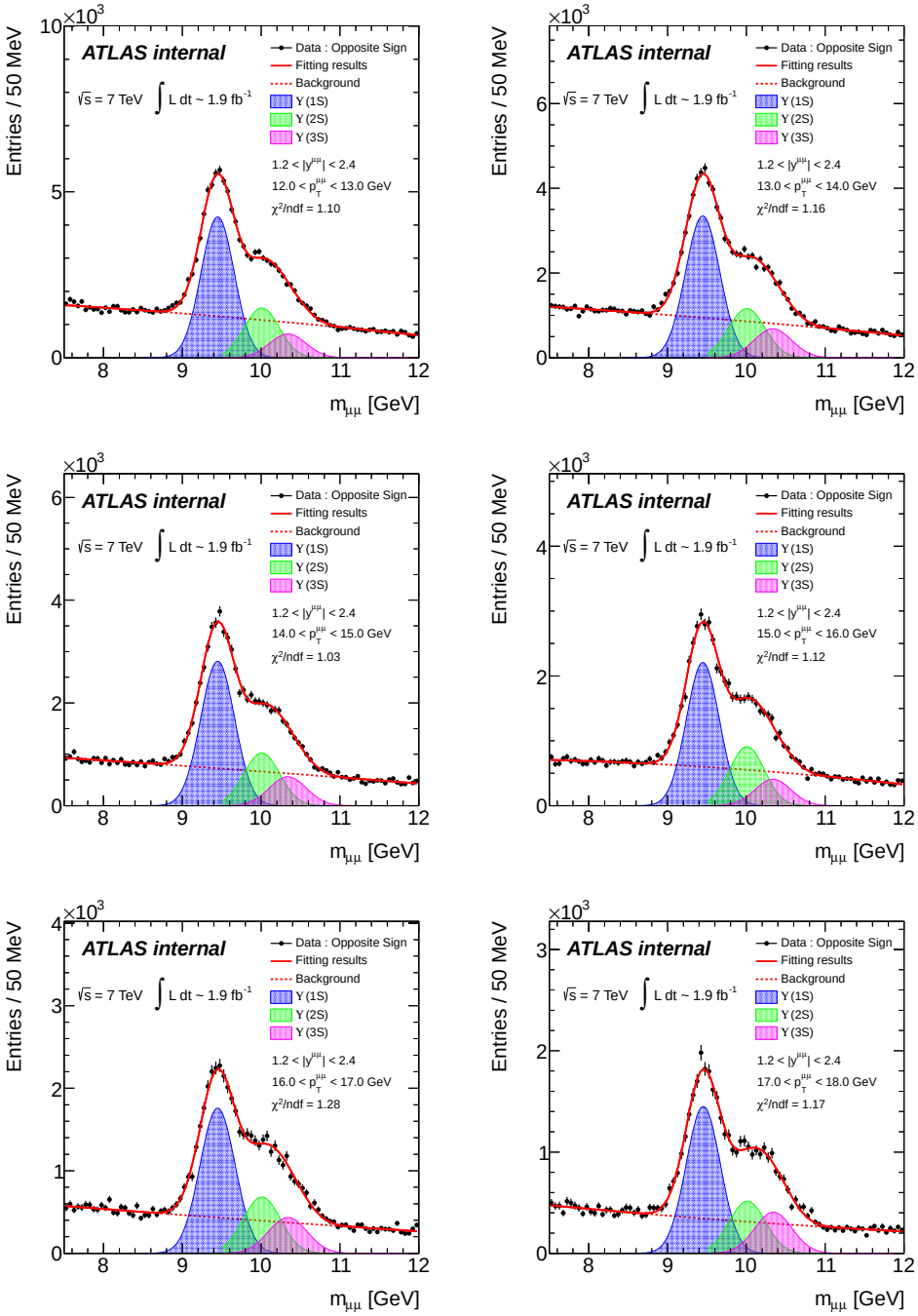
ATLAS internal
√s = 7 TeV ∫ L dt ~ 1.9 fb⁻¹
Data : Opposite Sign
Fitting results
Background
Υ(1S)
Υ(2S)
Υ(3S)
1.2 < |y^μμ| < 2.4
12.0 < p_T^μμ < 13.0 GeV
χ²/ndf = 1.10
13.0 < p_T^μμ < 14.0 GeV
χ²/ndf = 1.16
14.0 < p_T^μμ < 15.0 GeV
χ²/ndf = 1.03
15.0 < p_T^μμ < 16.0 GeV
χ²/ndf = 1.12
16.0 < p_T^μμ < 17.0 GeV
χ²/ndf = 1.28
17.0 < p_T^μμ < 18.0 GeV
χ²/ndf = 1.17
Entries / 50 MeV
m_μμ [GeV]

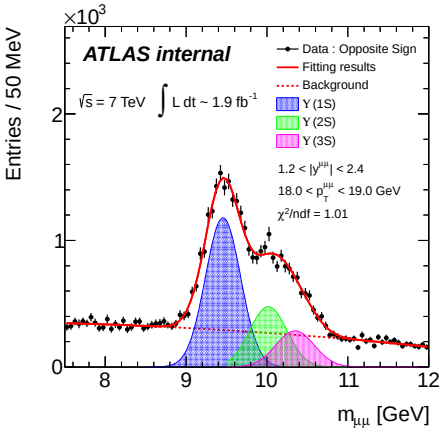
ATLAS internal
Data : Opposite Sign
Fitting results
Background
Υ(1S)
Υ(2S)
Υ(3S)
√s = 7 TeV ∫ L dt ~ 1.9 fb⁻¹
1.2 < |y^μμ| < 2.4
18.0 < p_T^μμ < 19.0 GeV
χ²/ndf = 1.01
Entries / 50 MeV
m_μμ [GeV]

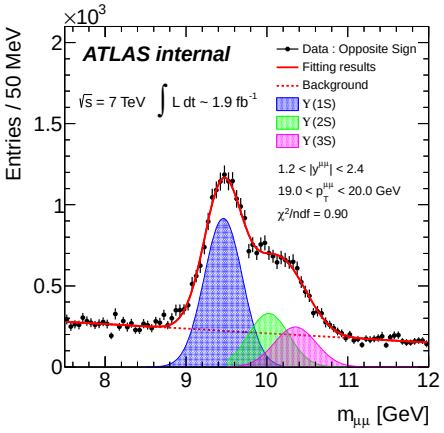
ATLAS internal
Data : Opposite Sign
Fitting results
Background
Υ(1S)
Υ(2S)
Υ(3S)
√s = 7 TeV ∫ L dt ~ 1.9 fb⁻¹
1.2 < |y^μμ| < 2.4
19.0 < p_T^μμ < 20.0 GeV
χ²/ndf = 0.90
Entries / 50 MeV
m_μμ [GeV]

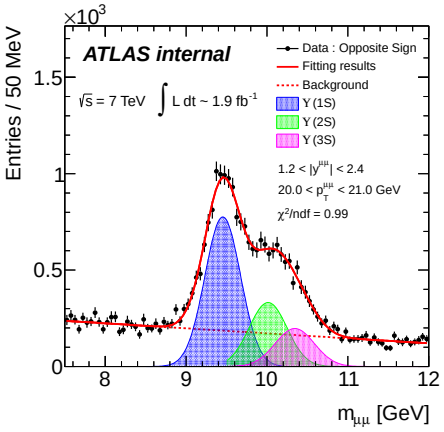
ATLAS internal
Data : Opposite Sign
Fitting results
Background
Υ(1S)
Υ(2S)
Υ(3S)
√s = 7 TeV ∫ L dt ~ 1.9 fb⁻¹
1.2 < |y^μμ| < 2.4
20.0 < p_T^μμ < 21.0 GeV
χ²/ndf = 0.99
Entries / 50 MeV
m_μμ [GeV]

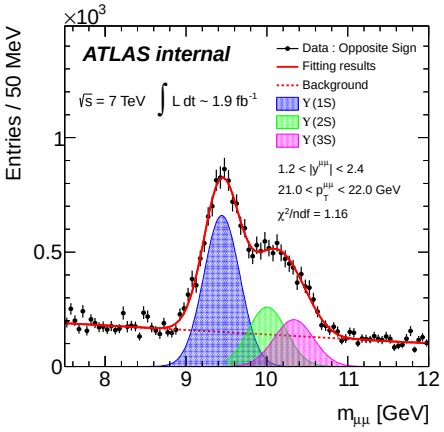
ATLAS internal
Data : Opposite Sign
Fitting results
Background
Υ(1S)
Υ(2S)
Υ(3S)
√s = 7 TeV ∫ L dt ~ 1.9 fb⁻¹
1.2 < |y^μμ| < 2.4
21.0 < p_T^μμ < 22.0 GeV
χ²/ndf = 1.16
Entries / 50 MeV
m_μμ [GeV]

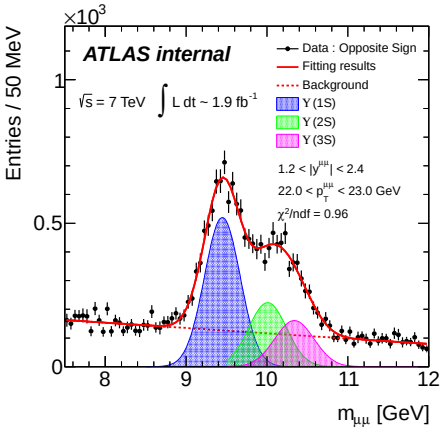
ATLAS internal
Data : Opposite Sign
Fitting results
Background
Υ(1S)
Υ(2S)
Υ(3S)
√s = 7 TeV ∫ L dt ~ 1.9 fb⁻¹
1.2 < |y^μμ| < 2.4
22.0 < p_T^μμ < 23.0 GeV
χ²/ndf = 0.96
Entries / 50 MeV
m_μμ [GeV]

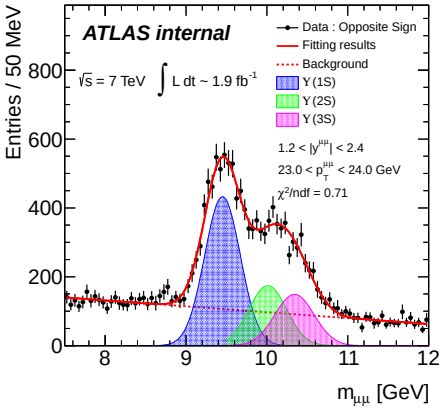
ATLAS internal
Data : Opposite Sign
Fitting results
Background
Υ(1S)
Υ(2S)
Υ(3S)
√s = 7 TeV ∫ L dt ~ 1.9 fb⁻¹
1.2 < |y^μμ| < 2.4
23.0 < p_T^μμ < 24.0 GeV
χ²/ndf = 0.71
Entries / 50 MeV
m_μμ [GeV]

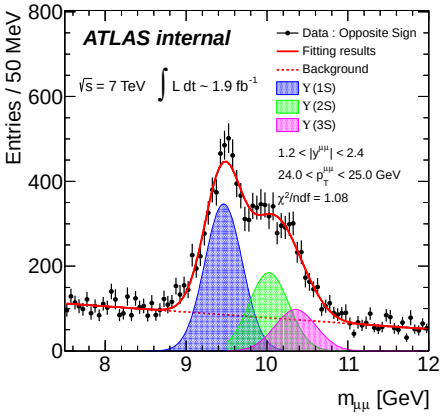
ATLAS internal
√s = 7 TeV ∫ L dt ~ 1.9 fb⁻¹
Data : Opposite Sign
Fitting results
Background
Υ(1S)
Υ(2S)
Υ(3S)
1.2 < |y^μμ| < 2.4
24.0 < p_T^μμ < 25.0 GeV
χ²/ndf = 1.08
Entries / 50 MeV
m_μμ [GeV]

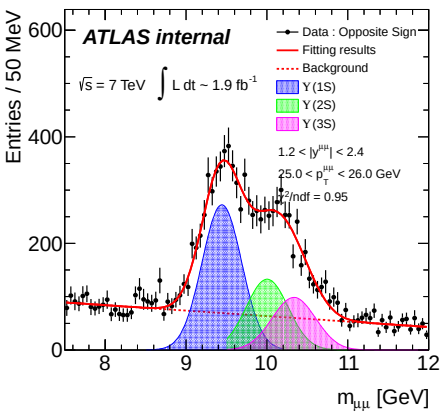
ATLAS internal
√s = 7 TeV ∫ L dt ~ 1.9 fb⁻¹
Data : Opposite Sign
Fitting results
Background
Υ(1S)
Υ(2S)
Υ(3S)
1.2 < |y^μμ| < 2.4
25.0 < p_T^μμ < 26.0 GeV
χ²/ndf = 0.95
Entries / 50 MeV
m_μμ [GeV]

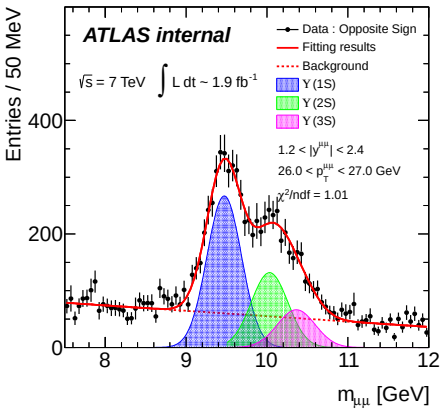
ATLAS internal
√s = 7 TeV ∫ L dt ~ 1.9 fb⁻¹
Data : Opposite Sign
Fitting results
Background
Υ(1S)
Υ(2S)
Υ(3S)
1.2 < |y^μμ| < 2.4
26.0 < p_T^μμ < 27.0 GeV
χ²/ndf = 1.01
Entries / 50 MeV
m_μμ [GeV]

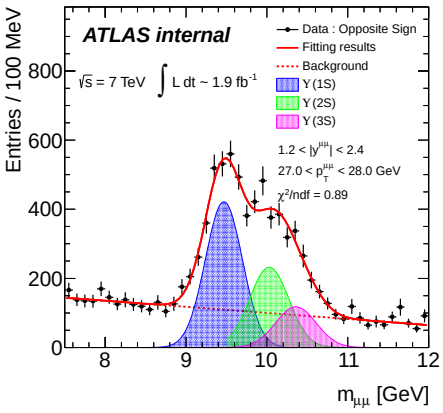
ATLAS internal
√s = 7 TeV ∫ L dt ~ 1.9 fb⁻¹
Data : Opposite Sign
Fitting results
Background
Υ(1S)
Υ(2S)
Υ(3S)
1.2 < |y^μμ| < 2.4
27.0 < p_T^μμ < 28.0 GeV
χ²/ndf = 0.89
Entries / 100 MeV
m_μμ [GeV]

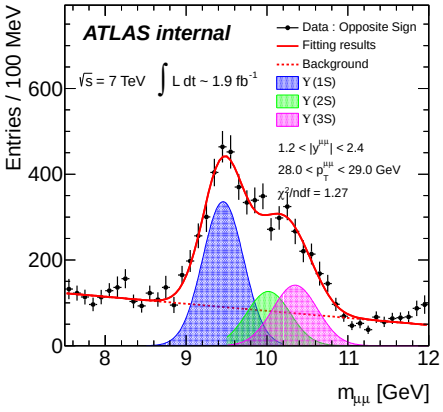
ATLAS internal
√s = 7 TeV ∫ L dt ~ 1.9 fb⁻¹
Data : Opposite Sign
Fitting results
Background
Υ(1S)
Υ(2S)
Υ(3S)
1.2 < |y^μμ| < 2.4
28.0 < p_T^μμ < 29.0 GeV
χ²/ndf = 1.27
Entries / 100 MeV
m_μμ [GeV]

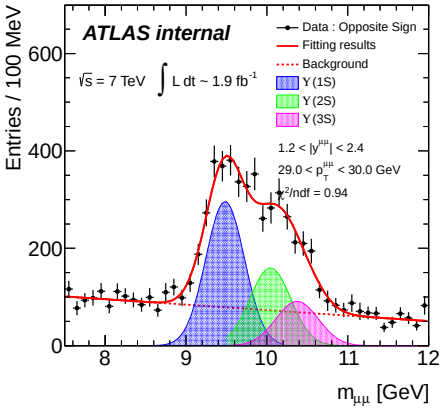
ATLAS internal
√s = 7 TeV ∫ L dt ~ 1.9 fb⁻¹
Data : Opposite Sign
Fitting results
Background
Υ(1S)
Υ(2S)
Υ(3S)
1.2 < |y^μμ| < 2.4
29.0 < p_T^μμ < 30.0 GeV
χ²/ndf = 0.94
Entries / 100 MeV
m_μμ [GeV]

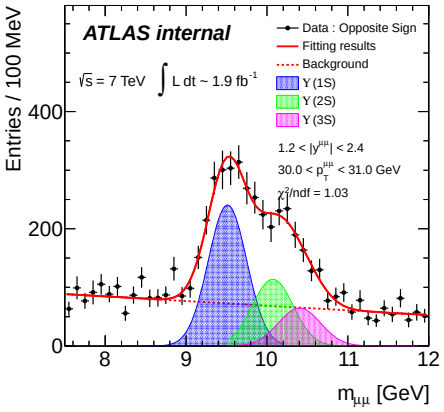
ATLAS internal
Data : Opposite Sign
Fitting results
Background
Υ(1S)
Υ(2S)
Υ(3S)
√s = 7 TeV ∫ L dt ~ 1.9 fb⁻¹
1.2 < |y^μμ| < 2.4
30.0 < p_T^μμ < 31.0 GeV
χ²/ndf = 1.03
Entries / 100 MeV
m_μμ [GeV]

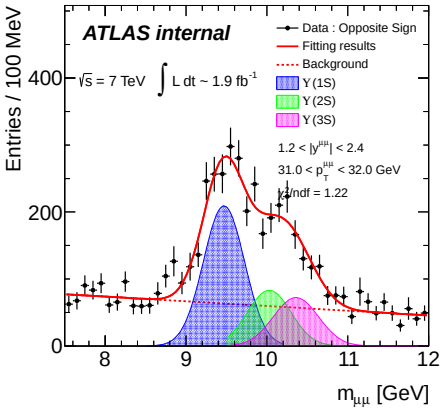
ATLAS internal
Data : Opposite Sign
Fitting results
Background
Υ(1S)
Υ(2S)
Υ(3S)
√s = 7 TeV ∫ L dt ~ 1.9 fb⁻¹
1.2 < |y^μμ| < 2.4
31.0 < p_T^μμ < 32.0 GeV
χ²/ndf = 1.22
Entries / 100 MeV
m_μμ [GeV]

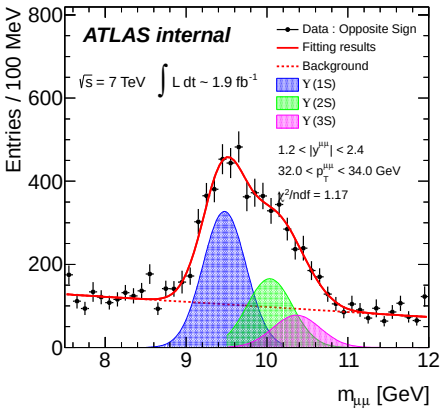
ATLAS internal
Data : Opposite Sign
Fitting results
Background
Υ(1S)
Υ(2S)
Υ(3S)
√s = 7 TeV ∫ L dt ~ 1.9 fb⁻¹
1.2 < |y^μμ| < 2.4
32.0 < p_T^μμ < 34.0 GeV
χ²/ndf = 1.17
Entries / 100 MeV
m_μμ [GeV]

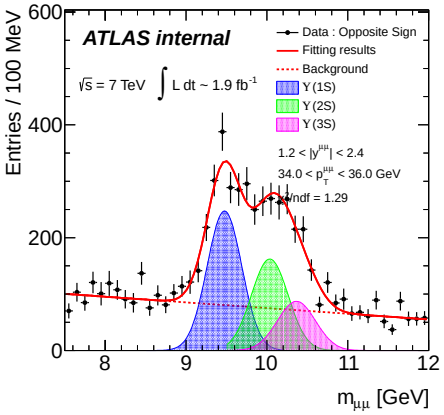
ATLAS internal
Data : Opposite Sign
Fitting results
Background
Υ(1S)
Υ(2S)
Υ(3S)
√s = 7 TeV ∫ L dt ~ 1.9 fb⁻¹
1.2 < |y^μμ| < 2.4
34.0 < p_T^μμ < 36.0 GeV
χ²/ndf = 1.29
Entries / 100 MeV
m_μμ [GeV]

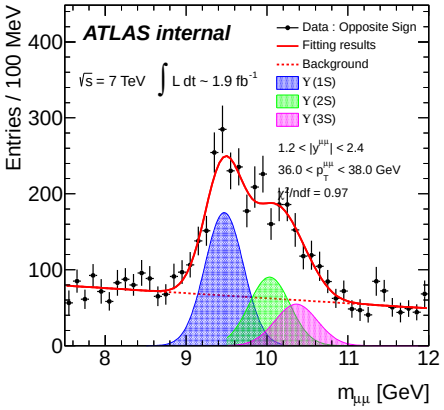
ATLAS internal
Data : Opposite Sign
Fitting results
Background
Υ(1S)
Υ(2S)
Υ(3S)
√s = 7 TeV ∫ L dt ~ 1.9 fb⁻¹
1.2 < |y^μμ| < 2.4
36.0 < p_T^μμ < 38.0 GeV
χ²/ndf = 0.97
Entries / 100 MeV
m_μμ [GeV]

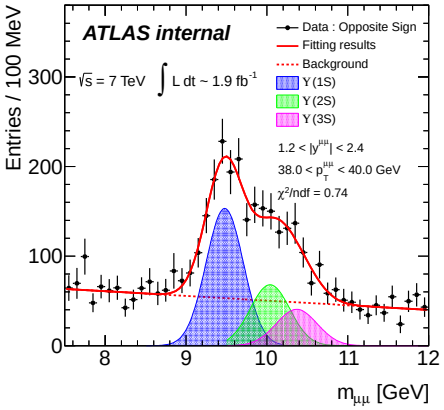
ATLAS internal
Data : Opposite Sign
Fitting results
Background
Υ(1S)
Υ(2S)
Υ(3S)
√s = 7 TeV ∫ L dt ~ 1.9 fb⁻¹
1.2 < |y^μμ| < 2.4
38.0 < p_T^μμ < 40.0 GeV
χ²/ndf = 0.74
Entries / 100 MeV
m_μμ [GeV]

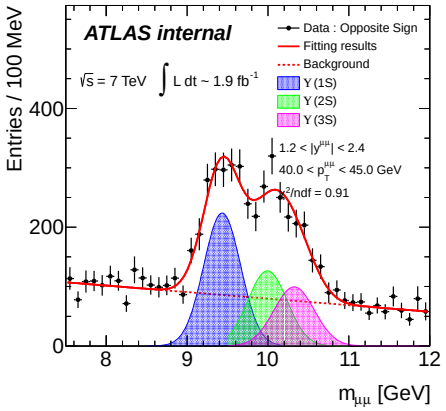
ATLAS internal
Data : Opposite Sign
Fitting results
Background
Υ(1S)
Υ(2S)
Υ(3S)
√s = 7 TeV ∫ L dt ~ 1.9 fb-1
1.2 < |yμμ| < 2.4
40.0 < pTμμ < 45.0 GeV
χ2/ndf = 0.91
Entries / 100 MeV
mμμ [GeV]

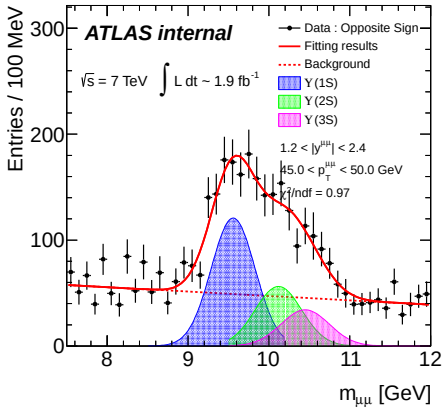
ATLAS internal
Data : Opposite Sign
Fitting results
Background
Υ(1S)
Υ(2S)
Υ(3S)
√s = 7 TeV ∫ L dt ~ 1.9 fb-1
1.2 < |yμμ| < 2.4
45.0 < pTμμ < 50.0 GeV
χ2/ndf = 0.97
Entries / 100 MeV
mμμ [GeV]

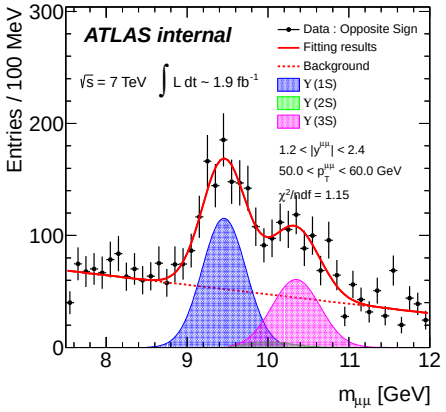
ATLAS internal
Data : Opposite Sign
Fitting results
Background
Υ(1S)
Υ(2S)
Υ(3S)
√s = 7 TeV ∫ L dt ~ 1.9 fb-1
1.2 < |yμμ| < 2.4
50.0 < pTμμ < 60.0 GeV
χ2/ndf = 1.15
Entries / 100 MeV
mμμ [GeV]

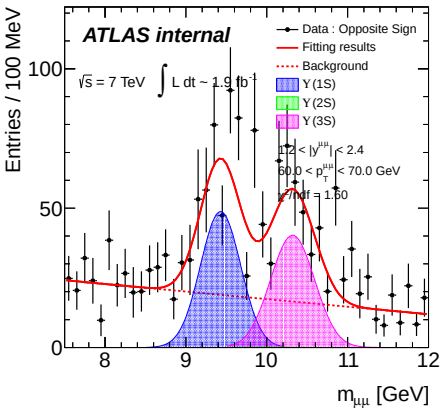
ATLAS internal
Data : Opposite Sign
Fitting results
Background
Υ(1S)
Υ(2S)
Υ(3S)
√s = 7 TeV ∫ L dt ~ 1.9 fb-1
1.2 < |yμμ| < 2.4
60.0 < pTμμ < 70.0 GeV
χ2/ndf = 1.50
Entries / 100 MeV
mμμ [GeV]

Table G.3: ϒ mass fitting plots for fiducial cross-section as a function of y.

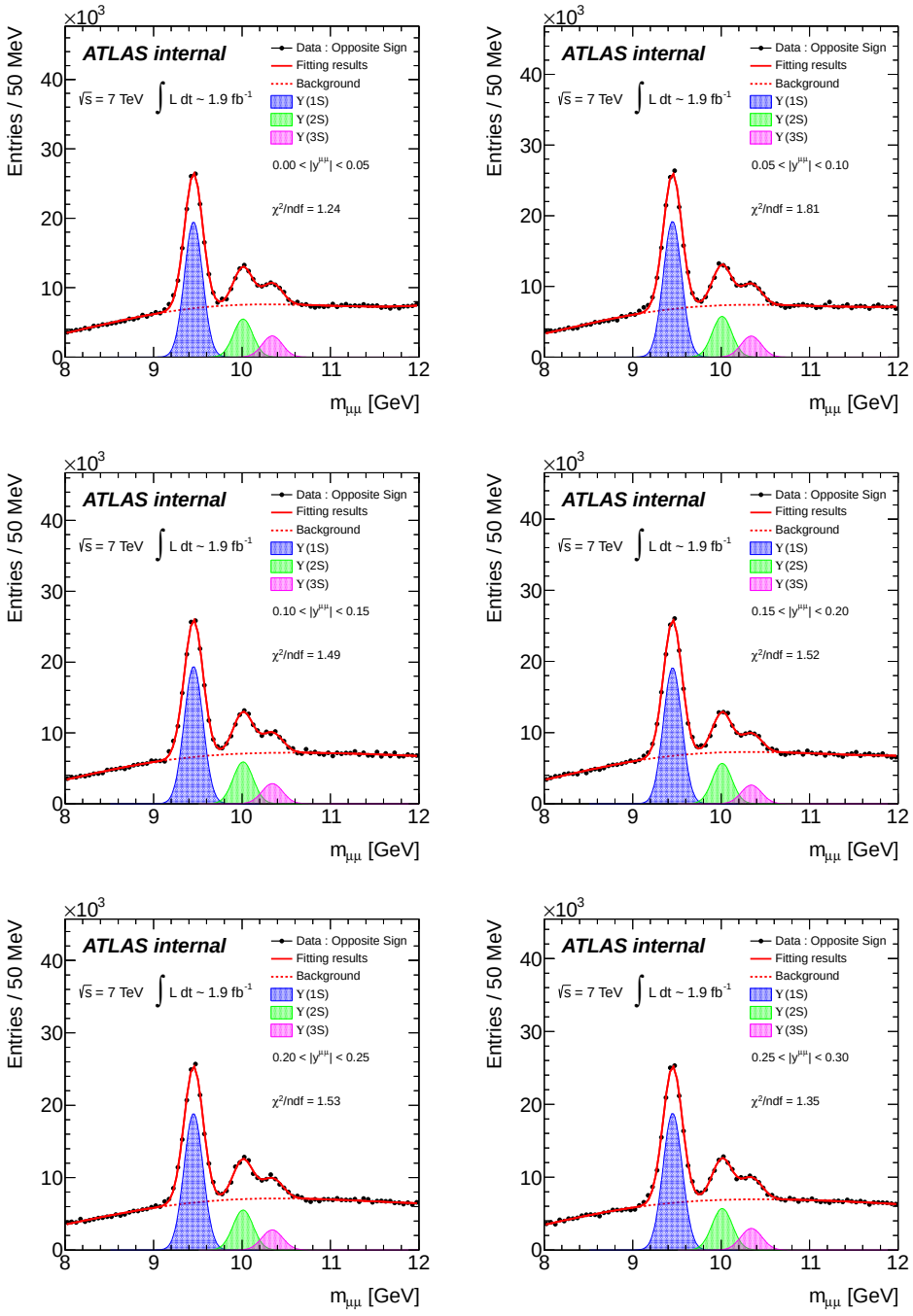

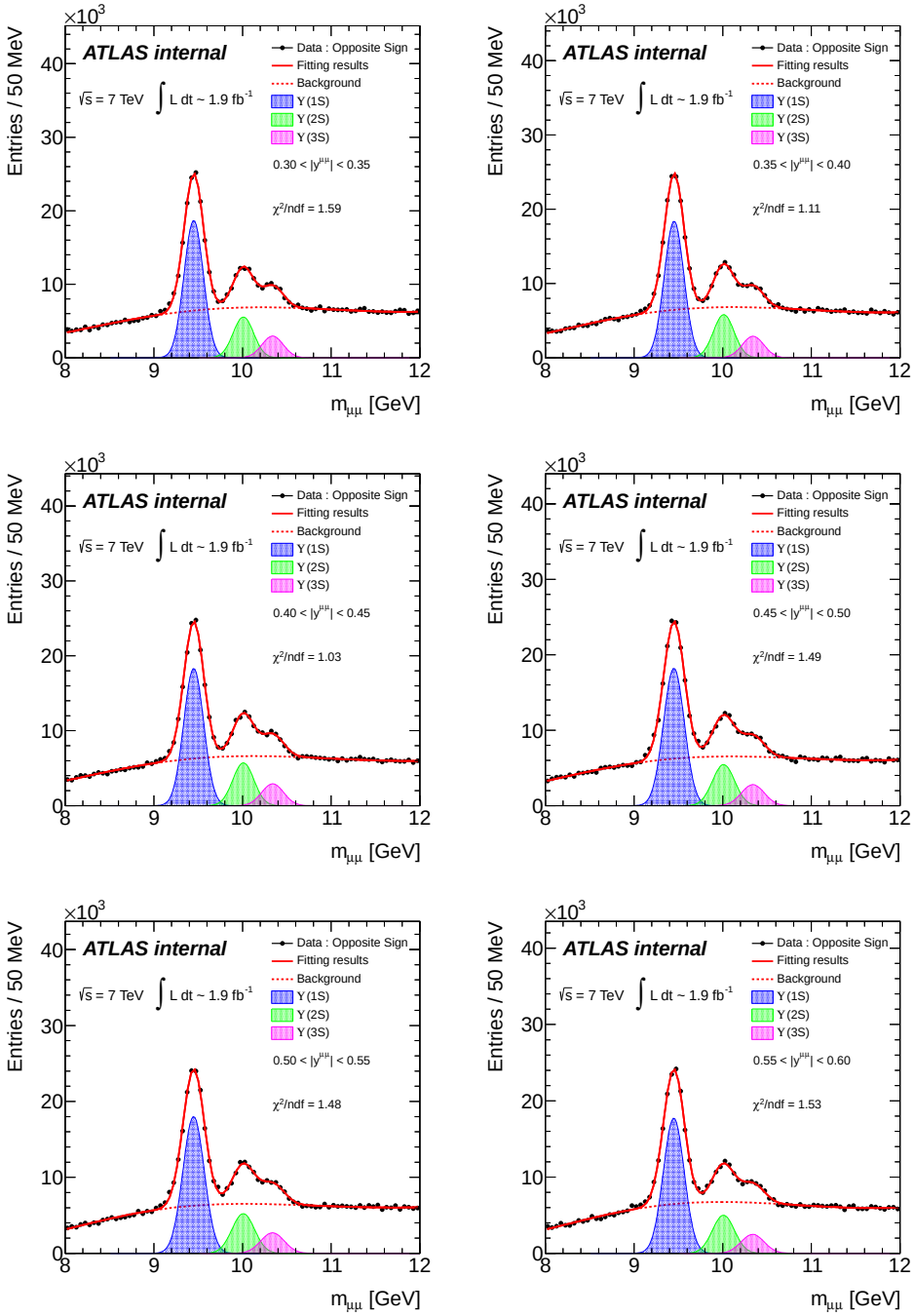
×10^3
Entries / 50 MeV
ATLAS internal
√s = 7 TeV ∫ L dt ~ 1.9 fb^-1
Data : Opposite Sign
Fitting results
Background
Υ(1S)
Υ(2S)
Υ(3S)
0.30 < |y^μμ| < 0.35
χ²/ndf = 1.59
m_μμ [GeV]
×10^3
Entries / 50 MeV
ATLAS internal
√s = 7 TeV ∫ L dt ~ 1.9 fb^-1
Data : Opposite Sign
Fitting results
Background
Υ(1S)
Υ(2S)
Υ(3S)
0.35 < |y^μμ| < 0.40
χ²/ndf = 1.11
m_μμ [GeV]
×10^3
Entries / 50 MeV
ATLAS internal
√s = 7 TeV ∫ L dt ~ 1.9 fb^-1
Data : Opposite Sign
Fitting results
Background
Υ(1S)
Υ(2S)
Υ(3S)
0.40 < |y^μμ| < 0.45
χ²/ndf = 1.03
m_μμ [GeV]
×10^3
Entries / 50 MeV
ATLAS internal
√s = 7 TeV ∫ L dt ~ 1.9 fb^-1
Data : Opposite Sign
Fitting results
Background
Υ(1S)
Υ(2S)
Υ(3S)
0.45 < |y^μμ| < 0.50
χ²/ndf = 1.49
m_μμ [GeV]
×10^3
Entries / 50 MeV
ATLAS internal
√s = 7 TeV ∫ L dt ~ 1.9 fb^-1
Data : Opposite Sign
Fitting results
Background
Υ(1S)
Υ(2S)
Υ(3S)
0.50 < |y^μμ| < 0.55
χ²/ndf = 1.48
m_μμ [GeV]
×10^3
Entries / 50 MeV
ATLAS internal
√s = 7 TeV ∫ L dt ~ 1.9 fb^-1
Data : Opposite Sign
Fitting results
Background
Υ(1S)
Υ(2S)
Υ(3S)
0.55 < |y^μμ| < 0.60
χ²/ndf = 1.53
m_μμ [GeV]

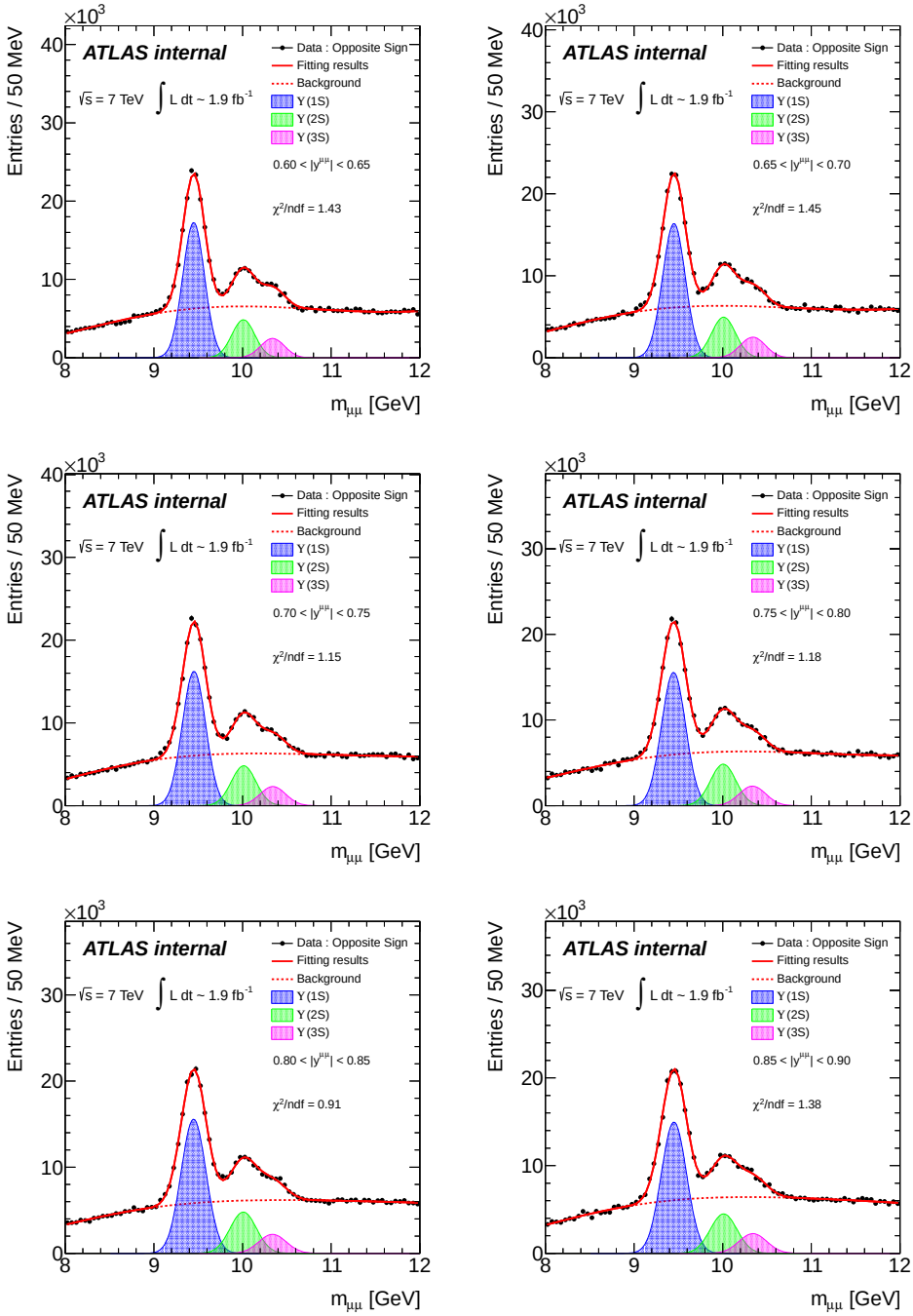
ATLAS internal
√s = 7 TeV ∫ L dt ~ 1.9 fb-1
Data : Opposite Sign
Fitting results
Background
Υ(1S)
Υ(2S)
Υ(3S)
0.60 < |yμμ| < 0.65
χ2/ndf = 1.43
0.65 < |yμμ| < 0.70
χ2/ndf = 1.45
0.70 < |yμμ| < 0.75
χ2/ndf = 1.15
0.75 < |yμμ| < 0.80
χ2/ndf = 1.18
0.80 < |yμμ| < 0.85
χ2/ndf = 0.91
0.85 < |yμμ| < 0.90
χ2/ndf = 1.38
Entries / 50 MeV
mμμ [GeV]
×10³

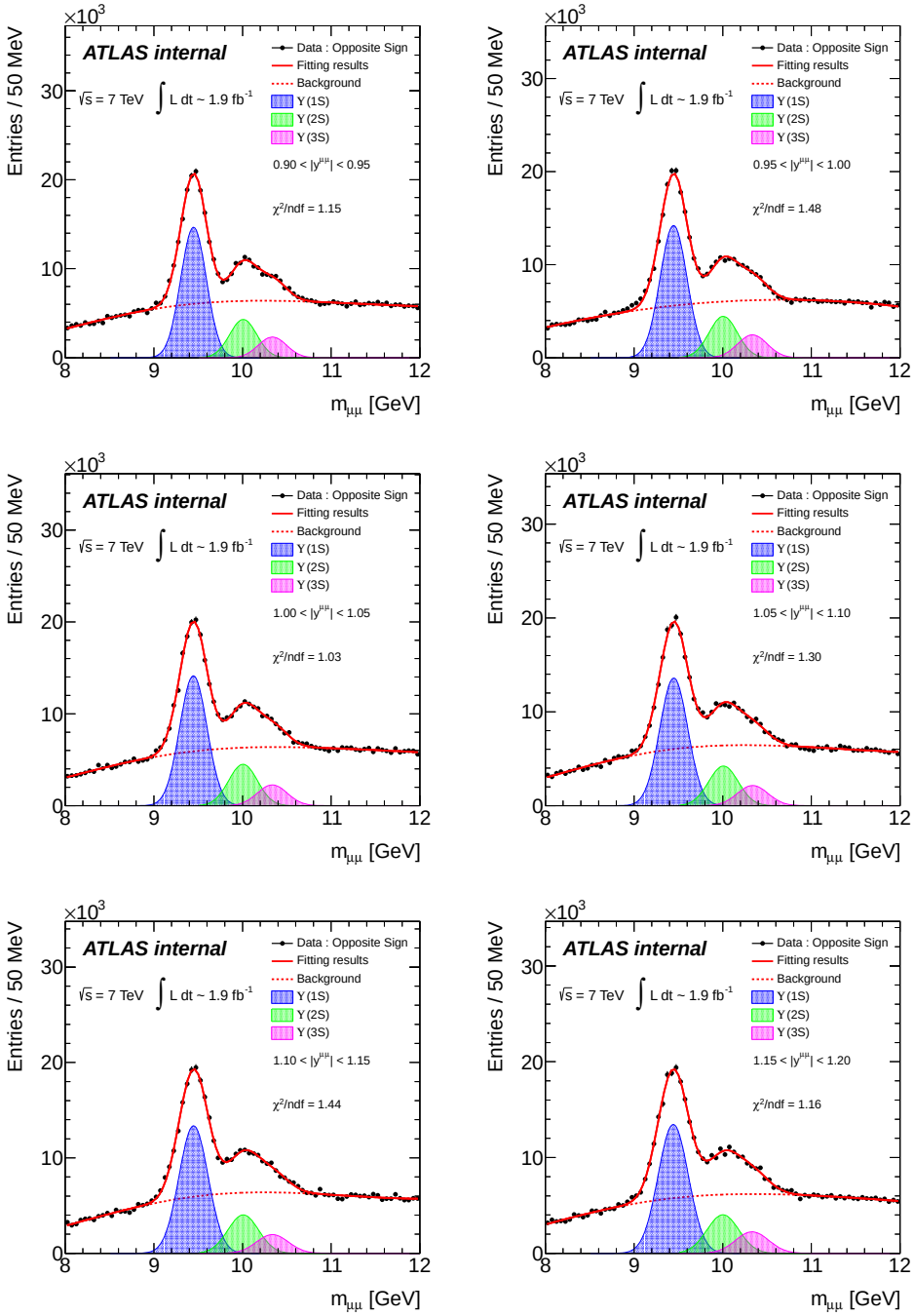
ATLAS internal
Data : Opposite Sign
Fitting results
Background
Υ(1S)
Υ(2S)
Υ(3S)
√s = 7 TeV ∫ L dt ~ 1.9 fb⁻¹
0.90 < |y^μμ| < 0.95
χ²/ndf = 1.15
0.95 < |y^μμ| < 1.00
χ²/ndf = 1.48
1.00 < |y^μμ| < 1.05
χ²/ndf = 1.03
1.05 < |y^μμ| < 1.10
χ²/ndf = 1.30
1.10 < |y^μμ| < 1.15
χ²/ndf = 1.44
1.15 < |y^μμ| < 1.20
χ²/ndf = 1.16
×10³
Entries / 50 MeV
m_μμ [GeV]

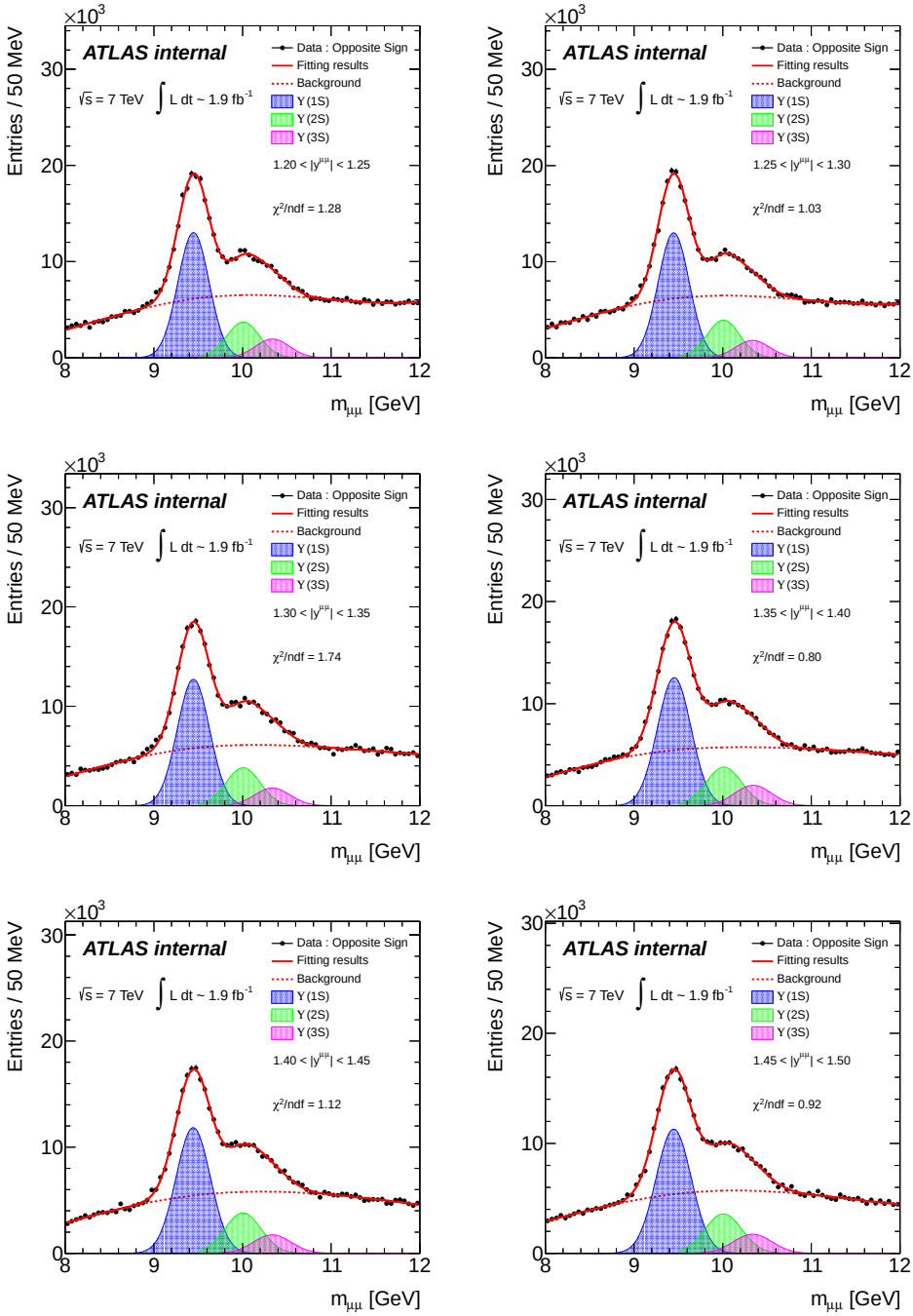
ATLAS internal
√s = 7 TeV ∫ L dt ~ 1.9 fb-1
Data : Opposite Sign
Fitting results
Background
Υ(1S)
Υ(2S)
Υ(3S)
1.20 < |yμμ| < 1.25
χ2/ndf = 1.28
1.25 < |yμμ| < 1.30
χ2/ndf = 1.03
1.30 < |yμμ| < 1.35
χ2/ndf = 1.74
1.35 < |yμμ| < 1.40
χ2/ndf = 0.80
1.40 < |yμμ| < 1.45
χ2/ndf = 1.12
1.45 < |yμμ| < 1.50
χ2/ndf = 0.92
Entries / 50 MeV
mμμ [GeV]
×10³

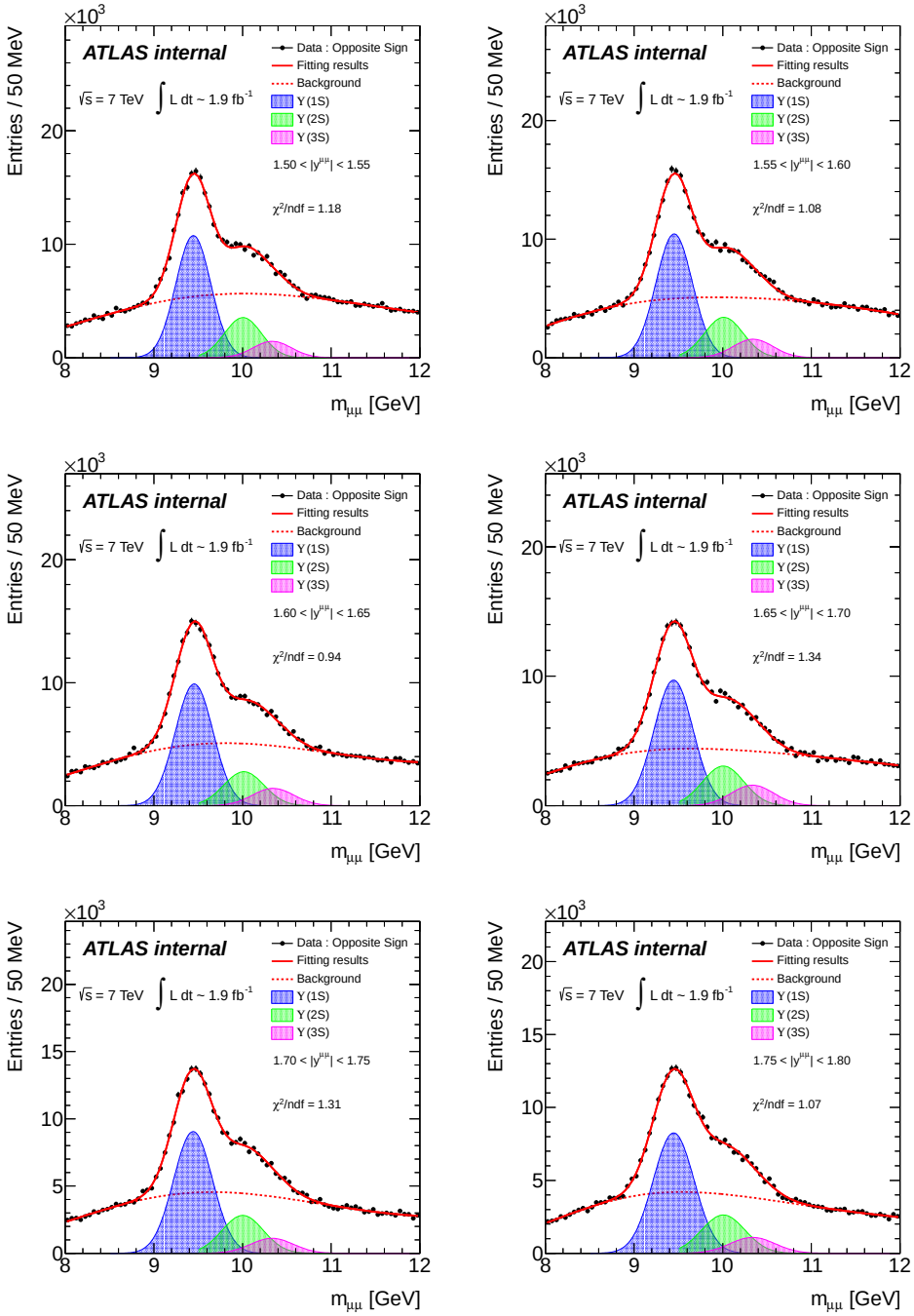
ATLAS internal
√s = 7 TeV ∫ L dt ~ 1.9 fb-1
Data : Opposite Sign
Fitting results
Background
Υ(1S)
Υ(2S)
Υ(3S)
1.50 < |yμμ| < 1.55
χ2/ndf = 1.18
1.55 < |yμμ| < 1.60
χ2/ndf = 1.08
1.60 < |yμμ| < 1.65
χ2/ndf = 0.94
1.65 < |yμμ| < 1.70
χ2/ndf = 1.34
1.70 < |yμμ| < 1.75
χ2/ndf = 1.31
1.75 < |yμμ| < 1.80
χ2/ndf = 1.07
Entries / 50 MeV
×10^3
mμμ [GeV]

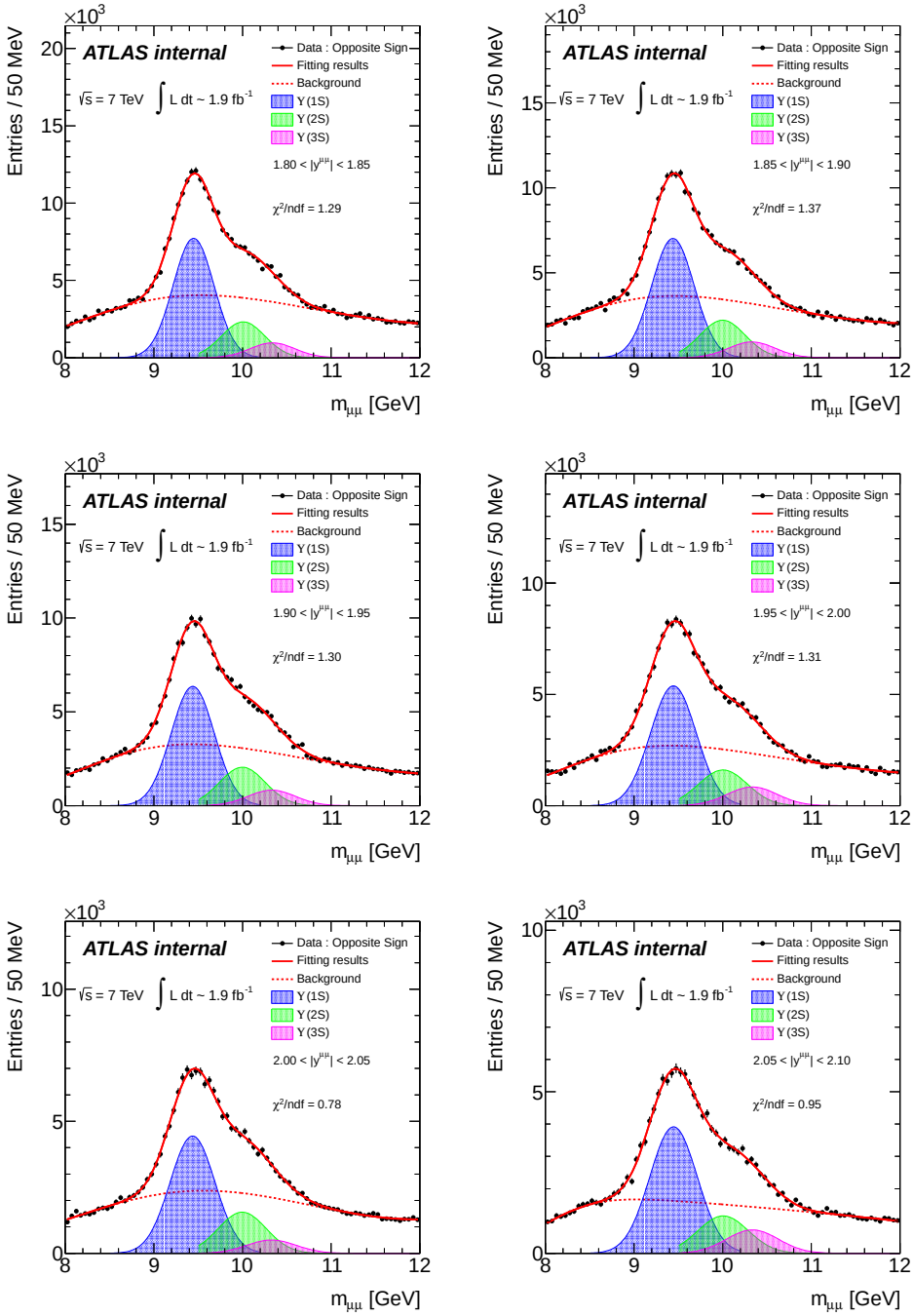
×10^3
Entries / 50 MeV
ATLAS internal
√s = 7 TeV ∫ L dt ~ 1.9 fb^-1
Data : Opposite Sign
Fitting results
Background
Υ(1S)
Υ(2S)
Υ(3S)
1.80 < |y^μμ| < 1.85
χ²/ndf = 1.29
1.85 < |y^μμ| < 1.90
χ²/ndf = 1.37
1.90 < |y^μμ| < 1.95
χ²/ndf = 1.30
1.95 < |y^μμ| < 2.00
χ²/ndf = 1.31
2.00 < |y^μμ| < 2.05
χ²/ndf = 0.78
2.05 < |y^μμ| < 2.10
χ²/ndf = 0.95
m_μμ [GeV]

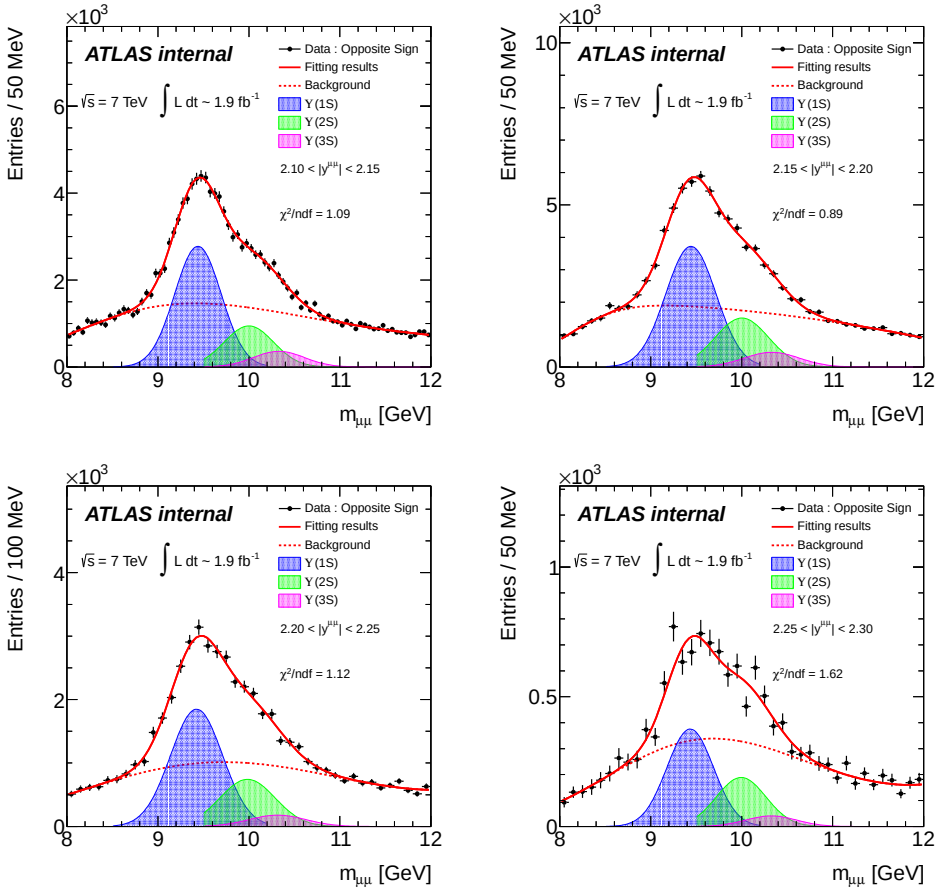
×10^3
ATLAS internal
Data : Opposite Sign
Fitting results
Background
Υ(1S)
Υ(2S)
Υ(3S)
√s = 7 TeV ∫ L dt ~ 1.9 fb^-1
2.10 < |y^μμ| < 2.15
χ²/ndf = 1.09
Entries / 50 MeV
m_μμ [GeV]
×10^3
ATLAS internal
Data : Opposite Sign
Fitting results
Background
Υ(1S)
Υ(2S)
Υ(3S)
√s = 7 TeV ∫ L dt ~ 1.9 fb^-1
2.15 < |y^μμ| < 2.20
χ²/ndf = 0.89
Entries / 50 MeV
m_μμ [GeV]
×10^3
ATLAS internal
Data : Opposite Sign
Fitting results
Background
Υ(1S)
Υ(2S)
Υ(3S)
√s = 7 TeV ∫ L dt ~ 1.9 fb^-1
2.20 < |y^μμ| < 2.25
χ²/ndf = 1.12
Entries / 100 MeV
m_μμ [GeV]
×10^3
ATLAS internal
Data : Opposite Sign
Fitting results
Background
Υ(1S)
Υ(2S)
Υ(3S)
√s = 7 TeV ∫ L dt ~ 1.9 fb^-1
2.25 < |y^μμ| < 2.30
χ²/ndf = 1.62
Entries / 50 MeV
m_μμ [GeV]

Appendix H

CP-odd Higgs Updated Results

In this section, we show some plots for the analysis using 2011 dataset with 1.9 fb^{-1} integrated luminosity.

Figure H.1 shows the variables, χ^2/n.d.f and $E_T^{cone20}/p_T(\mu)$, in the Likelihood Ratio selection.

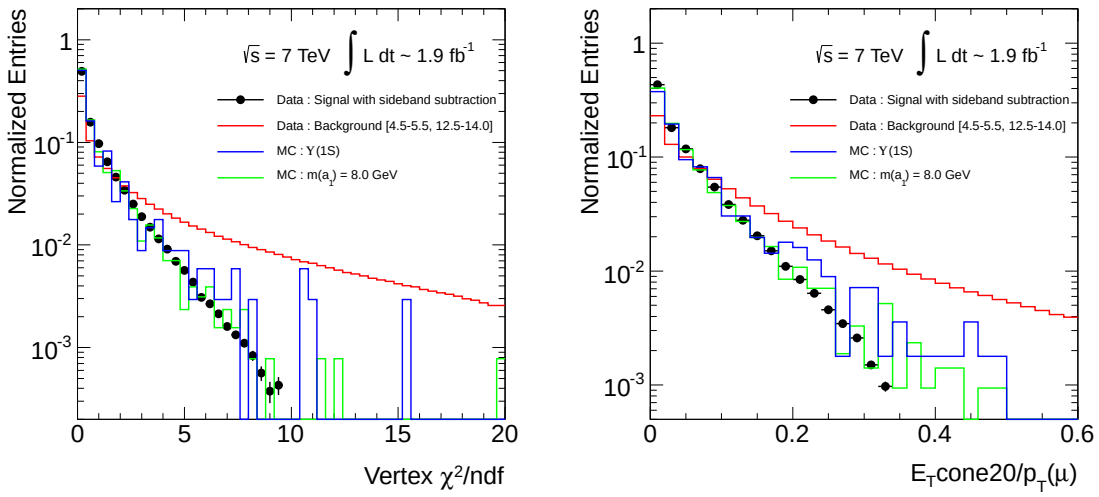

(a) (b)

Figure H.1: The variables for the Likelihood Ratio: (a) vertex χ^2/n.d.f; (b) $E_T cone20/p_T(\mu)$

The ratios for vertex χ^2/n.d.f and $E_T cone20/p_T(\mu_{1,2})$ are calculated by comparing the background and signal PDFs, and are parametrized by simple polynomials that are shown in Fig. H.2.

The signal-background separation power of the LR selection is shown in Fig. H.3(a), the signal efficiency versus background reject rate is shown in Fig. H.3(b), and Fig. H.3(c) shows the relation of $\varepsilon_{LR}(a_1)/\sqrt{N_{bkgd}}$ with the discriminating variable R. The optimized value of the R cut is also shown.

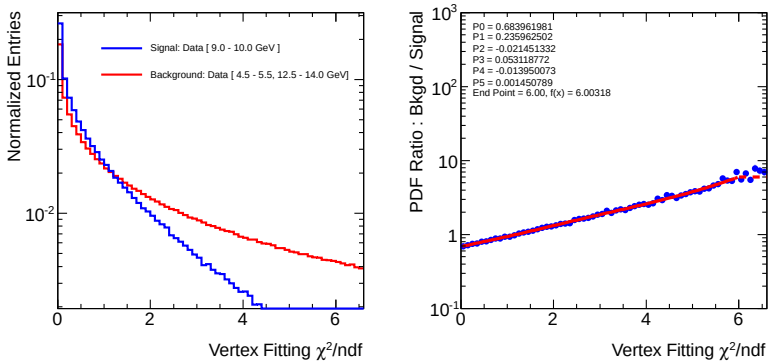

(a)

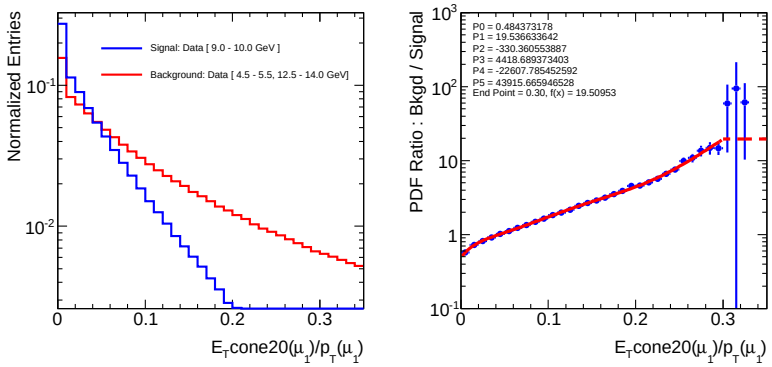

(b)

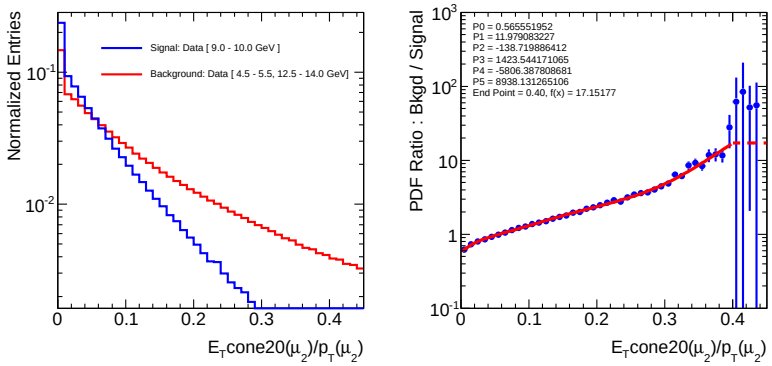

(c)

Figure H.2: The ratios of background to signal PDFs for (a) vertex χ^2/n.d.f; (b) $E_T cone20/p_T(\mu_1)$; and (c) $E_T cone20/p_T(\mu_2)$.

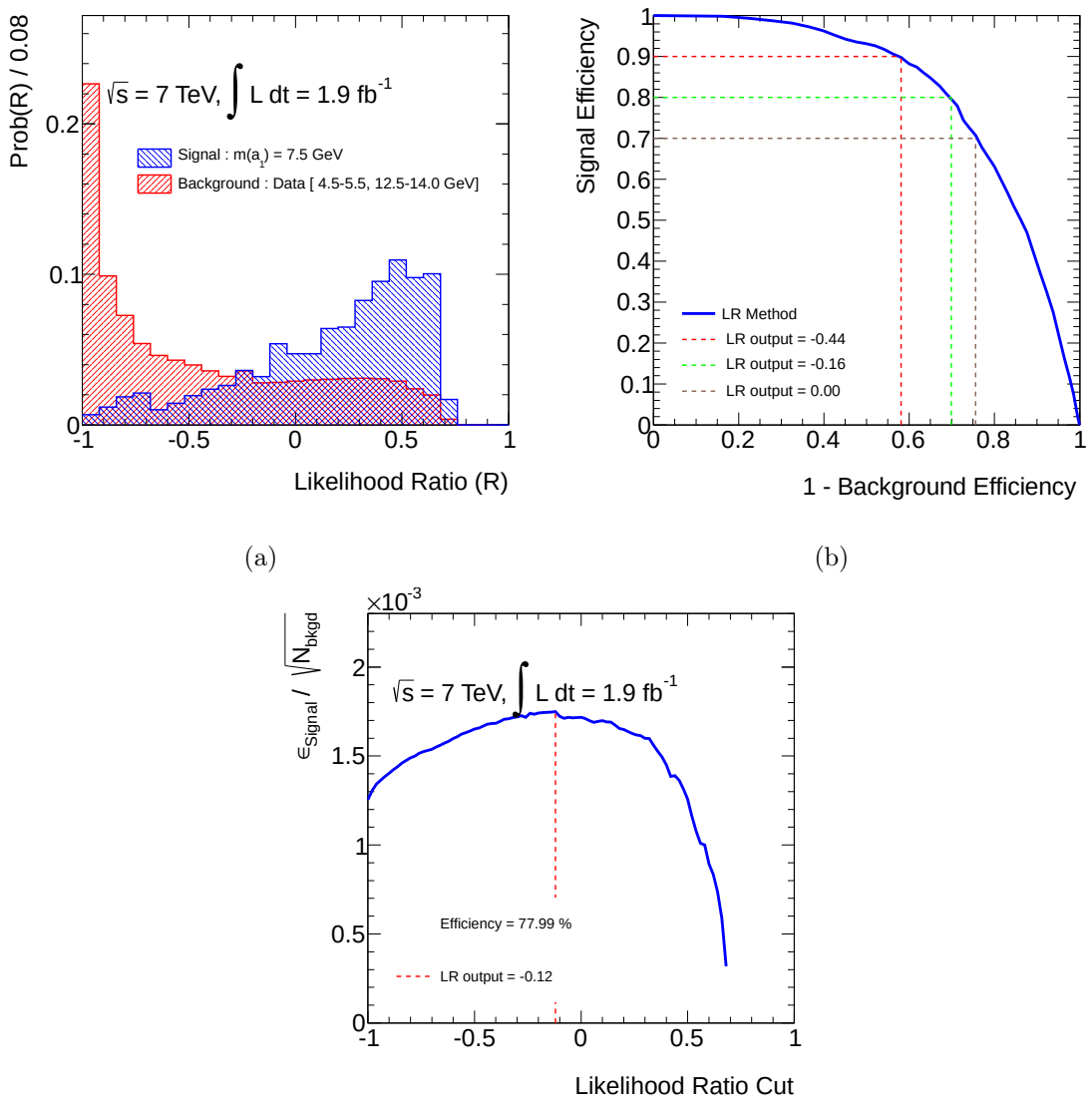

Figure H.3: (a) Separation power of the Likelihood Ratio distributions. (b) Signal efficiency versus background reject rate. (c) The relation of $\varepsilon_{LR}(a_1)/\sqrt{N_{bkgd}}$ with the discriminating variable R.